

THÈSE DE DOCTORAT  
DE L'UNIVERSITÉ PARIS-SACLAY  
PRÉPARÉE AU COMMISSARIAT À L'ÉNERGIE ATOMIQUE  
ET AUX ÉNERGIES ALTERNATIVES

ÉCOLE DOCTORALE n° 576  
Particules, Hadrons, Énergie, Noyau, Instrumentation,  
Image, Cosmos et Simulation (PHENIICS)  
Spécialité de doctorat : Instrumentation

**Conception de profileurs non intrusifs  
pour le faisceau de protons de ESS**

Par

**M. Florian Benedetti**

NNT :

*Thèse présentée et soutenue à Saclay, le 23 septembre 2019*

Composition du Jury :

Mme	GLORIA LUZÓN	Professeure Universidad de Zaragoza	(Rapporteur)
M.	PETER FODK	Chercheur senior GSI Darmstadt	(Rapporteur)
M.	PATRICK PUZO	Professeur Université Paris Sud	(Examineur)
M.	JULIEN PANCIN	Ingénieur-chercheur CEA Ganil	(Examineur)
M.	CYRILLE THOMAS	Ingénieur-chercheur ESS Lund	(Examineur)
Mme	ESTHER FERRER RIBAS	Ingénieure-chercheuse CEA Saclay	(Directrice de thèse)
M.	JACQUES MARRONCLE	Ingénieur-chercheur CEA Saclay	(Responsable de thèse)





# Acknowledgments



# Contents

Acknowledgments	i
<b>1 Brief introduction to sciences using neutrons</b>	<b>1</b>
1.1 Introduction . . . . .	3
1.2 History . . . . .	3
1.3 Neutron and neutron interaction with matter . . . . .	4
1.4 Application of neutron probes . . . . .	5
1.5 Neutron production . . . . .	7
1.5.1 Radioisotope sources . . . . .	7
1.5.2 Nuclear research reactors . . . . .	8
1.5.3 Spallation sources . . . . .	8
1.6 The need of a European Spallation Source . . . . .	10
1.7 Bibliography . . . . .	11
<b>2 European Spallation Source and beam diagnostic devices</b>	<b>13</b>
2.1 Introduction . . . . .	15
2.2 European Spallation Source . . . . .	15
2.3 ESS collaboration and ESS activities at CEA/IRFU . . . . .	17
2.4 ESS accelerator . . . . .	17
2.4.1 Ion source and Low Energy Beam Transport . . . . .	18
2.4.2 Radio Frequency Quadrupole . . . . .	19
2.4.3 Medium Energy Beam Transport and Drift Tube Linac . . . . .	20
2.4.4 Superconducting cavities . . . . .	20
2.5 Transport lines and target . . . . .	21
2.6 ESS neutron instruments . . . . .	22
2.7 Beam diagnostic overview . . . . .	24
2.7.1 Beam current monitor . . . . .	25
2.7.2 Beam position monitor . . . . .	26
2.7.3 Beam loss monitor . . . . .	26
2.8 Invasive beam profile measurements . . . . .	27
2.8.1 Interceptive screen . . . . .	27
2.8.2 Wire scanner . . . . .	28
2.8.3 SEM-Grid . . . . .	29
2.9 Non-invasive beam profile measurements . . . . .	29
2.9.1 Laser wire profiler . . . . .	29
2.9.2 Fluorescence Profile Monitor . . . . .	29
2.10 Ionization Profile Monitor and summary . . . . .	30
Bibliography . . . . .	33

<b>3</b>	<b>Prototype simulations and design</b>	<b>37</b>
3.1	Introduction . . . . .	39
3.2	ESS requirements . . . . .	40
3.3	IPM simulations overview . . . . .	41
3.4	Particle through matter . . . . .	42
3.4.1	Interaction of charged particles with matter . . . . .	42
3.4.2	Electron ion pairs production . . . . .	43
3.4.3	Calculation . . . . .	45
3.4.4	Pressure uniformity . . . . .	47
3.5	Extraction field . . . . .	48
3.5.1	Maxwell equations at steady state . . . . .	49
3.5.2	Solving Poisson's equation . . . . .	50
3.5.3	COMSOL . . . . .	52
3.5.4	Criteria . . . . .	54
3.5.5	IPM polarity . . . . .	57
3.5.6	IPM cross-interaction . . . . .	58
3.5.7	Field corrections . . . . .	60
3.5.8	Grid . . . . .	63
3.6	Initial momentum . . . . .	65
3.6.1	Thermal distribution . . . . .	65
3.6.2	Momentum transfer during ionization process . . . . .	65
3.7	Space charge effect . . . . .	67
3.7.1	Lorentz transformation of electromagnetic fields . . . . .	67
3.7.2	ESS/CEA Space Charge algorithm . . . . .	68
3.7.3	Results . . . . .	68
3.8	Readout systems . . . . .	70
3.8.1	Ramo-Shockley theorem . . . . .	70
3.8.2	Strips based detection . . . . .	70
3.8.3	Interaction of low energy particles . . . . .	72
3.8.4	Semiconductor based detection . . . . .	73
3.8.5	MCP based detection . . . . .	74
3.9	Summary . . . . .	76
	Bibliography . . . . .	77
<b>4</b>	<b>Prototype tests at IPHI</b>	<b>83</b>
4.1	Introduction . . . . .	86
4.2	Preliminary tests of silicon detector . . . . .	86
4.2.1	IRMA . . . . .	86
4.2.2	Test setup . . . . .	87
4.2.3	Results and limitations . . . . .	88
4.3	IPM design overview . . . . .	89
4.3.1	IPM . . . . .	89
4.3.2	MCP . . . . .	91
4.3.3	Camera . . . . .	91
4.3.4	Strips . . . . .	92
4.3.5	CAMEL board and FASTER system . . . . .	93
4.3.6	High voltage power supplies . . . . .	93
4.3.7	Control System . . . . .	94

4.3.8	Test bench . . . . .	95
4.3.9	Reference measurement . . . . .	96
4.4	IPHI and test campaigns . . . . .	97
4.4.1	IPHI accelerator . . . . .	97
4.4.2	Overview of the two test campaigns . . . . .	98
4.5	Processing data . . . . .	99
4.5.1	Processing camera . . . . .	99
4.5.2	Processing strip . . . . .	100
4.5.3	Processing scintillator screen data and review of the reference measurements . . . . .	101
4.6	Beam environnement characterization . . . . .	102
4.6.1	Vacuum analysis . . . . .	102
4.6.2	Beam position . . . . .	103
4.6.3	Beam current . . . . .	105
4.6.4	Beam tuning . . . . .	106
4.7	IPM characterization . . . . .	107
4.7.1	Beam size convergence . . . . .	107
4.7.2	Cross interaction . . . . .	108
4.7.3	Comparison size . . . . .	109
4.7.4	Field uniformity . . . . .	110
4.7.5	Grid . . . . .	111
4.7.6	MCP . . . . .	112
4.7.7	Phosphorus screens . . . . .	112
4.7.8	Extrapolation to ESS conditions with the strips IPM . . . . .	114
4.7.9	Extrapolation to ESS conditions with the optical IPM . . . . .	115
4.7.10	Electron measurement with MCP . . . . .	116
4.8	Summary . . . . .	117
4.9	Bibliography . . . . .	119
<b>5</b>	<b>Conclusion and outlook</b>	<b>123</b>
	The cold NPM project for ESS . . . . .	125
	Preliminary design review . . . . .	125
	Prototypes and test bench development . . . . .	126
	Beam tests at IPHI . . . . .	126
	Ongoing works and final design . . . . .	127
	Background signal estimation . . . . .	127
	MCP calibration . . . . .	128
	Remote acquisition system . . . . .	128
	Final IPM design and production . . . . .	129
	Bibliography . . . . .	133
	<b>Acronyms</b>	<b>135</b>
	<b>List of Figures</b>	<b>143</b>
	<b>List of Tables</b>	<b>145</b>
	<b>Résumé en Français</b>	<b>147</b>

Drawings of the prototypes and test bench	149
Conference proceeding and scientific documents	157
Abstract	

# Chapter 1

## Brief introduction to sciences using neutrons





## Contents

---

<b>1.1 Introduction</b> . . . . .	<b>3</b>
<b>1.2 History</b> . . . . .	<b>3</b>
<b>1.3 Neutron and neutron interaction with matter</b> . . . . .	<b>4</b>
<b>1.4 Application of neutron probes</b> . . . . .	<b>5</b>
<b>1.5 Neutron production</b> . . . . .	<b>7</b>
1.5.1 Radioisotope sources . . . . .	7
1.5.2 Nuclear research reactors . . . . .	8
1.5.3 Spallation sources . . . . .	8
<b>1.6 The need of a European Spallation Source</b> . . . . .	<b>10</b>
<b>1.7 Bibliography</b> . . . . .	<b>11</b>

---

## 1.1 Introduction

This chapter introduces the general context behind the European Spallation Source (ESS), which is a facility in construction in Lund (Sweden). As every spallation source, it will make use of a particle accelerator and a heavy metal target to create neutrons. Even if, the work presented in this thesis strictly concerns the accelerator part alone, it is important to give a quick overview of neutron science to answer the following question: "Why building a 1.8 €billion euros neutron source is crucial for science in Europe?"

After a brief historical review about the neutron discovery, this chapter presents what a neutron is and why its properties are interesting for probing matter and structures. A concrete application of neutron science will be illustrated. Finally, the different ways of producing neutrons are also briefly presented as well as the advantages and drawbacks of each method.

## 1.2 History

Historically, the neutron was the last component of the atom to be discovered. The electron was discovered first by J.J. Thomson in 1897 using a vacuum tube. The electrons are elementary negatively charged components of all atoms. Since, the atoms are neutral there must be an other component of the atom with an opposite charge. However, Thomson was not able to really answer the question of how the atom is structured.

Almost in parallel, the discovery of natural radioactivity by H. Becquerel in 1896 and M. and P. Curie in 1898 opened a new field of possibility for physical experiments. In 1909, E. Rutherford observed that atoms consist of nuclei that concentrate all mass and charges [1]. From this observation he proposed a new atomic model, later improved by N. Bohr. Then in 1919, he observed that light atoms eject hydrogen when they are impinged by alpha particles: the proton was discovered. However, this experiment does not explain the differences of mass and of charge between atoms.

In 1930, W. Bothe and H. Becker found out that neutral radiations were emitted when beryllium, boron or lithium were bombarded by alpha particles (original paper

[2]), but they were unable to understand, and actually misinterpreted, the nature of these neutral particles.

By means of an ionization chamber, few years later, I. and F. Joliot-Curie observed that the neutral radiation, produced as described above, generated protons when it impacted on a light hydrogen-based compound. However, they concluded that the proton ejection could be due to a photon scattering (similar to Compton scattering which was discovered 8 years before) [3].

In 1932, J. Chadwick performed a more accurate measurements of proton recoils for several light elements [4]. He discarded the hypothesis of an elastic collision with gamma rays on the basis of energy and momenta conservation. The neutral particle had to have a mass close to that of protons: the neutron was discovered.

### 1.3 Neutron and neutron interaction with matter

A neutron is a non-elementary particle with no charge. Its mass is  $939.56 \text{ MeV}/c^2$  ( $1.67 \cdot 10^{-27} \text{ kg}$ ). A neutron does not have the strong electromagnetic interaction with the electrons of atoms, unlike charged particles and photons. Neutrons can travel long distances without major interactions. The neutron has a spin of  $\frac{1}{2}$  and a low magnetic moment. Therefore it is possible to polarize a neutron beam. The magnetic moment allows the interaction with magnetic fields in the structure of matter. A neutron interacts mainly with the elements of the nucleus through strong interactions. A free neutron has a lifetime of 881.5s and decays into a proton, an electron, and an antineutrino. Following the principle of wave-particle duality, neutrons can be described both as particles and as waves. By exploiting the De Broglie equation, the energy  $E_n$  and wavelength  $\lambda$  associated to a neutron are related by:

$$E_n = \frac{h^2}{2m_n\lambda^2}$$

It is convenient to classify neutrons on the basis of the two above mentioned observables as "relativistic", "fast", ... as shown in Table 1.1.

**Table 1.1** – *Neutron classification according to the neutron energy and wavelength. Different sources report different conventions. The range limits here presented are taken from [5].*

Characteristic	Energy	Speed	Wavelength
Fast neutrons	> 1 MeV	> $1.38 \cdot 10^7 \text{ m/s}$	> $2.86 \cdot 10^{-4} \text{ \AA}$
Intermediate neutrons	> 1 eV	> $1.38 \cdot 10^4 \text{ m/s}$	> 0.28 $\text{ \AA}$
Epithermal neutrons	> 100 meV	> $4.37 \cdot 10^3 \text{ m/s}$	> 0.9 $\text{ \AA}$
Thermal neutrons	> 12 meV	> $1.51 \cdot 10^3 \text{ m/s}$	> 0.28 $\text{ \AA}$
Cold neutrons	> 0.12 meV	> 151 m/s	> 26 $\text{ \AA}$
Ultra cold neutrons	< 300 neV	< 6 m/s	< 500 $\text{ \AA}$

Fast neutrons can be slowed down to the desired energy with the help of moderators. These moderators are mainly composed of light elements. Indeed the energy transfer during elastic scattering on light elements is efficient. The most common moderators are hydrogen, water, heavy water and graphite.

There are several processes behind the interaction of neutrons with matter [6] that can be classified in two categories: collision or absorption processes. In a collision where the nucleus structure remains the same. The collision can be:

- Elastic: in a (n,n) collision the kinetic energy of the system is preserved. The neutron can transfer part of its kinetic energy to the nucleus. If so, the direction of the neutron is changed.
- Inelastic: in (n,n') collision the kinetic energy of the system is not preserved and therefore the target nucleus is left in an excited state.

In absorption processes, the nucleus structure is altered by the neutron. Such processes can be subdivided as follows:

- Radiative capture: in (n, $\gamma$ ) reactions, the neutron is captured by the nucleus followed gamma emission
- Particle emission: in (n,p), (n, $\alpha$ ), ... but also (n,2n), (n,np),... reactions, the compound nucleus ejects one or more nucleons, or even a cluster of nucleons
- Fission: this phenomenon concerns heavy elements which, under the impact of a neutron, separate into (most of the times) two lighter elements

The above listed processes occur for incident neutron energies up to hundreds of MeV. The total neutron cross section (reaction probability) for a certain isotope, is the sum of all previous interaction cross sections.

Above few hundreds MeV (pion production threshold) more interactions take place. The measurements of neutron cross sections remain a fundamental aspect of nuclear physics and application.

## 1.4 Application of neutron probes

Soon after neutron discovery in 1932, neutron scattering was found to be a unique tool for probing matter. The use of advanced neutron scattering methods for investigating different materials became really popular in the 1960s, with the rise of research reactors. Since, as seen in the previous paragraph, different neutron energies correspond to different wavelengths, neutrons of diverse speeds can access diverse type of information. The energy selection influences also the selection of the field of application: nuclear science or engineering. More techniques based on neutron scattering have been developed, each one relying on the peculiar characteristics of the incident neutral nucleons. In the present section, the different techniques are introduced in simplified manner to illustrate the huge possibilities provided by neutron scattering. A more rigorous approach can be found on the websites of the various institute specialized in this domain [7–9].

Neutron radiography is an imaging method that measures the transmission of neutrons in a sample. This method is similar to the well-known X-ray radiography. However, neutrons are more sensitive to light elements whereas for X-rays the higher the atomic number of the material they pass through, the more efficient is their attenuation. Neutrons have the ability to probe structure deeply and give good contrasts on dense materials. Neutron radiography is therefore an interesting complement to the X-rays one and these two methods are often combined. Its applications are extremely varied: from explosives imaging to archaeology. For instance, Fig. 1.1 shows a comparison between X-ray and neutron radiography performed on an Indonesian dagger sheath. One can see that the neutrons give a good information of the internal

wooden structure whereas the X-rays allow a fine detail of the metallic surface of the sheath.

Reflectometry is mainly used to characterize the surface of samples such as thin films, interfaces and layered structures. In reflectometry, a monochromatic neutron beam is projected on the surface of the sample to be tested. The reflection profile is measured as a function of the incidence angle and neutron energy.

Diffraction is a wide family of techniques for studying the diffraction pattern of a sample subjected to a neutron flux. The scale of measurement is in the order of nanometer to below Ångström range. This technique is mainly used to study the properties of crystals and powders.

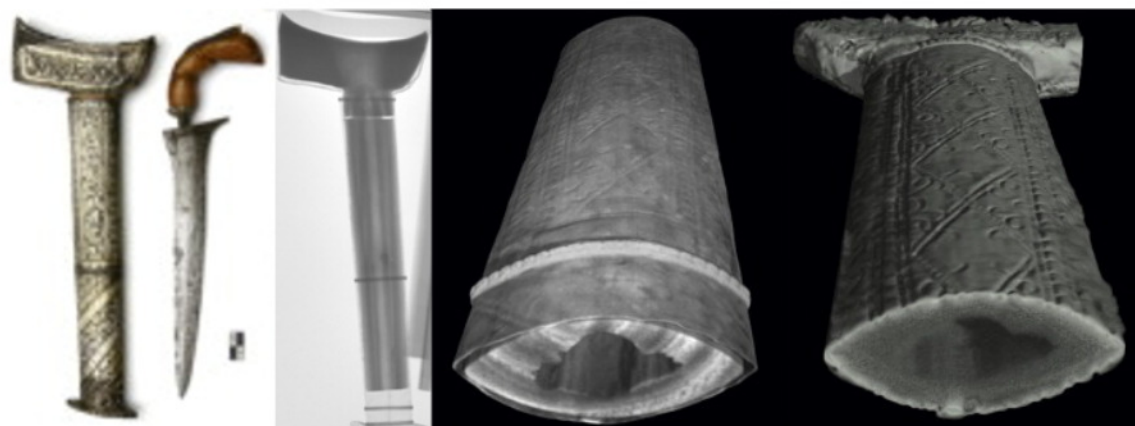


**Figure 1.1** – *Neutron and X-ray radiography of a dagger sheath. From left to right: the imaged sheath, neutron transmission image, neutron tomography and X-ray tomography [10]*

The Small Angle Neutron scattering (SANS) is a specific diffractive and reflective techniques and is used to probe nanostructures. The method is very interesting for studying molecules, polymers, drugs... The typical setup of a SANS experiment is as follows: a collimated neutron beam, selected in speed with a monochromator, is sent directly to the sample. Some of the incident neutrons are deflected due to elastic collisions. The angle between the deflected neutrons and the beam is measured by mean of a 2D detector located several meters further along the beam axis.

The latest technique is neutron spectrometry which consists in measuring the energy of the neutrons after an inelastic scattering on the sample. Several setup are possible to characterize scattered neutrons: Time of Flight (ToF) measurement, triple-axis method, spin echo measurement and backscattering spectrometry. Each of these detections covers different spatial and temporal ranges. For instance, ToF measurements are particularly suitable for short timescale whereas spin echo methods have very good resolutions at low neutron energies.

All the methods presented above can be combined together to perform more advanced measurements. Fig. 1.2 shows the different methods using neutrons with the scale of the different time and wavelength magnitudes. To take advantage of these methods it is necessary to have access to a neutron source, and to be concise, the brighter the source, the more efficient (in terms of statistics acquired in a certain time and therefore accuracy) the measurement.



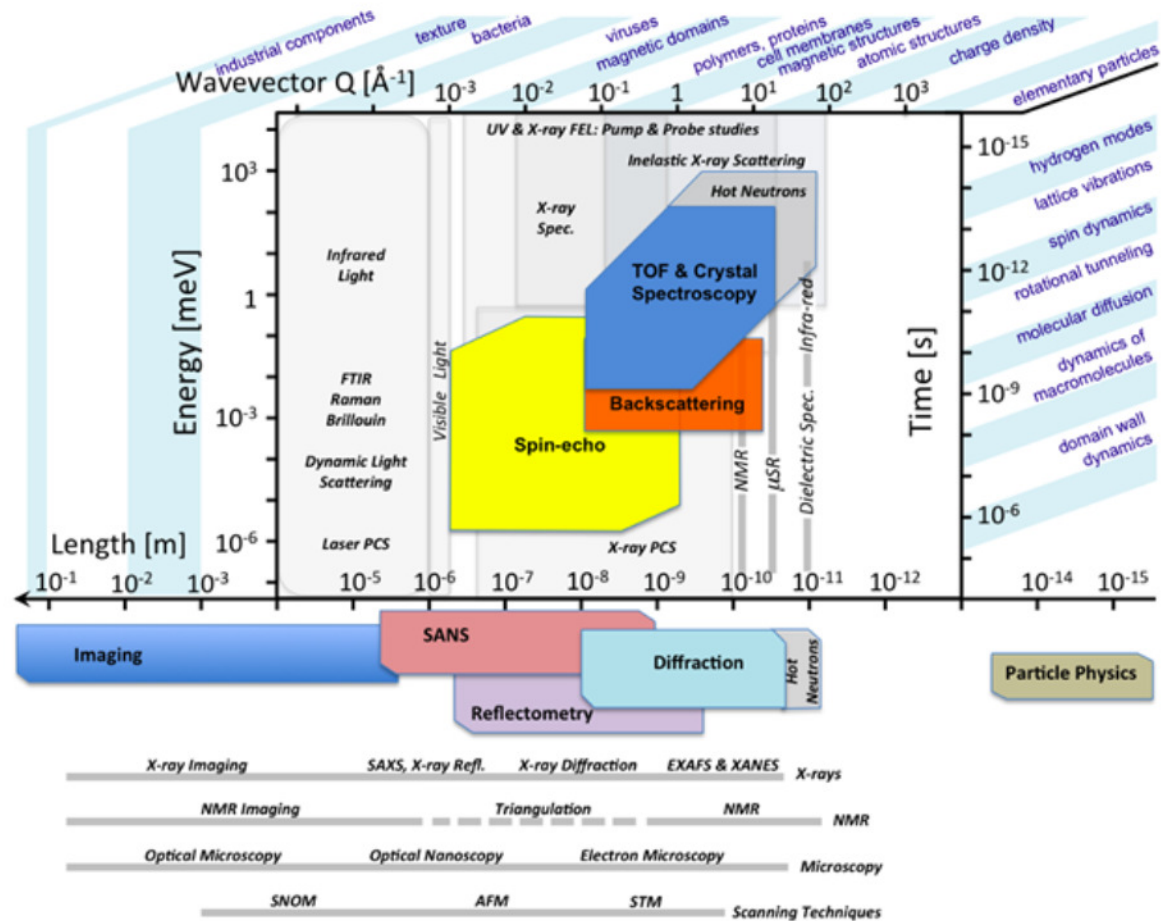


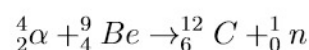
Figure 1.2 – Ranges of distances and times of existing neutron scattering techniques [11].

## 1.5 Neutron production

Producing neutrons is not a trivial task compared to producing charged particles or even photons. The following sections report on a non exhaustive list of neutron sources.

### 1.5.1 Radioisotope sources

The first neutron sources were based on radionuclides. Two distinct types of sources can be used. The first one is based on  $\alpha$  or  $\gamma$  emitters, generally encapsulated in Beryllium, Lithium or Boron media, leading to the this nuclear reaction for instance:



This type of source is inexpensive but its activity depends on the alpha emitter activity and the quality of the mixture.

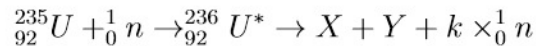
The second type of source is based on radioisotopes that undergo spontaneous fission decays. The amount of neutrons created during the fission depends on the radioelement. The most commonly used spontaneous fission source is Californium-252 that emits around  $2.314 \cdot 10^6$  neutrons per second per microgram and has a half

life of 2.63 years.  $^{252}\text{Cf}$  is a synthesized element usually created in nuclear reactors, so it is expensive to produce.

The main advantage of these sources are their compactness and their "ease of use". They are suitable for small size experiments, but do not scale for larger experiments. For this reason, they were quickly overtaken by research reactors.

### 1.5.2 Nuclear research reactors

In the following only binary fission is considered. A  $^{235}\text{U}$  nucleus splits into two lighter nuclei under the impact of a neutron. The fission reaction also leads to neutron emission and energy release:



with the fission fragments  $X$  and  $Y$ , and  $k$  the number of neutrons released during the fission reaction. In conventional reactors, the neutrons are thermalized in order to increase the probability of further fissions on other Uranium-235 nuclei, creating a chain reaction. In average, each fission of an  $^{235}\text{U}$  nucleus generates around 2.5 neutrons.

The fission reaction is the basis of nuclear power plants and research reactors used to produce neutrons. Currently, it is the most widely used method to produce steady state intense neutron beams. The moderation of neutrons is done directly in the reactor pool. Some reactors can work in pulsed mode, but it is not straightforward, whilst it is more efficient using neutron chopper afterward if neutron time of flight measurements are needed.

About ten research reactors dedicated to users are open in Europe, two of them are located in France:

- The Laue-Langevin Institute (ILL): an international facility based on a 58.3 MW high flux reactor.
- The Léon Brillouin Laboratory (LLB): a national facility based on a 14 MW high flux reactor.

The number of users for both these facilities represents one third of the total number for all European neutron facilities.

Fusion reactions also produce neutrons, but the current technology does not allow exploitation as a neutron source.

### 1.5.3 Spallation sources

The term spallation defines the process of neutrons production by bombarding a target with energetic heavy particles (protons, deuterons, neutrons). The description of this model was proposed by R. Saber in 1946 [12]. The process takes place in two stages. When the incident particle has sufficient energy, typically between 200 MeV and a few GeV, it can interact with several nucleons of a nucleus per intranuclear cascade. In this process, nucleons are ejected from the nucleus. After a cascade, the nucleus is in an excited state that can lead to several forms of de-excitation: mainly fission and evaporation of light elements. Fig. 1.3 illustrates the spallation process.

The neutrons are generated with a wide energy spectrum whose maximum energy is slightly below the energy of the incident particle energy. The number of neutrons produced by spallation depends on the properties of the target and the incident

particle. A dense material stops most of the emitted particles, except gammas and neutrons. The most popular materials are Tungsten, Lead and Mercury as well as actinides<sup>1</sup>. The optimal energy to trigger spallation reactions is between 2 GeV and 5 GeV.

As already mentioned, a spallation neutron source uses an accelerator and a target to produce neutrons following the process described above. A spallation source is totally controlled by its accelerator.

The first studies of this type of source were carried out in the early 1970s and the first generation sources were built in the late 1970s [13]. In Europe the first major spallation source was ISIS (UK) inaugurated in 1985 [14]. These sources met success and a new generation of spallation sources was considered. The second generation sources were achieved in 2000-2010 with SNS (ORNL, USA) [15], JSNS (J-PARC, Japan) [16] and CSNS (China) [17]. However, no major second-generation source has been built in Europe<sup>2</sup>.

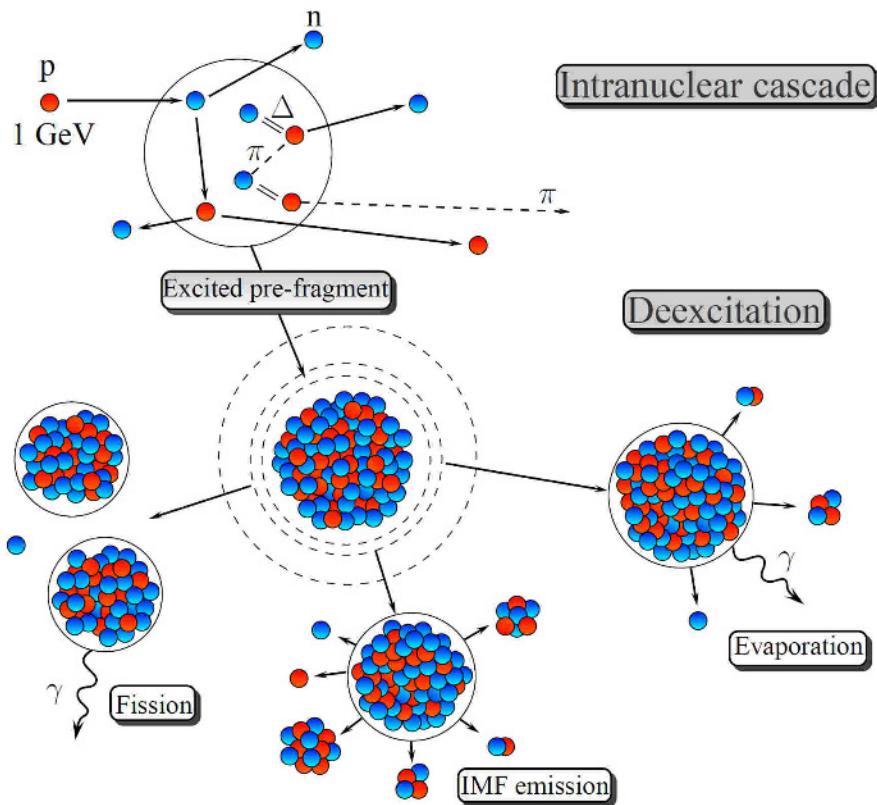


**Figure 1.3** – Schematic view of the spallation process [19]. The incident protons interact with nucleons of the target. An intranuclear cascade occurs leaving the target atom in an excited state. Depending on the properties of the excited nucleus, different de-excitation process may occur. IMF stands for intermediate mass fragment.

1. Actinides should be avoided because they lead to unwanted fissions.

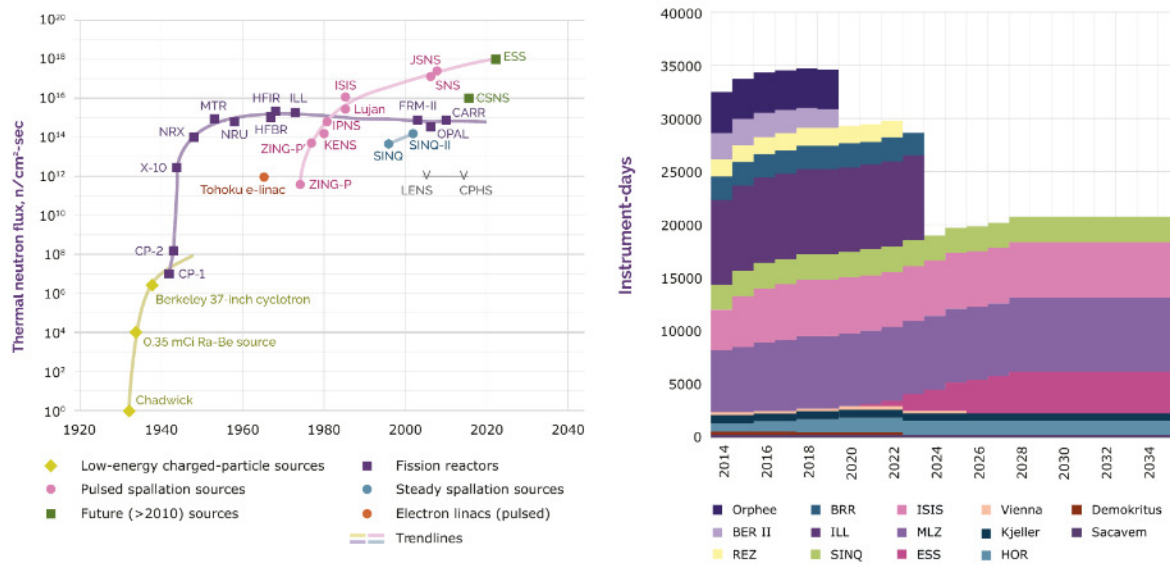
2. SINQ [18] (PSI, Switzerland) is not considered since it is a steady state spallation source.

## 1.6 The need of a European Spallation Source

Neutron probe is a popular tool in the European scientific community and for a long time Europe was a leader in neutron production. However, the future does not look so good with a decrease of the time access on neutron lines for scientists. These are the conclusions of an European Strategy Forum on Research Infrastructures (ESFRI) report in 2016 [20].

The majority of neutron sources is based on reactors built before the 1980s. The LLB reactor is 39 years old whereas ILL reactor diverged in 1967. In Europe, despite the success of ISIS<sup>3</sup>, no second generation of pulsed neutron source like SNS has been built. At the same time, only few new reactors have been built in recent years. Most neutron sources will be shut down within less than 20 years.

The European Spallation Source (ESS) is a project of a new facility delivering an intense pulsed neutron source. ESS is a crucial project to maintain the level of expertise of neutron users in Europe and to stimulate a renewal in neutron production, both in the form of new research reactors and accelerator-driven sources.



(a) Evolution of thermal neutron sources from the neutron discovery to a near future. (b) Evolution of the European neutron facilities over the next 15 years.


Figure 1.4 – Status and outlook of neutron sources (from the ESFRI report) [20].

3. ISIS was supposed to operate during 20 years but is still running after 35 years.



## 1.7 Bibliography

### References

- [1] E. Rutherford. “The scattering of alpha and beta particles by matter and the structure of the atom”. In: *Phil. Mag. Ser.6* 21 (1911), pp. 669–688. DOI: 10.1080/14786440508637080 (cit. on p. 3).
- [2] W. Bothe and H. Becker. “Künstliche Erregung von Kern- $\gamma$ -Strahlen”. In: *Zeitschrift für Physik* 66.5 (May 1930), pp. 289–306. ISSN: 0044-3328. DOI: 10.1007/BF01390908. URL: <https://doi.org/10.1007/BF01390908> (cit. on p. 4).
- [3] Irène Curie and F. Joliot. “Preuves expérimentales de l’existence du neutron”. In: *J. Phys. Radium* 4.1 (1933), pp. 21–33. DOI: 10.1051/jphysrad:019330040102100 (cit. on p. 4).
- [4] J. Chadwick. “The Existence of a Neutron”. In: *Proceedings of the Royal Society A: Mathematical, Physical and Engineering Sciences* 136.830 (June 1932), pp. 692–708. DOI: 10.1098/rspa.1932.0112 (cit. on p. 4).
- [5] *Neutron Physics*. Paul Scherrer Institut PSI. 2019. URL: <https://www.psi.ch/de/niag/neutron-physics> (visited on 07/01/2019) (cit. on p. 4).
- [6] William R. Leo. *Techniques for Nuclear and Particle Physics Experiments*. Springer Berlin Heidelberg, 1994. DOI: 10.1007/978-3-642-57920-2 (cit. on p. 5).
- [7] *Formation Annuelle à la Neutronique*. Laboratoire Léon Brillouin. 2019. URL: <http://www-llb.cea.fr/fanLLB/index.php> (visited on 07/01/2019) (cit. on p. 5).
- [8] *Neutron techniques*. Institut Laue-Langevin. 2019. URL: <https://www.iill.eu/neutrons-for-society/neutron-techniques/> (visited on 07/01/2019) (cit. on p. 5).
- [9] *ISIS Instruments*. ISIS Neutron and Muon Source. 2019. URL: <https://www.isis.stfc.ac.uk/Pages/Instruments.aspx> (visited on 07/01/2019) (cit. on p. 5).
- [10] Eberhard H. Lehmann and David Mannes. “Wood investigations by means of radiation transmission techniques”. In: *Journal of Cultural Heritage* 13.3, Supplement (2012). Wood Science for Conservation, S35–S43. ISSN: 1296-2074. DOI: <https://doi.org/10.1016/j.culher.2012.03.017>. URL: <http://www.sciencedirect.com/science/article/pii/S1296207412000660> (cit. on p. 6).
- [11] *Science Using Neutrons*. European Spallation Source. 2019. URL: <https://europeanspallationsource.se/science-using-neutrons> (visited on 07/01/2019) (cit. on p. 7).
- [12] R. Serber. “Nuclear Reactions at High Energies”. In: *Phys. Rev.* 72 (11 Dec. 1947), pp. 1114–1115. DOI: 10.1103/PhysRev.72.1114. URL: <https://link.aps.org/doi/10.1103/PhysRev.72.1114> (cit. on p. 8).
- [13]  Klein et al. “Spallation neutron sources”. In: *Proc. 1994 Linac Conf.* (Tsukuba, Japan). 1994, pp. 322–327 (cit. on p. 9).

- [14] J.W.G. Thomason. “The ISIS Spallation Neutron and Muon Source—The first thirty-three years”. In: *Nuclear Instruments and Methods in Physics Research Section A: Accelerators, Spectrometers, Detectors and Associated Equipment* 917 (2019), pp. 61–67. ISSN: 0168-9002. DOI: <https://doi.org/10.1016/j.nima.2018.11.129>. URL: <http://www.sciencedirect.com/science/article/pii/S0168900218317820> (cit. on p. 9).
- [15] T. E. Mason. “The Spallation Neutron Source: A Powerful Tool for Materials Research”. In: *AIP Conference Proceedings*. AIP, 2005. DOI: 10.1063/1.1949491 (cit. on p. 9).
- [16] S. Ikeda. “Japanese spallation neutron source”. In: *Applied Physics A* 74.1 (Dec. 2002), s15–s17. ISSN: 1432-0630. DOI: 10.1007/s003390201749. URL: <https://doi.org/10.1007/s003390201749> (cit. on p. 9).
- [17] Hesheng Chen and Xun-Li Wang. “China’s first pulsed neutron source”. In: *Nature Materials* 15.7 (July 2016), pp. 689–691. DOI: 10.1038/nmat4655 (cit. on p. 9).
- [18] Werner Wagner et al. “Status of SINQ, the only MW spallation neutron source—highlighting target development and industrial applications”. In: *Nuclear Instruments and Methods in Physics Research Section A: Accelerators, Spectrometers, Detectors and Associated Equipment* 562.2 (2006). Proceedings of the 7th International Conference on Accelerator Applications, pp. 541–547. ISSN: 0168-9002. DOI: <https://doi.org/10.1016/j.nima.2006.02.026>. URL: <http://www.sciencedirect.com/science/article/pii/S0168900206002385> (cit. on p. 9).
- [19] Thomas Gorbinet. “Study of the spallation reactions  $^{136}\text{Xe} + \text{p}$  and  $^{136}\text{Xe} + ^{12}\text{C}$  at 1 GeV per nucleon at the GSI facility (Darmstadt, Germany)”. Theses. Université Paris Sud - Paris XI, 2011. URL: <https://tel.archives-ouvertes.fr/tel-00660583> (cit. on p. 9).
- [20] *Neutron scattering facilities in Europe: Present status and future perspectives*. ESFRI Physical Sciences and Engineering Strategy Working Group - Neutron Landscape Group, 2016 (cit. on p. 10).

## Chapter 2

# European Spallation Source and beam diagnostic devices



## Contents

---

<b>2.1</b>	<b>Introduction</b>	<b>15</b>
<b>2.2</b>	<b>European Spallation Source</b>	<b>15</b>
<b>2.3</b>	<b>ESS collaboration and ESS activities at CEA/IRFU</b>	<b>17</b>
<b>2.4</b>	<b>ESS accelerator</b>	<b>17</b>
2.4.1	Ion source and Low Energy Beam Transport	18
2.4.2	Radio Frequency Quadrupole	19
2.4.3	Medium Energy Beam Transport and Drift Tube Linac	20
2.4.4	Superconducting cavities	20
<b>2.5</b>	<b>Transport lines and target</b>	<b>21</b>
<b>2.6</b>	<b>ESS neutron instruments</b>	<b>22</b>
<b>2.7</b>	<b>Beam diagnostic overview</b>	<b>24</b>
2.7.1	Beam current monitor	25
2.7.2	Beam position monitor	26
2.7.3	Beam loss monitor	26
<b>2.8</b>	<b>Invasive beam profile measurements</b>	<b>27</b>
2.8.1	Interceptive screen	27
2.8.2	Wire scanner	28
2.8.3	SEM-Grid	29
<b>2.9</b>	<b>Non-invasive beam profile measurements</b>	<b>29</b>
2.9.1	Laser wire profiler	29
2.9.2	Fluorescence Profile Monitor	29
<b>2.10</b>	<b>Ionization Profile Monitor and summary</b>	<b>30</b>
	<b>Bibliography</b>	<b>33</b>

---

## 2.1 Introduction

The topic of this thesis is the design of non-invasive ionization profile monitors for the ESS proton beam. The European Spallation Source is going to base neutron production on one of the most powerful linear proton accelerators ever built. Beam diagnostic is therefore an essential part of the project, necessary to insure fast tuning of the beam, monitor the beam during neutron production, and provide safety to the machine at any phase of the acceleration operation.

This chapter gives an overall vision of the ESS project. The different elements of the accelerator will be briefly detailed from the source to the target. In addition, some neutron instruments foreseen at ESS and their applications will be illustrated.

The second part of the chapter focuses on beam diagnostic devices and their diversity. An exhaustive list of beam diagnostics is not possible and only a few of them are presented here. The chapter concludes with the state of the art of non-invasive profilers based on the ionization of the residual gas.

## 2.2 European Spallation Source

The European Spallation Source (ESS) is a neutron source facility currently under construction in Lund, Sweden. The objective of ESS is clear: ESS will be the brightest

pulsed neutron source in the world and will give to Europe a modern flagship neutron source, as the ILL was.

ESS can be roughly summarized in 3 parts: a powerful linear accelerator, a large tungsten target and a multitude of neutron scattering instruments. Each of these elements represents a technological breakthrough in their respective fields.

Fig. 2.1 underlines the difference among ESS and existing neutron sources in terms of brightness<sup>1</sup>, compared to existing sources.

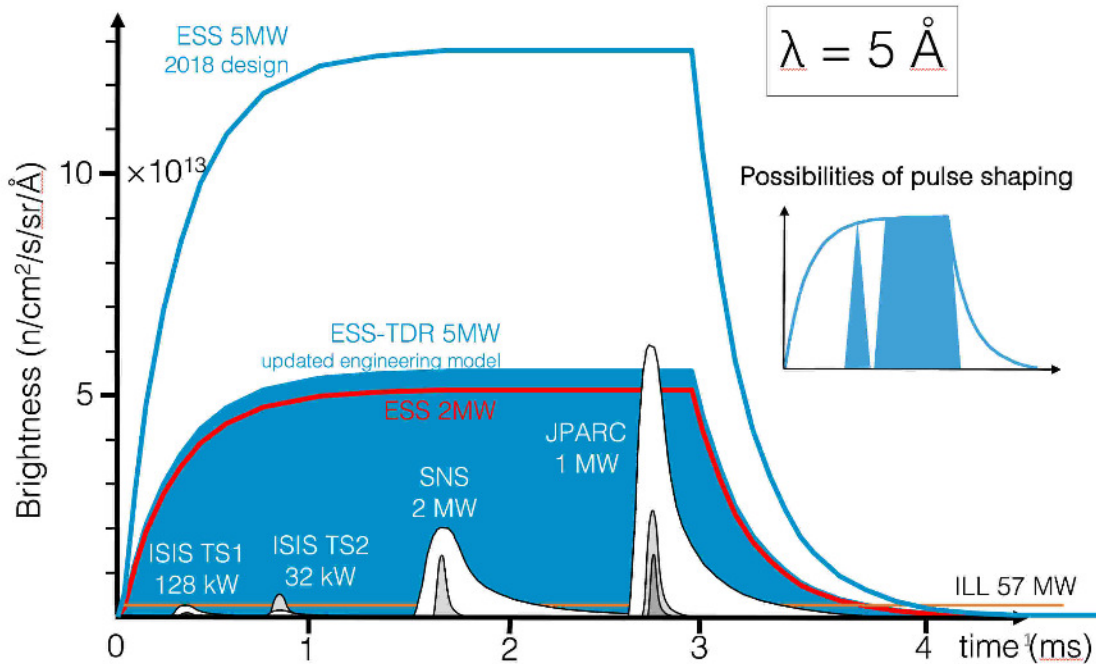


**Figure 2.1** – ESS neutron source brightness compared to others existing neutron sources.

The specificity of ESS is its linear pulsed high intensity accelerator, which will be one of the most powerful in world. The accelerator is linear from the source to the target and does not require an accumulation ring as SNS. The linac is massively based on superconducting cavities allowing to accelerate long and intense pulses in reasonable dimensions. The total construction cost is estimated at 1843 million € and the annual operating cost will be about 100 million €<sup>2</sup>.

The history of ESS is quite complex, its first studies and design dating back to the 1990s. These designs considerably changed over the years, along with the existing technologies. In the 2000s the project started to become reality, probably due to the beginning of construction of SNS and JSNS. In 2009 Lund was chosen to host the future installation. The site is close to the MAX V synchrotron, establishing a scientific hub dedicated to the studies of materials using large instruments. The final design of ESS was frozen in 2014 with an energy reduction from 2.5 to 2 GeV but an increase of the maximum current to 62.5 mA. The groundbreaking happened in 2014 and in 2017 the accelerator tunnel was completed. The target vault is still under construction. The total progress of the installation is rated at 59%. The source and

1. The plot does not have the same scale if power or neutron flux are considered.  
2. The price of electricity can fluctuate significantly, this budget is given as an indication.



the LEBT were delivered and are functional. The RFQ is expected to be delivered and connected to the LEBT and the MEBT in few weeks. The installation of cryogenic systems supplies is on going. The first protons on target are expected in 2021 whereas the user program will start in 2023.

## 2.3 ESS collaboration and ESS activities at CEA/IRFU

ESS is a very large project based on an international collaboration of many research Institutes. Today, the collaboration includes more than 140 institutes from 15 different countries with more than 40 European in kind agreements. France is very involved in the ESS project, particularly through two research organizations: the French National Centre for Scientific Research (CNRS) and the French Alternative Energies and Atomic Energy Commission (CEA).

CEA is a key player in research, development and innovation in four main areas: defence and security, nuclear and renewable energies, technological research for industry and fundamental research. The Institute for Research on the Fundamental laws of the Universe (IRFU) is one of the institutes attached to the fundamental research division of CEA. IRFU brings together three scientific disciplines: astrophysics, nuclear physics and particle physics. IRFU develops as well the associated technology required by the cutting-edge research.

## 2.4 ESS accelerator

The proton linear accelerator (LINAC or linac) of ESS is represented synthetically in Fig. 2.2. The total length from the source to the target is about 600 m and 356 m are dedicated to the acceleration. The first part accelerates the beam up to 90 MeV by means of conventional room temperature RF cavities. Then a cold part using superconducting cavities cooled with liquid helium is used to reach the highest energies.

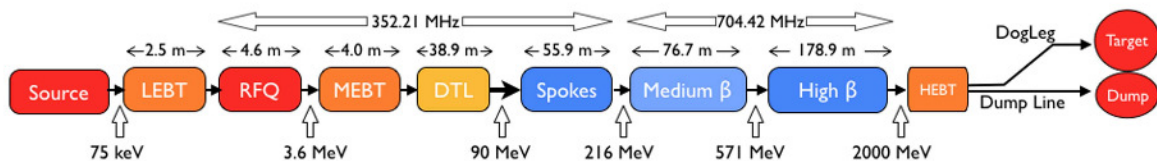


**Figure 2.2** – A simplified representation of the ESS linac. The blue blocks represent superconducting cavities where our beam profile monitors will be installed.

Table 2.1 summarizes the most important characteristics of the ESS linac. The particularities of ESS compared to other sources of spallation rely on its very long pulse and its high current. The average beam power is 5 MW and the peak power is 125 MW, making ESS one of the most powerful proton accelerator in the world.

In the next sections the role of each of the accelerator blocks is described in few words and detailed review of the ESS project are available in the following [1, 2].

Table 2.1 – ESS nominal conditions.

Characteristic	Value
Energy	2 GeV
Pulse current	62.5 mA
Pulse duration	2.86 ms
Repetition rate	14 Hz
Duty cycle	4 %
Power (peak)	5 MW (125 MW)
Radio Frequencies	352.21 MHz 704.42 MHz

### 2.4.1 Ion source and Low Energy Beam Transport

The source is the first stage of any accelerator: it creates and extracts the plasma. An Electron Cyclotron Resonance (ECR) source is a type of source particularly suitable for the production of plasma of mono specie at high intensity [3]. An ECR source is based on the superposition of a magnetic field and a RF wave. In a magnetic field the electrons orbit around the magnetic field lines with a frequency defined by:

$$\omega_e = \frac{eB}{m_e} \quad (2.1)$$

By injecting a powerful RF wave of the same frequency, the electrons will enter in resonance and reach sufficient energy to ionize the medium and create a plasma. In an ECR source the plasma is confined by the magnetic field. Then, a series of electrodes placed at very high potential extract the plasma from the confinement chamber. At the source output, the beam has an energy close to 100 keV. For instance the ESS source accelerates protons to 75 keV.

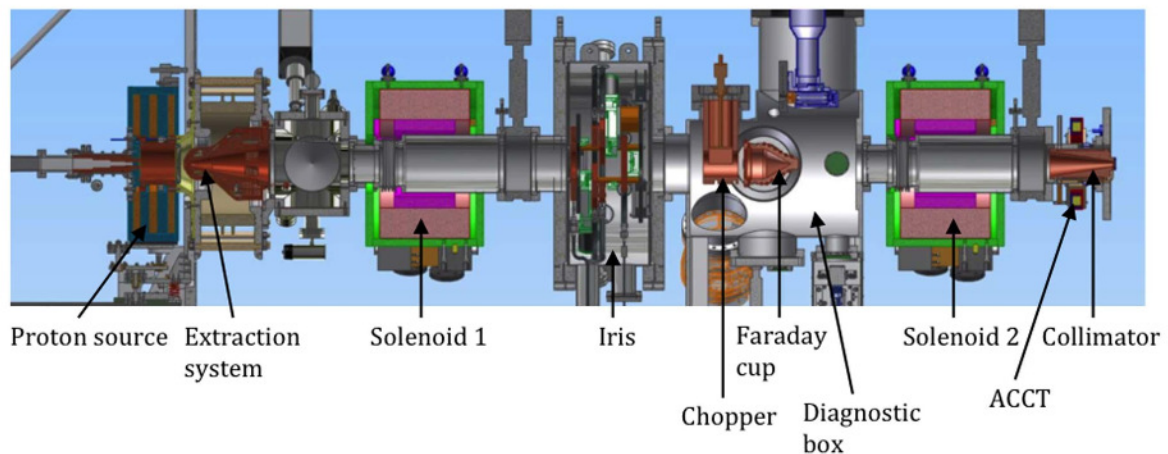


Figure 2.3 – The ESS proton source and the LETB.

At low energies the plasma is strongly affected by space charge effects and is therefore very divergent. The low energy beam transport line (LEBT) contains the space charge by using solenoids, and optimizes the injection of the plasma into the



first accelerating cavity (RFQ). Fig. 2.3 outlines the source and the LEBT of ESS. An iris allows to finely adjust the beam current and a Faraday cage is able to measure the current. This line also contains diagnostics that check the quality of the beam before the injection into the RFQ: the Alison scanners to measure the emittance of the beam, the Doppler to measure the transported fraction species ( $H^+$ ,  $H_2^+$ ,  $H_3^+$ ), and NPMs to measure the beam position and beam size. These diagnostics are critical to establish the matching condition to enter the RFQ.

The INFN Catania was in charge of the design and production of the source and the LEBT. CEA/IRFU was involved in two diagnostics: a Doppler Shift Unit [4] and an Allison [5]. The source was delivered at ESS and commissioned in 2018.

### 2.4.2 Radio Frequency Quadrupole

The principle of the Radio Frequency Quadrupole (RFQ) was imagined in the 1970s in Russia by I. M. Kapchinskiy and V. Tepliakov. The method quickly became popular and essential in very intense accelerators since it is still the most efficient method for bunching and accelerating particles at low energies.

At these energies, the space charge is so high that the beam divergence is enormous and must be compensated. A RFQ behaves as a sequence of focusing and defocusing elements that can contain the space charge. RF waves are propagated on four poles, usually vanes (Fig. 2.4a) or rods, with opposite amplitude between each pole (Fig. 2.4b). The RF variation allows to successively focus in one direction (and defocus in the other direction). A mechanical modulation of the vanes introduces a longitudinal electric field that will accelerate the particles (Fig. 2.4c). The roles of the RFQ are:

- containing and focusing the beam;
- structuring the beam into small bunches;
- accelerating the particles.

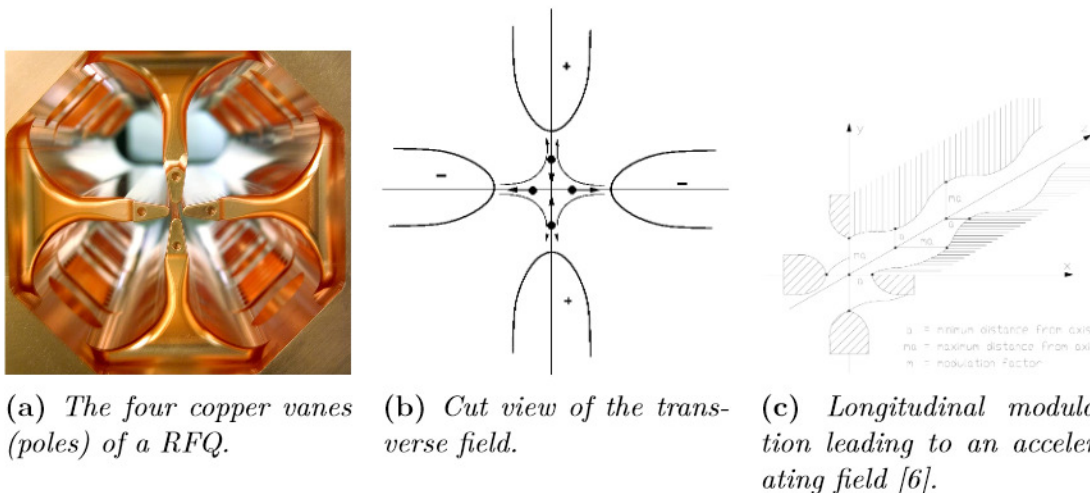


**Figure 2.4** – An RFQ structure bunches, focuses and accelerates charged particles by means of four poles that modulate the RF wave.

The simulations of such device are complicated and require specific codes to compute the propagation of the RF waves and the transport of particles inside the RFQ [7]. In addition, the conception of this type of cavities is extremely technical: for

instance the tolerance on the mechanical structures of the vanes is in the order of micrometers whereas the whole RFQ structure often exceeds meters.

The CEA/IRFU is in charge of the construction of the ESS RFQ [8] which accelerates the proton beam at the source exit from 75 keV up to 3.6 MeV and bunches them with a 352.21 MHz frequency.

### 2.4.3 Medium Energy Beam Transport and Drift Tube Linac

The medium energy beam transport (MEBT) is located just downstream of the RFQ and contains beam optical elements, buncher cavities and beam diagnostics allowing beam characterization and correction. Fig. 2.5 shows a block view of the MEBT and its different elements. Most diagnostics will be presented later in the chapter and a table of abbreviations is available at the end of the thesis. The MEBT has been developed by the ESS-Bilbao team.

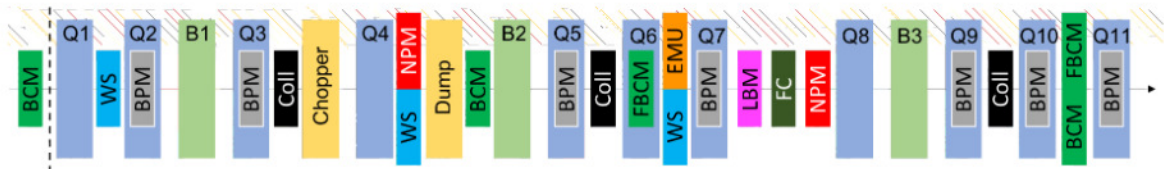


Figure 2.5 – Building blocks of the MEBT.

The MEBT prepares the beam for the injection in the Drift Tube Linacs (DTL)<sup>3</sup>. A DTL cavity is a cylindrical standing waves resonant structure. It uses coaxial cylinders (drift tubes) fixed at one end of support tubes. The acceleration occurs in the gaps between two cylinders. The cylinders are also designed to shield the field for particles during the deceleration phase. The length of these drift tubes increases along the structure since it is related to the particle velocity. Permanent quadrupole magnets are encapsulated within the coaxial cylinders allowing a radial focusing of the beam.

At ESS, the DTLs are designed to accelerate the beam from 3.62 MeV to 90 MeV. The ESS DTLs have similar design to the Linac4 DTLs. The DTLs are separated in five DTL tanks containing between 61 to 23 drift tubes. Fig. 2.6 presents some pictures of the ESS DTLs.

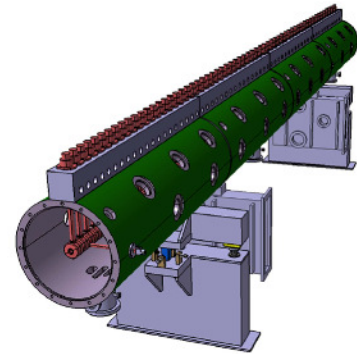


Figure 2.6 – A 3D drawing of a DTL tank.

### 2.4.4 Superconducting cavities

The DTLs are not optimized beyond 100 MeV because the length of the drift tubes becomes too long. Two solutions can be considered: increasing the accelerating field or increasing the radio frequency. However, both solutions are technically difficult to implement for long pulsed beams. Indeed, losses in the cavities become very high leading to inefficient acceleration and heating the cavities. The use of superconducting

3. Sometimes, the structure is referred as Alvarez Drift Tube Linac.



RF cavities overcomes these issues. These superconducting cavities act as perfect conductors when the transition temperature of the superconductor is reached: 9.2 K for niobium.

The cooling of these cavities is done by a liquid helium system working at 4.13 K, enclosed in a tank with thermal shielding, including circuitry for the cooling of cavities, couplers, magnets... The assembly process of such cryomodules must be done in clean conditions and in a particle free environment (ISO-5 cleanrooms). A defect on surfaces or contaminations may lead to a loss of the superconductivity capability locally, increasing the RF losses and temperature in this area: a quench. In addition, superconducting cavities are very affected by field emissions.

Our devices will be installed between two cryomodules, and therefore must be compliant with the constraints imposed by the use of superconducting cavities at ESS. The CEA/IRFU is responsible for the design and integration of medium and high beta cryomodules. Fig. 2.7 pictures one elliptical cryomodule.

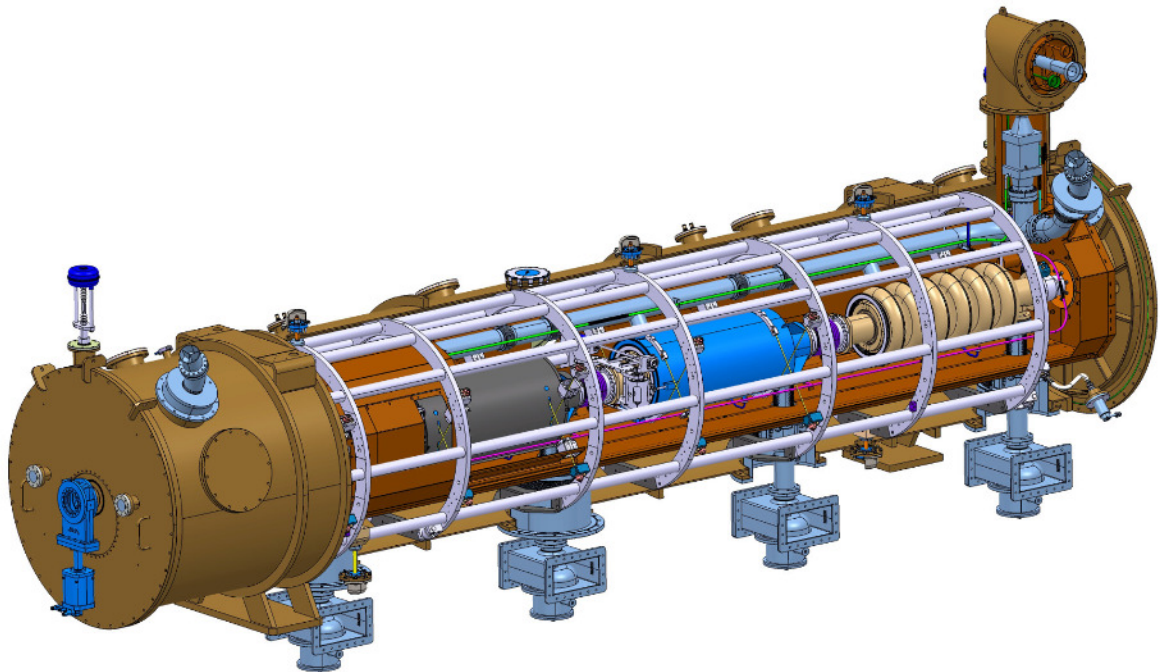


Figure 2.7 – *ESS medium beta elliptical cavities cryomodule.*

## 2.5 Transport lines and target

The protons are then transported in a high-energy beam transport (HEBT) line to the target<sup>4</sup>. A beam dump will be also used during the commissioning phase of the accelerator. The HEBT contains beam diagnostics and beam optic elements that prepare the beam for impacting on the target.

The ESS target should be designed to optimize the neutron yield from the spallation reaction and to sustain the 5 MW beam power. Two technologies are commonly used for spallation targets:

---

4. The target is at a different ground level compare to the accelerator.

- Solid targets with active cooling (ISIS, SINQ).
- Liquid targets with liquid recirculation (SNS, JSNS).

The solution chosen by ESS is a solid target wheel of diameter of 2.3 m. The wheel will rotate at 23.33 rpm. The wheel is composed of more than 7000 small tungsten bricks giving a total weight of around 5 tons. The bricks are cooled with liquid helium. The design of the target requires extensive thermal and mechanical studies. All these activities and the manufacturing of the target, as well as many other systems around the target, are under the responsibility of ESS-Bilbao.

The neutron flux is maximized by means of moderator-reflectors and thermalized by different water and liquid  $H_2$  moderators. The neutron brightness is more or less uniform over the 42 neutron ports around the target. The target moderators and all other systems (engine, cooling etc.) are contained in a shielded structure: the monolith. The monolith is visible in Fig. 2.8.

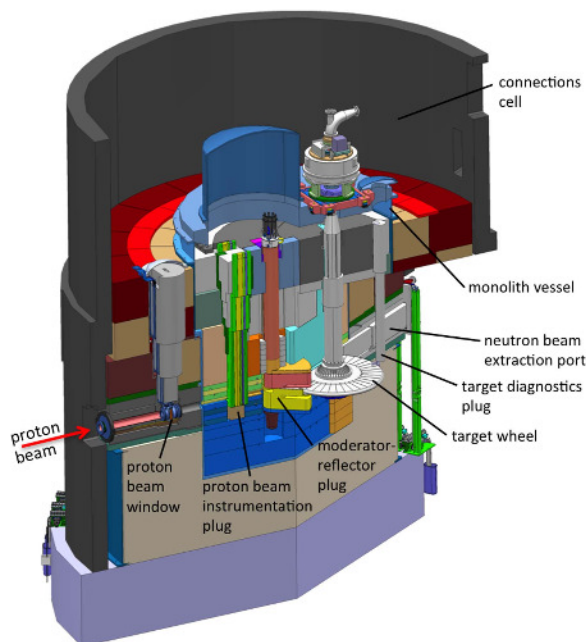


Figure 2.8 – The Tungsten wheel target inside the monolith structure.

## 2.6 ESS neutron instruments

When the ESS user programme will start in 2023, 15 instruments will be available for users. The installation of the first instruments began this year. These instruments have been reviewed and selected by scientific committees and validated by different ESS committees. Seven new instruments will be installed afterwards in a first extension phase. Finally in a more distant future, new instruments may be installed on the remaining neutron beam ports. Fig. 2.9 shows the setup of the 15 first neutron lines and instruments foreseen for the beginning of the user program. To give an idea of the scale, in the T-REX spectrometer the distance between the sample and the tungsten target is almost 170 meters.

Each instrument is the result of close collaborations between ESS and numerous institutes specialized in neutron scattering. As already explained, ESS is a user facility

and is open to both researchers and industrial actors from various fields. The different neutron scattering instruments at ESS will be used for a variety of applications. Therefore each instrument will be unique and will have to meet specific requirements. Table 2.2 briefly summarizes the 15 initial instruments with some examples of areas of applications [9, 10].

**Table 2.2** – *Overview of ESS neutron instruments [9, 10].*

Instrument	Description	Examples of application
Diffraction		
DREAM	Bispectral powder diffractometer	Crystallography, nanoscience, energy research
HEIMDAL	Hybrid diffractometer	Magnetic properties, engineering
MAGiC	Magnetism single crystal diffractometer	Magnetic properties
NMX	Macromolecular crystallography	Structural biology, drugs
BEAR	ToF diffractometer	Engineering
ODIN	Multi-purpose neutron imaging instrument	Engineering, geo-science, paleontology
Reflectometry		
FREIA	Liquids reflectometer	Life science, soft matter
ESTIA	Focusing reflectometer	Magnetic properties, thin films
SANS		
LOKI	Broadband SANS	Soft matter, biophysics
SKADI	General purpose SANS	Medical research, energy storage
Spectrometry		
T-REX	Bispectral chopper spectrometer	Crystals, superconductivity
VESPA	Vibrational spectrometer	Chemistry, materials science
MIRACLES	Backscattering spectrometer	Polymer science, energy materials, magnetic properties
BIFROST	Extreme environment spectrometer	Engineering, superconductivity
CSPEC	Cold chopper spectrometer	Life sciences, materials, chemistry





**Figure 2.9** – Scheme of the 15 neutron instruments that will be available at the start of the user program.

## 2.7 Beam diagnostic overview

Beam diagnostics are used to ensure the proper functioning of the accelerator, as well as the safety of people and of the installation. They allow to measure the different beam characteristics such as current, position, beam losses, energy, profile, emittance etc. For each beam characteristic, several methods can be considered, each of them having advantages and drawbacks. Beam diagnostics are at the crossroads of many areas of physics and electronics, belonging to the so-call transverse activities.

The accelerating technologies are often complicated and quite expensive. In general, the size of the accelerator is reduced as much as possible, the space along the beam tube is often limited. The choice of diagnostics installed on a line must therefore be done carefully according to the expectations. Neglecting diagnostics may be dramatic.

The present section briefly<sup>5</sup> introduces different beam diagnostics frequently en-

5. The proceedings of the CERN Accelerator School dedicated to beam diagnostics (the 2008

countered on high intensity linear accelerators. Complete description of beam diagnostics can be found in books [11], Joint Universities Accelerator School [12] or CERN Accelerator School [13].

### 2.7.1 Beam current monitor

The measurement of the beam current is perhaps the most basic information for an accelerator. Beam Current Monitors (BCM) detect how many beam particle per time are passing through a specific position in the accelerator. The transmission between the different accelerating blocks can thus be quantified.

The BCMs rely on very different methods depending on the minimum value of the currents that should be achieved. For ESS, the beam current can be considered as high. Two common families of methods for measuring high currents are presented in this section.

A Faraday cup (FC) is a destructive method of current measurement. It can be seen as a beam dump, isolated from the accelerator ground, where the charges from the beam are collected by mean of a readout electronics. FCs are often used in low energy parts of an accelerator (in the LEBT for instance) because they can operate both as current meters and beam dumps. At high energy, the size and the complexity of the FC design considerably increase. A FC is usually inserted downstream the iris allowing a fine current tuning, for avoiding the injection of the beam into the entire accelerator. The critical part of the FC design is the cooling system that must be sufficiently efficient to dissipate the thermal power deposited by the beam. Repellers, like electrodes or permanent magnets, must be used to avoid any parasitic current due to secondary electron emissions, during the impact of the beam particles.

A beam consists of many charged particles moving together within bunches, more or less in the same direction; therefore a beam generates an electromagnetic field. The magnetic field can be used to measure the beam current in a completely non-invasive manner by means of a current transformer (CT). The beam can be seen as a one turn primary winding, and therefore the induced voltage measured on the secondary winding is proportional to the beam current (Fig. 2.10). The measurement in the

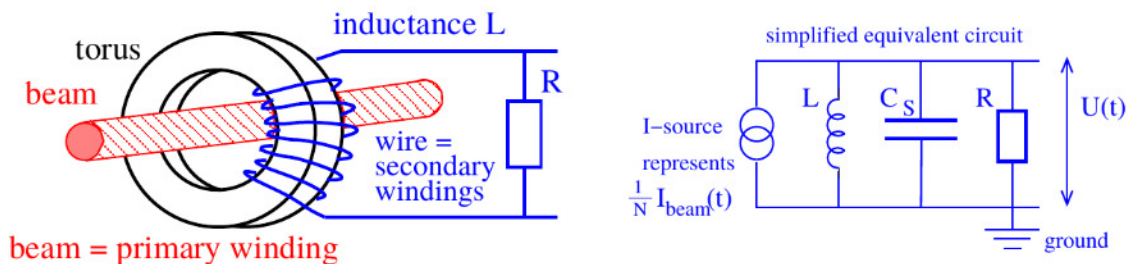


**Figure 2.10** – A simplified scheme of a passive current transformer [14].

secondary winding is carried out by an active devices, an operational amplifier for instance, reducing the limitations of a passive measurement. Different implementations of current transformers exist depending on the requirements:

---


edition) is about 600 pages.



- Alternative Current Transformer (ACCT): is the most common active transformer for pulsed beam.
- Fast Current Transformer (FCT): whose design is optimized for high-frequency current measurements, allowing bunch beam measurements for instance.
- Direct Current Transformer (DCCT): this type of transformers were developed to measure the DC component [15] of a beam using a method similar to fluxgate sensor.


These diagnostics can be developed in-house or purchased directly off the shelf. At ESS [16], 18 ACCTs from Bergoz Instrumentation [17] will be installed along the accelerator to measure the current.

## 2.7.2 Beam position monitor

 The position measurement is also essential information to ensure the minimum operation of the accelerator. As explained in the previous section, the charged particles generate an electromagnetic field, and the electric field creates image charges on the vacuum walls. The distribution of these image charges depends, among other things, on the position of the beam in the vacuum chamber. These charges can be measured by setting an electrode, isolated from the walls, with a readout electronics. This type of detector is called a pick up monitor and is widely used for beam position measurement. In reality there are several types of pick up monitors whose operating principle are different and can not be covered here.

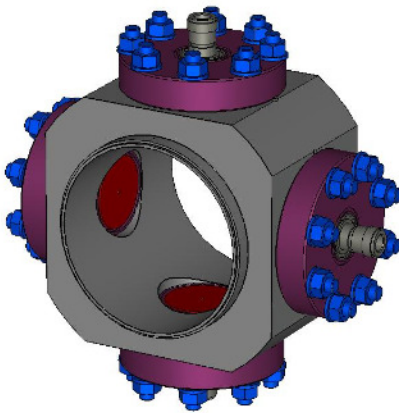


**Figure 2.11** – A 3d drawing of the ESS button BPMs designed at DESY.

A button BPM consists of four electrically isolated electrodes (buttons, visible in red on Fig. 2.11), generally face to face, each button connected to a  connector. The voltage due to the coupling between the beam and the button is then measured, and the position is calculated from the contributions of the four buttons. The measurement is not linear, so the value is corrected with a calibration factor, determined beforehand using a moving wire fed with RF signal. The bandwidth of this type of BPM is determined by the capacitance of the system (electrode, connection, cables), typically between 100 MHz and few GHz. Nowadays, the processing of the data relies on complex numerical RF processing (filter, modulation, cordic decomposition). At ESS, the BPM systems will be based on more than 90 BPMs installed along the linac, mainly button-type BPMs and few striplines.

## 2.7.3 Beam loss monitor

Beam Loss Monitors (BLM) are mandatory diagnostics in all accelerators, mainly in high power accelerator facilities. When particles are lost in the accelerator, they hit and pass through the beam tube elements producing different type of radiation. In an accelerator, the primary goal of BLM systems is to guarantee the safety of the installation. Indeed, when the loss rates are high, the devices around the accelerator



can be severely damaged.

BLMs are very often connected to the machine protection system (MPS) allowing a fast shut down of the accelerator if the losses are too high. BLMs relies on a wide range of radiation detection techniques.

At ESS two types of BLM are foreseen. The first type of beam loss monitors is based on ionization chambers (icBLM) [18]. These are the most common BLM types; icBLMs are widely used at CERN in LHC [19], SNS etc. In an icBLM, the losses ionize the gas in the chamber and a current is established between the electrodes. An icBLM has a high dynamic range, fast response and is cost effective.



**Figure 2.12** – *The ionization chamber of an icBLM.*

The second type of ESS BLMs is completely new: the neutron Beam Loss Monitors (nBLM) [20]. A nBLM is sensitive to fast neutrons and insensitive to photon ( $X$  and  $\gamma$ ) emitted by the accelerator cavities. In fact, two nBLM types, based on Micromegas detectors [21] were developed:

- A fast detector ( $< 50$  ns), sensitive to high losses allowing a very fast stopping of the beam.
- A slower detector ( $< 200$   $\mu$ s), with a higher sensitivity, allowing a finer monitoring of the losses.

A total of 266 icBLMs, 42 slow nBLMs and 42 fast nBLMs will be installed along the accelerator.

## 2.8 Invasive beam profile measurements

### 2.8.1 Interceptive screen

A luminescent screen provides a convenient way to measure profiles since this diagnostic is simple to implement. The screen is inserted directly in the beam path using an actuator. When particles pass through the material, they partly deposit their energies, exciting the medium. During the de-excitation process, most of the energy is released under the form of visible photons. The intensity of light from the screen is proportional to the number of incident particles and their energy deposition. It is possible to measure, with a single camera, the beam profile in two dimensions simply by tilting the screen.

The use of this diagnostic is strongly limited by the energy and intensity of the beam. At low energies and/or high current, the power to be dissipated can be locally

considerable, reaching saturation and altering the screen properties. In general, a permanent decrease of the light yield is observed [22] and in some extreme cases a deterioration of the screen surface is remarked.

A concrete use of this type of diagnostics will be briefly presented in Chapter 4 with some experimental results.

There is another type of intrusive diagnostics based on the optical transition radiation. The setup looks similar to the one just described, but the process behind is totally different. When a relativistic particle is subject to a sudden variation of the dielectric constant, i.e. passes the border of two different media, transition photons are emitted with precise angles depending on the particle, its velocity and the angle of incidence. This method is well adapted for high relativistic accelerators such as  $e^-$  linac [23, 24].

## 2.8.2 Wire scanner

A Wire Scanner (WS) is an invasive diagnostics that probes the beam with a micrometer wire, taut on a movable fork. The measurement in both directions of the transverse profile is possible by using a wire set at angle (typically  $45^\circ$ ) with respect to the WS translation. Two detection modes are possible depending on the energy of the beam to be analyzed.

The secondary electron emission mode is adapted to low beam energies. When the beam passes through the wire, secondary electrons are emitted from the surface of the wire and the other electron pairs are absorbed into the wire. The current read on the wire is proportional to the number of emitted electrons. As the beam deposits its energy, the wire also heats up; note that in a vacuum it is only cooled by radiation and conduction with the fork. At certain temperature the wire starts to emit electrons by thermoionic effect. This effect is not linear and interferes with the measurement.

For high energy beams, the detection strategy is completely different. When an energetic beam interact with the wire, electromagnetic cascades may occur. The shower can be detected outside the beam tube using a fast calorimeter. The most common calorimeter are scintillators.

The design of the wire is usually done in two steps [25]. The number of emitted electrons and the deposited energy is calculated first, for instance with Monte Carlo codes. Then thermal simulations are performed, with numerical partial differential equation solver, to determine the heating that occurs in a wire during the pulses. The two most commonly used materials for wires are tungsten and carbon, which have respectively very high melting and sublimation temperatures. The diameter of the beam is optimized according to the simulations and the wire material, typical the diameter of a wire is between 20 and  $100\ \mu\text{m}$ .

The method is sensitive to low beam currents. Wire scanners are used in linacs mainly in low current and/or at low cycle beam. In synchrotrons, the multiple passages of the beam leads to rapid heating of the wires. For both accelerators, the design of the wires is crucial. The interaction time must be minimized with fast translators. This is the flying wire method used on synchrotrons.

At ESS both types of wire are used, 3 SEM-WS will be installed in the MEBT. Then 10 EM-WS will be installed in the superconducting part [26]. The wire scanners will be used mainly during the commissioning of the machine, in fact the wire can



withstand the beam power only during low duty cycle ( $100\mu\text{s}$  at the nominal ESS current).

### 2.8.3 SEM-Grid


A Secondary Electron Emission grid (SEM-Grid) or harp grid is a multichannel version of the SEM WS. Several wires are taut on a frame in the same direction at several positions. To avoid crosstalk due to secondary electrons, an electron repeller (wire or electrode) is often set around the wires. A second wire plane can also be set in the transverse direction. Both grids are inserted in the beam tuned at low duty cycle and both profiles (X and Y) are measured in one shot. By using several SEM-grid successively the measurement of the transverse emittance is possible.

However, the readout electronics of the secondary emission currents of all wires is more complex due to the number of channels. The number of wires must be chosen according to the resolution requirements on the beam sizes and positions. The wires must meet the same constraints as the wire scanner. The system is not necessarily more robust because if one wire breaks it may short-circuit the other wires nearby.

## 2.9 Non-invasive beam profile measurements

### 2.9.1 Laser wire profiler

For negative ion beams, a specific method, based on photo neutralization process, allows an almost (considering beam particle losses that occur along the accelerator) non invasive profile measurement. Photo neutralization works as follows: when a photon has a sufficient energy, it can strip off an electron of a negative ion. The photo neutralization cross section depends mainly on the energy of ions and on the wavelength of photons. With a dipole magnet free electrons are separated from the  $H^-$  beam. Then, the electrons are collected and detected by a Faraday cup, a MCP or a semiconductor detector. The transverse profile is reconstructed by scanning the laser in the beam like a wire scanner.

This kind of device is popular on  $H^-$  ion accelerators such as SNS and LINA . The method does not require any element passing through the beam. Therefore the laser wire scanners are very well suited for high intensity beams. The method requires an advanced laser system (typically 1064 nm Nd:YAG laser in  $mJ$  range)<sup>6</sup> as well as quite complicated optical setups.

### 2.9.2 Fluorescence Profile Monitor

Fluorescence Profile Monitors (FPM) or Beam Induced Fluorescence (BIF) monitors are non-invasive diagnostics for transverse profile measurements. When the particles of the beam pass through the residual gas, they can excite the residual gas. Fluorescence photons are emitted when the excited molecules return to their fundamental states.

The fluorescence is a luminescent process characterized by a rapid de-excitation (few tens of nanoseconds). The fluorescence can occur with gases and each gas has

---

6. The laser can be distributed on several measuring stations with optical fibers.

its own emission spectra. Some gases have much larger effective cross-sections such as nitrogen, which is very often used. Fig. 2.13 shows a classic FPM assembly with an amplified detection readout and a gas injection system. In an ideal case, the light reflection capability of the vacuum chamber, where a FPM is mounted, must be as low as possible for reducing the background signal. This is commonly achieved by applying a black coating on the surface.

Light detection is however limited by several factors. The fluorescence photon is emitted within  $4\pi$  steradians, so the signal collected depends on the solid angle subtended by the detector. The fluorescence cross section follows the Bloch equation and decreases very quickly with the energy. FPMs are therefore preferred for low energy beam lines where the pressure is high. Otherwise, a FPM requires a gas injection system to increase the signal.

This kind of detector will be installed almost everywhere at ESS [27] except in the superconducting part where the very low pressure ( $10^{-9}$  mbar) and high beam energy no longer allows profile measurements with FPMs. Gas injection is not desired in the superconducting part of the accelerator.

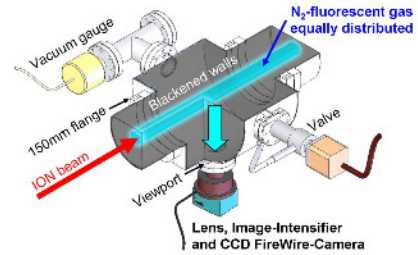


**Figure 2.13** – *Scheme of a BIF setup used at GSI [14].*

## 2.10 Ionization Profile Monitor and summary

In the previous sections different methods for measuring the transverse profile have been presented. None of these methods may be able to measure the transverse profile in the superconducting part of ESS at nominal beam conditions. Wire scanners are very common devices but can not handle the beam power under the nominal conditions. Moreover if one single wire melts it could contaminate the surrounding cavities. Laser Wire scanners are very elegant solutions, but they can only work with negative ions. The very low pressures in the cryogenic part prevent the use of FPMs and gas injection is not allowed at ESS.

As the superconducting accelerating part of the ESS linac is the longest in terms of acceleration elements, it would be harmful to leave this entire section without any transverse profile diagnostics.

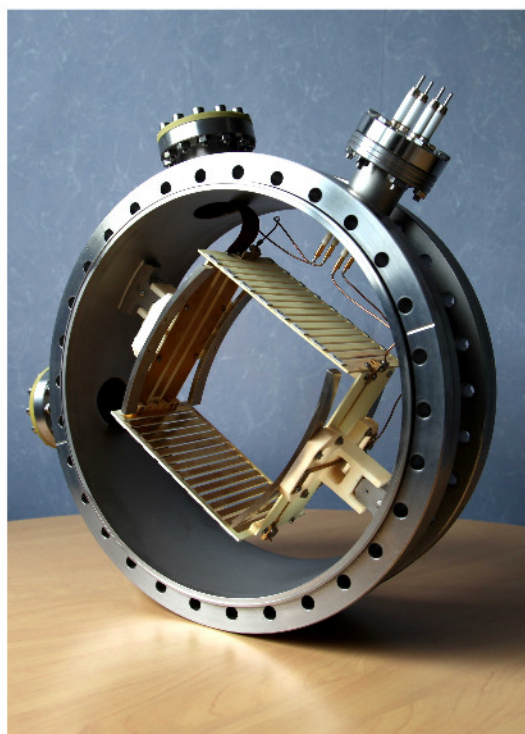
A Beam Gas Ionization (BGI) profile monitor or an Ionization Profile Monitor (IPM) is based on the direct collection of ionization by-products from the residual gas by an electric field. In the following we will use only the name IPM and the operation will be explained in much more detail in the next chapter. The method is non invasive as long as the electrical field does not bend the beam too much. An IPM is more complicated to implement and requires to set up some systems in vacuum. IPMs are quite common diagnostics on proton and hadron storage rings where pressures are very low, but they became popular on linear accelerators with the increasing use of superconducting cavities.

The method has been known since the late 1960s, but is continuously evolving with technological progress. First in terms of computing, nowadays computers are able to solve electromagnetic field equations, which greatly improves the understanding of

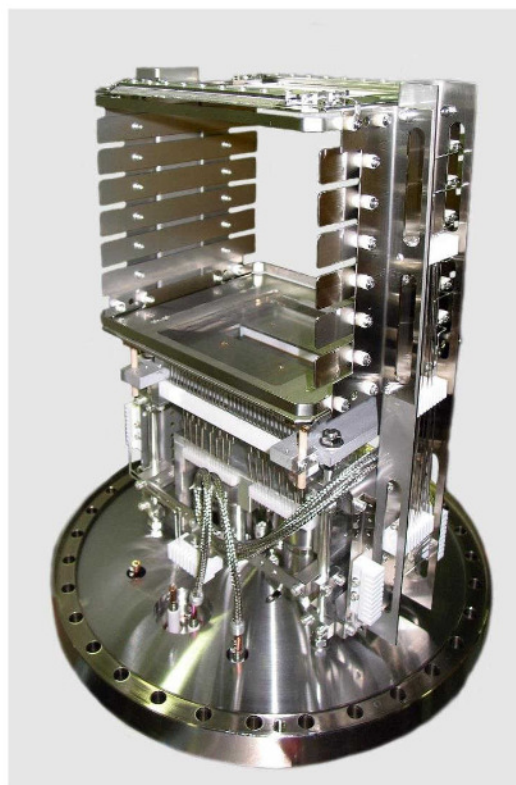
IPMs making possible to understand and correct, various errors on measurement. Moreover, the electronics become more and more sensitive, precise and fast. In the 90s, the rise of particle amplifier, like MicroChannel Plates and Channeltrons, have permitted the IPMs to operate under even more critical conditions in terms of energy and vacuum. Recently, the interest in semiconductor detectors has grown and an innovative IPM project using TimePix3 detectors is under development at CERN for the PS [28]. The first results are very promising [29] and offer a new perspectives on IPM usages.

The IPM method is now mature and used in several installations [30–35]. Fig. 2.14 shows 3 IPMs installed on 3 different accelerators. One can see directly that the design of an IPM is unique and tailor-made for its accelerator. This thesis deals about the development of IPMs for the superconducting part of the ESS accelerator. The different IPM technologies have been reviewed in order to select the most efficient one with respect to the ESS requirements.

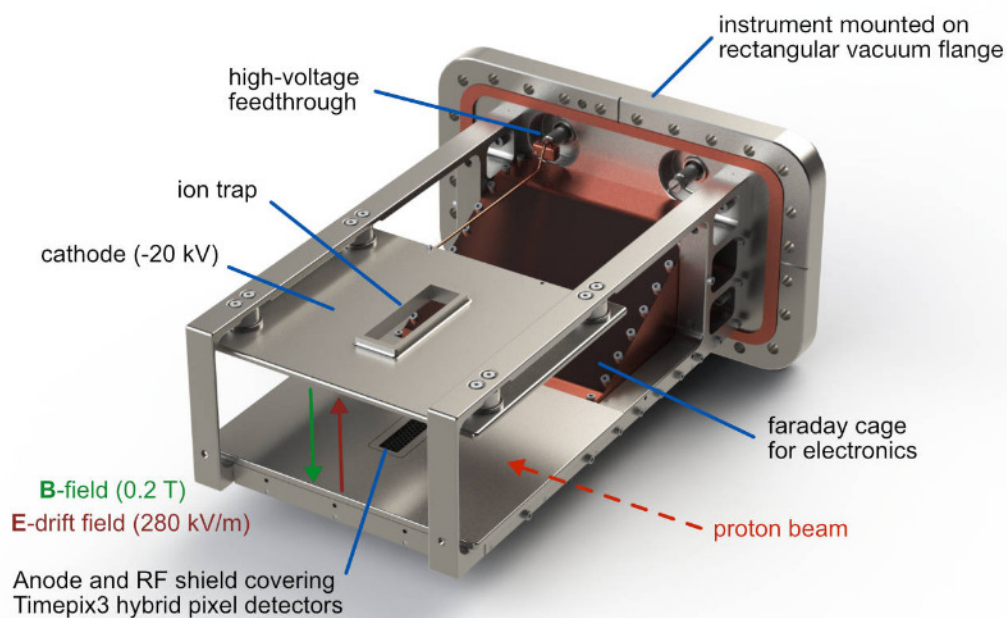




(a) One of the IPM at IFMIF [35].



(b) One of the IPM at GSI [14].



(c) The future IPM for the PS [29].

Figure 2.14 – Three different implementations of IPMs on three different accelerators.

## Bibliography

### References

- [1] S. Peggs. “ESS Technical Design Report”. In: (2013) (cit. on p. 17).
- [2] Roland Garoby et al. “The European Spallation Source Design”. In: *Physica Scripta* 93.1 (Dec. 2017), p. 014001. DOI: 10.1088/1402-4896/aa9bff (cit. on p. 17).
- [3] Sébastien Nickees (Nyckees). “Etude et développement d’une nouvelle source ECR produisant un faisceau intense d’ions légers”. 2012PA112426. PhD thesis. 2012. URL: <http://www.theses.fr/2012PA112426/document> (cit. on p. 18).
- [4] C.A. Thomas et al. “Development and Commissioning of the Doppler-Shift Unit for the Measurement of the Ion Species Fractions and Beam Energy of the ESS Proton Source”. In: *Proc. of International Particle Accelerator Conference (IPAC’17), Copenhagen, Denmark, 14-19 May, 2017*. (Copenhagen, Denmark). International Particle Accelerator Conference 8. <https://doi.org/10.18429/JACoW-IPAC2017-MOPVA037>. Geneva, Switzerland: JACoW, May 2017, pp. 936–938. ISBN: 978-3-95450-182-3. DOI: <https://doi.org/10.18429/JACoW-IPAC2017-MOPVA037>. URL: <http://jacow.org/ipac2017/papers/mopva037.pdf> (cit. on p. 19).
- [5] O. Tuske et al. “ESS Emittance Measurements at INFN CATANIA”. In: *Proc. of International Particle Accelerator Conference (IPAC’17), Copenhagen, Denmark, 14-19 May, 2017*. (Copenhagen, Denmark). International Particle Accelerator Conference 8. <https://doi.org/10.18429/JACoW-IPAC2017-MOPAB023>. Geneva, Switzerland: JACoW, May 2017, pp. 123–125. ISBN: 978-3-95450-182-3. DOI: <https://doi.org/10.18429/JACoW-IPAC2017-MOPAB023>. URL: <http://jacow.org/ipac2017/papers/mopab023.pdf> (cit. on p. 19).
- [6] A M Lombardi. “The radio frequency quadrupole (RFQ)”. In: (2006). DOI: 10.5170/CERN-2006-012.201. URL: <https://cds.cern.ch/record/1005049> (cit. on p. 19).
- [7] Romuald Duperrier. “TOUTATIS: A radio frequency quadrupole code”. In: *Phys. Rev. ST Accel. Beams* 3 (12 Dec. 2000), p. 124201. DOI: 10.1103/PhysRevSTAB.3.124201 (cit. on p. 19).
- [8] D. Chirpaz-Cerbat et al. “Status of the ESS RFQ”. In: *Proc. of IPAC’16*. (Busan, Korea). International Particle Accelerator Conference 7. Geneva, Switzerland: JACoW, June 2016, pp. 974–976. ISBN: 978-3-95450-147-2. DOI: [doi:10.18429/JACoW-IPAC2016-MOPOY054](https://doi.org/10.18429/JACoW-IPAC2016-MOPOY054) (cit. on p. 20).
- [9] *Instruments*. European Spallation Source. 2019. URL: <https://europeanspallationsource.se/instruments> (visited on 07/01/2019) (cit. on p. 23).
- [10] *Neutron users in Europe: Facility-Based Insights and Scientific Trends*. European Spallation Source, 2016 (cit. on p. 23).
- [11] Peter Strehl. *Beam Instrumentation and Diagnostics*. Particle Acceleration and Detection. Springer Berlin Heidelberg, 2006. ISBN: 9783540264040 (cit. on p. 25).

- [12] *Joint Universities Accelerator School*. <http://www.esi-archamps.eu/Thematic-Schools/Discover-JUAS> and <https://indico.cern.ch/category/3833/>. European Scientific Institute. 2019 (cit. on p. 25).
- [13] *CERN Accelerator School*. CERN. 2019. URL: <https://cas.web.cern.ch/> (cit. on p. 25).
- [14] Peter Forck. *Lecture Notes on Beam Instrumentation and Diagnostics*. Joint Universities Accelerator School. 2011. URL: <https://indico.cern.ch/event/569714/contributions/2303731/> (cit. on pp. 25, 30, 32).
- [15] K. Unser. “Beam Current Transformer with D.C. to 200 MHz Range”. In: *Proc. PAC1969*. (Washington D.C., USA). Mar. 1969, pp. 934–938. URL: [https://accelconf.web.cern.ch/accelconf/p69/PDF/PAC1969\\_0934.PDF](https://accelconf.web.cern.ch/accelconf/p69/PDF/PAC1969_0934.PDF) (cit. on p. 26).
- [16] H. Hassanzadegan et al. “Machine Protection Features of the ESS Beam Current Monitor System”. In: *Proc. 9th International Particle Accelerator Conference (IPAC’18), Vancouver, BC, Canada, April 29-May 4, 2018*. (Vancouver, BC, Canada). International Particle Accelerator Conference 9. <https://doi.org/10.18429/JACoW-IPAC2018-WEPAF088>. Geneva, Switzerland: JACoW Publishing, June 2018, pp. 2058–2060. ISBN: 978-3-95450-184-7. DOI: [doi:10.18429/JACoW-IPAC2018-WEPAF088](https://doi.org/10.18429/JACoW-IPAC2018-WEPAF088). URL: <http://jacow.org/ipac2018/papers/wepaf088.pdf> (cit. on p. 26).
- [17] *Bergoz Instrumentation*. Bergoz Instrumentation. 2019. URL: <https://www.bergoz.com/> (cit. on p. 26).
- [18] V. Grishin et al. “Ionization Chambers as Beam Loss Monitors for ESS Linear Accelerator”. In: *Proc. of International Beam Instrumentation Conference (IBIC’17), Grand Rapids, MI, USA, 20-24 August 2017*. (Grand Rapids, MI, USA). International Beam Instrumentation Conference 6. <https://doi.org/10.18429/JACoW-IBIC2017-WEPWC03>. Geneva, Switzerland: JACoW, Mar. 2018, pp. 454–457. ISBN: 978-3-95450-192-2. DOI: <https://doi.org/10.18429/JACoW-IBIC2017-WEPWC03>. URL: <http://jacow.org/ibic2017/papers/wepwc03.pdf> (cit. on p. 27).
- [19] Eva Barbara Holzer et al. “Beam Loss Monitoring for LHC Machine Protection”. In: *Physics Procedia* 37 (2012). Proceedings of the 2nd International Conference on Technology and Instrumentation in Particle Physics (TIPP 2011), pp. 2055–2062. ISSN: 1875-3892. DOI: <https://doi.org/10.1016/j.phpro.2012.04.110>. URL: <http://www.sciencedirect.com/science/article/pii/S1875389212019281> (cit. on p. 27).
- [20] T. Papaevangelou et al. “ESS nBLM: Beam Loss Monitors based on Fast Neutron Detection”. In: *Proc. 61st ICFA Advanced Beam Dynamics Workshop (HB’18), Daejeon, Korea, 17-22 June 2018*. (Daejeon, Korea). ICFA Advanced Beam Dynamics Workshop 61. <https://doi.org/10.18429/JACoW-HB2018-THA1WE04>. Geneva, Switzerland: JACoW Publishing, July 2018, pp. 404–409. ISBN: 978-3-95450-202-8. DOI: [doi:10.18429/JACoW-HB2018-THA1WE04](https://doi.org/10.18429/JACoW-HB2018-THA1WE04). URL: <http://jacow.org/hb2018/papers/tha1we04.pdf> (cit. on p. 27).



- [21] Y. Giomataris et al. “MICROMEAS: a high-granularity position-sensitive gaseous detector for high particle-flux environments”. In: *Nuclear Instruments and Methods in Physics Research Section A: Accelerators, Spectrometers, Detectors and Associated Equipment* 376.1 (1996), pp. 29–35. ISSN: 0168-9002. DOI: [https://doi.org/10.1016/0168-9002\(96\)00175-1](https://doi.org/10.1016/0168-9002(96)00175-1). URL: <http://www.sciencedirect.com/science/article/pii/0168900296001751> (cit. on p. 27).
- [22] C. Simon et al. “Scintillating Screens Investigations with Proton Beams at 30 keV and 3 MeV”. In: *Proc. of International Beam Instrumentation Conference (IBIC'16), Barcelona, Spain, Sept. 13-18, 2016*. (Barcelona, Spain). International Beam Instrumentation Conference 5. doi:10.18429/JACoW-IBIC2016-MOPG79. Geneva, Switzerland: JACoW, Feb. 2017, pp. 274–277. ISBN: 978-3-95450-177-9. DOI: doi:10.18429/JACoW-IBIC2016-MOPG79. URL: <http://jacow.org/ibic2016/papers/mopg79.pdf> (cit. on p. 28).
- [23] D. Nölle. “Electron Beam Diagnostics for the European XFEL”. In: *Proc. DIPAC09*. (Basel, Switzerland). May 2009, pp. 158–160. URL: <http://accelconf.web.cern.ch/AccelConf/d09/papers/tuoa04.pdf> (cit. on p. 28).
- [24] B Bolzon et al. “Results of the High Resolution OTR Measurements at KEK and comparison with simulations”. In: *Proc. IBIC2013*. (Oxford, UK). Sept. 2013, pp. 204–207. URL: <http://accelconf.web.cern.ch/AccelConf/IBIC2013/papers/mopf04.pdf> (cit. on p. 28).
- [25] B. Cheymol. “Estimation of the Thermal Load and Signal Level of the ESS Wire Scanner”. In: *Proc. of LINAC2014*. (Geneva, Switzerland). International Linear Accelerator Conference 27. Aug. 2014, pp. 137–139 (cit. on p. 28).
- [26] B. Cheymol. “Scintillator Detectors for the ESS High Energy Wire Scanner”. In: *Proc. of ICFA Advanced Beam Dynamics Workshop on High-Intensity and High-Brightness Hadron Beams (HB'16), Malmö, Sweden, July 3-8, 2016*. (Malmö, Sweden). ICFA Advanced Beam Dynamics Workshop on High-Intensity and High-Brightness Hadron Beams 57. doi:10.18429/JACoW-HB2016-MOPL018. Geneva, Switzerland: JACoW, Aug. 2016, pp. 232–236. ISBN: 978-3-95450-185-4. DOI: doi:10.18429/JACoW-HB2016-MOPL018. URL: <http://jacow.org/hb2016/papers/mopl018.pdf> (cit. on p. 28).
- [27] C. Thomas et al. “Design and Implementation of Non-Invasive Profile Monitors for the ESS LEBT”. In: *IBIC 2016: Proceedings of the 5th International Beam Instrumentation Conference (2016)* (cit. on p. 30).
- [28] J.W. Storey et al. “Development of an Ionization Profile Monitor Based on a Pixel Detector for the CERN Proton Synchrotron”. In: *Proc. IBIC2015*. (Melbourne, Australia). 2015, pp. 470–473. ISBN: 978-3-95450-176-2. DOI: 10.18429/JACoW-IBIC2015-TUPB059. URL: <http://accelconf.web.cern.ch/AccelConf/IBIC2015/papers/tupb059.pdf> (cit. on p. 31).
- [29] J.W. Storey et al. “First Results From the Operation of a Rest Gas Ionisation Profile Monitor Based on a Hybrid Pixel Detector”. In: *Proc. IBIC'17*. (Grand Rapids, MI, USA). 2017, pp. 318–322. ISBN: 978-3-95450-192-2. URL: <http://accelconf.web.cern.ch/AccelConf/ibic2017/papers/we2ab5.pdf> (cit. on pp. 31, 32).

- [30] John Krider. “Residual gas beam profile monitor”. In: *Nuclear Instruments and Methods in Physics Research Section A: Accelerators, Spectrometers, Detectors and Associated Equipment* 278.3 (1989), pp. 660–663. ISSN: 0168-9002. URL: [https://doi.org/10.1016/0168-9002\(89\)91188-1](https://doi.org/10.1016/0168-9002(89)91188-1) (cit. on p. 31).
- [31] K. Wittenburg. “Experience with the Residual Gas Ionisation Beam Profile Monitors at the DESY Proton Accelerators”. In: *Proc. EPAC1992*. 1992, pp. 1133–1135. URL: [http://accelconf.web.cern.ch/AccelConf/e92/PDF/EPAC1992\\_1133.PDF](http://accelconf.web.cern.ch/AccelConf/e92/PDF/EPAC1992_1133.PDF) (cit. on p. 31).
- [32] K. Satou et al. “A Prototype of Residual Gas Ionization Profile Monitor for J-PARC RCS”. In: *Proc. EPAC2006*. (Edinburgh, Scotland). 2006, pp. 1163–1165. URL: <http://accelconf.web.cern.ch/AccelConf/e06/PAPERS/TUPCH065.PDF> (cit. on p. 31).
- [33] T. Giacomini et al. “Ionization Profile Monitors - IPM @ GSI”. In: *Proc. DIPAC2011*. (Hamburg, Germany). 2011, pp. 419–421. URL: <http://accelconf.web.cern.ch/AccelConf/DIPAC2011/papers/tupd51.pdf> (cit. on p. 31).
- [34] Denton K. Morris et al. “Operational use of ionization profile monitors in the Fermilab Main Injector”. In: *Proc. NA-PAC2011*. (New York, USA). 2011, pp. 519–521. URL: <http://accelconf.web.cern.ch/AccelConf/PAC2011/papers/mop222.pdf> (cit. on p. 31).
- [35] Jan Egberts. “IFMIF-LIPAc Beam Diagnostics. Profiling and Loss Monitoring Systems”. Theses. Université Paris Sud - Paris XI, 2012. URL: <https://tel.archives-ouvertes.fr/tel-00772158> (cit. on pp. 31, 32).

## **Chapter 3**

# **Prototype simulations and design**



## Contents

---

<b>3.1</b>	<b>Introduction</b>	<b>39</b>
<b>3.2</b>	<b>ESS requirements</b>	<b>40</b>
<b>3.3</b>	<b>IPM simulations overview</b>	<b>41</b>
<b>3.4</b>	<b>Particle through matter</b>	<b>42</b>
3.4.1	Interaction of charged particles with matter	42
3.4.2	Electron ion pairs production	43
3.4.3	Calculation	45
3.4.4	Pressure uniformity	47
<b>3.5</b>	<b>Extraction field</b>	<b>48</b>
3.5.1	Maxwell equations at steady state	49
3.5.2	Solving Poisson's equation	50
3.5.3	COMSOL	52
3.5.4	Criteria	54
3.5.5	IPM polarity	57
3.5.6	IPM cross-interaction	58
3.5.7	Field corrections	60
3.5.8	Grid	63
<b>3.6</b>	<b>Initial momentum</b>	<b>65</b>
3.6.1	Thermal distribution	65
3.6.2	Momentum transfer during ionization process	65
<b>3.7</b>	<b>Space charge effect</b>	<b>67</b>
3.7.1	Lorentz transformation of electromagnetic fields	67
3.7.2	ESS/CEA Space Charge algorithm	68
3.7.3	Results	68
<b>3.8</b>	<b>Readout systems</b>	<b>70</b>
3.8.1	Ramo-Shockley theorem	70
3.8.2	Strips based detection	70
3.8.3	Interaction of low energy particles	72
3.8.4	Semiconductor based detection	73
3.8.5	MCP based detection	74
<b>3.9</b>	<b>Summary</b>	<b>76</b>
	<b>Bibliography</b>	<b>77</b>

---

## 3.1 Introduction

In the previous chapter, different ways to measure a transverse beam profile have been described. At ESS, both invasive and non-invasive profilers will be installed along the accelerator. The beam profile will be also recorded at the target location and upstream of the beam dump [1]. The interceptive measurements are mainly done with wire scanners (WS). These devices cannot handle the huge beam power of ESS at nominal conditions, and will be only used at low beam duty cycle (maximum  $100\ \mu\text{s}$  at  $62.5\ \text{mA}$ ) [2]. Therefore, Non invasive Profile Monitors, or NPM, will take over for higher beam power. The acronym NPM refers to two types of devices depending on the



detection principle. Ionization Profile Monitors (IPM) will be implemented exclusively in the cryogenic part of the accelerator whereas Fluorescence Profile Monitors (FPM) are foreseen for all the remaining parts of the linac [3]. Our team is in charge of the design and the production of ten IPMs. More information about the whole beam diagnostic framework at ESS is available in these documents [4, 5].

The present chapter is dedicated to the studies and simulations performed in order to design the future IPMs for ESS. Indeed, the ESS conditions are challenging and the feasibility of IPMs is not guaranteed. In the following, the goals and requirements of this project will be defined, and the reasons why IPMs have been foreseen will be clarified. Then, several feasibility key-points will be reported and explained, including expected counting rates, profile distortion effects and simulations of the readout.

## 3.2 ESS requirements

This section is necessary to underline the different requirements and specifications that the IPMs should match. ESS has defined requirements for the whole machine, and they are organized on different levels starting from installation up to subsystems. Every subsystem must meet its specification levels. In the case of the NPM system, the most important ones are defined in the beam instrument (level 4) and non invasive profile monitor (level 5) requirements:

- Total measurement error of the transverse beam profile in the RMS extension of less than  $\pm 10\%$ .
- The measurements and report of the relevant data at a repetition rate of 14 Hz.
- A dynamic range of 1000.

Each cold NPM consists of a consecutive pair of IPMs, each IPM measuring a transverse projection. The pair is plugged in a specific vacuum vessel: the Linac Warm Unit (LWU). The design of the LWU was frozen just few weeks after the kickoff meeting of cold NPM project (May 2016). Two slightly different LWU designs have to be considered for the IPMs: one for the Spoke section and another for the Elliptical section. A pair of wire scanners is also mounted on the LWU. Although, as previously pointed out, these devices work only at low duty cycle, they are allocated their own space in the beam line. The IPMs should not therefore geometrically trespass into the WS area. The minimal pipe radius is respectively 50 mm and 25 mm for the Elliptical and the Spoke LWU. The detector has been designed to match all the previous mechanical specifications.

The IPMs will be located between two cryomodules in the cold accelerator area. The LWU vessels are not cooled down, but their proximity to the superconducting cavities imposes a high vacuum level and a clean environment. Indeed, a too high pressure or a contamination may damage the cavities. An operating pressure of  $10^{-9}$  mbar is foreseen, but the vacuum level may be even lower during the operation. Safety valves will be closed in case of the vacuum reaches  $10^{-7}$  mbar. Hence, quantitatively the IPM design must be compliant with a high to ultra high vacuum level and an ISO-5 [6] particle-free environment. Fig. 3.1 shows the LWU vessel located between two cryomodules. One can see the two CF 200 flanges devoted to X and Y IPMs and the two rectangular CF flanges for the X and Y wire scanners.

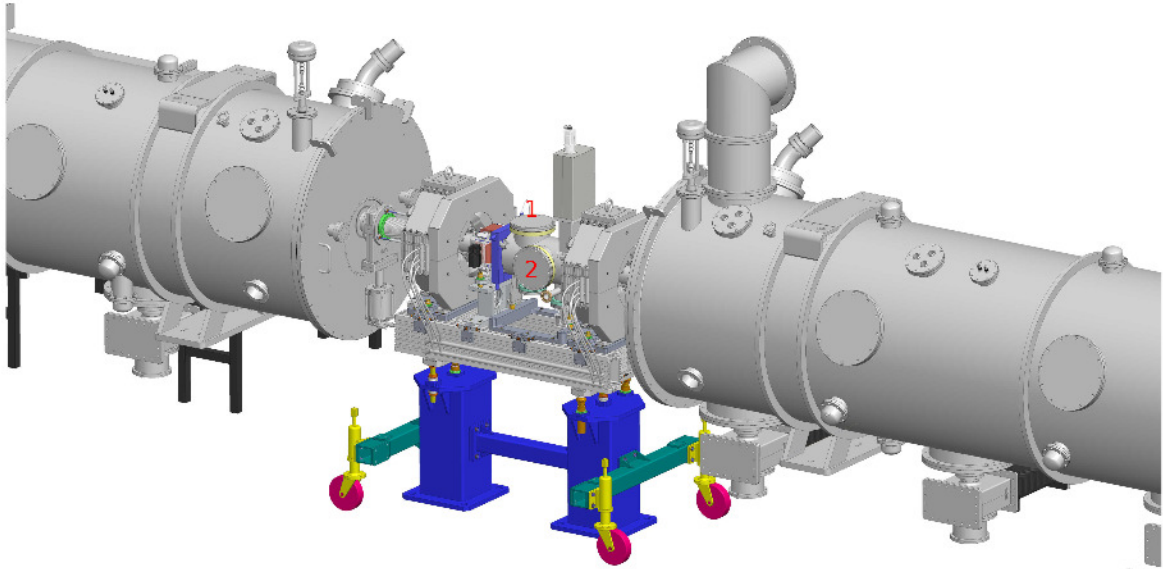


**Figure 3.1** – The LWU vessel located between two quadrupole magnets and two cryomodules. The IPMs will be mounted on the CF 200 flanges 1 and 2.

### 3.3 IPM simulations overview

As explained in the previous chapter, an Ionization Profile Monitor (IPM) is a non-invasive detector (NPM) that measures the transverse profile of a beam. Its principle of operation is shown in Fig. 3.2 and can be summarized in 3 main steps:

1. Beam protons pass through the vacuum, inducing ionizations of the residual gas molecules: electron/ion pairs are created.
2. Inside the IPM, a strong electric field drives electrons or ions towards a segmented readout system.
3. The profile is reconstructed in one transverse direction. For a complete profile, a pair of IPMs, rotated by  $90^\circ$  with respect to each other, is mandatory.

Unfortunately, there is no software that allows a full simulation of an IPM. Each step requires specific tools. As a consequence, a non-negligible work is necessary to link together the results obtained by the different steps of the simulations. Each simulation can be split in the 3 main parts, as reported just above. This chapter deals with all the simulations and approximations that have been developed to design our detector.

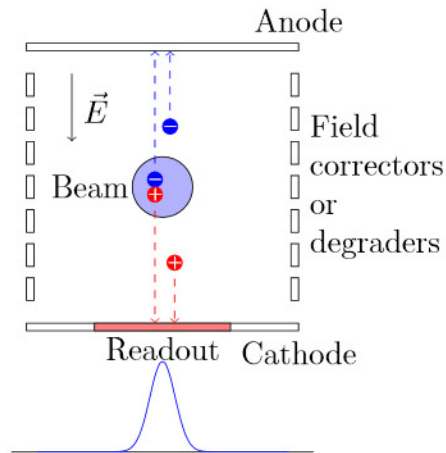


**Figure 3.2** – Visual explanation of how an IPM works. The electric field between the electrodes can be reverted by inverting the polarity, making it possible to choose if detecting ions or electrons. Field correctors or degraders, left and right, improve the field uniformity.

It is important to underline that designing IPMs to work in the requested conditions is really challenging. Preliminary studies were carried out by the NPM team in order to check the feasibility of the IPM design. The efforts have been focussed on the following hot topics:

- Quantification of the ionization signal in terms of number of produced electron/ion pairs, for ensuring that the signal is sufficiently high for reconstructing a profile per pulse, despite of the low gas pressure and ionization cross section at high proton energy.
- The extraction field must be as uniform as possible in order to lead efficiently and correctly the ionization by-products toward the readout.
- The space charge effect induced by the beam and the initial momentum of ionization electrons/ions, which may distort the profile, must be evaluated.
- The choice of an efficient readout technology which must match ESS working conditions.

All these points will be presented in the next sections.

## 3.4 Particle through matter

The interactions of particles with matter are an important aspect of particle detection [7, 8]. A particle will lose energy when it passes through a medium. The physical process behind the energy transfer mainly depends on the characteristics of the particle and the medium. These topics have been studied and improved over the last century. They often combine complicated theoretical laws with approximations or empirical models. This topic is very wide, hence in the following only the pertinent information for this study will be reported.

As explained before, the IPMs rely on the by-product collection of the ionized residual gas. The number of ionized particles gives the signal strength which has to be compliant to the readout sensitivity. Therefore, we need to know how many particles are generated by the beam itself along the residual gas enclosed in the accelerator beam pipe. Then we should understand how these secondary particles create a signal in the sensitive part of our IPM.

### 3.4.1 Interaction of charged particles with matter

For heavy charged particles, the main interaction is due to electromagnetic interactions of the incident particle with the orbiting electrons of the medium. A particle is considered heavy if its mass is much higher than the mass of an electron. The incident particle transfers a small amount of its energy to an electron of the medium at each electronic collision. In 1930, H. Bethe (original paper [9]) proposed an equation that describes the mean rate of energy losses per distance unit by a heavy charged particle. The so-called Bethe equation derives from coulomb interactions. This equation has been improved over years [10, 11]. The expression of the linear stopping power for heavy charged particles is defined by the following equation [12, p. 446]:

$$-\left\langle \frac{dE}{dx} \right\rangle = K\rho \frac{Z}{A} \frac{z^2}{\beta^2} \left[ \frac{1}{2} \ln \left( \frac{2m_e \beta^2 \gamma^2 T_{max} c^2}{I^2} \right) - \beta^2 - \frac{\delta(\beta\gamma)}{2} - \frac{C}{Z} \right] \quad (3.1)$$

where  $K$  is a constant factor defined by  $K = 4\pi N_a r_e^2 m_e c^2$ ,  $r_e$  is the classical electron radius,  $m_e$  is the electron mass,  $N_a$  the Avogadro constant and  $c$  the speed of light



in vacuum. For convenience, the stopping power is usually expressed in MeV/cm. In this case,  $K$  is equal to  $0.307075 \text{ MeV mol}^{-1} \text{ cm}^2$ .

Terms in the Bethe equation can be dissociated in two groups. First, the incident particle related terms. The maximum transfer energy for one collision is given by the following equation:

$$T_{max} = \frac{2m_e\beta^2\gamma^2c^2}{1 + \frac{2\gamma m_e}{M} + \left(\frac{m_e}{M}\right)^2} \quad (3.2)$$

where,  $M$  and  $m_e$  are respectively the incident particle and electron masses. The  $\beta$  and  $\gamma$  variables have their normal significance as Lorentz factors.

Finally, the terms related to the medium,  $Z$ ,  $A$  and  $\rho$  are respectively the atomic number, the mass number and the density of the given medium. In most of the cases the  $\frac{Z}{A}$  ratio is close to 0.5 except when a medium contains hydrogen. Sometimes, the Bethe equation is given independently from the density. The mean excitation energy  $I$  is the only non-trivial variable in the Bethe equation [13, 14]. The computation is quite complicated because it requires to measure the oscillator strength for each material. Table 3.1 gives the  $I$  value for common materials.

Two correction factors are often used to improve the accuracy of the Bethe equation at low and high energies. The term  $\frac{\delta(\beta\gamma)}{Z}$  corrects for the density effects at relativistic energies [15]. The shell correction  $\frac{C}{Z}$  improves the accuracy at low energies [16].

Fig. 3.3 shows the mass stopping power of a proton in two different media. The blue region represents the energy range of protons in the cryogenic part of ESS, where IPMs will be located. One can see that the minimum of energy loss is reached around 2 GeV.

The Bethe model has been tested and improved with respect to experimental data [18]. However, at very low or high energies<sup>1</sup> the Bethe equation is no more usable. In these regions specific models are used to describe the energy loss in matter [19, 20].

The Bethe model is also not compatible with low mass particles like electrons and positrons and must be modified for these particles [21][12, p. 452]. At low energies, electrons lose their energies by ionization like ions, whereas at energies above few MeV, electrons also lose energy through bremsstrahlung radiation.

### 3.4.2 Electron ion pairs production

We just defined the mean energy loss rate of a charged particle per unit of distance. When a particle passes through a medium, it may transfer its energy to the medium, which for now we consider as composed of atoms not bound in molecules. If the energy is sufficient, an ionization happens: one or more electrons are ejected from the electronic shells, leading to the creation of an ion and free electron(s). In case of molecules, the ionization process may be dissociative i.e. it may break the molecular bounds. The cross section for dissociative ionization is far lower than the one for pure ionization [22].

By introducing  $W$ , the average energy for producing an ion/electron pair in a medium, we can estimate the number of ion/electron pairs created in a given readout length  $\Delta x$  of materials [23, 24] as:

1. Below MeV and above hundred GeV for protons.

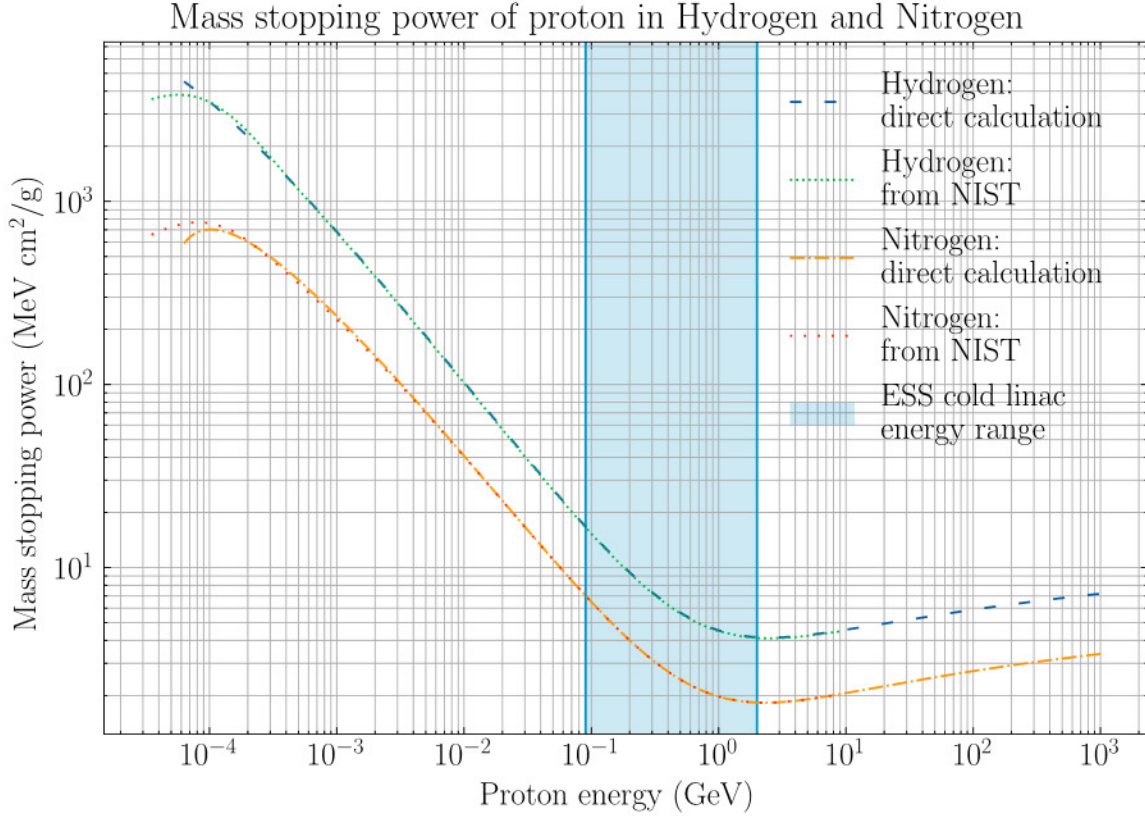


**Figure 3.3** – Typical mass stopping power plot for a proton. Here the mass stopping power is plotted for a proton in hydrogen and nitrogen. The calculation was done using the Bethe formula and has been cross-checked with the NIST PSTAR table which contains both computed and experimental values [17]. The Bethe equation gives correct results between  $0.2 < \beta\gamma < 100$ . However at lower and higher energies the Bethe formula is no more reliable.

$$N_{electrons} = \frac{\langle \frac{dE}{dx} \rangle}{W} \Delta x \quad (3.3)$$

When an electron is ejected, it has a certain probability for ionizing other atoms if its energy is high enough. These secondary electrons are called delta rays or delta electrons. This phenomenon becomes rare and negligible when the medium has a very low density like in a vacuum system. The  $W$  parameter includes the delta ray electrons, hence the  $W$  value is biased [12, p. 470] for the case at hand, since the IPMs work at very low pressure. Table 3.1 gives, as an example, the  $W$  values for several materials at Normal Temperature and Pressure<sup>2</sup> (NTP).

When the medium is a mixture of several compounds, its mean stopping power needs to be calculated as the sum of the mean stopping power of its components weighted by their mass proportion. As a consequence, the total number  $N_{total}$  of electron/ion pairs results:

$$N_{total} = \sum_{n=First}^{Last} N_{compound} = \sum_{n=First}^{Last} w_n \frac{\langle \frac{dE}{dx} (\rho_n, I_n, A_n, Z_n) \rangle}{W_n} \Delta x \quad (3.4)$$

2. 20 °C, 1 atm.



**Table 3.1** – Mean excitation energy, average energy to produce a pair and density values for several mediums at Normal Temperature and Pressure (NTP). Complete reviews of  $I$  and  $W$  values are available in [25][24].

Gas	$I$ (eV)	$W$ (eV)	$\rho$ (kg/m <sup>3</sup> )
$H_2$	18.8	36.43	0.0899
$CO$	85.9	34.5	1.165
$CO_2$	85.00	34.21	1.842
$N_2$	82.00	36.39	1.165

The calculation can be done for each single element or for each molecule in the compound. This latter is recommended since the  $I$  values are in general higher for molecules [12, p. 451].

### 3.4.3 Calculation

Following the physics introduction reported above, this subsection is dedicated to the estimation of the number of primary particles that will be created at the ESS conditions. Two different approaches have been done: naive computation of Bethe equation and simulations through a software.

The Bethe formula can be implemented in a spreadsheet or a C++ code once the composition of the medium and the  $I$  value of each compound is known. The expected pressure in the cryogenic part at ESS is around  $10^{-9}$  mbar, and the gas composition is given in Table 3.2.

**Table 3.2** – Expected residual vacuum gas characteristics in the cold part of the ESS Linac, provided by ESS vacuum group.

Gas	Mass percentage (%)	$p_i$ (mbar)	$\rho_i$ (g/cm <sup>3</sup> )
$H_2$	79	$7.9 \cdot 10^{-10}$	$6.52 \cdot 10^{-17}$
$CO$	10	$1.0 \cdot 10^{-10}$	$1.15 \cdot 10^{-16}$
$CO_2$	10	$1.0 \cdot 10^{-10}$	$1.80 \cdot 10^{-16}$
$N_2$	1	$1.0 \cdot 10^{-11}$	$1.14 \cdot 10^{-17}$

We assume that the residual gas follows the "perfect gas" law. We also assume that the linear density scaling of Bethe equation remains true in high vacuum [26, p. 108][27]. Hence, the partial pressure and the density for each gas is calculated with respect to the tabulated pressures. The primary signal is computed at ESS nominal conditions given in Table 2.1.

Fig. 3.4 shows the number of electron ion pairs created for each gas species versus the ESS proton beam energy. The different IPMs locations are marked by a blue line. One can see that the gas density has a strong influence on the primary signal. Although the hydrogen is the main species in terms of proportion, its contribution to the signal is close to the one from carbonate species. Note that the  $W$  value may overestimate the number of pairs created due to secondary delta rays.

We have also used the Garfield++ software to compute the number of primary ionizations. This software is normally intended for the modelization of gaseous detec-

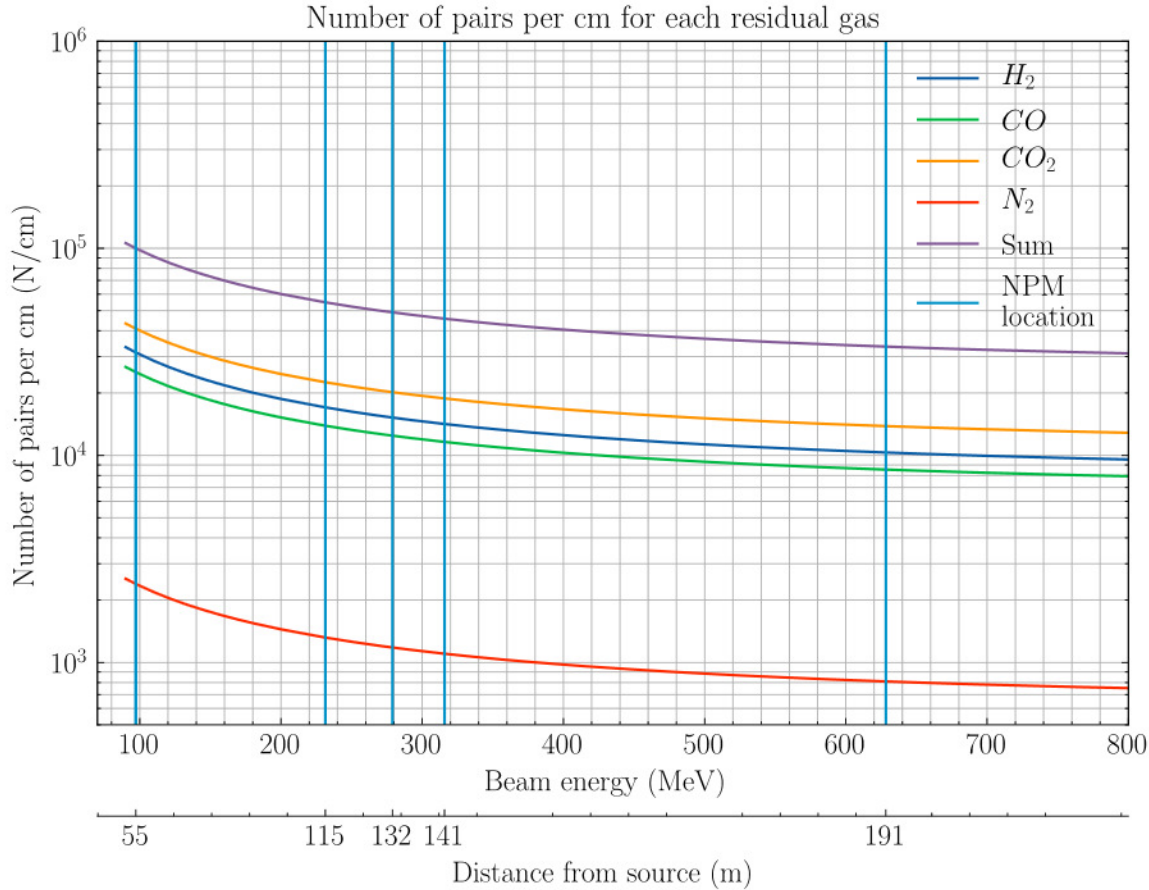


**Figure 3.4** – Expected number of ionization by-products per centimeter at ESS nominal conditions according to the Bethe equation. Each vertical line corresponds to an IPM location.

tors. It allows to simulate the creation of electron/ion pairs due to the ionization of gas by an incident particle, the transport and amplification of these electrons in the gas and the signal induced on a readout plane. In our case, we simulated only the pair creation in the residual gas. For this step Garfield++ uses two programs internally:

- Magboltz: a Fortran routine that computes different properties of a gas mixture and performs the transport of electrons in this mixture [28].
- Heed ++ [29]: a C ++ code that implements an ionization model based on the photoabsorption ionization (PAI) [20].

A dummy detector, a cube of ten centimeter side, is implemented and filled with the same gas composition as in Table 3.2. Protons are shot into this detector and the information on the electrons created in the gas is saved in a ROOT file [30, 31] for post processing. This is done for different proton energies and vacuum levels.

Table 3.3 reports the value of the expected number of electrons/ions pairs per cm obtained from the direct calculation (Bethe equation) and from the results of the Garfield++ simulations. One can see that the Garfield++ value is always lower than the calculation by a constant factor 0.52. These value are important since they will be used to determine the readout technology and its electronics.

**Table 3.3** – Comparison of expected number of electrons between calculation using Bethe equation and results from Garfield++.

Energy	$N_{Bethe}$	$N_{garfield}$	Factor
97.2	100210	52537	0.52
231.4	54970	27463	0.50
278.9	49160	26124	0.53
315.8	45850	23769	0.52
628.3	33600	17522	0.52

### 3.4.4 Pressure uniformity

The primary signal is strongly dependent on the pressure inside the vacuum chamber. A gradient in the pressure may cause a change in the signal shape. It is therefore interesting to simulate the vacuum level in the LWU to check the existence of such gradient in the residual gas of the IPMs.

A simulation has been done with the Molflow+ software developed at CERN [32]. It simulates the vacuum in a steady state by using Monte Carlo and Ray Tracing methods. The user defines his geometry, as well as the desorption and adsorption rates of each surface. As visible in Fig. 3.5, the implemented geometry does not contain all the structures and surfaces. Two dummy squared facets of 5 cm side are inserted in the center of each IPM. The pressure profiles are then measured on these facets. No information about the real pumping speed, surface conditions or other vacuum characteristics is input in the program since the only goal of this simulation is for checking the non-uniformity effect of the residual gas pressure for both IPMs. We have also checked the case of an unwanted outgassing which may occur on one side of the IPMs. No significant change has been observed.

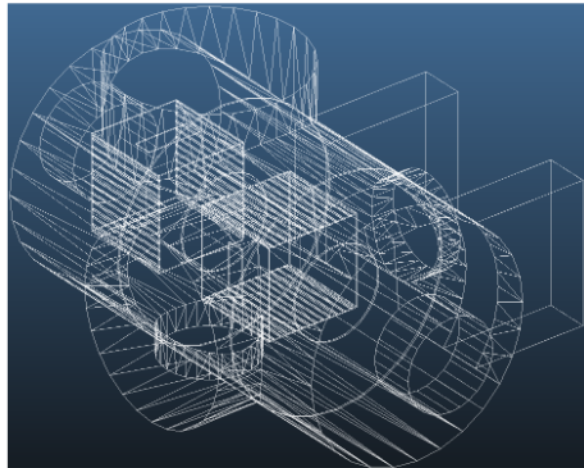
**Figure 3.5** – The LWU geometry implemented in Molflow+.

Fig. 3.6 shows the results from the simulations. The pressure levels seem to be uniform for both IPMs along the transverse direction, and it may not affect the profile measurement. The pressure is slightly lower in the second IPM because the pumping group is closer.

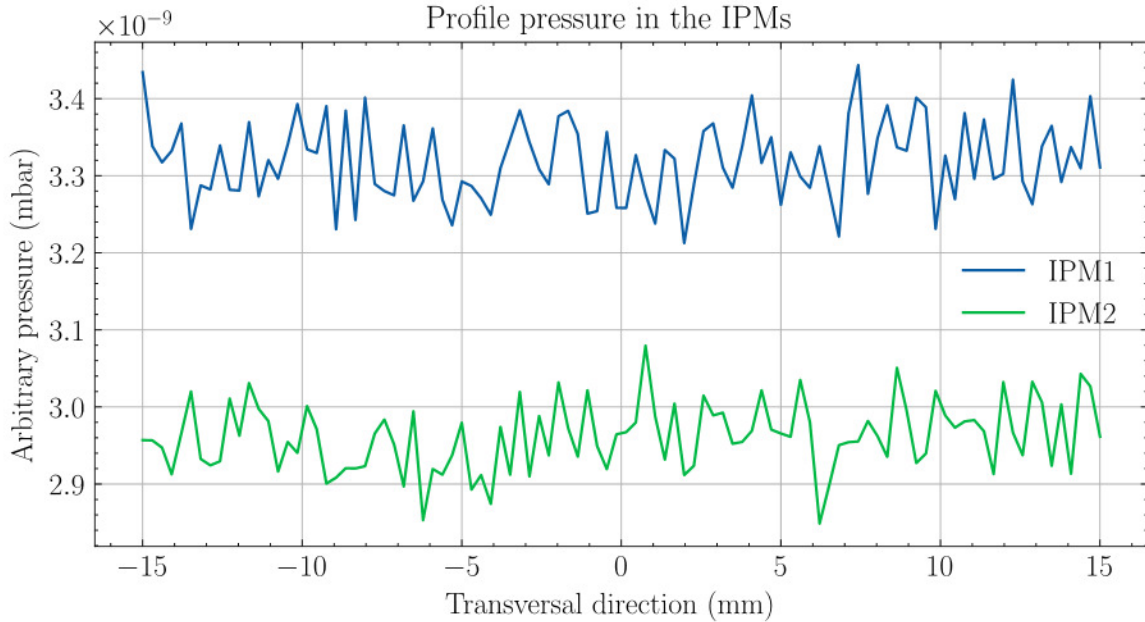


Figure 3.6 – Simulated profile pressure in the center of IPMs.

### 3.5 Extraction field

The IPMs can be seen as parallel plate detectors. In an ideal IPM these plates are infinite sized. The extraction field is then completely oriented in a single direction, normal to the detection plane and the projection of the profile on this plane is perfect. In reality, the plates have finite dimensions, comparable to the gap between the two electrodes. In these conditions the field is no longer uniform.

The effects induced by the cage sides are no longer negligible; field uniformity is strongly influenced by the needle effects of the plates. Also, the geometry of the vacuum chamber affects the field uniformity: it is considered to be at ground

but walls close to the IPMs modify the electric field lines inside the IPMs. In addition, the cross-interaction between the electric fields of two close by IPMs is very strong.

Finally, the way to create the field with high voltage (HV) power supplies has an important influence on the electric field itself. We will see later that some readouts can only work in certain HV configurations, unless major modifications of the set-up are considered.

The non-uniformity of the electric field is very problematic because it creates distortion effects and prevents the correct measurement of the beam profile as shown in Fig. 3.7. It also determines the maximum size of the detection area, which must be

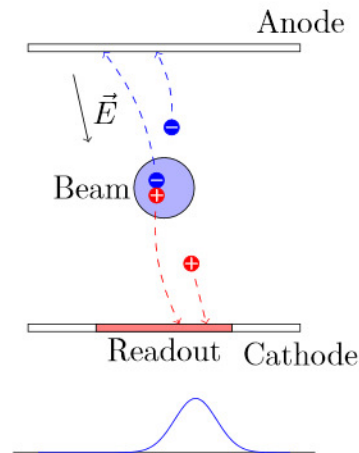


Figure 3.7 – Non-uniformities leading to mirage effects on the profile measurement.



in a zone where the electric field is as uniform as possible. To overcome the distortion effect, the field line must be as straight as possible. Several solutions can be considered to improve the field uniformity:

- The distance between the two electrodes can be reduced. In this case, the IPMs will tend to a configuration close to the infinite parallel plates assumption. Following the same logic, the size of both electrodes could be increased. These solutions are mainly limited due to mechanical considerations. To stay on the safe side, the distance between two plates was chosen to be at least equal to the diameter of the beam pipe. Moreover, the whole assembly of one IPM must hold on a CF 200 flange.
- Using field correctors or field degraders [26, p. 103]. This is done by placing conductors on each side. Each corrector is set to a certain potential in order to constrain the field. This solution is easy to implement, compact, and very versatile. However, it requires a large number of HV feedthroughs or the use of resistors in vacuum. The longitudinal field can also be slightly improved in a same way.
- Inserting grounded conductors between the two IPMs [26, p. 132] to protect against the IPM cross-interaction. The longitudinal correctors also reduced the cross-interaction.
- Optimizing the geometry of HV electrodes. For example, with a curved geometry with reinforcements on the edges it is possible to correct the field transversely and longitudinally. Hence, "there is no more need of field correctors" as said in [33].

Aside the above listed solutions, software corrections may be a way to correct the non uniformities. However, as previously explained the non-uniformity of the extraction field is not the only phenomenon responsible for the distortions of the measured profile. It is therefore extremely difficult to implement it, because it requires a perfect mapping of the extraction field to decouple it from other phenomena. Physical corrections are simpler to implement.

### 3.5.1 Maxwell equations at steady state

Electric and magnetic fields are perfectly described by the Maxwell's equations. Since we are in vacuum, the Maxwell's equations can be reduced to:

$$\vec{\nabla} \cdot \vec{E} = \frac{\rho}{\epsilon_0} \quad (\text{Maxwell-Gauss's Law})$$

$$\vec{\nabla} \times \vec{E} = -\frac{\partial \vec{B}}{\partial t} \quad (\text{Maxwell-Faraday's Law})$$

$$\vec{\nabla} \cdot \vec{B} = 0 \quad (\text{Maxwell-Thomson's Law})$$

$$\vec{\nabla} \times \vec{B} = \vec{J} + \frac{\partial \vec{E}}{\partial t} \quad (\text{Maxwell-Ampère's Law})$$

The time derivatives cancel when the field variations over time are negligible compared to the studied phenomena. So, the coupling effects between the electric and the magnetic fields disappear. Therefore, the electrostatic field depends only on the Gauss's law. In electrostatic, it is quite convenient to introduce the electric potential:

$$\vec{E} = -\vec{\nabla}V \quad (3.5)$$



### 3.5.2 Solving Poisson's equation

The electric potential follows the Poisson's equation:

$$\vec{\nabla}^2 V = -\frac{\rho}{\epsilon_0} \quad (3.6)$$

or in a more generic notation:

$$\Delta v = f \quad (3.7)$$

with  $f$  the right hand side function.

The solution of this equation can be found analytically, by relying on the use of complex numbers or Laplace transforms. However, when the size of the problem increases the solution becomes harder to compute, and solving the Poisson's equation on complicated domains is almost impossible. Numerical methods allow to approximate the solutions of partial differential equations (PDE) on non trivial domains. There are many schemes to solve numerically PDE. In this section we will briefly present three methods that are often used. It is important to understand how they work and to know their limitations or pitfalls. In numerical schemes, the domain is discretized in a finite set of points. Then, the solution is approximated at each point with respect to initial and/or boundary conditions. To solve a problem, it must be well posed: the problem must admit a single unique solution that depends continuously on the variables and conditions [34]. It turns out that the Poisson's equation is a well-posed problem if a Dirichlet condition is applied.

Finite Difference Method (FDM) is a popular way to solve numerically the Poisson's equation. In FDM, the domain is discretized regularly with a step  $h$ . The Taylor's theorem allows to approximate the value of a function by a polynomial equation that depends on its derivatives nearby:

$$v(x+h) = v(x) + hv'(x) + \frac{h^2}{2}v''(x) + \frac{h^3}{6}v'''(x) + O(h^4) \quad (3.8)$$

$$v(x-h) = v(x) - hv'(x) + \frac{h^2}{2}v''(x) - \frac{h^3}{6}v'''(x) + O(h^4) \quad (3.9)$$

From these formulas, the second derivative can be expressed:

$$\frac{\partial^2 v}{\partial x^2} = \frac{v(x+h) - 2v(x) + v(x-h)}{h^2} + O(h^2) \quad (3.10)$$

and in case of a two-dimensional domain it is written as follows:

$$\begin{aligned} \Delta v &= \frac{\partial^2 v}{\partial x^2} + \frac{\partial^2 v}{\partial y^2} \\ &= \frac{v(x+h, y) + v(x-h, y) + v(x, y+h) + v(x, y-h) - 4v(x, y)}{h^2} + O(h^2) \end{aligned} \quad (3.11)$$

Each point of the domain can be expressed according to its neighbors. Then, it is possible to write a set of linear equations in matrix form by choosing wisely the indexing order. For example, when the domain is decomposed line by line, one can obtain the same system of equations repeated for each inner line<sup>3</sup>.

$$Id \cdot v_u + A \cdot v_c + Id \cdot v_d = D \quad (3.12)$$

---

3. The first and last lines have a slightly different set of equations due to boundary conditions.

Where  $Id$  is the identity matrix,  $v_u$  are the unknown values of the upper line,  $v_d$  of the lower line,  $v_c$  of the current line,  $A = \begin{pmatrix} -4 & 1 & 0 & \dots \\ 1 & -4 & 1 & \dots \\ 0 & 1 & -4 & \dots \\ \vdots & \vdots & \vdots & \ddots \end{pmatrix}$  is the square matrix of FDM schemes and  $D$  is vector of Dirichlet values. Then, the global matrix is assembled by combining the sub-matrices for each line.

$$\begin{bmatrix} A & Id & 0 & \dots \\ Id & A & Id & \dots \\ 0 & Id & A & \dots \\ \vdots & \vdots & \vdots & \ddots \end{bmatrix} \cdot \begin{bmatrix} v \\ v \\ v \\ \dots \end{bmatrix} = \begin{bmatrix} D \\ D \\ D \\ \dots \end{bmatrix} \quad (3.13)$$

One can see that the problem is solved by inverting the  $A$  matrix. This matrix is very sparse and can be inverted with iterative methods rather than a direct inversion. FDM is straightforward and allows to quickly solve Poisson's equation on a linear structured mesh. For instance, it is very useful for calculating an electric field generated by a charge density. However, FDM cannot be used when the geometry becomes too complex.

The Finite Element Method (FEM) is more suitable for solving PDE on complicated domains. The FEM uses the weak formulation of the Poisson's equation. By introducing a test function  $\varphi$ , this weak form can be written easily thanks to an integration by parts:

$$\int_{\Omega} \varphi \Delta v d\Omega = \int_{\Omega} \varphi f d\Omega \quad (3.14)$$

$$- \int_{\Omega} \vec{\nabla} \varphi \cdot \vec{\nabla} v d\Omega + \int_{\Sigma} \varphi \vec{\nabla} v \cdot \vec{n} d\Sigma = \int_{\Omega} \varphi f d\Omega \quad (3.15)$$

with  $\Sigma$  the boundary domain. One can see that the Laplacian disappeared from the formulation. An approximation of  $v$  is done in the reduced domain by means of low order polynomial functions. Again, a finite system of linear equations can be written, and the problem is solved by inverting the matrix. The correct choice of test functions and the way to index elements lead to very sparse matrix which can be inverted easily. Unlike the FDM, the solution is approximated on the whole reduced domain and not locally. FEM supports complicated meshes as long as they are continuous and solves all kinds of PDEs that may be much more complex than the Poisson's equation.

With FEM, the whole domain is fully discretized in its entire volume. In case of electrostatic field, it is possible to use the Boundary Element Method (BEM). With the BEM, the Poisson's equation is first solved on boundaries. Then, the electric field can be evaluated at any point in the domain from the contributions of all boundaries. The discretization is also performed only on the boundaries and not on the entire geometry. So, the dimension of the problem is reduced and the matrix to be reversed is much smaller. On the other hand, the matrix is no longer sparse.

Most of the commercial simulation softwares [35–37] rely on FEM or BEM. We have used mainly the COMSOL software for the simulations of extraction fields.

### 3.5.3 COMSOL

COMSOL is a commercial all-in-one multi-physics simulation software able to solve various problems from structural mechanical analysis to optical raytracing [38]. We used COMSOL with the AC/DC module [39] to simulate the static electric field in the IPM box. COMSOL allows to quickly define, simulate and post process physical models. The typical workflow is divided in three main steps as follow.

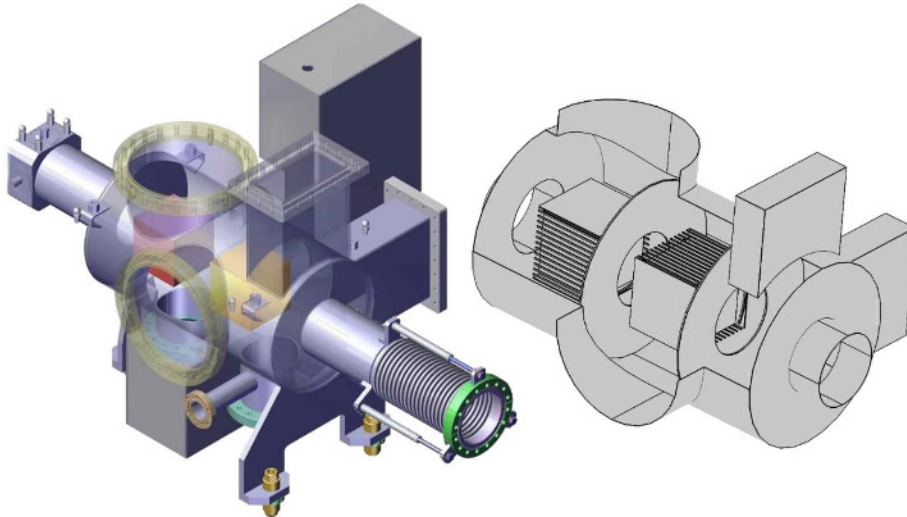


**Figure 3.8** – A drawing of LWU (left) and its implementation in COMSOL (right).

The first step is to implement the detector geometry into COMSOL. The software includes basic CAD features allowing to quickly create two or tridimensional geometries. The users can directly import a mesh from files generated by external CAD tools. Care should be taken for importing a CAD file: it often contains many details and thus increases the CPU time consumption. It is much faster to directly implement the geometry with COMSOL. In our case, only the inner shape of the vacuum chamber and the IPMs have been defined. All other conductive bodies that enclose the vacuum are not relevant for an electrostatic simulation. Therefore, the geometry could be simplified. Fig. 3.8 shows, on the left, a 3D drawing of the ESS vacuum vessel with the two IPMs inside. And on the right, an example of the simplified geometry implemented in COMSOL.

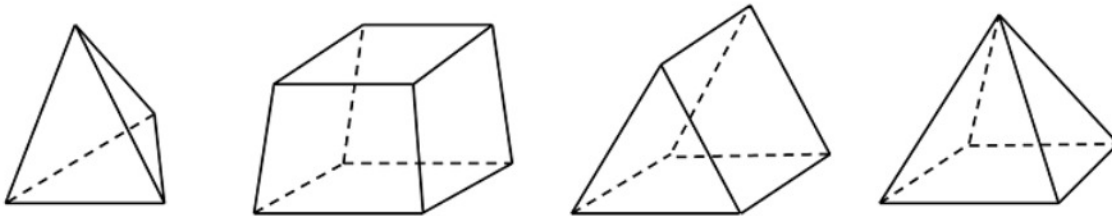


**Figure 3.9** – Mesh elements included in the COMSOL software. From left to right: tetrahedron, hexahedron, prism and pyramid [40]. COMSOL uses tetrahedral elements by default to mesh a 3D geometry in AC/DC module.

The next step consists in the discretization of the previous geometry in many Lagrange elements in order to form a mesh. Fig. 3.9 shows the main meshing elements available in COMSOL. For an electrostatic tri-dimensional study, COMSOL

uses quadratic tetrahedral elements by default. The meshing algorithm tries to create elements fitting well the geometry. For the inner small parts of the geometry, the size of elements will be reduced. Conversely, mesh cells will become bigger and bigger in coarse regions of the geometry. This behavior is not desirable for us, since the IPM region of interest has no geometrical variations. The geometry would not be not described accurately. Fortunately, the user can change the characteristics and the nature of the elements in specific regions of the defined geometry. We used a tetrahedral mesh everywhere but in the IPM box, where a cubic mesh with high granularity is defined. The meshing step is very memory consuming, but a poorly optimized mesh may destroy performances.

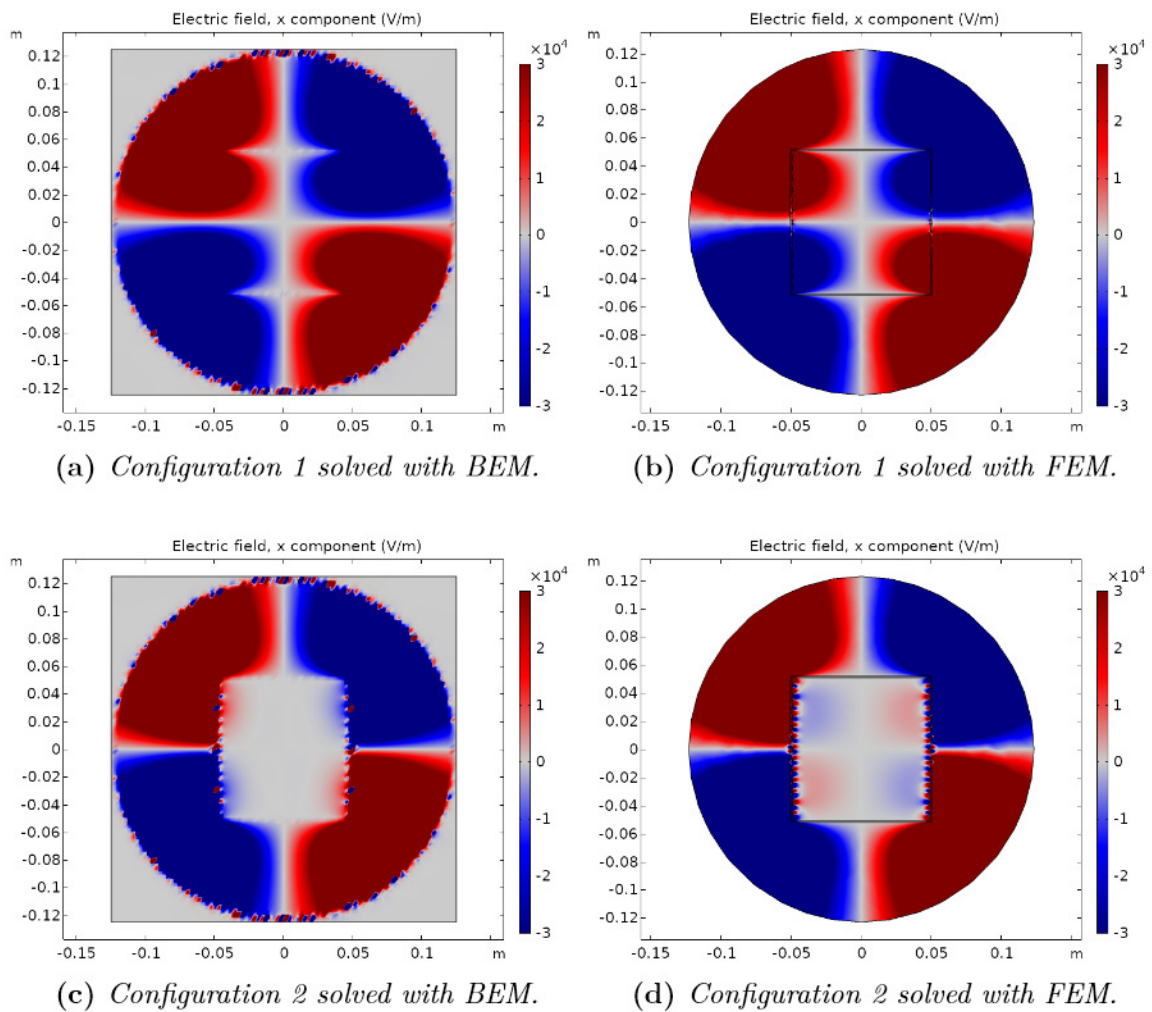


**Figure 3.10** – Comparison between BEM and FEM for two different IPM configurations. The configuration 1 covers the case of simple parallel plates. In configuration 2, the field is constrained by field correctors on each side (see Section 3.5.7). Some differences appear for configuration 2 especially on the side of the IPM where the field variations are important.

The last step is to define boundary conditions. COMSOL hides completely the mathematical aspect of the FEM/BEM and directly expresses the boundary conditions by associating them a physical meaning. This means that, when using AC/DC module, the user should fix potentials or charge densities on boundaries. A more detailed description of each boundary condition type can be found in the reference



manual. COMSOL is able to solve electrostatic problems by means of FEM or BEM since version 5.3a. We compared the FEM and BEM for same configurations and we found out that results are slightly different as shown in Fig. 3.10. We decided to use mainly FEM since it is the legacy method in COMSOL. Once solved, the results can be visualised directly in COMSOL. Data can be also exported to an external file in text format (comma separated values or VTU format).

Below are listed the relevant assumptions made in our COMSOL model:

- All conductors and insulators are supposed to be perfect.
- Field correctors and electrodes are thicker than in reality since it is not feasible to describe a micrometer deposition layer in a meter scale simulation.
- Neither the resistor chain at the back of field correctors, nor the connection wires, feedthroughs and connectors are implemented.
- The vacuum vessel is supposed to be at the same ground as the power supplies, and without any charge on its surface.

### 3.5.4 Criteria

It is necessary to define criteria to quantify the uniformity of the electric field in order to compare several simulations. In this thesis, we will use mainly:

- Visual approaches (isocolors and streamlines) that are sufficient at first to underline big differences between two models.
- A statistical criterion
- Particle tracking

In this section, we will explain briefly the two last criteria.

For the statistical criterion, the whole data set is sliced in the longitudinal direction. In each slice, the quadratic mean value of each electric field component is computed in a small cylinder at the center of the IPM.

$$\vec{E}_{mean} = \frac{\sum_{i=1}^N \sqrt{\vec{E}_i^2}}{N} \quad (3.16)$$

The only pitfall of this method is the size of the area. The mean value must be computed on an area that covers at least the beam<sup>4</sup>. On the other hand, if the area is too big, then the mean value will be biased due to field correctors on each side of the IPMs. To choose the area size, we proceed as follows. A charged particle is released at rest in a dummy IPM where the field is perfectly uniform, except in a small region. In this region, we add a component perpendicular to the field lines and equal to 1% of the main field value. When the particle reaches the readout, the total deviation is recorded. Then the region is shifted and the computation is repeated. Table 3.4 tabulates results.

One can see that the deviation is quite important when the particle has almost no kinetic energy, i.e. when the particle is created. At the end of the drift, the particle has far higher kinetic energy and is therefore less affected by field non-uniformities. This means that, the field must be optimized to be as much uniform as possible at the center of the IPM. The non-uniformities on the IPM sides are less of a concern. So, we decided to compute the quadratic mean inside a circle of at least 2 cm radius.

---

4. We assume that the beam is centered.



**Table 3.4** – *Example of deviation of the trajectory of a particle in an IPM. A particle is released in the center of an IPM with a straight field everywhere, but in a certain range a parasitic field component is added and set to 1% of the main field. The 0 coordinate is the IPM center whereas the readout is located at distance of 5 cm.*

	Range (cm)					
	[0, 5]	[0, 1]	[1, 2]	[2, 3]	[3, 4]	[4, 5]
Deviation ( $\mu\text{m}$ )	500	347	85	42	20	5.6
%	100	69.4	17	8.4	4	1.12

However, it is impossible to predict the real effects on the profile since the quadratic mean shadows the direction of the field.

The tracking algorithm is, in theory, the most relevant criterion for an IPM. Charged particles are released in the center of the IPM and we observe them drifting in the field cage along the field lines generated by the electric and magnetic fields, thanks to the Lorentz's force:

$$\vec{F} = m \cdot \vec{a} = q \cdot (\vec{E}(\vec{r}, t) + \vec{v} \times \vec{B}(\vec{r}, t)) \quad (3.17)$$

Once the tracking is done the relative error on  $\sigma$  can be computed:

$$|\Delta\sigma_{beam}| = \left| \frac{\sigma_{final} - \sigma_{initial}}{\sigma_{initial}} \right| \quad (3.18)$$

Initial particle positions are drawn following an ESS pulse shape with well defined longitudinal and time characteristics. The equation of motion is integrated with a numerical integrator. The value of the field at an arbitrary position is interpolated from values computed by COMSOL. These steps are repeated until the particles reach the detection system. The simplest numerical method is probably the Euler integration, written as follow in the case of the Lorentz's force:

$$\vec{v}_i = \vec{v}_{i-1} + \frac{q}{m} (\vec{E}(\vec{r}_{i-1}, t) + \vec{v}_{i-1} \times \vec{B}(\vec{r}_{i-1}, t)) \cdot \Delta t \quad (3.19)$$

$$\vec{r}_i = \vec{r}_{i-1} + \vec{v}_i \cdot \Delta t \quad (3.20)$$

This algorithm was implemented in C++ and Python code. Since the above reported calculation procedure reduces to a first order integrator, its accuracy is poor. Higher orders methods, like Runge-Kutta integrators, provide higher accuracy, thus they are very popular integrators for solving various types of ordinary differential equations (ODE). Nevertheless, when a magnetic field is present, even the Runge-Kutta integrators results in insufficient accuracy. The Boris algorithm [41] provides a workaround for this problem. The speed  $\vec{v}_{i+1}$  at the time step  $i + 1$  is calculated from the speed

$\vec{v}_i$  at the time step  $i$  by splitting the computation in 4 substeps:

$$\vec{v}^- = \vec{v}_i + \frac{q}{m} \frac{\Delta t}{2} \vec{E} \quad (3.21)$$

$$\vec{v}' = \vec{v}^- + \frac{q}{m} \frac{\Delta t}{2} (\vec{v}^- \times \vec{B}) \quad (3.22)$$

$$\vec{v}^+ = \vec{v}^- + \frac{\frac{q}{m} \Delta t}{1 + (\frac{q}{m} \frac{\Delta t}{2} \vec{B})^2} (\vec{v}' \times \vec{B}) \quad (3.23)$$

$$\vec{v}_{i+1} = \vec{v}^+ + \frac{q}{m} \frac{\Delta t}{2} \vec{E} \quad (3.24)$$

where  $\vec{v}^-$  is the speed after applying half of the electric field,  $\vec{v}'$  and  $\vec{v}^+$  account for the magnetic field rotation, and in equation (3.24) the last half of the electric field contribution is added.

One can see that the E and B fields are separated. This algorithm is almost a standard in particle in cell (PIC) codes because it remains extremely accurate even during long integration times [42]. The comparison between Euler and Boris methods is shown in Fig. 3.11b, where an electron drifts in an electromagnetic field (2kV/cm and 0.2 T in the same direction). The electron position is computed with both Boris and Euler method. With the Euler method, the electron acquires "numerical" energy. In this example the deviation is negligible but the effect will be higher with realistic fields. The Boris method should be used mainly when a strong magnetic field is present.

During the tracking, the field is evaluated at each step in order to calculate the new velocity and position. The field values must be interpolated because the original field dataset is composed of discrete values. The mesh is usually not structured with FEMs, therefore the interpolation is not trivial and several approaches can be considered. The interpolation can be done by a nearest neighbor (NN) search. In this case the returned value is the closest point, among the mesh ones, to the considered coordinate with respect to a metric distance. This method anyhow leads to errors if the mesh is not regular enough. A first improvement of the results obtained with this method is achieved by weighting the returned values with the distances of closest points. This is known as Shepard interpolation. However, the accuracy is still perfectible. Radial Basis Function (RBF) interpolation is one of the most powerful interpolation method working on unstructured data [43]:

$$f(x_i) = \sum_{n=0}^N w_n \phi(\|x_i - x_n\|) \quad (3.25)$$

where  $f$  is the interpolation function evaluated at  $x_i$  and calculated as the sum of  $N$  radial basis functions  $\phi$ . The  $w$  coefficient is defined by a set of linear equations that depends only on  $f$  and on the distances between each original point.

$$\begin{bmatrix} \phi(\|x_0 - x_0\|) & \phi(\|x_0 - x_1\|) & \phi(\|x_0 - x_2\|) & \cdots \\ \phi(\|x_1 - x_0\|) & \phi(\|x_1 - x_1\|) & \phi(\|x_1 - x_2\|) & \cdots \\ \phi(\|x_2 - x_0\|) & \phi(\|x_2 - x_1\|) & \phi(\|x_2 - x_2\|) & \cdots \\ \vdots & \vdots & \vdots & \ddots \end{bmatrix} \cdot \begin{bmatrix} w_0 \\ w_1 \\ w_2 \\ \cdots \end{bmatrix} = \begin{bmatrix} f(x_0) \\ f(x_1) \\ f(x_2) \\ \cdots \end{bmatrix} \quad (3.26)$$

As already mentioned,  $\phi$  is the RBF or kernel function. For example, for a gaussian kernel with a shape parameter  $\epsilon$ :

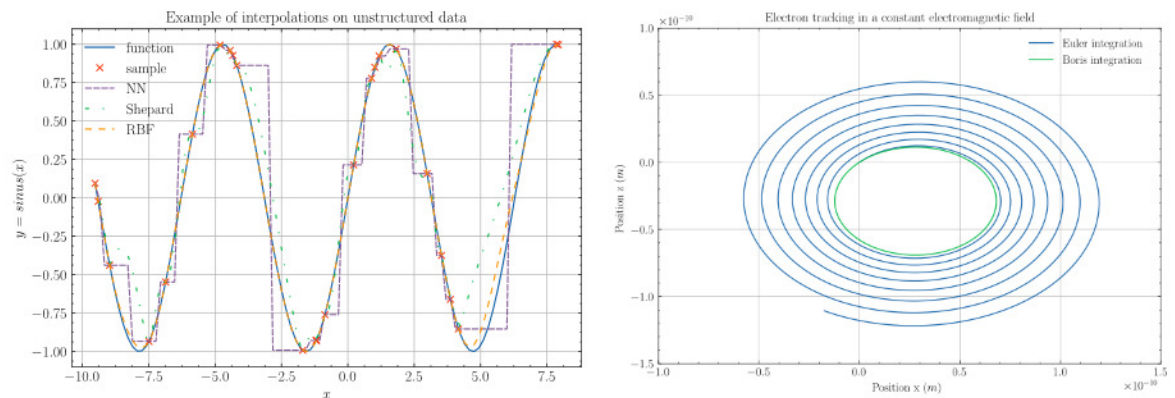
$$\phi(\|x - x_n\|) = e^{-\epsilon(\|x - x_n\|)^2} \quad (3.27)$$

We mainly used the RBF method to interpolate our fields during the particle tracking. Fig. 3.11a shows the comparison between the NN, Shepard and RBF interpolations. One can see that the RBF interpolation is far more accurate than the two others and it provides good approximation with moderate computation time.

It is important to keep in mind that the total error during the particle tracking is proportional to the error in each step:

$$\epsilon_{total} \propto \epsilon_{integration} \propto \epsilon_{interpolation} \propto \epsilon_{gradient} \propto \epsilon_{FEM} \quad (3.28)$$

Unfortunately, we can not give a confidence level on our simulations since the determination of the total error is not trivial and was not investigated due to lack of time. In such a context, we repeated the simulations until we observed a convergence.



(a) *Interpolations on a randomly sampled sinus functions. The RBF interpolation gives good accuracy compared to the others two interpolations (NN and Shepard).*

(b) *Integrations of motion and position in a constant electromagnetic field. Euler (and RK) gains numerical energy whereas the Boris method shows excellent accuracy over time.*

**Figure 3.11** – *Interpolations and integrations are critical steps of the particle tracking. An incorrect use of numerical tools may lead to biased results.*

The tracking algorithm has been implemented in a C++ code. All vector operations are performed by the Eigen [44] package and a homemade code. The nanoflann library [45] was exploited to build a kd-tree from the field data. A kd-tree allows to quickly search a set of points inside the whole dataset. The interpolation routine is homemade and relies on the previously mentioned libraries. The routine implements the nearest neighbors and RBF interpolations. The numerical integration of positions and velocities are performed by either an homemade code or using the Odeint library [46, 47]. Particles are tracked in parallel jobs with the Intel TBB library [48].

### 3.5.5 IPM polarity

In an IPM, the extraction field can be generated with different kinds of high voltage configurations. However, some readouts can not operate at high voltages. In this case, the readout electrode must be at ground level in order to avoid damages to the readout. Hence, the choice of the HV configuration is fully determined by the choice of the readout. In the following, we will consider two configurations:

- Symmetric configuration when the readout can work at high voltage. In this case, the electrodes have opposite potential.
- Asymmetric configuration when the readout electrode is at ground and the other electrode is at a certain potential.

The two configurations have been simulated in COMSOL and the results are presented in the Fig. 3.12. One can see that without any correction the extraction field in symmetric configuration is much more uniform.

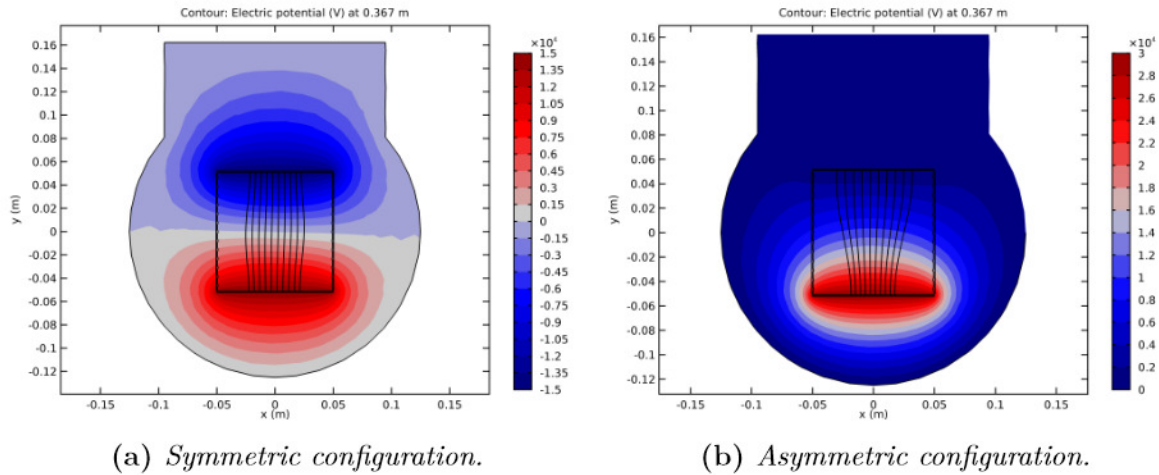


**Figure 3.12** – *Transverse comparison between symmetric and asymmetric configuration.*

In this configuration (Fig. 3.12a), the field focuses the particles in the transverse plane but also in the longitudinal plane. This explains why the particle number on the readout is higher than the expected number. For this configuration, only the transverse plane should be corrected.

In asymmetric configuration (Fig. 3.12b), the field is defocusing in the transverse plane, but also in the longitudinal one. The projection of the beam will be much broader than expected and many particles are lost during the particle drifts. Therefore, the electric field must be improved in both planes.

### 3.5.6 IPM cross-interaction

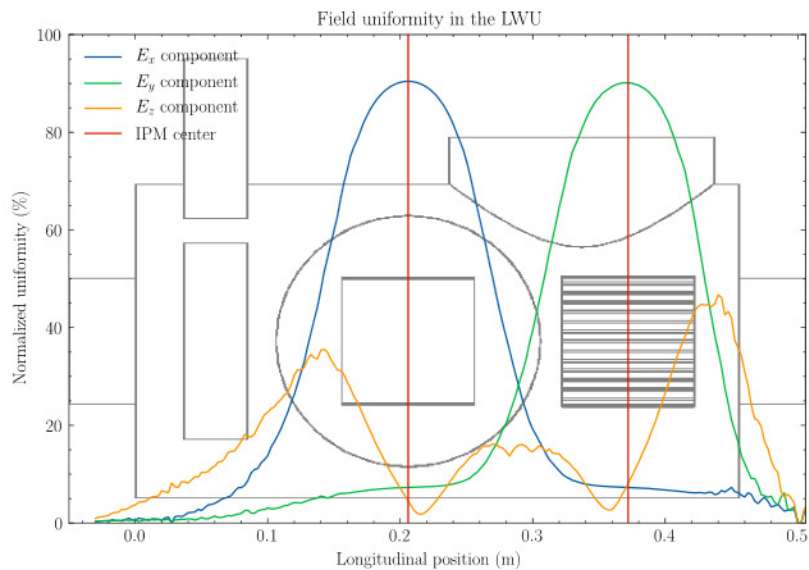
The IPMs are in close proximity due to the limited room of the vacuum chamber, in order to measure the beam profile in both transverse directions at the same location. This proximity leads to a coupling effect between the two IPMs due to fringe fields. Moreover, the uniformity of the electric field is strongly related to the geometry that encloses the IPMs. The LWU walls are at ground potential, hence the uniformity of the electric field in the IPMs depends on their position in the LWU. This means that the electric field in each IPM has to be corrected individually.

We simulated in COMSOL different IPM configurations with and without grounded disks separating the IPMs and located at different positions. The IPMs cannot be shifted too much in the inner volume of the vacuum vessel because the space is limited by the WS on the left and by the LWU walls on the right.

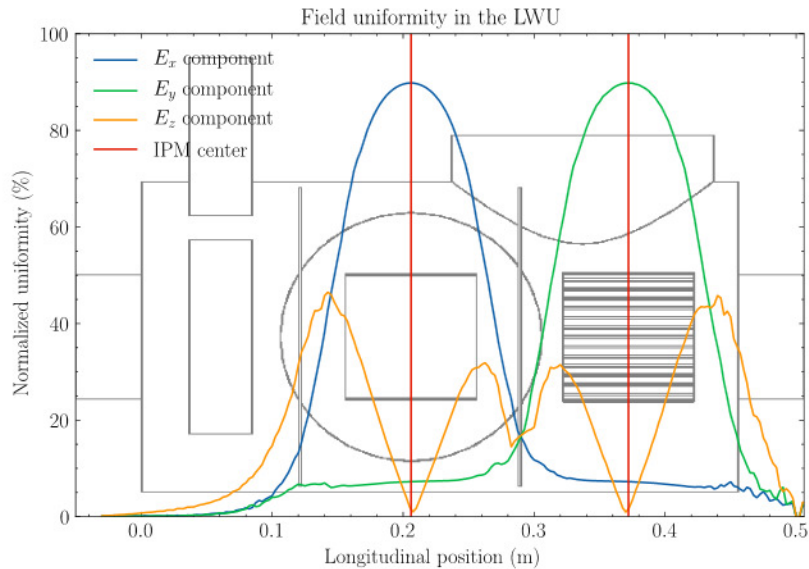
Fig. 3.13 shows the quadratic mean values for each electrical field component (as described in section 3.5.4) inside the geometry of the LWU with the two IPMs



implemented. When disks are present, the fields  $E_x$  and  $E_y$  are constrained within the space in-between them. The cross interaction effect is not lowered, but more flattened. This means that the effect on profile is constant over the readout size. Also with disks, the minimum  $E_z$  value is in the middle of the IPMs, so the readout location is the same for the both IPMs. Note that the field shapes of IPM1 and IPM2 look more similar when disk are present, because electric field is less dependant to the LWU geometry. This effect is quite useful because the same corrections can be applied to both IPMs, simplifying the optimization of field correctors. Using disks is therefore a straightforward solution to shield IPMs and to simplify the design of the IPMs .



(a) *Electric field without disk.*



(b) *Electric field with disks.*

Figure 3.13 – Influence of shielding disks on the IPM electric field along the LWU.



### 3.5.7 Field corrections

The electric field is improved by means of field correctors (also called field degraders) and the curved electrode pairs. Fig. 3.14 shows the COMSOL geometry of an example of IPM that has been simulated. One can see the degraders on each side and the curved electrodes at the top and bottom of each IPM.

The field correctors will constrain the electric potential on the side of the IPM. Thus, the iso-potential will be more flat in the IPM, leading to a better electric field uniformity. In practice, field degraders are just conductive strips connected to a voltage source directly powered by HV. One can directly connect them to power supplies. This method would allow to finely tune the potential on the electrodes, but it would also require HV feedthroughs for each electric potential. Unfortunately, we could not implement this solution since the available space on the IPM flange is restricted. We instead exploited directly the existing high voltages used for polarizing the IPM electrodes for feeding a resistor bridge as shown in Fig. 3.15. The potential at each field corrector is simply given by the Ohm law:

$$V_i = \frac{\sum_{k=1}^i R_k}{\sum_{j=1}^N R_j} V_{HV} \quad (3.29)$$

This method has some drawbacks. The choice of resistors is limited, since not all resistance values are commercially available [49]. In addition, the use of resistors in a clean vacuum is not really recommended since it often requires welding. Also, the resistors should be able to sustain high radioactive levels, mainly considering that, if one of them is damaged the entire bridge is affected.

Finally we decided to use 13 degraders, regularly spaced by 7.5 mm from each other, on each side of the IPM. A degrader is 2 mm width and 100 mm long (in longitudinal direction). The 7<sup>th</sup> degrader is located in the middle plane of the IPM.

The electric potential value which gives the best uniformity is computed with COMSOL for each degrader. The resistor chain is determined from these values with respect to the equation (3.29). For each corrector, two commercial resistors are mounted in series allowing values as close as possible to the optimal one. Resistors are selected within the MΩ range, reducing the power consumption of power supplies. The field simulation is recomputed with the real resistors and potential values.

In the case of the symmetrical IPM, only the first 6 degraders must be calculated since the 7<sup>th</sup> is grounded

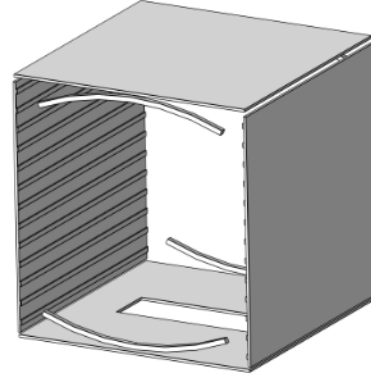


Figure 3.14 – IPM geometry in COMSOL.

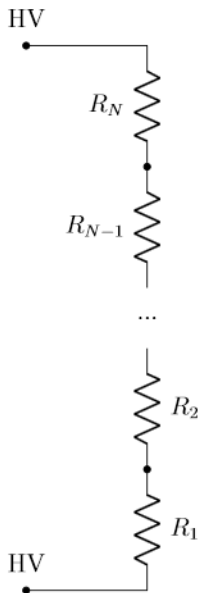
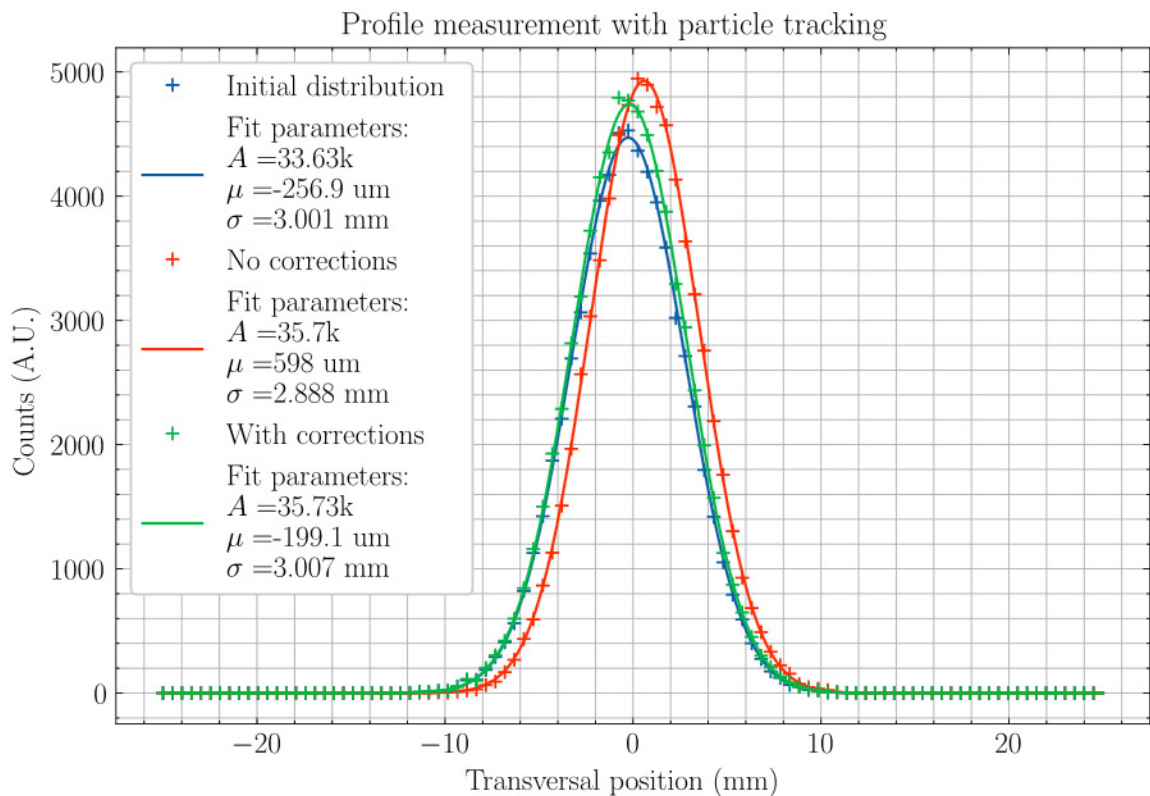


Figure 3.15 – Resistor chain.

and the last 6 potentials are held at opposite potentials with respect to the first 6 ones. The voltage and resistor values of the degrader chain for symmetric IPM are tabulated in the Table 3.5.

**Table 3.5** – Resistor chain characteristics for the field degraders in the symmetric IPM.

	HT	1	2	3	4
Resistor (M $\Omega$ )	13.4	20.715	24.3	20.332	
Voltage (kV)	15	13.56	11.32	8.71	6.52
	5	6	7		
	20.51	20	20		
	4.31	2.15	0		



**Figure 3.16** – Particle tracking for real symmetric field configuration with and without correctors (degraders and disks). The proton beam is assumed to be gaussian with  $\sigma_{beam} = 3$  mm.

A particle tracking was performed with the real corrected field and the results are shown in Fig. 3.16. Note that, even without correction, the symmetrical IPM gives fairly good results. The focusing effect, shown in the previous section, is visible and explains why there are more particles on readout than expected. When the field correctors are enabled, the profile is extremely well reconstructed with an error of less than 0.2%. This fulfills the requirements of ESS on the profile error.

For the asymmetric IPM, we proceeded in the same way. Also in this case, the resistor chain had to be optimized as well as the two curved electrodes. Table 3.6 gives the values of resistances and potentials in the case of the asymmetric IPM.

**Table 3.6** – Resistor chain characteristics for the field degraders and curved electrodes in the asymmetric IPM.

	Curved	HT	1	2	3	
Resistor (M $\Omega$ )	20.5	17.2	15.5	22.2		
Voltage (kV)	30	27.63	25.64	23.85	21.29	
	4	5	6	7	8	9
24.1	19.5	20	19.5	13.5	16	17.2
	18.5	16.25	13.94	11.69	10.13	8.28
	10	11	12	13	Ground	Curved
17.2	13.4	18.51	13.5	9.1		
	6.3	4.74	2.6	1.05	0	2850

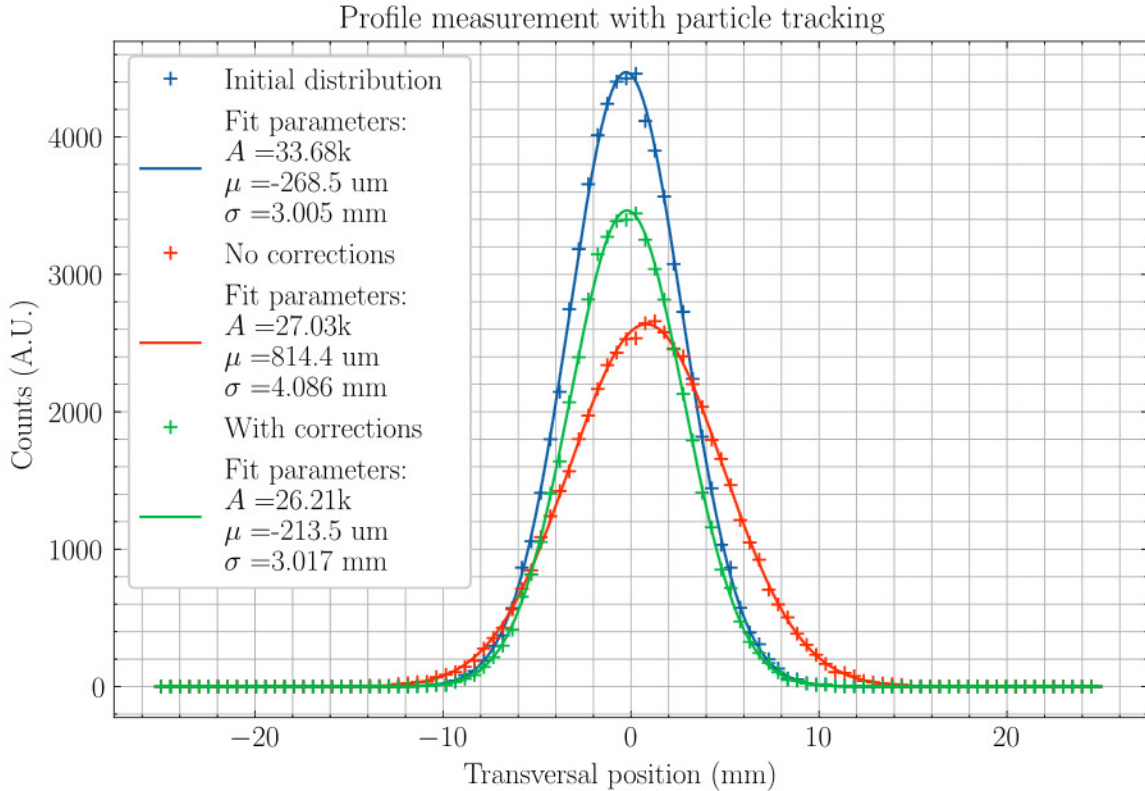


**Figure 3.17** – Particle tracking for real asymmetric field configuration with and without correctors (degraders and disks). The proton beam is assumed to be gaussian with  $\sigma_{beam} = 3\text{ mm}$ .

The results of the particle tracking for this case, are shown in Fig. 3.17. The

asymmetric field defocuses particles in both directions when the correctors are missing. So the reconstructed profile is 35 % wider and some particles do not even reach the readout. The shift in position is due to the cross interaction between the two IPMs. When corrections are enabled, the obtained transverse profile is much better: the error on the profile is only 0.4 %. The position is also corrected thanks to the shielding disks and curved electrodes, therefore no more shift appears. However, the correction on the longitudinal field is not as good as in the case of symmetric configuration and some particles are still lost during the drift: only 77 % of the particles will reach the readout.

### 3.5.8 Grid

As shown in Fig. 3.14, the readout electrode is not completely filled: a rectangular slit allows the ions or electrons to move toward the readout system. This slit is relatively big ( $2 \times 5 \text{ cm}^2$ ) with respect to the electrode dimensions ( $10 \times 10 \text{ cm}^2$ ), so it affects the electric field uniformity. A wire mesh can easily overcome this problem. Indeed in the close proximity of the mesh the field is not very straight, but at farther distances the field becomes constant. The mesh allows to have always the same field uniformity in the IPM whatever readout is used. On the other hand, it represents an obstacle for the incident particles, therefore the grid must be chosen carefully.

Actually, many of our colleagues are involved in the development of Micromegas detectors [50]. So we have access to several types of mesh. We started with a stainless steel mesh with a pitch of  $450 \mu\text{m}$  and a wire size of  $50 \mu\text{m}$ , so the optical transparency is about 90 %. A first approximation can be made with the Fourier series of the electric potential as proposed by Feynman [51]:

$$V(x, y) = \sum_{n=0}^{\infty} A_n \cdot \cos\left(-\frac{2\pi nx}{\lambda}\right) \cdot \exp\left(-\frac{2\pi ny}{\lambda}\right) \quad (3.30)$$

In this case the grid is regularly spaced in the  $x$  direction by a step  $\lambda$ . If we are at a distance  $k \cdot \lambda$  away from the grid the first harmonic is attenuated by a factor  $e^{-2\pi k}$ . This tendency can be easily confirmed with the FEM or BEM method. Fig. 3.18 shows the electrical potential close to the mesh for two different field configurations. One can see that the field is almost constant starting from less than 1 mm distance from the mesh. So there will be no problem using this grid.

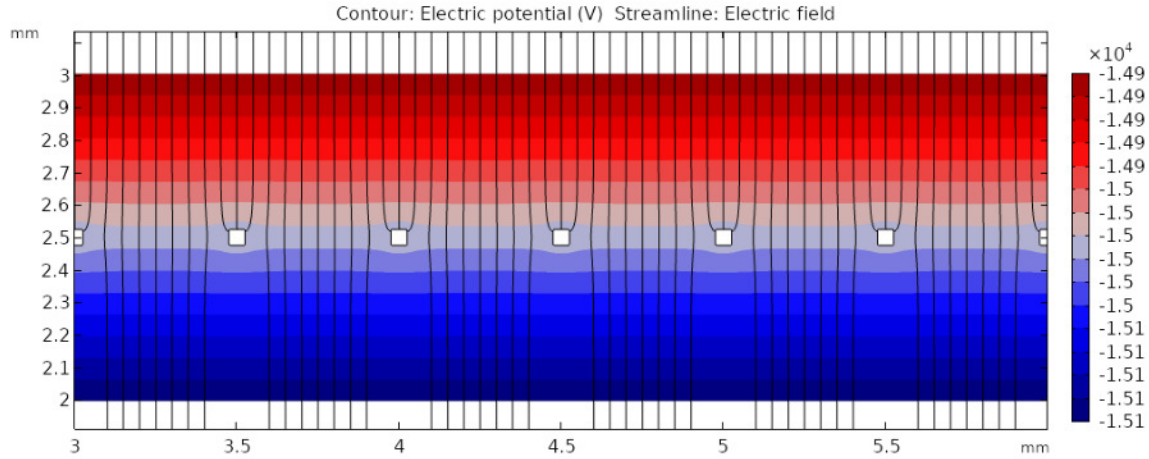
The grid is an obstacle for the incoming particles, and the number of stopped particles is directly related to the optical transparency of the grid. However it is possible to improve the transmission by increasing the field on one side of the grid. A simple analytical model has been demonstrated in the case of wire grid [52]. We assume that our grid follows this model<sup>5</sup>:

$$\frac{E_r}{E_d} \geq \frac{1 + \frac{2\pi r}{\lambda}}{1 - \frac{2\pi r}{\lambda}} \quad (3.31)$$

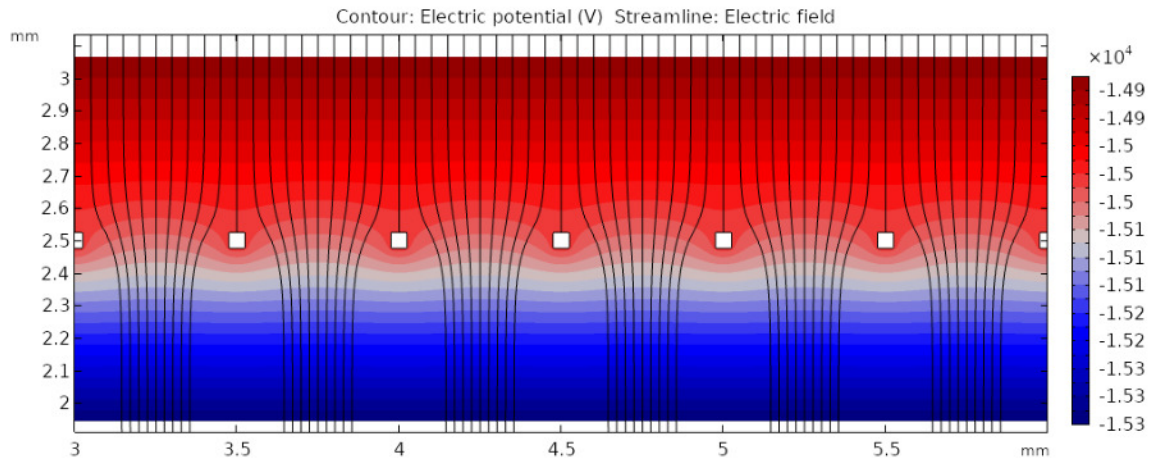
where  $E_r$  is the field on the readout region,  $E_d$  is the field on the drift region and  $r$  the wire diameter. For our grid configuration the ratio  $\frac{E_r}{E_d}$  must be higher than 4.38. An example is given in Fig. 3.18. The top figure shows a case where  $E_r = E_d$ . The

5. This is not really true since our grid is not made of cylindric wires.





(a) Configuration 1: The field is constant (up: 3 kV/cm; down: 3 kV/cm). The mesh transmission is close to the optical transparency.



(b) Configuration 1: The field is higher below the grid (up: 3 kV/cm; down: 6 kV/cm). The mesh transmission is higher than the optical transparency.

**Figure 3.18** – Electrical simulations of a 50/450  $\mu\text{m}$  grid. Two different field configurations were simulated. Both shows that the electrical field becomes uniform few mm away from grid. However the particle transmission differs due different ratios of the electric fields imposed in the two regions.

field lines may be stopped by the grid wires. In the bottom figure,  $E_r = 2 \cdot E_d$  and the field lines are attracted into the readout region due to the field difference.

The grid can be polarized in order to use it as a Frish grid. For some readout, it allows to get rid of certain signal contributions. More details will be given in section 3.8.1 of this chapter.

Finally, the grid may be also used to shield the readouts against possible electromagnetic noises created by all the radio-frequency devices. The effectiveness of the grid is clear. The wavelengths for the two ESS frequencies<sup>6</sup> are respectively 80 cm and 40 cm. The pitch of our grid is far less than these wavelengths.

6. We only considered the first harmonic.



## 3.6 Initial momentum

So far, we assumed that the ions and/or electrons were created without initial velocity i.e. at rest in a pure electric field. In this case, electrons and ions give same results and the value of the extraction field does not matter. In reality, these particles have a non-negligible initial speed and may be affected by parasitic electromagnetic fields. This can greatly affect the profile, thus the extraction field must be increased in order to minimize such distortion. In the following sections, we will try quantify these effects to determine the nominal value of the extraction field.

### 3.6.1 Thermal distribution

A first approximation of the initial speed of ions can be done thanks to the distribution of Maxwell-Boltzmann. The distribution of the speeds with respect to the particle mass and the temperature is given by the following equation:

$$F(\mathbf{v}) = \left( \frac{m_{part}}{2\pi k_b T} \right)^{\frac{3}{2}} \exp \left( -\frac{m_{part} \mathbf{v}^2}{2k_b T} \right) \quad (3.32)$$

Where,  $k_b$  is the Boltzmann constant,  $T$  the temperature,  $\mathbf{v}$  is the speed vector of the considered particle and  $m_{part}$  its mass. The Maxwell-Boltzmann distribution works well for perfect gases at low densities. We assumed that is true for the ESS residual gas. The speed is uniformly distributed along all directions ( $4\pi$ ).

The Fig. 3.19 shows the normalized distributions for some of the molecules present in the ESS residual gas. One can see directly that the speed of the fastest ion is below 5000 m/s. A field of few hundred volts per centimeter is more than enough to compensate this effect.

It gives no significant difference during the particle tracking. So, we can completely neglect the thermal motion for ions.

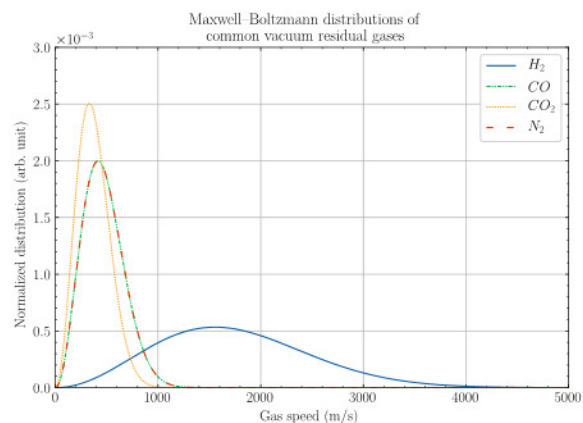


**Figure 3.19** – *Maxwell-Boltzmann distribution for some species of ESS residual gas.*

### 3.6.2 Momentum transfer during ionization process

Garfield++ can be used again to quantify the spectra of the momentum and the energy transferred to the ionized electrons. Fig. 3.20 shows this energy spectrum and the emission angle (or polar angle) distribution for several energies of a proton beam ( $\sigma = 3$  mm). The energy follows a Landau-like distribution with some Auger electrons. The polar angle is calculated with respect to the direction of the beam, while the azimuthal angle is uniform with respect to the transverse plane. A large proportion of electrons are perpendicularly ejected to the direction of propagation.

Particle tracking can be performed in order to quantify the influence of the initial momentum of electrons. Fig. 3.21a presents the relative error on the profile caused

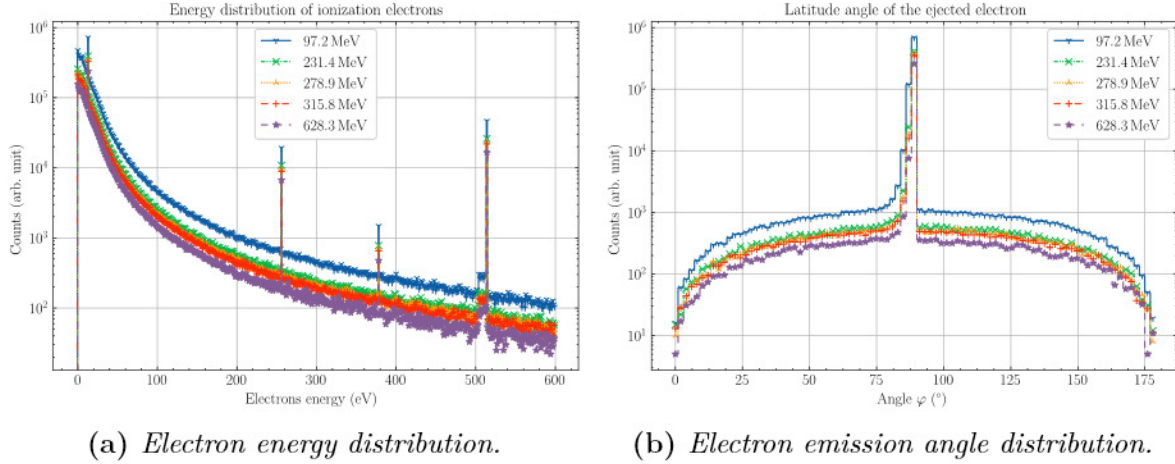


**Figure 3.20** – *Energy and emission angle of the ionized electrons.*

by the initial energy as a function of the extraction field. Note that it is impossible to fully compensate the error with realistic electric field values (below 6 kV/cm). Usually, when a profiler works in electron mode, a magnetic field parallel to the extraction field is added forcing the electrons to spin around the field direction. In the Fig. 3.21b, a general example of correction done with a magnetic field is presented. In the range of  $10^{-3}$  to  $5 \cdot 10^{-2}$  T, the Larmor radius is still too high to constraint electrons drifting along the field lines. A magnetic field of at least 0.1 T completely compensates the initial momentum of electrons. However the generation of such a magnetic field requires imposing dipole magnets. At ESS this solution is not feasible because the available space on LWU is not sufficient to put two magnets close-by.

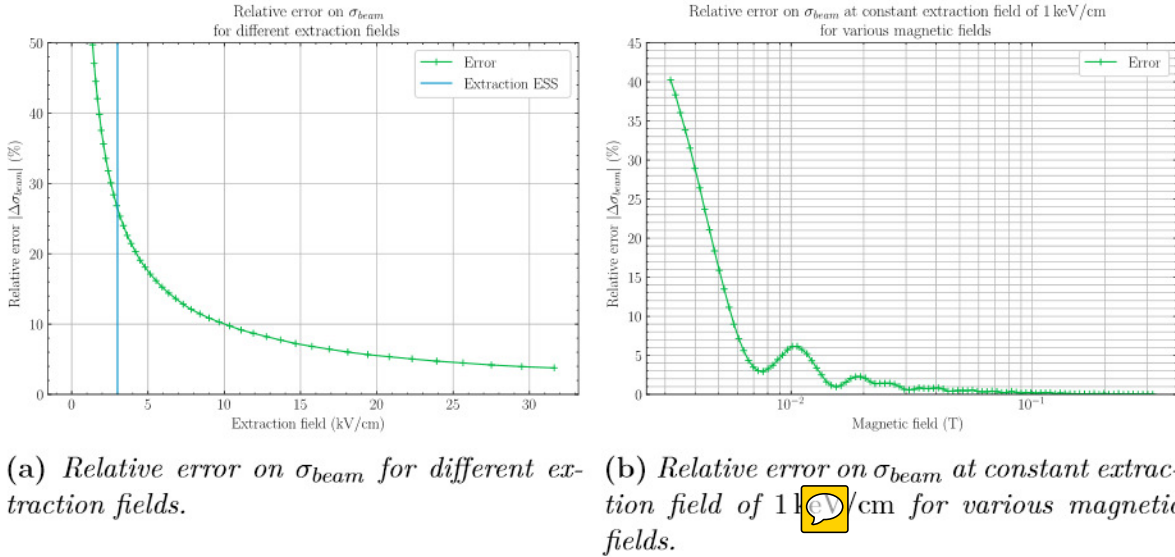


**Figure 3.21** – *Results from particle tracking with electrons considering initial energy.*

We wanted to study the ion behavior, but unfortunately Garfield++ does not give the energy spectrum of the ions. We have considered the momentum conservation of a pure ionization process, meaning the molecule dissociation in one electron and an ion. The ion momenta follow then the same electron distribution depicted by Garfield++. Therefore, the speed of a ion is proportional to the speed of electron weighted by their

mass ratio. For instance, the speed of a 100 eV electron is around  $5.9 \cdot 10^6$  m/s, while the  $H_2^+$  ion speed is only 1614 m/s. In these conditions, the speed of ions is below the thermal motion and calculations are therefore useless.

## 3.7 Space charge effect

The last effect that can greatly affect the measurement of the profile is the Space Charge. The protons of the beam bunches are in motion, so a strong radial electric field and a circular magnetic field are created around the beam axis. Each ESS bunch is composed of  $10^9$  protons. The effect of the space charge is not intuitive: electrons are light and may see less bunches but they are more sensitive to magnetic field. On the other hand, the ions are more massive and less sensitive to the EM fields but will undergo these fields many more times. Therefore, simulations were carried out to quantify this effect.

The space charge effect is a critical aspect of IPMs in general and several simulations were developed or are under development [53, 54]. Recently, a python framework dedicated to the IPM simulations, including space charge effects, has been released [55]. The code is developed at GSI but is open to everyone. However in this thesis, only the in-house code developed by ESS and CEA will be described.

### 3.7.1 Lorentz transformation of electromagnetic fields

The physic basis behind the space charge remains the Maxwell equations presented in the section 3.5.1. These equations were unified before the discovery of special relativity by Einstein in 1905 but it appears that they were already compatible with special relativity [51].

Let's consider a simple case. A frame  $F'$  is in motion with the speed  $v$  along the  $z$  axis with respect to frame  $F$ . The passage from one frame to the other is done by Lorentz transformation:

$$\begin{aligned} ct' &= \gamma(ct - \beta z), \\ x' &= x \\ y' &= y \\ z' &= \gamma(z - \beta ct) \end{aligned} \tag{3.33}$$

with  $\beta$  and  $\gamma$  the Lorentz factors.

$$\beta = \frac{v}{c}, \quad \gamma = \frac{1}{\sqrt{1 - \beta^2}} \tag{3.34}$$

The transformation is reverted by changing the sign of the lorentz factors in Eq (3.33).

Now let's take charges moving in a same way. The charges are not subject to any acceleration and do not diverge<sup>7</sup>. In the frame  $F$  the charges are in motion with  $v$  speed while in the  $F'$  the charges are completely immobile. Therefore in this frame

---

7. Without these two conditions, the Lorentz transformation must be computed with the tensor formalism [51].

the charges generate a purely electrostatic field, which can be computed using the Gauss's law. Electric and magnetic fields can be transformed as well:

$$\mathbf{E} = \begin{pmatrix} \gamma \bar{E}_x \\ \gamma \bar{E}_y \\ \bar{E}_z \end{pmatrix}, \quad \mathbf{B} = \begin{pmatrix} -\gamma v_b \frac{\bar{E}_y}{c^2} \\ \gamma v_b \frac{\bar{E}_x}{c^2} \\ 0 \end{pmatrix} \quad (3.35)$$

As a consequence, a purely electrostatic field in frame  $F'$  gives an electromagnetic field in the frame  $F$ . This simple case outlines the space charge problematic: in an IPM the ionization by-products are affected by the electromagnetic field created by the pulse beam.

### 3.7.2 ESS/CEA Space Charge algorithm

A simulation code has been developed in the frame of a Collaboration between ESS and CEA, in order to quantify the effects of space charge on the profile measurement with respect to the ESS beam conditions [56, 57]. The code is based on the analytical evaluation of the electric field for a Gaussian charge distribution and a full description of this model is available here [58, Eq. (16-18)].

A simplified workflow of the simulation program is given in the following section. A particle, ion or electron, is drawn according to the characteristics of the ESS beam, which is assumed to follow a gaussian distribution in 3D. The electric field of the beam is calculated in the moving frame from the equations given in the references. In this frame the beam width is spread by a factor. The resulting electromagnetic field in the frame of the IPM is calculated using the Lorentz transformations of fields. A Runge Kutta integrator computes the new particle position according to the electromagnetic field of the bunches and the extraction field of the IPM. At each integration step the fields of the beam are recalculated taking into account the new position of the bunches and the periodicity of the bunches. The particle is tracked until it reaches the readout plane.

### 3.7.3 Results

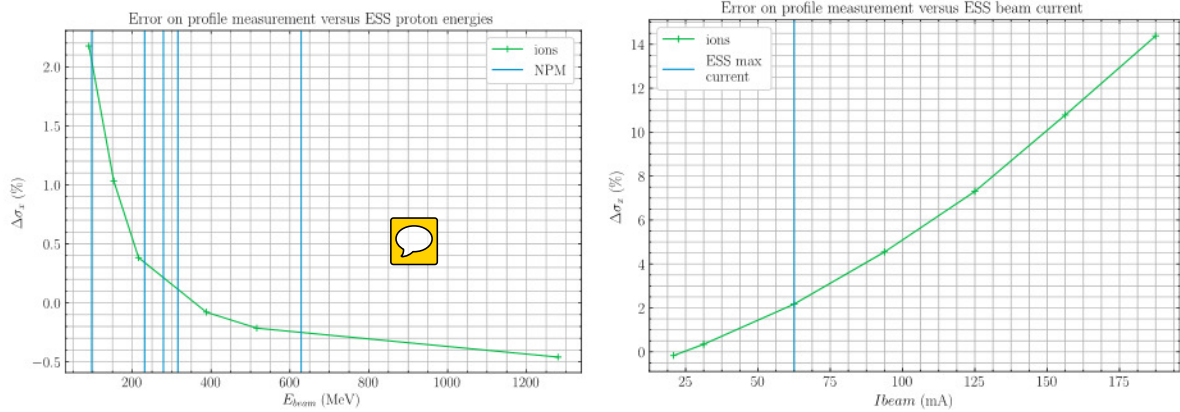
The effect of space charge depends on many beam parameters, therefore several simulations has been done to cover a wide range of ESS conditions. In the following only a small amount of the results is presented.

Two interesting results are given in Fig. 3.22. On the left hand side, the relation between the space charge and the beam energy is shown. The space charge has a higher impact on the profile when protons are at lower energy. On the right hand side, the influence of the beam current on the measurement error is visible. As expected the error increases linearly with the beam current.

In Fig. 3.23, an example of the ESS beam size measured from profiles obtained with ions and electron is presented. The proton energy and beam current have been set to 90 MeV and 62.5 mA. The value of the extraction field used in the simulation is chosen to be technically achievable. It is clear that the effect is stronger for electrons than for ions.

The duty cycle of the beam plays a role in the distortion of the profiles. Electrons, being light, reach the detector within the passage of one bunch, therefore they feel the combined electric and magnetic forces most of the time along their pass. On



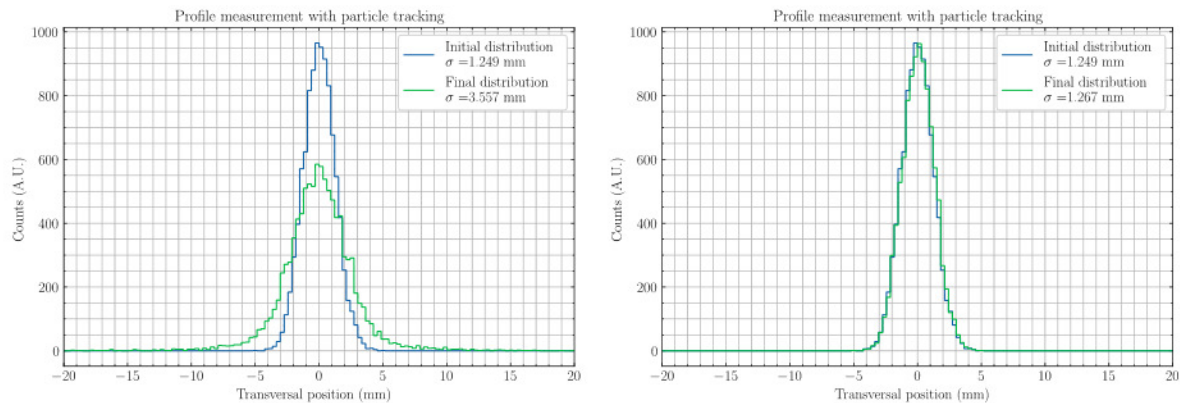


(a) Error on the profile measurement with  $H_2^+$  ions, due to space charge effects for several beam energy ( $I_{beam} = 62.5$  mA).

(b) Error on the profile measurement with  $H_2^+$  ions, due to space charge effects for several beam current ( $E_{beam} = 90$  MeV).

**Figure 3.22** – Effect of beam current and energy on the profile measurement. Beam initial conditions:  $\sigma_x = \sigma_y = 1.25$  mm,  $\sigma_z = 2.80$  mm. Extraction field comes from a COMSOL simulation, with an expected value around 2 kV/cm.

the other hand, ions are more massive and experience the passage of several bunches before reaching the detector. Hence, the forces from the bunches ions feel are weighted by the duty cycle of the varying electric field generated in  $Ft$ . For the case of ESS, the bunches are 3 ps long, and the period between them is 2.84 ns. So the integrated force seen by the ions is weaker than as the one experienced by the electrons.



(a) Profile measurement with electrons

(b) Profile measurement with  $H_2^+$  ions

**Figure 3.23** – Final simulation of beam measurement with particles tracking considering the non-uniformities, initial momentum and space charge effect. Beam conditions: 90 MeV,  $\sigma_x = \sigma_y = 1.25$  mm,  $\sigma_z = 2.80$  mm. Extraction field comes from a COMSOL simulation, with an expected value around 2 kV/cm.

The maximum accepted uncertainty of the beam size measurement is 10%. Our simulations pointed out that the impact of space charge effects is stronger for electrons than for ions. Moreover, as discussed in the previous section, lighter ionisation by-products are emitted with larger energies, and higher extraction fields are needed to minimize their tracks in directions perpendicular to the electric field lines. It is therefore clear that, to respect the 10% limit uncertainty mentioned above, the IPMs



have to work in ion mode detection. In such conditions, the designed instrument is expected to deliver reliable information on the ESS beam profile and size.

## 3.8 Readout systems

The information about the ionized particles that reach the readout is well known thanks to all the previous simulations. However, the readout system has not been defined yet. The main requirements on the readout are the following:

- The system must be sensitive enough to detect small amounts of positive or negative charges as calculated in the section 3.4.3.
- It should be compliant with high vacuum and ISO-5 environnement.
- The readout should be able to work in a radiative environnement.
- The reliability of the devices should be high, limiting the maintenance actions.

The conductive strip detection system is the most robust solution, but its sensitivity is limited. When the signal is too low, it must be amplified. This can be done, for instance, with Micro Channel Plates (MCP). Semiconductor detectors are also interesting, since they are highly sensitive. This novel method is developed by CERN and shows promising results.

In this section the operating principle of each method is described as well as its advantages and drawbacks.

### 3.8.1 Ramo-Shockley theorem

In particle detectors the signal is due to the motion of charges within the detector rather than the direct collection of charges by the electrodes. This theorem has been independently demonstrated by Ramo and Schockley [59, 60]. The total charge induced on an electrode at a time  $t$  by a charged particle  $q$  can be easily determined if the particle velocity  $\mathbf{v}$  and the weighting field  $\mathbf{E}_w$  of the electrode are known:

$$i_n = q\mathbf{v} \cdot \mathbf{E}_{wn} \quad (3.36)$$

The weighting field is the virtual field calculated as follow: all charges are removed, the electrode of interest is set at 1 V while the other electrodes are grounded. This field therefore strongly depends on the electrode and detector geometry.

Note that if two particles have the same trajectories but opposite charges, their signals will cancel out. In practice, ions and electrons go in opposite directions in a constant electric field, so their signals add up. However the electron is much faster, thus it creates a very fast signal while the ion signal is more spread over time.

In general, a so-called Frisch grid is used to get rid off one of the components of the signal, placed at a slightly different potential with respect to the reading electrodes. This grid confines the weighting fields in a restricted area and only the particles reaching this zone will induce signal. The grid must have a good transmission (as seen in section 3.5.8) and its inefficiency should remain as low as possible [61, 62].

### 3.8.2 Strips based detection

Conductive strips is the simplest method to implement. Electrodes are etched on a PCB with a thin layer of copper; bare strips are radiation hard.

This method is a direct application of the Ramo-Schockley's theorem: each strip has its own sensitivity field that depends mainly on its width and its pitch with respect to the other electrodes. The signal contribution of ions or electrons can be computed for each electrode.

The performances of this method depend on the readout electronics. In an ideal world, a transimpedance amplifier is sufficient. It converts and amplifies the induced current into voltage, then the voltage is digitized by an ADC. The gain of a transimpedance is proportional to the value of the feedback resistance.

The reality is much more complex since the electronic elements are not perfect. First, the sensor has a parasitic capacitance and resistance, as well as every components in the analog chain. Nuclear detectors have non negligible impedance that reduces the gain stability of transimpedances. For low signal, the feedback resistance must be high enough, but the Johnson's (or thermal) noise increases linearly with the resistance. At some point, the signal to noise ratio will be too low, so the signal may be not recovered.

The charge amplifier is very popular for nuclear detectors (Fig. 3.24). In this configuration, a capacitor is added in the feedback loop. It compensates the sensor capacitance and allows stable and high gain, but the bandwidth is smaller. A resistor or a switch can be put in parallel to the feedback capacitor allowing the discharge of the capacitor. Note that amplifiers have their own characteristics that will also limit the bandwidth and gain regardless of the amplifier configuration.

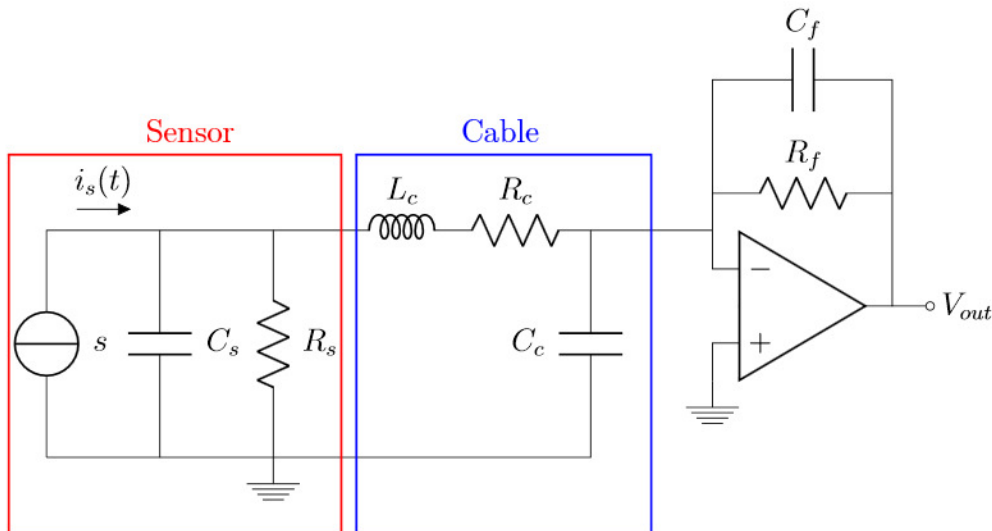


**Figure 3.24** – Typical circuit of a charge amplifier with an operational amplifier. The  $R_f$  and  $C_f$  should be chosen according to sensor characteristics. Strips sensors have low resistance but non negligible capacitance. Usually, cables are modeled by succession of LRC cells, for convenience just one cell is drawn here.

Due to the high vacuum level in the IPMs, the signal induced by the ionization of the residual gas in the strips may be lower than the electronic noise. In such eventuality, it is necessary to find a way to amplify the ionization signal.

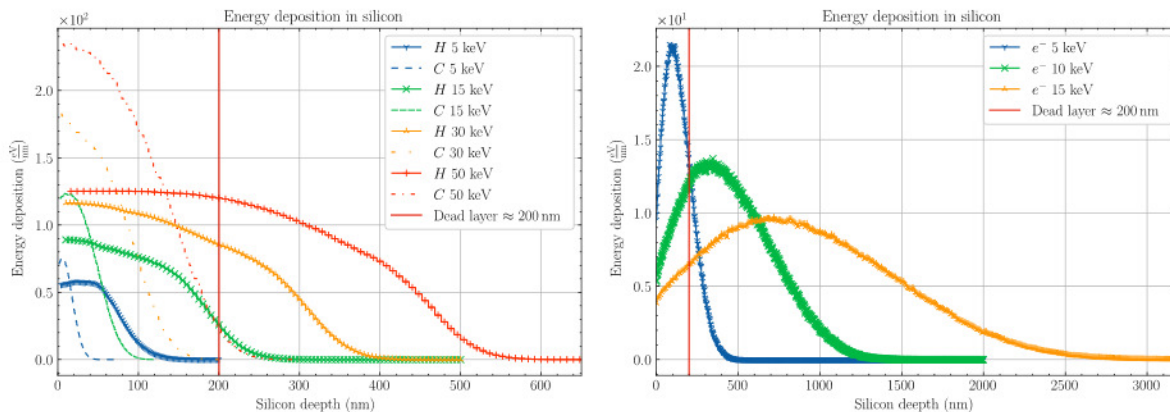
### 3.8.3 Interaction of low energy particles

In general, the higher the density of a material, the higher the interaction probability is. Therefore, in a high density medium, a primary particle will create many secondary particles. The more secondaries produced, the higher the signal on the readout electronic. In our detectors the vacuum level is so high that really few secondaries are produced. Two solid state detector technologies have been foreseen in order to evaluate the sensitivity.

At first, we should ensure that the detection of low energy ions or electrons is possible for these detectors. The models based on the Bethe equation, presented in section 3.4, are not precise enough in this energy range. Therefore more specific models must be considered. For such a purpose, we have used the well known SRIM and GEANT4 Monte Carlo codes. The former was employed for ions, while the latter for electrons.

The SRIM software simulates the interaction of heavy charged particles in matter [63]. The user defines different layers of compounds and the properties of the incident particle in a graphical interface. Then, SRIM computes the energy depositions, the stopping range, atomic displacements and atom vacancies in the layers.

Geant4 is a software toolkit that simulates the interaction of particles in a detector [64, 65]. It is a useful tool for simulating detectors of nuclear or high energy physics. The user describes a detector geometry, associates materials to volumes, defines the characteristic of the primary particles and adds physical processes that will be used for each particle interaction. In our case three models are particularly interesting: the IRCU73 model (ions), the Livermore model (ions and electrons) and the Penelope model (electrons) [66–68]. They describe the electromagnetic interaction of charged particles with matter at low energies. A simulation that uses the previous models has been developed from an example provided in Geant4 (TestEM11). In the developed GEANT4 simulation, a cube is sliced into different layers and the energy loss in each layer is saved.



(a) Energy deposition in a silicon layer for various ions. (b) Energy deposition in a silicon layer for electrons.

**Figure 3.25** – Energy deposition in a silicon layer for ions and electrons at low kinetic energies.

Fig. 3.25 shows the simulated energy deposition for different ions (left) and electrons (right) in a silicon cube. For a same incident energy, the electrons deposit

their energies along a higher range compared to the ions. Heavy ions are completely stopped before 200 nm for energies below 15 keV. We want to remind that heavy ions may represent two-thirds of the expected signal.

### 3.8.4 Semiconductor based detection

A semiconductor is a crystalline material that can be a conductor or an insulator depending on the temperature. In a semiconductor, electrons in the valence band are able to reach the conduction band, more easily when the temperature increases. The vacancies created by electrons in the valence band are called holes. Some elements in groups III to VI of the periodic table are natural semiconductor. However, the semiconducting capabilities of these materials can be greatly increased by implanting impurities in their crystalline structure. In  $p$ -doping the hole concentration increases whereas  $n$ -doping boosts the free electrons concentration. Under the action of an electric field, electrons and holes diffuse into the crystal structure. The propagation speed depends mainly on the mobility of charge carriers  $\mu$ .

$$v_{carrier} = \mu_{carrier} \mathbf{E} \quad (3.37)$$

When highly doped  $p$  and  $n$  semiconductors are put in contact, the charge concentration of both carriers presents an important gradient at the interface, known as depletion region. Therefore, the electrons move to the  $p$  doped region, leading to an electric field which blocks the electron flows. Thereafter, the junction is at equilibrium. In reverse bias mode, a positive potential is applied between  $n$  and  $p$  regions, then the depletion zone becomes bigger and the capacitance of the junction decreases. When a charged particle passes through the silicon detector, it deposits its energy and electron/hole pairs are created as described in the section 3.4 of this chapter. The charge carriers drift in the semiconductor due to the bias voltage, inducing a signal on electrodes as described by the Ramo-Shokley theorem, also valid for semiconductors.[70].

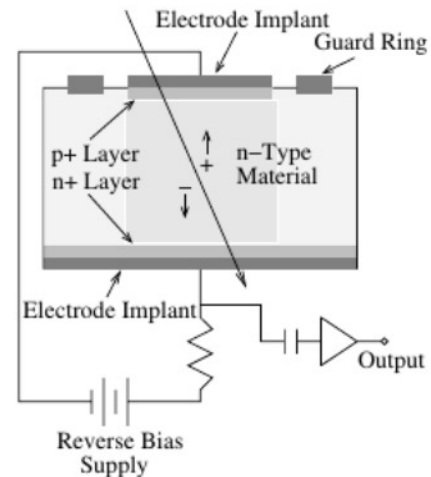


**Figure 3.26** – Principle of a simple semiconductor detector [69].

$$i(t) = \mathbf{E}_{wpixel} (q_{electron} v_{electron} + q_{hole} v_{hole}) \quad (3.38)$$

where  $\mathbf{E}_{wpixel}$  is the weighting field of a pixel pad,  $\mathbf{E}_{bias}$  is the field due to  $V_{bias}$ ,  $v$  is the speed of the charge carriers and  $q$  their charges. Table 3.7 lists the properties of common semiconductors used in radiation detection.

In monolithic sensors, the detection and the electronic functions are integrated together in the same substrate. These sensors achieve very small dimensions due to their high level of integration. Usually, monolithic sensors are developed for a specific purpose and are produced in large quantity reducing the costs.

In hybrid pixel detectors, detection and readout functions are physically separated. The detection matrix is placed on the readout electronics and the connection between



**Table 3.7** – *Properties of common semiconductors [71, 72] used as radiation detectors. Properties are given at NTP conditions.*

Property	<i>Si</i>	<i>Ge</i>	<i>CdTeZn</i>
Density (g/cm <sup>3</sup> )	2.33	5.32	5.78
<i>W</i> value (eV)	3.6	2.95	4.64
Breakdown (V/m)	$\approx 3 \cdot 10^5$	$\approx 10^5$	$\approx 10^5$
<i>e</i> <sup>-</sup> mobility (cm <sup>2</sup> /V/s)	$\leq 1400$	$\leq 3900$	$\leq 1100$
<i>h</i> mobility (cm <sup>2</sup> /V/s)	$\leq 450$	$\leq 1900$	$\leq 100$
Usage	General purpose	$\gamma$ -ray	<i>X</i> -ray
Cost	Cheap	Expensive	Moderate

the pads and the readout circuits is ensured by bumps. The reading system is independent of the detection matrix making this technology more generic and accessible for small volumes.

Semiconductor sensors could be interesting as readout system for the IPMs. An electron of 15 keV deposits all its energy and creates a few thousand of electron/hole pairs in the sensitive silicon layer. Unlike strips or MCPs the energy of the incident particle is recovered, enabling background discrimination. At last, electronic dead times are typically in the ns to  $\mu$ s range.

On the other hand, the use of semiconductor with ions at low energies ( $< 30$  keV) is uncertain. Indeed, an aluminium coating is often deposited on the top of the sensor for insuring a correct polarization and the superficial layer of the sensor are not active, which represents about a hundred nm dead zone. As shown in Fig. 3.25a,  $H_2^+$  ions loose 15 keV in 200 nm silicon layer, meaning that most of the electron/hole pairs are created and deposited before reaching the sensitive layer.

Low energetic ions may also produce more damages than electrons in the semiconductor lattice. The creation of charge traps and the depletion zone modifications are the worst damage scenarios. Modern semiconductors often implement a pixel calibration circuit to compensate non uniformities.

### 3.8.5 MCP based detection

A MicroChannel Plate (MCP) generates electrons from incident ionizing particles [73]. It can be seen as a glass lead plate drilled with micro-metric tilted holes. A specific coating is applied on its input surface to increase secondary emissions. When a particle hits the MCP hole entrance, secondary electrons are emitted. Due to the difference of potential applied between the MCP faces, secondaries are drawn towards the channel output and strike hole walls again, creating more and more electrons. Then, electrons are collected on a detection plane that can be a single electrode, multiple electrodes or a phosphorus screen depending on the read-out requirements. Fig. 3.27 shows some schematic representations of how an MCP works.

MCPs have a high efficiency for low energy ions and electrons. MCPs are also sensitive to photons via compton and photoelectric effect interactions (from gamma rays to VUV). The detection of neutron is also possible by adapting the composition of the coating. MCPs are fully vacuum compatible. MCPs are also extremely fast amplifiers and time resolution is in the order of a few hundred picoseconds for a single

stage MCP. The spatial resolutions of a MCP depends on its channel size and spacing. However both resolutions are limited by the readout used. Phosphorus screens provide high spatial resolution but screen are not fast as the MCP. Electrode readout allows to read fast and low signals with an efficient electronic.

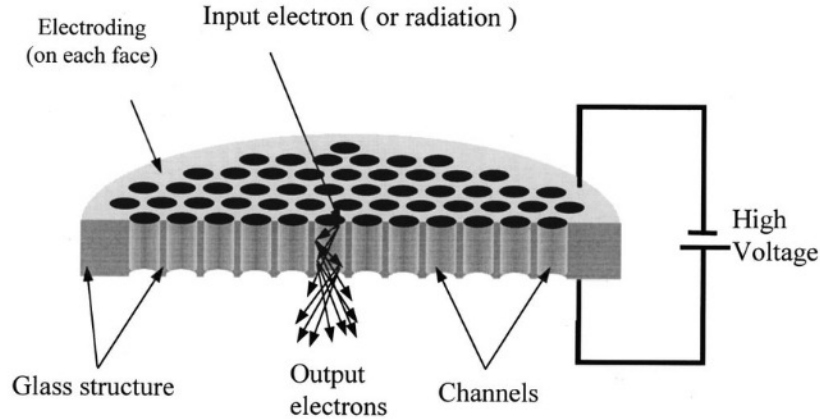
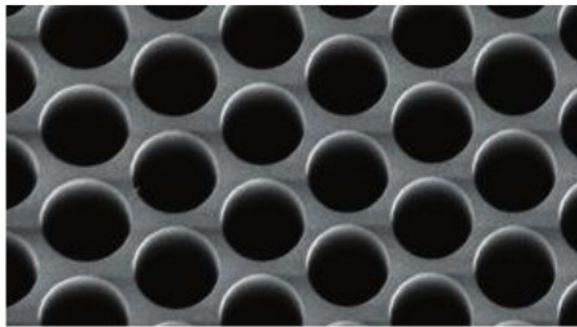
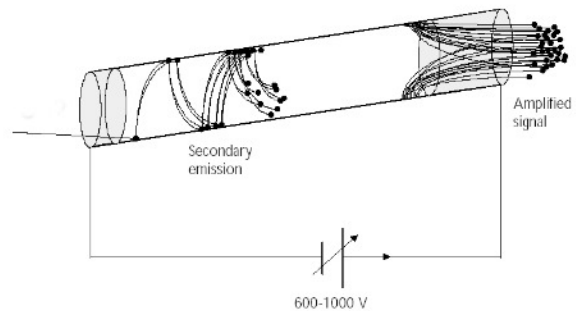


Figure 3.27 – Sectional view of a MCP [74].

The gain or multiplication factor for a single MCP is about  $10^2$  to  $10^4$  depending on the  $V_{MCP}$  voltage, usually from 600 to 1000 V. Several MCPs can be stacked to increase the gain to  $10^6$  or even higher. Typical configurations are single stage, chevron stack (double stages) or Z stack (triple stages). Obtaining an analytical expression of the gain is not trivial since it strongly depends on the characteristics of the MCP and its coating. MCP manufacturers often express the gain as an exponential function of the potential applied.



(a) SEM picture of MCP holes [75].



(b) Description of how an MCP amplifies incident particle.

Figure 3.28 – Schematic views of how a MCP works.

Unfortunately MCPs have some drawbacks, the first one being ageing. Indeed the coating is damaged by the incident particles, thus the gain is not stable and decreases over the time. A second disadvantage is the MCP gain limitation due to saturation. If the incident particle flux is too high, holes may be saturated, and they cannot amplify anymore. When this happens to a channel, it takes some time to recover, generating dead time.

### 3.9 Summary

This chapter exposed all the studies that have been performed to prove the feasibility of an IPM for the cold part of the ESS accelerator. Three key points were identified: the number of ionization particles, the distortion on the profile and the choice of the readout system.

The ESS conditions are particularly unfavorable for the ionization cross sections since the high vacuum level in the accelerator does not help. Direct calculations and simulations show that the order of magnitude of the number of ionization particles is about a few thousand particles per pulse per cm for nominal ESS conditions. This number of primary particles seems sufficient to perform a profile measurement assuming that these particles may be detected by the readout.

The non-uniformity of the electric field can be corrected effectively using field correctors and shielding disks regardless of the configuration used. However the symmetrical mode is easier to correct and reduces the maximum voltage required.

The simulations clearly show that the ions are less sensitive to the phenomenon of space charge. The profile measurement with electrons introduces an error that does not fulfil the ESS requirements, since it is impossible to install a correction magnet to constrain the trajectories of the electrons. Therefore the measurement of the profile will be done in ions configuration.

The use of ions complicates the choice of the readout. Strips are an extremely robust method but it requires a low noise electronics. MCPs amplify the signal but these devices suffer of aging effect. Silicon detectors are very promising because they are very sensitive, resistant and fast. However, the detection of low energetic ions with these detector is not assured and their implementations are quite complex.

All of these studies were presented during a Preliminary Design Review (January 2017) which marked the beginning of the construction phase of the different prototypes.

## Bibliography

### References

- [1] T.J. Shea. “Proton Beam Measurement Strategy for the 5 MW European Spallation Source Target”. In: *IBIC 2013: Proceedings of the 2nd International Beam Instrumentation Conference* (2013) (cit. on p. 39).
- [2] B. Cheymol, A. Jansson, and T. J. Shea. “Wire scanner design for the European Spallation Source”. In: *IBIC 2013: Proceedings of the 2nd International Beam Instrumentation Conference* (2013), pp. 830–832 (cit. on p. 39).
- [3] C. Thomas et al. “Design and Implementation of Non-Invasive Profile Monitors for the ESS LEBT”. In: *IBIC 2016: Proceedings of the 5th International Beam Instrumentation Conference* (2016) (cit. on p. 40).
- [4] S. Peggs. “ESS Technical Design Report”. In: (2013) (cit. on p. 40).
- [5] T.J. Shea. “Overview and Status of Diagnostics for the ESS Project”. In: *Proc. of International Beam Instrumentation Conference (IBIC’17), Grand Rapids, MI, USA, 20-24 August 2017*. 2018. DOI: 10.18429/JACoW-IBIC2017-M02AB2 (cit. on p. 40).
- [6] *ISO 14644-1:2015 — Cleanrooms and associated controlled environments – Part 1: Classification of air cleanliness by particle concentration*. Standard. Geneva, CH: International Organization for Standardization, 2015 (cit. on p. 40).
- [7] Glenn F. Knoll. *Radiation Detection and Measurement*. John Wiley and Sons Ltd, Aug. 4, 2010. 864 pp. ISBN: 0470131489 (cit. on p. 42).
- [8] William R. Leo. *Techniques for Nuclear and Particle Physics Experiments*. Springer Berlin Heidelberg, 1994. DOI: 10.1007/978-3-642-57920-2 (cit. on p. 42).
- [9] H. Bethe. “Zur Theorie des Durchgangs schneller Korpuskularstrahlen durch Materie”. In: *Annalen der Physik* 397.3 (1930), pp. 325–400. DOI: 10.1002/andp.19303970303 (cit. on p. 42).
- [10] Enrico Fermi. “The Ionization Loss of Energy in Gases and in Condensed Materials”. In: *Physical Review* 57.6 (Mar. 1940), pp. 485–493. DOI: 10.1103/physrev.57.485 (cit. on p. 42).
- [11] U Fano. “Penetration of Protons, Alpha Particles, and Mesons”. In: *Annual Review of Nuclear Science* 13.1 (Dec. 1963), pp. 1–66. DOI: 10.1146/annurev.ns.13.120163.000245 (cit. on p. 42).
- [12] M. Tanabashi et al. “Review of Particle Physics”. In: *Physical Review D* 98.3 (Aug. 2018). DOI: 10.1103/physrevd.98.030001 (cit. on pp. 42–45).
- [13] M. J. Berger et al. “Stopping Powers for Electrons and Positrons, ICRU Report 37”. In: *Journal of the International Commission on Radiation Units and Measurements* os19.2 (Dec. 1984), NP–NP. DOI: 10.1093/jicru/os19.2.report37 (cit. on p. 43).



- [14] M. J. Berger et al. “Stopping Power and Ranges for Protons and Alpha Particles, ICRU Report 49”. In: *Journal of the International Commission on Radiation Units and Measurements* os25.2 (May 1993), NP–NP. DOI: 10.1093/jicru/os25.2.report49 (cit. on p. 43).
- [15] R.M. Sternheimer, M.J. Berger, and S.M. Seltzer. “Density effect for the ionization loss of charged particles in various substances”. In: *Atomic Data and Nuclear Data Tables* 30.2 (Mar. 1984), pp. 261–271. DOI: 10.1016/0092-640x(84)90002-0 (cit. on p. 43).
- [16] H. Bichsel. “Shell corrections in stopping powers”. In: *Physical Review A* 65.5 (Apr. 2002). DOI: 10.1103/physreva.65.052709 (cit. on p. 43).
- [17] Stephen Seltzer. *Stopping-Powers and Range Tables for Electrons, Protons, and Helium Ions, NIST Standard Reference Database 124*. eng. 1993. DOI: 10.18434/t4nc7p (cit. on p. 44).
- [18] L. E. Porter and Hong Lin. “Methods of calculating the Barkas-effect correction to Bethe–Bloch stopping power”. In: *Journal of Applied Physics* 67.11 (1990), pp. 6613–6620. DOI: 10.1063/1.345094 (cit. on p. 43).
- [19] James F. Ziegler and Jochen P. Biersack. “The Stopping and Range of Ions in Matter”. In: *Treatise on Heavy-Ion Science*. Springer US, 1985, pp. 93–129. DOI: 10.1007/978-1-4615-8103-1\_3 (cit. on p. 43).
- [20] W. W. M. Allison and J. H. Cobb. “Relativistic Charged Particle Identification by Energy Loss”. In: *Annual Review of Nuclear and Particle Science* 30.1 (Dec. 1980), pp. 253–298. DOI: 10.1146/annurev.ns.30.120180.001345 (cit. on pp. 43, 46).
- [21] Foster F. Rieke and William Prepejchal. “Ionization Cross Sections of Gaseous Atoms and Molecules for High-Energy Electrons and Positrons”. In: *Physical Review A* 6.4 (Oct. 1972), pp. 1507–1519. DOI: 10.1103/physreva.6.1507 (cit. on p. 43).
- [22] C. Dimopoulou et al. “Breakup of H<sub>2</sub> in Singly Ionizing Collisions with Fast Protons: Channel-Selective Low-Energy Electron Spectra”. In: *Physical Review Letters* 93.12 (Sept. 2004). DOI: 10.1103/physrevlett.93.123203 (cit. on p. 43).
- [23] J. Weiss and W. Bernstein. “Energy Required to Produce One Ion Pair for Several Gases”. In: *Physical Review* 98.6 (June 1955), pp. 1828–1831. DOI: 10.1103/physrev.98.1828 (cit. on p. 43).
- [24] H. Bichsel et al. “Average energy required to produce an ion pair, ICRU Report 31”. In: *Journal of the International Commission on Radiation Units and Measurements* os16.2 (May 1979), pp. 18–32. DOI: 10.1093/jicru/os16.2.18 (cit. on pp. 43, 45).
- [25] Sachie Kamakura et al. “Mean excitation energies for the stopping power of atoms and molecules evaluated from oscillator-strength spectra”. In: *Journal of Applied Physics* 100.6 (Sept. 2006), p. 064905. DOI: 10.1063/1.2345478 (cit. on p. 45).
- [26] Jan Egberts. “IFMIF-LIPAc Beam Diagnostics. Profiling and Loss Monitoring Systems”. Theses. Université Paris Sud - Paris XI, 2012. URL: <https://tel.archives-ouvertes.fr/tel-00772158> (cit. on pp. 45, 49).

- [27] Hajime Ishimaru, Shinkichi Shibata, and Mitio Inokuti. “Ionization cross sections of gases for protons at kinetic energies between 20 MeV and 385 GeV, and applications to vacuum gauges in superconducting accelerators”. In: *Physical Review A* 51.6 (June 1995), pp. 4631–4639. DOI: 10.1103/physreva.51.4631 (cit. on p. 45).
- [28] S.F. Biagi. “A multiterm Boltzmann analysis of drift velocity, diffusion, gain and magnetic-field effects in argon-methane-water-vapour mixtures”. In: *Nuclear Instruments and Methods in Physics Research Section A: Accelerators, Spectrometers, Detectors and Associated Equipment* 283.3 (Nov. 1989), pp. 716–722. DOI: 10.1016/0168-9002(89)91446-0 (cit. on p. 46).
- [29] I.B. Smirnov. “Modeling of ionization produced by fast charged particles in gases”. In: *Nuclear Instruments and Methods in Physics Research Section A: Accelerators, Spectrometers, Detectors and Associated Equipment* 554.1-3 (Dec. 2005), pp. 474–493. DOI: 10.1016/j.nima.2005.08.064 (cit. on p. 46).
- [30] Rene Brun and Fons Rademakers. “ROOT — An object oriented data analysis framework”. In: *Nuclear Instruments and Methods in Physics Research Section A: Accelerators, Spectrometers, Detectors and Associated Equipment* 389.1-2 (Apr. 1997), pp. 81–86. DOI: 10.1016/s0168-9002(97)00048-x (cit. on p. 46).
- [31] I. Antcheva et al. “ROOT — A C++ framework for petabyte data storage, statistical analysis and visualization”. In: *Computer Physics Communications* 180.12 (2009), pp. 2499–2512. DOI: <https://doi.org/10.1016/j.cpc.2009.08.005> (cit. on p. 46).
- [32] R. Kersevan and J.-L. Pons. “Introduction to MOLFLOW+: New graphical processing unit-based Monte Carlo code for simulating molecular flows and for calculating angular coefficients in the compute unified device architecture environment”. In: *Journal of Vacuum Science & Technology A: Vacuum, Surfaces, and Films* 27.4 (July 2009), pp. 1017–1023. DOI: 10.1116/1.3153280 (cit. on p. 47).
- [33] D. A. Bartkoski, C. Deibele, and Y. Polsky. “Design of an ionization profile monitor for the SNS accumulator ring”. In: *Nuclear Instruments and Methods in Physics Research Section A: Accelerators, Spectrometers, Detectors and Associated Equipment* 767 (Dec. 2014), pp. 379–384. DOI: 10.1016/j.nima.2014.09.020 (cit. on p. 49).
- [34] J. Hadamard. “Sur les problèmes aux dérivées partielles et leur signification physique”. In: *Princeton University Bulletin* 13 (1902), pp. 49–52 (cit. on p. 50).
- [35] Inc Dassault Systemes. *CST Studio Suite*. 2019. URL: <https://www.cst.com/> (cit. on p. 51).
- [36] Inc ANSYS. *ANSYS , Maxwell*. 2019. URL: <https://www.ansys.com/fr-fr/products/electronics/ansys-maxwell> (cit. on p. 51).
- [37] Inc INTEGRATED Engineering Software. *Coulomb, a 3D Electric Field Solver*. 2018. URL: <https://www.integratedsoft.com/Products/coulomb.aspx> (cit. on p. 51).
- [38] Inc COMSOL. *COMSOL Multiphysics 5.3a Reference Manual*. 2019. URL: <https://www.comsol.com/> (cit. on p. 52).

- [39] Inc COMSOL. *COMSOL Multiphysics 5.3a AC/DC Module User's Guide*. 2019. URL: <https://www.comsol.com/> (cit. on p. 52).
- [40] Inc COMSOL. *Meshing your geometry various element types*. 2013. URL: <https://www.comsol.com/blogs/meshing-your-geometry-various-element-types/> (cit. on p. 52).
- [41] J. P. Boris. “Relativistic plasma simulation — Optimization of a hybrid code”. In: *Proceedings of the Fourth Conference on the Numerical Simulation of Plasmas*. 1970, pp. 3–67 (cit. on p. 55).
- [42] Hong Qin et al. “Why is Boris algorithm so good?” In: *Physics of Plasmas* 20.8 (Aug. 2013), p. 084503. DOI: 10.1063/1.4818428 (cit. on p. 56).
- [43] Grady Wright. “Radical Basis Function Interpolation: Numerical and Analytical Developments”. PhD thesis. University of Colorado, 2003 (cit. on p. 56).
- [44] Gaël Guennebaud, Benoît Jacob, et al. *Eigen v3*. 2010. URL: <http://eigen.tuxfamily.org> (cit. on p. 57).
- [45] Jose Luis Blanco and Pranjal Kumar Rai. *nanoflann: a C++ header-only fork of FLANN, a library for Nearest Neighbor (NN) with KD-trees*. <https://github.com/jlblancoc/nanoflann>. 2014 (cit. on p. 57).
- [46] Karsten Ahnert et al. “Odeint – Solving Ordinary Differential Equations in C++”. In: AIP, 2011. DOI: 10.1063/1.3637934 (cit. on p. 57).
- [47] Mario Mulansky and Karsten Ahnert. “Odeint library”. In: *Scholarpedia* 9.12 (2014), p. 32342. DOI: 10.4249/scholarpedia.32342 (cit. on p. 57).
- [48] Intel. *Threading Building Blocks, widely used C++ template library for task parallelism*. 2019. URL: <https://www.threadingbuildingblocks.org/> (cit. on p. 57).
- [49] Vishay. *Standard Series Values in a Decade for Resistances and Capacitances*. Tech. rep. 2012. URL: <https://www.vishay.com/docs/28372/e-series.pdf> (cit. on p. 60).
- [50] Y. Giomataris et al. “MICROMEAS: a high-granularity position-sensitive gaseous detector for high particle-flux environments”. In: *Nuclear Instruments and Methods in Physics Research Section A: Accelerators, Spectrometers, Detectors and Associated Equipment* 376.1 (1996), pp. 29–35. ISSN: 0168-9002. DOI: [https://doi.org/10.1016/0168-9002\(96\)00175-1](https://doi.org/10.1016/0168-9002(96)00175-1). URL: <http://www.sciencedirect.com/science/article/pii/0168900296001751> (cit. on p. 63).
- [51] Richard Phillips Feynman, Robert Benjamin Leighton, and Matthew Sands. *The Feynman Lectures on Physics, Vol. II: Mainly Electromagnetism and Matter*. 2011. ISBN: 9780465024940. URL: <http://www.feynmanlectures.caltech.edu/> (cit. on pp. 63, 67).
- [52] O. Bunemann, T. E. Cranshaw, and J. A. Harvey. “Design of grid ionization chambers”. In: *Canadian Journal of Research* 27a.5 (1949), pp. 191–206. DOI: 10.1139/cjr49a-019 (cit. on p. 63).

- [53] M. Sapinski et al. “Ionization Profile Monitor Simulations - Status and Future Plans”. In: *Proc. of International Beam Instrumentation Conference (IBIC'16), Barcelona, Spain, Sept. 13-18, 2016*. (Barcelona, Spain). International Beam Instrumentation Conference 5. doi:10.18429/JACoW-IBIC2016-TUPG71. Geneva, Switzerland: JACoW, Feb. 2017, pp. 521–524. ISBN: 978-3-95450-177-9. DOI: doi:10.18429/JACoW-IBIC2016-TUPG71. URL: <http://jacow.org/ibic2016/papers/tupg71.pdf> (cit. on p. 67).
- [54] Mariusz Sapinski and Dominik Vilsmeier. *The IPMSim collaboration*. 2019. URL: <https://ipmsim.gitlab.io/index.html> (cit. on p. 67).
- [55] Dominik Vilsmeier and Mariusz Sapinski. *Virtual-IPM*. 2019. URL: <https://gitlab.com/IPMSim/Virtual-IPM> (cit. on p. 67).
- [56] C.A. Thomas, F. Belloni, and J. Marroncle. “Space Charge Studies for the Ionisation Profile Monitors for the ESS Cold Linac”. In: *Proc. of International Beam Instrumentation Conference (IBIC'16), Barcelona, Spain, Sept. 13-18, 2016*. (Barcelona, Spain). International Beam Instrumentation Conference 5. Geneva, Switzerland: JACoW, Feb. 2017, pp. 556–559. ISBN: 978-3-95450-177-9. DOI: doi:10.18429/JACoW-IBIC2016-TUPG81 (cit. on p. 68).
- [57] F. Belloni, C.A. Thomas, and J. Marroncle. “Space Charge Studies for the ESS Cold Linac Beam Profiler”. In: *Proc. of International Beam Instrumentation Conference (IBIC'18), Shanghai, China, Sept. 9-13, 2018*. (Shanghai, China). International Beam Instrumentation Conference 5. JACoW, pp. 371–374. DOI: doi:10.18429/JACoW-IBIC2018-WE0C0 (cit. on p. 68).
- [58] Rainer Wanzenberg. *Nonlinear Motion of a Point Charge in the 3D Space Charge Field of a Gaussian Bunch*. 2010. URL: [http://www.desy.de/~mpywar/paper/2010/Internal\\_Report\\_M\\_10-01.pdf](http://www.desy.de/~mpywar/paper/2010/Internal_Report_M_10-01.pdf) (cit. on p. 68).
- [59] S. Ramo. “Currents Induced by Electron Motion”. In: *Proceedings of the IRE* 27.9 (Sept. 1939), pp. 584–585. DOI: 10.1109/JRPROC.1939.228757. URL: <http://dx.doi.org/10.1109/JRPROC.1939.228757> (cit. on p. 70).
- [60] W. Shockley. “Currents to Conductors Induced by a Moving Point Charge”. In: *J. Appl. Phys.* 9.10 (1938), p. 635. DOI: 10.1063/1.1710367. URL: <http://dx.doi.org/10.1063/1.1710367> (cit. on p. 70).
- [61] V.A. Khriachkov et al. “Direct experimental determination of Frisch grid inefficiency in ionization chamber”. In: *Nuclear Instruments and Methods in Physics Research Section A: Accelerators, Spectrometers, Detectors and Associated Equipment* 394.1 (1997), pp. 261–264. DOI: [https://doi.org/10.1016/S0168-9002\(97\)00601-3](https://doi.org/10.1016/S0168-9002(97)00601-3) (cit. on p. 70).
- [62] A. Göök et al. “Application of the Shockley–Ramo theorem on the grid inefficiency of Frisch grid ionization chambers”. In: *Nuclear Instruments and Methods in Physics Research Section A: Accelerators, Spectrometers, Detectors and Associated Equipment* 664.1 (2012), pp. 289–293. DOI: <https://doi.org/10.1016/j.nima.2011.10.052> (cit. on p. 70).
- [63] James F. Ziegler. *SRIM2013 software*. 2013. URL: <http://www.srim.org/> (cit. on p. 72).



- [64] J. Allison et al. “Geant4 developments and applications”. In: *IEEE Transactions on Nuclear Science* 53.1 (Feb. 2006), pp. 270–278. DOI: 10.1109/tns.2006.869826 (cit. on p. 72).
- [65] J. Allison et al. “Recent developments in Geant 4”. In: *Nuclear Instruments and Methods in Physics Research Section A: Accelerators, Spectrometers, Detectors and Associated Equipment* 835 (Nov. 2016), pp. 186–225. DOI: 10.1016/j.nima.2016.06.125 (cit. on p. 72).
- [66] R. Bimbot et al. “Stopping of ions heavier than Helium, ICRU Report 73”. In: *Journal of the International Commission on Radiation Units and Measurements* 5.1 (2005). DOI: doi:10.1093/jicru/ndi001 (cit. on p. 72).
- [67] Dermott E. Cullen, John H. Hubbell, and Lynn Kissel. “Photon and Electron Interaction Data”. In: (). URL: <https://www-nds.iaea.org/epdl97/> (cit. on p. 72).
- [68] Francesc Salvat, Jose Maria Fernández-Varea, Josep Sempau Roma, et al. “PENELOPE-2008: A Code System for Monte Carlo Simulation of Electron and Photon Transport”. In: (2009) (cit. on p. 72).
- [69] Syed Naeem Ahmed. *Physics and Engineering of Radiation Detection*. Academic Press, 2007. ISBN: 9780120455812 (cit. on p. 73).
- [70] G. Cavalleri et al. “Extension of Ramo’s theorem as applied to induced charge in semiconductor detectors”. In: *Nuclear Instruments and Methods* 92.1 (Mar. 1971), pp. 137–140. DOI: 10.1016/0029-554x(71)90235-7 (cit. on p. 73).
- [71] G. Zegrya et al. *New Semiconductor Materials, Characteristics and Properties*. 2005. URL: <http://matprop.ru/> (visited on 05/22/2019) (cit. on p. 74).
- [72] Y Eisen. “Current state-of-the-art industrial and research applications using room-temperature CdTe and CdZnTe solid state detectors”. In: *Nuclear Instruments and Methods in Physics Research Section A: Accelerators, Spectrometers, Detectors and Associated Equipment* 380.1 (1996), pp. 431–439. DOI: [https://doi.org/10.1016/S0168-9002\(96\)00319-1](https://doi.org/10.1016/S0168-9002(96)00319-1) (cit. on p. 74).
- [73] Joseph Ladislav Wiza. “Microchannel plate detectors”. In: *Nuclear Instruments and Methods* 162.1-3 (June 1979), pp. 587–601. DOI: 10.1016/0029-554x(79)90734-1 (cit. on p. 74).
- [74] Whikun Yi et al. “Characteristic features of new electron-multiplying channels in a field emission display”. In: *Journal of Vacuum Science & Technology B: Microelectronics and Nanometer Structures* 19.6 (2001), p. 2247. DOI: 10.1116/1.1420206 (cit. on p. 75).
- [75] Hamamatsu. *MicroChannel Plate and MicroChannel Plate assembly*. 2018. URL: [https://www.hamamatsu.com/eu/en/product/optical-sensors/electron\\_ion-sensor/mcp/index.html](https://www.hamamatsu.com/eu/en/product/optical-sensors/electron_ion-sensor/mcp/index.html) (cit. on p. 75).

## Chapter 4

### Prototype tests at IPHI



## Contents

---

<b>4.1</b>	<b>Introduction</b>	<b>86</b>
<b>4.2</b>	<b>Preliminary tests of silicon detector</b>	<b>86</b>
4.2.1	IRMA	86
4.2.2	Test setup	87
4.2.3	Results and limitations	88
<b>4.3</b>	<b>IPM design overview</b>	<b>89</b>
4.3.1	IPM	89
4.3.2	MCP	91
4.3.3	Camera	91
4.3.4	Strips	92
4.3.5	CAMEL board and FASTER system	93
4.3.6	High voltage power supplies	93
4.3.7	Control System	94
4.3.8	Test bench	95
4.3.9	Reference measurement	96
<b>4.4</b>	<b>IPHI and test campaigns</b>	<b>97</b>
4.4.1	IPHI accelerator	97
4.4.2	Overview of the two test campaigns	98
<b>4.5</b>	<b>Processing data</b>	<b>99</b>
4.5.1	Processing camera	99
4.5.2	Processing strip	100
4.5.3	Processing scintillator screen data and review of the reference measurements	101
<b>4.6</b>	<b>Beam environnement characterization</b>	<b>102</b>
4.6.1	Vacuum analysis	102
4.6.2	Beam position	103
4.6.3	Beam current	105
4.6.4	Beam tuning	106
<b>4.7</b>	<b>IPM characterization</b>	<b>107</b>
4.7.1	Beam size convergence	107
4.7.2	Cross interaction	108
4.7.3	Comparison size	109
4.7.4	Field uniformity	110
4.7.5	Grid	111
4.7.6	MCP	112
4.7.7	Phosphorus screens	112
4.7.8	Extrapolation to ESS conditions with the strips IPM	114
4.7.9	Extrapolation to ESS conditions with the optical IPM	115
4.7.10	Electron measurement with MCP	116
<b>4.8</b>	<b>Summary</b>	<b>117</b>
<b>4.9</b>	<b>Bibliography</b>	<b>119</b>

---



## 4.1 Introduction

The simulations presented in the previous chapter show that the profile measurement with IPMs may match the ESS requirements. However, some critical points, mainly the choice of the readout, are not fully clarified, so the feasibility must be proven experimentally. From the results of the simulations, we converged to a first prototype design. Designing and testing prototypes is also a great opportunity to validate the simulations and gain feedback before the production phase. The present chapter presents the different prototypes that have been developed and tested as well as the results obtained. Moreover, the chapter follows closely the real chronology of the project.

The feasibility of silicon detection has been checked. A small test bench has been developed and installed in an ion implanter facility. The test has been done with a tailored silicon detector kindly provided by the CERN-BI team. The result and the consequences on the project will be discussed briefly.

Then, a full test bench has been designed including several IPMs and reference measurements. The different levels of integration for each component of the test bench will be described in order to give a global overview.

Finally, the test bench has been installed at a 3 MeV accelerator. Two test campaigns have been carried out and the different IPMs have been tested and characterized. The setups and most of the results are presented in this chapter.

## 4.2 Preliminary tests of silicon detector

The readout using silicon detectors seems very promising but detection is not assured for ions at low energies. It requires significant development in terms of electronics: complex PCB design, placement and alignment of the chips, wire bonding, development of a backend electronics, etc. Therefore, we decided to test a proof of concept before directly developing a complete IPM with a silicon detector. If the test shows that detection with ions is possible then this solution can be considered at ESS, otherwise it will be discarded. A low energetic ion source is necessary for testing the silicon option.

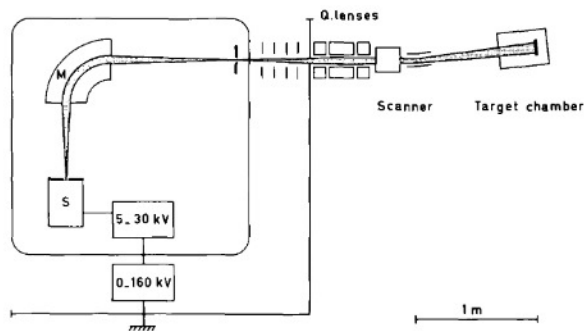
### 4.2.1 IRMA

An implanter is a small ion accelerator used to implant various elements into a target substrate. The depth of the implantation is proportional to the ion energy<sup>1</sup>. This kind of sources is particularly useful for material and irradiation science, and it may be the most efficient way to test the silicon detectors for us.

The IRMA implanter [1] relies on a Bernas-Nier source [2] for creating a plasma from injected gas. The plasma is then extracted and charge filtered by means of a magnet. The post acceleration is performed by an electrostatic tube. Finally, a set of steerers allows a fine beam scanning on the target. The IRMA implanter can accelerate a large number of ion species between 5 keV and 190 keV with currents of the order of  $\mu\text{A}$  scale. Fig. 4.1 presents a schematic representation of IRMA and a picture of the facility.

---

1. See section 3.4 and 3.8.3 in the previous chapter.



(a) Schematic view of the implanter.

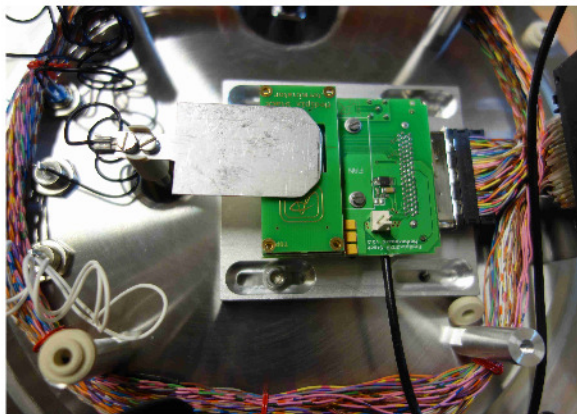


(b) The source is in the cage in background. The test bench was installed on the target chamber, on the left.

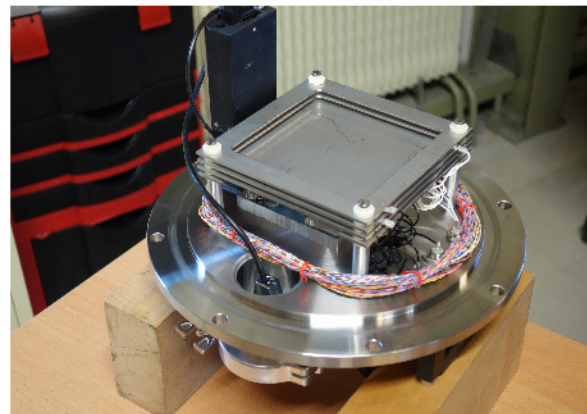
Figure 4.1 – IRMA installation.

### 4.2.2 Test setup

The test bench consists of a mechanical support on which is mounted the detector system. The current range at IRMA is important (from hundred pA to  $\mu\text{A}$ ) compared to the expected ionization current per ESS pulse (few fA). The average current has been reduced by the following solutions. The beam was scanned in both directions at 80 Hz and 400 Hz on a perpendicular stopping plate. A hole was drilled at the center of the plate, reducing the current by a factor of 12723. At the end, the number of incident particles was around hundred thousand (hundred fA) per IRMA “pulse”. A simple Faraday cup measures the current after reduction. The entire setup is visible in Fig. 4.2.



(a) The TimePix chip is just behind the Faraday cup.



(b) A plate with a drilled hole reduced the incoming current. The beam is scanned on the plate.

Figure 4.2 – IRMA setup. A dedicated test bench has been developed for testing the TimePix chips.

The detector tested at IRMA is a silicon pixelated matrix ( $256 \times 256$  with a pixel size  $56 \mu\text{m}$ ) on top of a TimePix chip. The matrix is very specific since the metal-

lization layer has been replaced by a heavily doped layer allowing the polarization of the detector. The TimePix measures either the Time over Threshold (ToT) or the Time of Arrival (ToA). ToT is the total time during which the signal generated by the incident particle is above a threshold set by the user. This value is therefore proportional to the energy deposited by the particles in the pixels. The ToA gives the time difference of an incident particle with respect to a reference time.

The TimePix detector used was already equipped of a complete solution [3, 4] integrating a readout electronics controllable by PC. The software allows to configure the TimePix and acquire images with the value of ToT or ToA for each pixel.

### 4.2.3 Results and limitations

The test performed at IRMA concerns the determination of the detection limit with the lightest possible ions i.e.  $H_2^+$ . The images at two energies and integrated signal for a full scan are shown in Fig. 4.3.

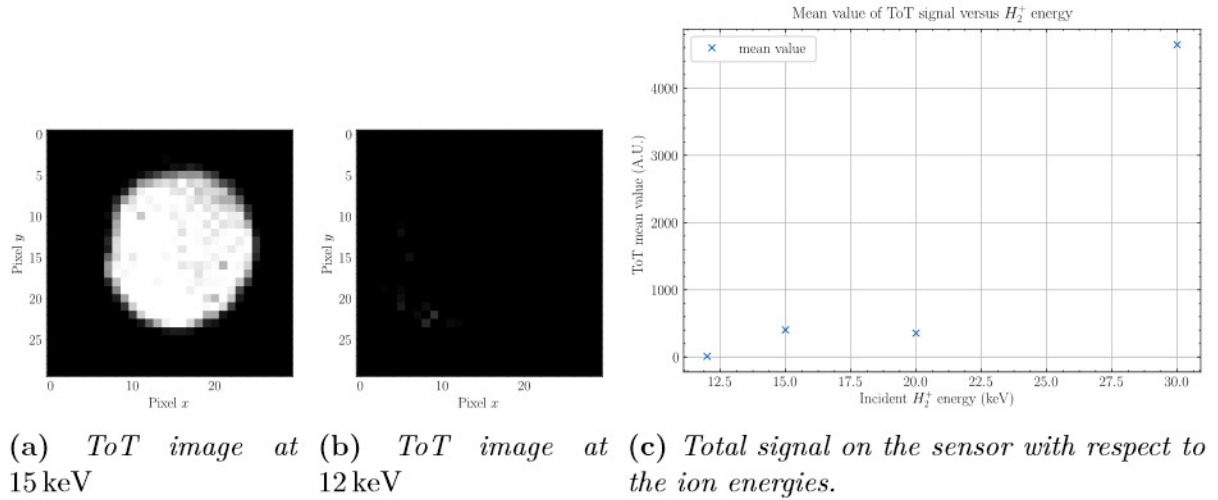


Figure 4.3 – Main results from IRMA tests with  $H_2^+$  ions.

The scan range is limited to few values because tuning the ion implanter to different energies was time consuming. For 15 keV ions the detection seems to work correctly, but the signal vanishes for ions with an energy of 12 keV or less. The limit of detection is therefore between these two values, and is very close to the energy that ions can reach in the IPMs. The residual gas at ESS is mainly a compound of ions heavier than  $H_2^+$ . These heavy ions will not be detected by the readout, reducing the already low signal of the IPM. One can see that the point at 20 keV is unlikely. The measurement for this point was performed at the end of the day after few hours of irradiations at low energy. Ideally we should have taken more measurements at different energies.

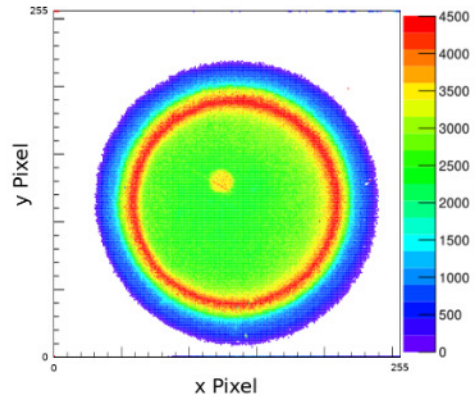


Figure 4.4 – The gain has changed after the irradiation.



Few days after the test, the integrity of the sensor has been tested by illuminating it with an UV-VIS LED (peak emission at 365 nm). Fig. 4.4 shows a small zone of the pixel matrix with different gain, corresponding to the IRMA beam position irradiation. Clearly the sensor was damaged, but unfortunately we can not give an accurate estimation of the deposited dose. Note that the gain has increased in the irradiated region whereas we expect a reduction as we observed at IRMA.

At last we decided to discard the possibility of using silicon detectors because of the signal weakness, not compliant with IPMs working in the mandatory ion mode, and for the damages induced by ions as previously seen. The development cost of a silicon solution is not worth considering the possible risks of non-detection. In our quest for feasibility demonstration, we faced several issues:

- Triggered acquisitions were not possible, imposing to take long integration time to avoid missing the beam interaction with the silicon detector.
- Consequently, despite calculations, the beam sweeping on the detector varied from time to time explaining partly our impossibility to evaluate the dose.
- The data campaign was concentrated on a single day. We discovered the facility and its constraints at the same time as dealing with our measurements.

Still, we hope to have the opportunity to retest the silicon detector at IRMA, or at another ion implanter facility, to fully determine the ion detection limit and investigate more on ion damaging. Nowadays, TimePix3 has completely replaced its ancestor. This new integrated circuit provides the ability to measure at a same time the ToT and ToA, with a higher timing resolution and an efficient data protocol. Also, the readout electronics has been improved allowing advanced triggering option of the chip.

## 4.3 IPM design overview

### 4.3.1 IPM

The IPM consists of five PCB plates: two for the electrodes, two for the field correctors and one for supporting the readout. The two electrode plates face each other, as well as the correction plates. The electrode closest to the readout is grooved in its center with a conductive grid fixed on it, for insuring the electric field uniformity (see explanations on the previous chapter). The top electrode has a 5.5 mm radius circular hole in its center to allow illumination from a calibration source. The field correctors were engraved directly on the inner PCB face and resistors are welded on the outer side. SMD resistor type 2512 (1 % precision, 3000 V max) are used.

All PCB boards are firmly encapsulated in two frames made of insulating material. Two materials have been used: PEEK and MACOR. MACOR is a machinable ceramic that provides very high electrical insulation (more than 50 kV/mm DC), good thermal conduction and withstands high temperatures (800 °C). It is also compatible with vacuum despite its porous appearance. Even if it has very interesting mechanical properties, it must be handled with care<sup>2</sup>. PEEK (Polyether Ether Ketone) is a plastic polymer used in aggressive chemical environments. It is both an electrical (around 16 kV/mm) and a thermal insulator. It does not tolerate temperatures above 250 °C. PEEK can be used under vacuum, but its performance is much lower than

---

2. The author personally attest this fact after he screwed too tightly on a frame MACOR.

MACOR. On the other hand, it is cheaper and easier to handle.

The two frames are screwed to a MACOR support fixed on the flange via two stainless steel rods. The ceramic support ensures a perfect insulation of the IPM with the vacuum chamber. The IPMs has been designed so that the cage is completely independent of the readout used. For IPMs using strips, it is also possible to rotate the IPM by  $90^\circ$  to change the direction of the measurement. The connections to the different high voltages are wired with bare copper protected by ceramic beads. Vacuum feedthroughs are COTS components that can support voltages up to 30 kV.

An IPM prototype fully mounted on its flange is pictured in Fig. 4.5.

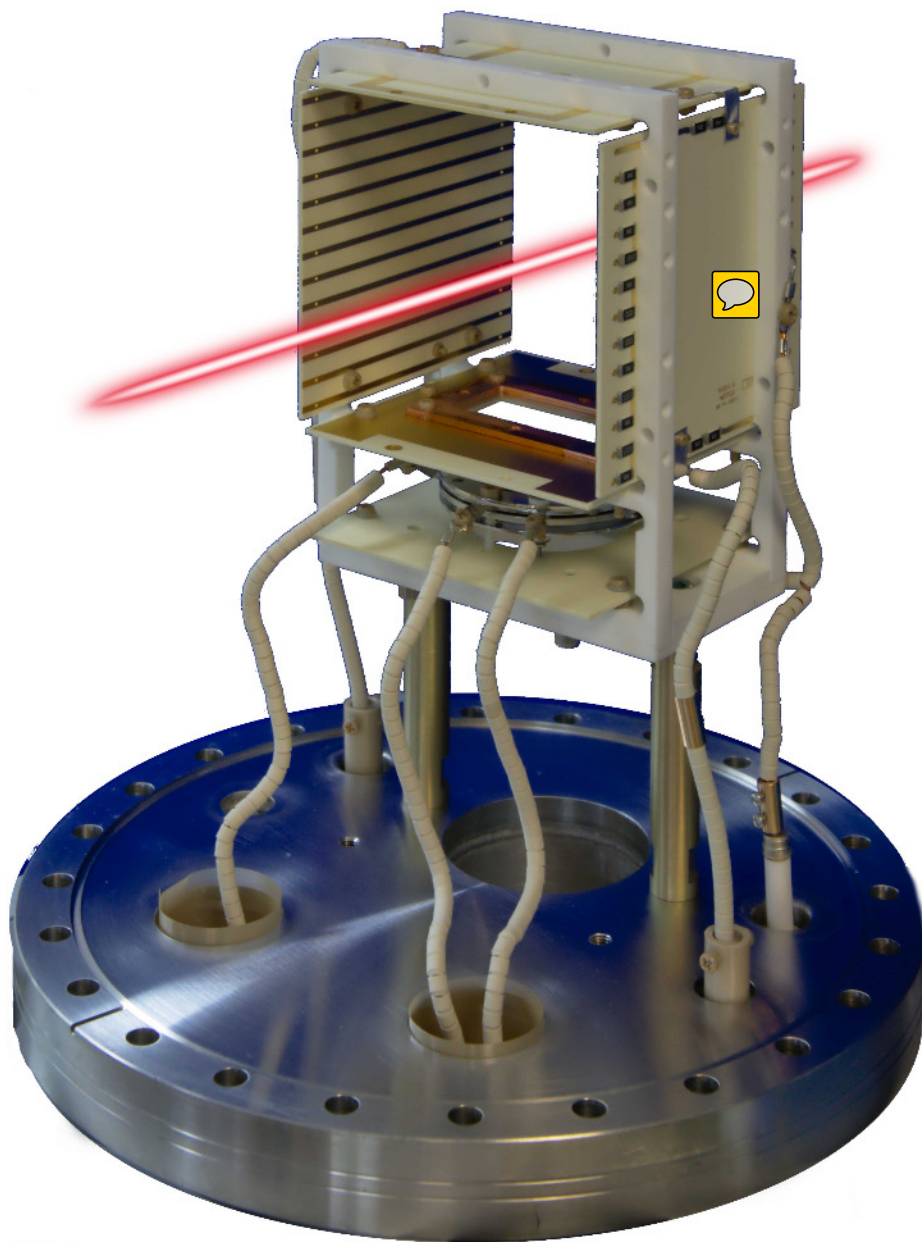


Figure 4.5 – One of the IPM prototypes. The MCP is visible below the cage.



### 4.3.2 MCP

A total of four MCPs has been bought from two different suppliers, Hamamatsu and Photonis: a simple single stage MCP and a single stage MCP coupled with a phosphorus screen. The simple MCPs will be used with the strips IPMs if the signal becomes too low.

The MCP and phosphorus assemblies are key components of the optical IPMs and two different phosphorus screens were considered:

- P43 is a very luminescent material but has a strong remanence.
- P46 has a fast decay time but lower yield.

Since intra-pulse acquisition is not a requirement for ESS both screens may be considered.

The characteristics of each MCP (and phosphorus screen) are given in the Table 4.1.

**Table 4.1** – *Main characteristics of the MCPs used during the beam tests. The two MCPs from Hamamatsu have the same characteristics, except that one has a phosphorus screen as readout.*

	Hamamatsu	Photonis 1	Photonis 2
Active radius	40 mm	40 mm	40 mm
Channel diameter	12 $\mu\text{m}$	10 $\mu\text{m}$	25 $\mu\text{m}$
Channel pitch	15 $\mu\text{m}$	12 $\mu\text{m}$	32 $\mu\text{m}$
Open Area Ratio	60 %	55 %	45 %
Bias angles	8°	8°	8°
Screen type	P43 <i>Gd<sub>2</sub>O<sub>2</sub>S : Tb</i>	P46 <i>Y<sub>3</sub>Al<sub>5</sub>O<sub>12</sub> : Ce</i>	-
Gain relative	1	0.3	-
Wavelength	545 nm	530 nm	-
Decay time range	ms	$\mu\text{s}$	-

### 4.3.3 Camera

A vision system is necessary for recording light from the phosphorus screen. A camera with a lens should be sufficient in our case.

The sensor is the core component of a camera, so it is better to choose it first, on the basis of the requirements. For our application high resolution is not mandatory, so pixels could be relatively large in order to increase light collection and dynamic range. Sony IMX249 fits well with these prerequisites. It is a consumer CMOS sensor with big pixels and low noise. Its EMVA characteristics are summarized in the Table 4.2 [5].

AlliedVision, Basler and FLIR propose several cameras based on the IMX249 sensor with different interfaces, features, form factors, prices and availability. We restricted our choice to GigE cameras since they allow long cable length and Power over Ethernet (PoE) which are quite useful features for an accelerator experiment. At the end, we chose the FLIR Blackfly-PGE-23S6M-C [6].

**Table 4.2** – *Main features of the Sony IMX249 sensor*

Property	Value
Resolution	1936 (H) $\times$ 1216 (V)
Pixel size	5.86 $\mu\text{m}$
Sensor diagonal size	13.4 mm (Type 1/1.2)
Well capacity	32000 $e^-$
Dynamic Range	70 dB
QE at 525 nm	70 %
Electrons noise	6.8 $e^-$
ADC	8, 10 or 12 bits
Max frame rate	30 fps

The last step is the choice of a correct lens for the camera. Unfortunately lens suppliers do not provide full characteristics of their lenses, hence only the thin lens approximation has been considered in our calculations. The distance from the back of the phosphorus screen to the external air-side of the viewport is 247 mm. The active area radius of our MCPs is around 25 mm, while the sensor side measures 11.34 mm. The required magnification therefore amounts to 0.2268 at least. Table 4.3 shows magnification factors for several focal lengths. So, a focal length of 50 mm fits very well with our configuration.

**Table 4.3** – *Magnification for several common focal lengths, at a working distance of 247 mm.*

Focal length (mm)	5	15	28	35	50	75	100	150
Magnification	0.02	0.069	0.127	0.165	0.255	0.436	0.68	1.546

Lenses with 50 mm focal length are rather standard and commercially available at moderate cost. In addition these lenses have a large numerical aperture (or small F-number) so they provide a large photon capture efficiency.

#### 4.3.4 Strips

The strips were manufactured in the same way as the other PCBs presented above. Two strip configurations have been foreseen. The first one is the linear strips: the strips have the same width of 800  $\mu\text{m}$  and an identical spacing of 920  $\mu\text{m}$ . A total of 32 strips were etched on the PCB, representing an active area of about 3 cm. The second version is called Gaussian because the strips on the borders are wider than the ones in the center. The idea is that the strips on edges detect only few particles, so it is not necessary to have very thin strips since they will probably be in the noise. Therefore, the number of strips is reduced to 18 with variable width from 0.8 mm to 9 mm, leading to a total active area of 5 cm. The table gives the values for the first 9 gaussian strips, the 9 remaining strips are the mirror of the first ones.

Table 4.4 – Positions and sizes of the first half of gaussian strips.

Strip	1	2	3	4	5	6	7	8	9
Size	9	5	3	2	1.5	1	0.9	0.8	0.8
Position	20.52	13.4	8.28	6.66	4.79	3.42	2.35	1.38	0.46

### 4.3.5 CARMEL board and FASTER system

The strips are read by the CARMEL card [7] from the FASTER system. FASTER is a versatile acquisition platform developed by LPC at Caen [8]. CARMEL is an electrometer VITA-57 card based on two DDC316 chips from Texas Instrument [9]. Each chip integrates 16 acquisition channels connected to a dual integrator circuit allowing continuous measurement, as shown in Fig. 4.6. The DDC316 chip covers integration times from  $10\ \mu\text{s}$  to  $1\ \text{ms}$  and three measurement ranges are available:  $3\ \text{pC}$ ,  $6\ \text{pC}$ ,  $12\ \text{pC}$ . The DDC316 can read only positive charges, so an homemade current injector has been developed to add an offset allowing the measurement of negative charges.

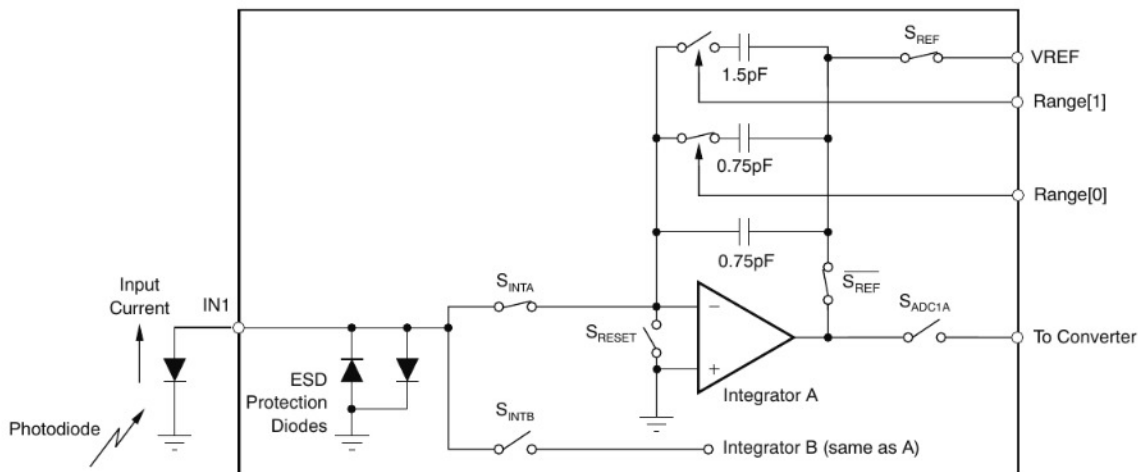


Figure 4.6 – The DDC316 architecture with dual integrators.

Two CARMEL boards can be plugged in a motherboard compatible with microTCA crates. All modules in a crate are controlled by a software that configures the entire system, runs acquisitions and visualizes [10] the data online. The data can be saved in a binary format and a library allows to read them afterwards.

### 4.3.6 High voltage power supplies

An IPM requires high voltages to create the extraction field and to supply the MCP when it is used as readout. All power supplies come from iseg-HV [11] and cover range from  $0\ \text{kV}$  to  $30\ \text{kV}$  with negative or positive polarities.

MCPs allow complete floating configuration. This means that the readout can work at very high potential. We refer to this configuration as symmetric since the MCP is at the opposite value of the extracting electrode, as explained in the previous chapter. In this case, the electric field is more uniform if no corrections are applied.

However, it increases the number of high voltage power supplies and the design complexity (Fig. 4.7b). Of course MCPs work also correctly at ground potential (Fig. 4.7a) and we refer to this set-up as asymmetric. The strips IPMs support only the asymmetric configuration and do not require more than one high voltage. During the two test campaigns we were able to work in both configurations.

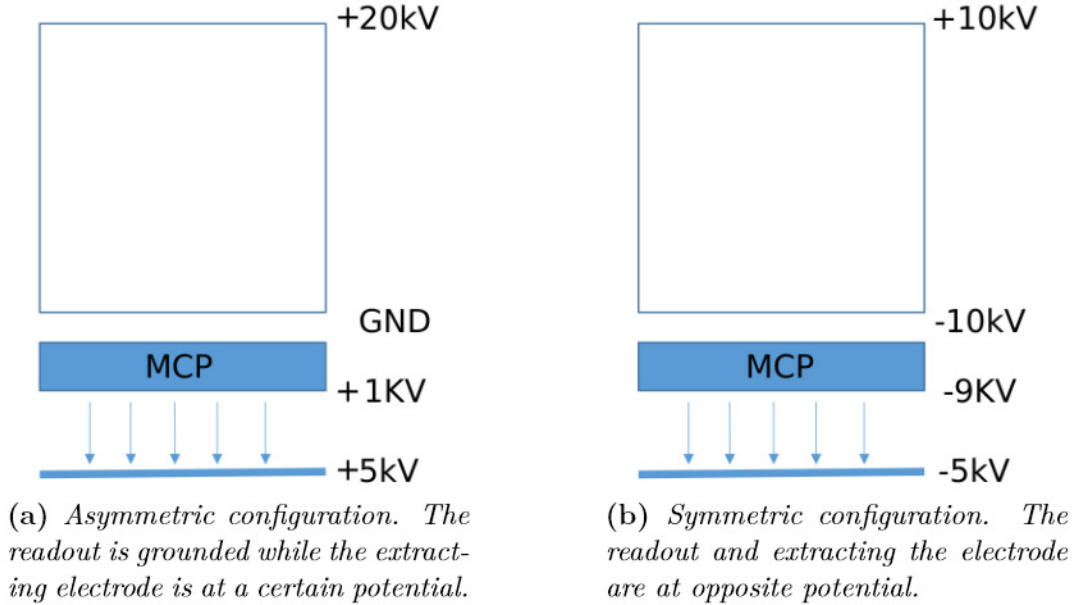


Figure 4.7 – *Asymmetric or symmetric configuration, MCPs allow both.*

### 4.3.7 Control System

The whole ESS Control System (CS) will rely on the Experimental Physics and Industrial Control System (EPICS) toolkit. The ESS CS team has specified its own EPICS standards to ensure the sustainability of the control system over the years. We will also test our IPMs at an accelerator whose control system is EPICS compatible. Therefore, EPICS has some importance to our project and we tried to use it as much as possible for our prototypes. In this section we will briefly describe EPICS and how we have integrated our test bench under such environment.

EPICS provides a set of tools and protocols to facilitate the integration of control systems [12]. Originally developed for real-time systems, it now supports many platforms. EPICS has become an open source project in 2004, since many laboratories and collaborations have contributed to its development. One of the most important component of EPICS is the Channel Access (CA): it is a protocol that defines how the data are exchanged between clients and servers on a network. A server provides Process Variables (PVs) to clients. PVs are useful data (for instance a current, a voltage or a temperature) associated with metadata (timestamp, units). A client can access and edit a PV value by knowing its name. In practice a server is often a hardware controlled by software, often called software Input/Output Controller (softIOC). A client is for instance an operator interface (OPI) which allows to view and modify the PV from one or more softIOCs.

The whole system employed for the test bench is almost fully compatible with the version 3.16 of EPICS base. The PointGrey GigE cameras are well supported by the



AreaDetector module [13]. A custom plugin, developed by ESS, performs a gaussian fit on the profile for every image. Raw images are saved into HDF5 files [14]. This format allows to pack various datasets together, for instance the raw IPM images with some beam information. Since all high voltage power supplies have their own SPCI Ethernet interface, thus a simple softIOC with StreamDevice[15] was enough to control and monitor them. Three OPIs have been developed in order to control cameras, power supplies and a GEO BRICK controller<sup>3</sup>. They run under the BOY module of the ESS Control System Studio version 4.5. An Archiver Appliance records and saves slow process variables from the power supplies, the vacuum systems and the accelerator [16].

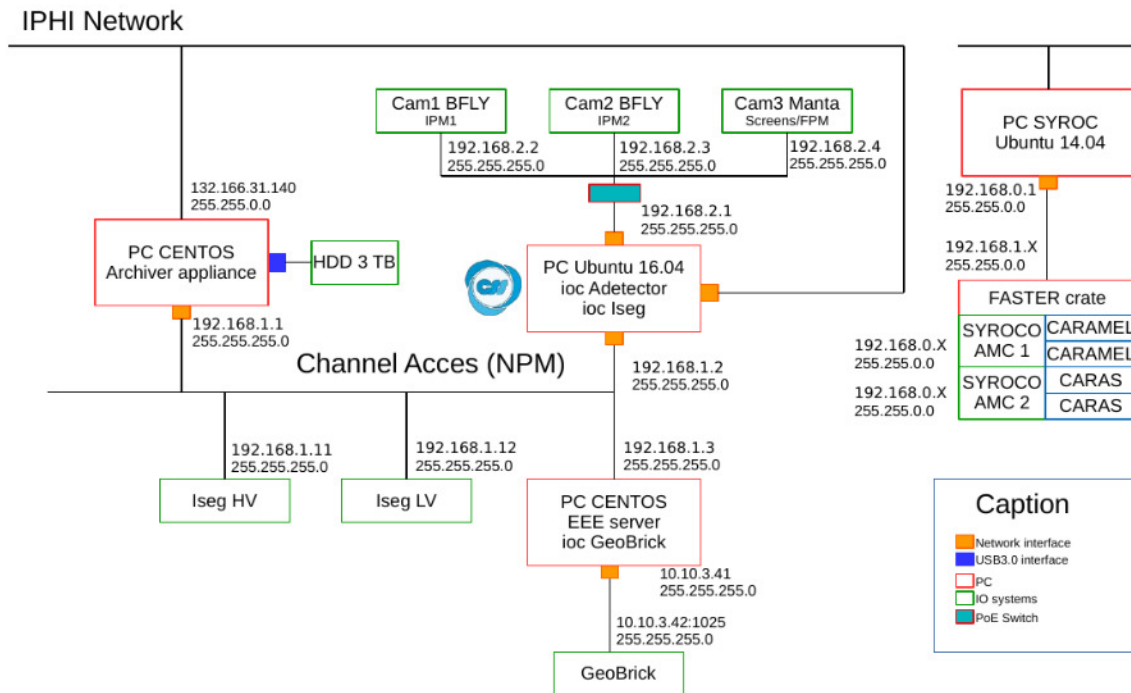


Figure 4.8 – EPICS network setup during beam tests.

### 4.3.8 Test bench

A test bench has been also developed in order to test the prototypes. The bench can be split into two different independent parts.

The first part (upstream) is roughly similar to the ESS LWU chamber (scale 1) on which two IPMs can be inserted. The idea is to be close to the ESS conditions in term of high voltages and electrical fields. The second part (downstream) offers one more IPM slot and two viewports for reference measurements in order to compare with the IPM ones. Fig. 4.9 is a technical drawing of the test bench. One can see the resemblance of the upstream part with the LWU vessel previously shown in Fig. 3.1 and 3.8.

3. Motor to move scintillating screens vertically to intercept the beam or to be safely moved far from it, see section 4.3.9 for more details.

The IPMs can be mounted independently in Y or X directions thanks to their design, thus it is even possible to measure the same transverse profile with all three IPMs.

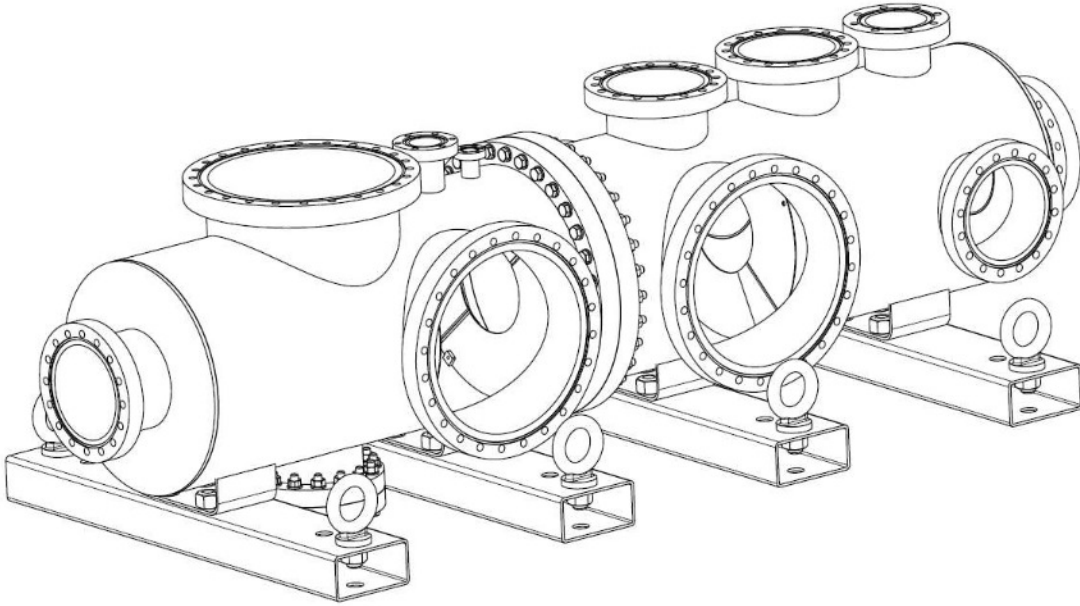


**Figure 4.9** – *IPM test bench. The left part is similar to the LWU vessel, while on the right part more viewports are added for testing purposes.*

The test bench is pumped by 3 turbomolecular pumps with an average pumping speed of about 150 L/s at 3 different locations along the bench. The vessel can be baked using a heating system. The objective is to reach quickly the minimal vacuum level required to operate. Thus, during the tests it is possible to modify the IPMs without sacrificing too much beam time. The whole system reaches a vacuum level of  $1 \cdot 10^{-7}$  mbar in about ten hours (one night) after an intervention. An RGA and vacuum gauges monitor the vacuum level as close as possible to the IPMs.

### 4.3.9 Reference measurement

We carried out reference measurements for diagnosing possible issues on the prototypes and to allow a complete comparison with the prototypes, giving more confidence on the measurement. Two methods have been foreseen and implemented for this purpose.

The first method uses scintillator screens, which is interceptive. The screens are mounted on a racket that can be inserted into the beam using a translator controlled remotely through a GEO BRICK controller. Three scintillator screens have been kindly provided by our colleagues at Saclay. Table 4.5 sums up the main characteristics of each screen.

The second system foreseen is a Fluorescence Profile Monitor (FPM). This system is developed by our ESS colleagues, indeed it will be the future NPM of the ESS MEBT. The FPM relies on an Image Intensifier (II) and a CMOS camera. Such an image intensifier is made of a photocathode, converting photons in electrons, which

**Table 4.5** – *Properties of the 3 scintillator screens [17, 18] used as reference measurement.*

Property	Prelude420 $Lu^{1.8}Y^{2.2}SiO_5$ Ce	YAG : Ce : $Y_3Al_5O_{12}(Ce)$	BGO $Bi_4Ge_3O_{12}$
Density (g/cm <sup>3</sup> )	7.1	4.57	7.13
Light yield ( $\gamma$ /keV)	33	8	8 – 10
Typical wavelength (nm)	420	550	480
Typical decay time (ns)	36	70	300

are then amplified by a single or a double MCP stage, before to be converted back into photons through a phosphor screen. The high sensitivity of an II allows to detect the unique photo-electron. The FPM is a totally non invasive method.

## 4.4 IPHI and test campaigns

We had the opportunity to test twice our prototypes at the IPHI accelerator. In the following sections, the accelerator and the two campaigns are briefly introduced. Pictures of the installation are shown in Fig. 4.11.

### 4.4.1 IPHI accelerator

IPHI is a high intensity linear proton accelerator located at CEA/Saclay. The project started in the late 90's [19] but protons were accelerated up to 3 MeV only in April 2016 [20].

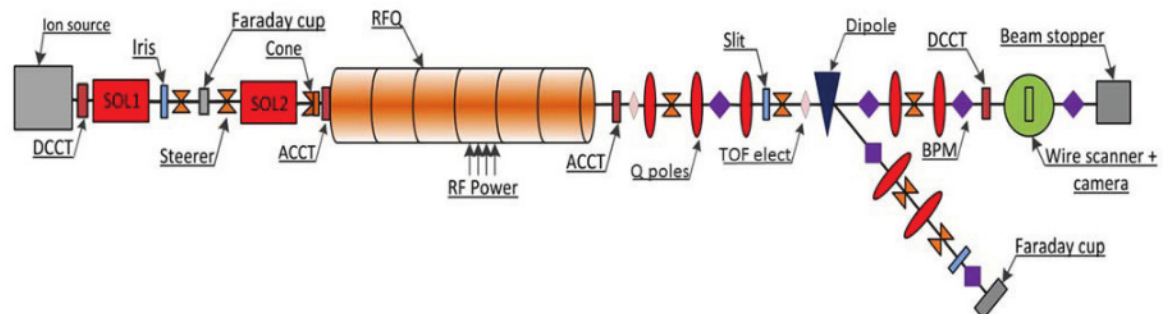


**Figure 4.10** – *Schematic view of the IPHI accelerator. The layout is almost up to date except that the slits have been removed. Our test bench was installed just after the last BPM on the deviated line. There is no other beam profiler measurement on this line.*

Proton plasma is created by an electron cyclotron resonance source (ECR), and transported toward a radio frequency quadrupole (RFQ) by a low energy beam transport line (LEBT). An iris, at the source exit, ensures a fine tuning of the current, and two solenoids focus and filter the plasma before the injection into the RFQ. Then, the protons are accelerated up to 3 MeV and bunched at a frequency of 352 MHz. A



medium energy beam transport line (MEBT), downstream from the RFQ, contains focusing elements, steerers and beam diagnostics. A bit further, the dipole magnet can distribute the protons over two beam lines.

The main line has a dedicated beam stop of 300 kW, allowing the commissioning of the accelerator at high intensity and duty cycle. The secondary line is more modular but restricted to beam at lower intensity and duty cycle (few hundred Watt). This line is open for external user experiments. We were, with the nBLM team, one of the first experiments on the deviated line [21].

Fig. 4.10 shows a schematic view of the IPHI accelerator, and Table 4.6 sums up the main differences between IPHI and ESS. Even if IPHI does not have the same characteristics, it is close to our laboratory and very convenient for testing purpose. The extrapolation from IPHI to ESS conditions will be done as soon as the following product  $I_{beam} \times P_{gas} \times \sigma(E_{beam})$  is kept constant for both facilities.

**Table 4.6** – Comparison between IPHI and ESS accelerators.

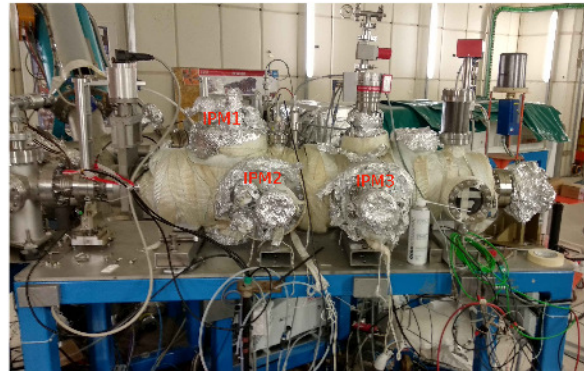
	IPHI accelerator	ESS accelerator
Energy	3 MeV	2 GeV
Max current	100 mA	62.5 mA
Max pulse duration	up to DC	2.86 ms
Max pulse repetition	-	14 Hz
Vacuum range	$5 \cdot 10^{-7}$ to $1 \cdot 10^{-8}$ mbar	$1 \cdot 10^{-9}$ mbar

#### 4.4.2 Overview of the two test campaigns

In this section, we want to introduce the story behind our two test campaigns, and give an overview of the issues we faced.



(a) The casemate of IPHI. The test bench is visible in foreground



(b) The test bench fully equipped.

**Figure 4.11** – The test bench installed at IPHI accelerator.

The prototypes were not ready for the beginning of the first campaign. Hence, they were debugged on site, and we encountered many technical problems (sparks, readout synchronization). We finally got our first profile after some fixes on our prototypes, and by reducing the maximum operating voltage. However, our prototypes were not

able to measure the beam profile on demand, working sporadically, and we observed strange artifacts on the profiles. We solved this problem by asking a fine tuning of the beam parameters to a beam physicist. We became even more confident with our detectors when Beam Position Monitor (BPM) systems were switched on allowing a comparison with our measurements, see section 4.6.2.

Just after the first campaign the detectors were improved by minor changes on the HV connection design. Therefore, the decision was made to perform a second test campaign at IPHI. The results of the first campaign were confirmed and improved during this second one. The beam time was shared between four experiments, with different requirements on the beam parameters. Unfortunately, the schedule was not respected due to technical problems and other external issues, so we had to manage our tests daily and get along with the other experiments. For the above reasons, we did not manage to perform all the advanced tests we had planned to do. Table 4.7 summarizes our two beam test campaigns

Table 4.7 – *Summary of the two campaigns.*

	First campaign	Second campaign
Starting date	19/02/2018	14/09/2018
First profile	01/03/2018	14/09/2018
Ending date	13/04/2018	26/10/2018
IPM 1	Linear strips (Y)	Gaussian strips (X)
IPM 2	Hamamatsu MCP (Y)	Photonis MCP (Y)
IPM 3	Gaussian strips (Y)	Linear strips (Y)

## 4.5 Processing data

In the following sections, the data processing is briefly explained based on several methods. Each method has its own characteristics, so the data processing is different depending on the IPM. The term beam size refers to the  $\sigma_{beam}$  of the beam. The error bars in the following plots are given for a confidence level of 95 %. This assumes that the variation follows a normal distribution.

### 4.5.1 Processing camera

The optical IPM gives directly an image of the beam in longitudinal and transverse directions. Thanks to EPICS and AreaDetector, all images and related acquisition information are packed together in an HDF5 file. The processing of data is done with different Python packages [22–24]. In a first step, dead pixels are removed: the standard deviation of the image is computed and each deviating pixel is smoothed by a convolution filter ( $3 \times 3$  kernel). The algorithm works well if two dead pixels are not neighbours, otherwise higher order kernel must be used. Then, the image is cropped to a region of interest i.e. the active surface of the MCP. If necessary, the image is filtered in the frequency domain via a Fast Fourier Transform (FFT) [25]. FFT filtering is a very efficient method when the images have many recurring pattern that are even visible by a human eye. At ESS, more advanced methods like wavelets



[26, 27] may be more suitable for filtering patterns with some spatial dependencies. Indeed, the images may have some discrete spots rather than a continuous image<sup>4</sup>. Note that beam images are quite parsimonious in the frequency domain. The profile is reconstructed by summing all pixels in the longitudinal direction. An example of an almost raw image is visible in Fig. 4.12.

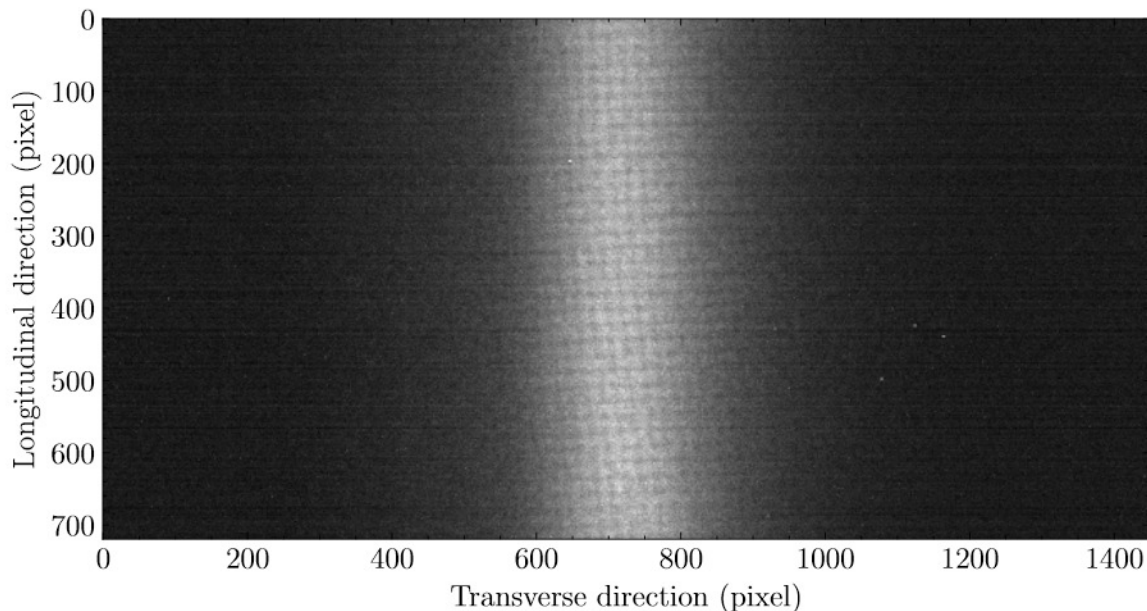


**Figure 4.12** – *An example of a beam image recorded by the camera. The image has just been cropped to a region of interest. The shadow of the grid is visible.*

### 4.5.2 Processing strip

The processing of data from strips is completely different and more complex. Indeed only a small part of the recorded signal is meaningful since the chips integrate continuously. The duration of the beam pulse was always short during the tests (from  $50 \mu\text{s}$  to  $1 \text{ms}$ ), therefore only a small amount of data is really useful.

The data are processed as follows with ROOT[28, 29] routines. First, the pedestal of each strips is subtracted. If  $N$  successive points are above a given threshold, then the pulse is considered as triggered. A pulse is detected when the previous condition is met on several strips at same time. Finally the successive  $N$  integrations are summed giving the charge collected for one pulse. For Gaussian strips the charges are weighted according to the size of the strip.

An example of a raw signal is given in the Fig. 4.13. On the left hand side, one can see the signal recorded during 45 s. Each peak corresponds to the passage of the beam. The signal for one pulse is visible on the right hand side.

---

4. More details in section 4.7.9.

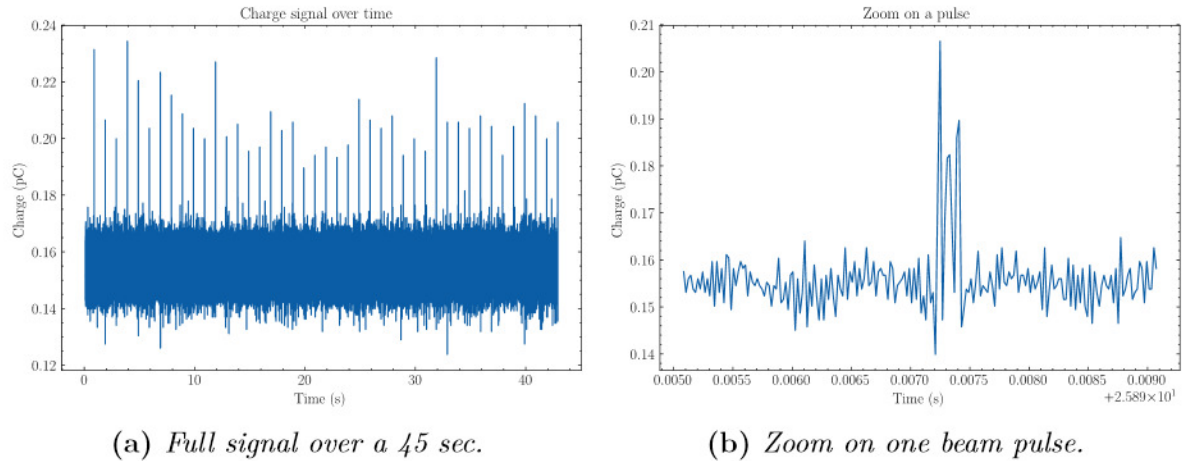


Figure 4.13 – Example of charge signal recorded on one strips.

### 4.5.3 Processing scintillator screen data and review of the reference measurements

Scintillator screens can only operate at low duty cycles, typically few mA and few hundred  $\mu\text{s}$ . Even under these conditions, the beam destroyed two of the three screens. The signal is so strong that the camera in front of the screen is completely saturated, as well as the camera of the optical IPM one meter away. Measurements with the scintillator screens are only possible if a neutral density (ND) filter is set in front of the lens. The signal from the scintillating screen completely overlaps with the one from the phosphorus screen and since we use monochromatic camera, there is no way to recover the beam profile from the optical IPM. For the strips IPM the working conditions are already too low for a correct measurement. Therefore, it is not possible to compare the IPM beam profiles with the scintillating screens in real time.

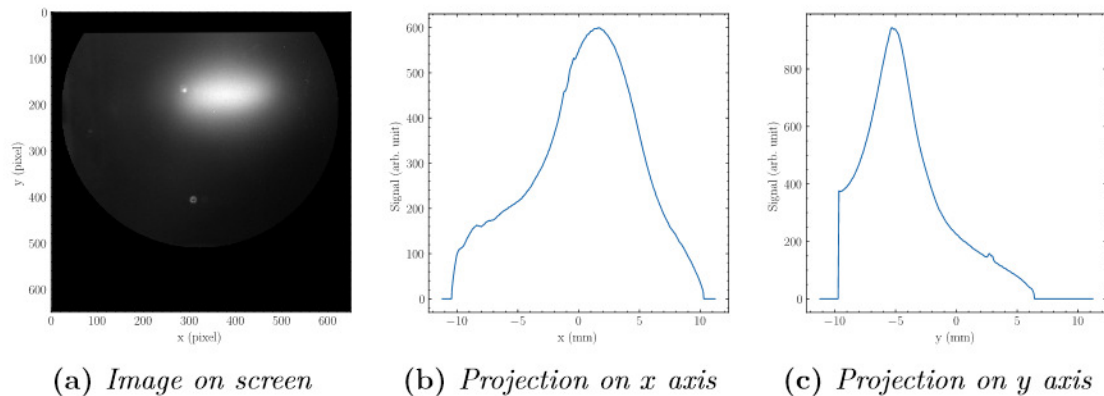
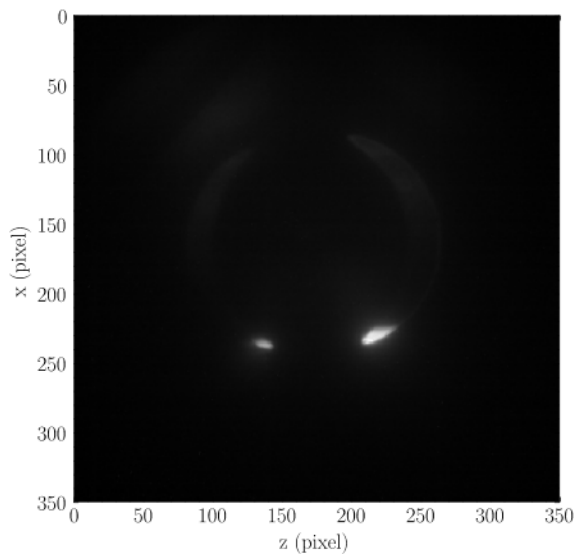


Figure 4.14 – Beam profile measurement with the  $Y_3Al_5O_{12}(Ce)$  screen.

Fig. 4.14 shows an example of a profile measurement recorded on the  $Y_3Al_5O_{12}(Ce)$  screen. The processing is almost the same as the optical IPM: hot pixels are corrected and the images are cropped. Then, a homography [30, 31] is performed to correct the orientation of the screens. The measurement of the beam size is quite complicated because the baseline of the profile is not straight, therefore the fits have a very poor

quality. One can see that the profile is quite wide in the  $x$ -plane because of the dispersion due to the dipole.

The conditions are also not favorable for measurements with FPMs. The viewports are very close to the beam dump and when this stops beam particles stray light is emitted. The vacuum chamber (and the entire accelerator) allows light to propagate easily due to reflections on 304L steel. The vacuum is quite low so the expected fluorescence signal will be even weaker. Increasing the beam intensity does not help since the parasitic light from the beam dump becomes more significant. Our concerns were confirmed when we added a sleeve with a black coating to shield the FPMs field of view from the rest of the vessel. The parasitic light is shown in Fig. 4.15. All the attempts to minimize this effect remained unsuccessful.



**Figure 4.15** – *Image recorded with the FPM system. The light coming from outside of the sleeve does not permit a correct measurement.*

## 4.6 Beam environnement characterization

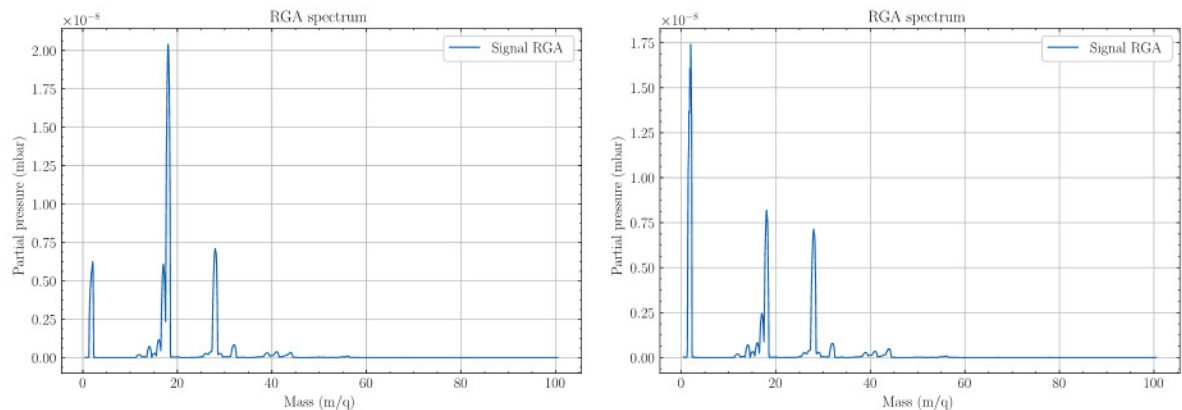
First of all, it is necessary to present the experimental conditions under which our detectors have been characterized. One of the major problems encountered during these tests was the lack of information about the beam. The two types of diagnostics available at IPHI on the deviated line are current monitors and BPMs, whose calibration is uncertain. During the first weeks of the test campaign, it was impossible to know if the strange beam position oscillations observed were due to the beam or to the detectors themselves. The next sections show the tests carried out in order to understand the origin of the instabilities

### 4.6.1 Vacuum analysis

Understanding the vacuum conditions is very important in order to correctly extrapolate our results to ESS conditions. During the tests, the vacuum parameters

were recorded in real time<sup>5</sup>. However, neither the RGA, nor the vacuum gauge were calibrated. It is assumed that the RGA provides a qualitative information about the proportions of each specie in the residual gas, whereas the vacuum level is given more precisely by the vacuum gauge.

We measured two main types of RGA spectra as shown in Fig. 4.16. The left one is obtained when the chamber had not been baked or after a water contamination. As a consequence, the water peak dominates and the pressure is in the range of  $10^{-7}$  mbar. After few days of pumping or after drying, the RGA spectra tend towards the second case, on the right. In this case the vacuum level is about  $10^{-8}$  mbar and hydrogen is the main molecular specie. One can see some quite heavy elements on the two spectra, possibly oil residues. Indeed one of our turbo pumps was contaminated with oil from its old primary pump.



(a) An RGA spectrum dominated by water peaks. (b) An RGA spectrum after few days of pumping or baking.

Figure 4.16 – Two types of RGA spectra recorded during the tests.

When the beam is running, the pressure increases slightly as well as the amplitude of all the peaks in the RGA spectrum. We suppose that these effects are mainly due to the heating of the beam dump. In the same way, the pressure increases when the resistance chains are fed, probably due to the Joule effect. On some RGA spectra, the hydrogen peak is subject to overshoots when the beam is running.

### 4.6.2 Beam position

The first observation we made on the profile measurements was the significant variation of the beam position between two pulses. At first, we thought to an electrostatic charge and discharge phenomenon, that induced beam position oscillation. However, this hypothesis was discarded when finally the BPM system was started. For the first time, we were able to compare our measurements with another device. Fig. 4.17 shows the position of the beam recorded by IPM and a BPM on a time scale of about one hour. The big sharp transitions are the consequences of beam moving under the electrostatic steerer scans. However, there are quite a few smaller variations between two steerer steps. A variation exceeding 2 mm (5% of our readout size) can be observed from pulse to pulse. The IPM position is the center of the gaussian

<sup>5</sup>. The vacuum gauge can provide a measurement at every pulse whereas a full RGA scan takes around two minutes



fit of the profile; this nice correlation started giving us confidence in our monitoring systems.

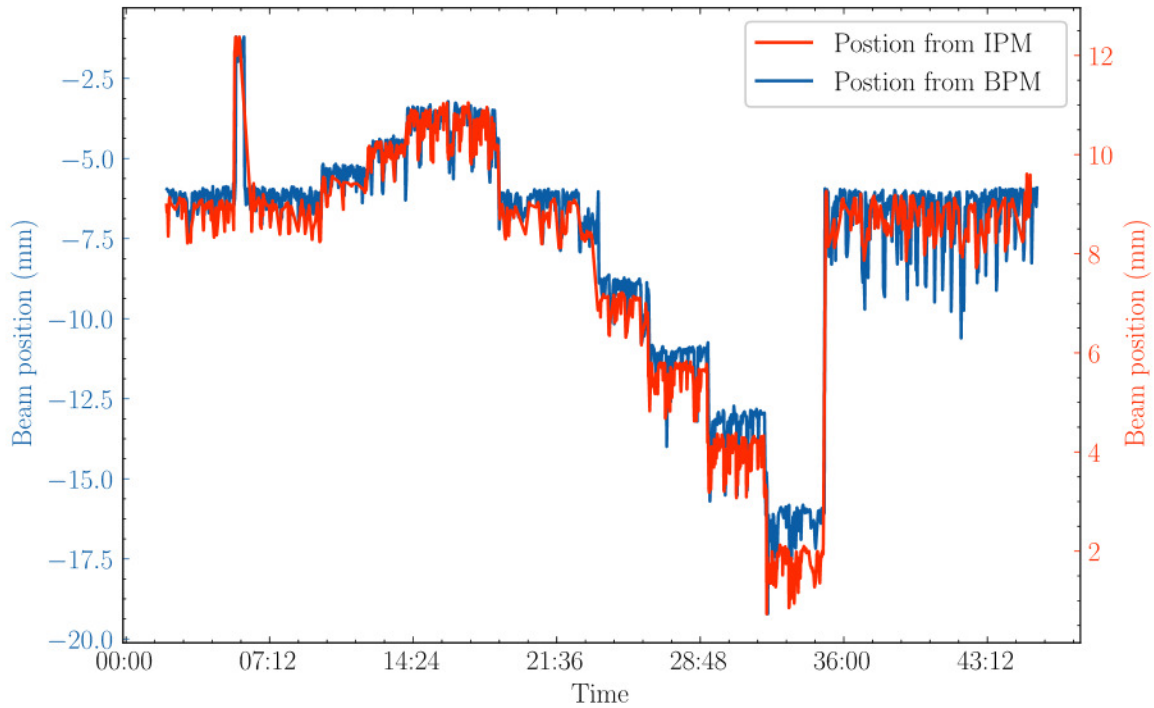


**Figure 4.17** – *Beam position versus time, measured with a BPM on the IPM. A steerer has been used to move the beam (step transitions). However, small variations between two steerer steps were not expected. The BPM positions were directly extracted from IOCs without any processing.*

This is a major issue since MCPs have a good space resolution, but we are not allowed to fully benefit of this feature. Indeed, all our measurements have been affected by those parasitic variations and therefore the level of confidence on the measurement is reduced. The histograms of beam size and position over 480 consecutive pulses are reported in Fig. 4.18.

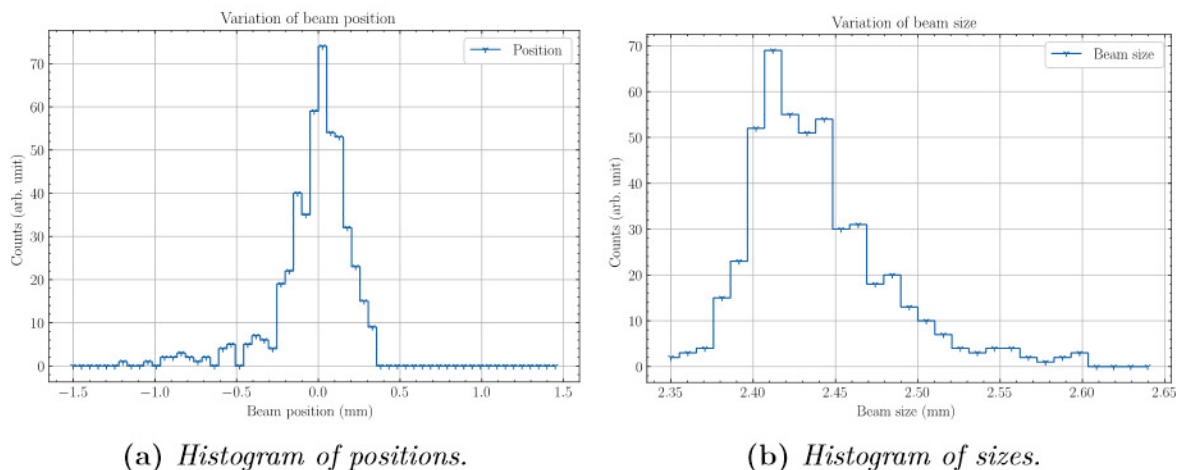


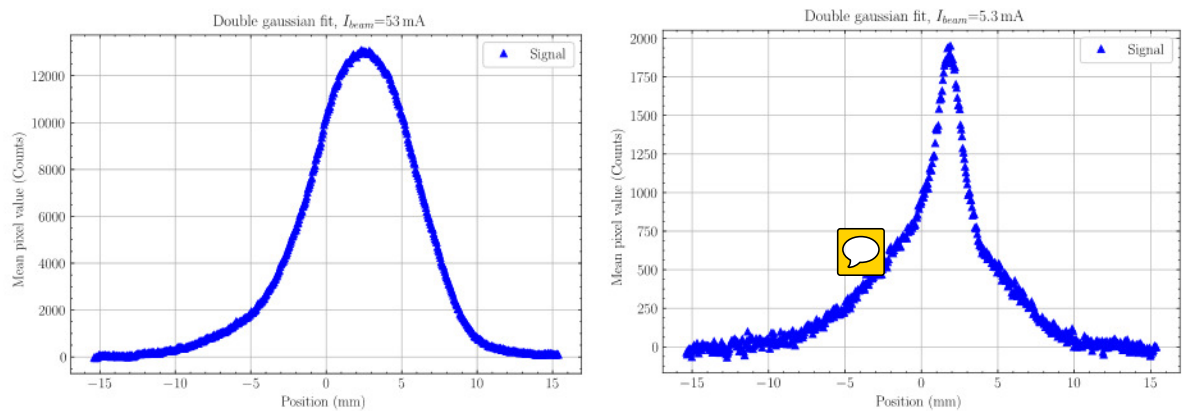
**Figure 4.18** – *Histograms of the beam position and size for 480 consecutive pulses.*

One can see that both distributions are asymmetric and have a similar shape. The linear regression between size and position has been calculated from several runs and shows a non-zero slope. On the other hand the correlation factor between size and position is not so high usually and varies between 0.5 and 0.8 mm from run to run. Anyway, these uncertainties can be seen as systematic errors, thus measurement errors may be calculated and reduced quadratically from the oscillating components!

The main explanation given by IPHI experts about these variations is that the beam is more unstable when the pulse beam is shorter. However, we did not have time to confirm this hypothesis.

### 4.6.3 Beam current

At IPHI the current is finely adjustable thanks to the iris located at the source exit; IPHI has been designed to work with a continuous beam up to 100 mA. To be in conditions close to those of ESS in term of counting rates, the current and duration of the pulse must be lowered. Varying the beam current is very important because it allows to check many properties of the detector. However, the shape of the IPHI beam changes greatly with current. This phenomenon is illustrated in Fig. 4.19a and 4.19b. When the currents are high, the beam looks like a Gaussian with one of its shoulders with a longer tail. At medium and low current, the size of the beam decreases as well as its amplitude. However, a kind of halo appears and this becomes more and more important as the current decreases. At very low current the beam core disappears completely and only the halo remains.

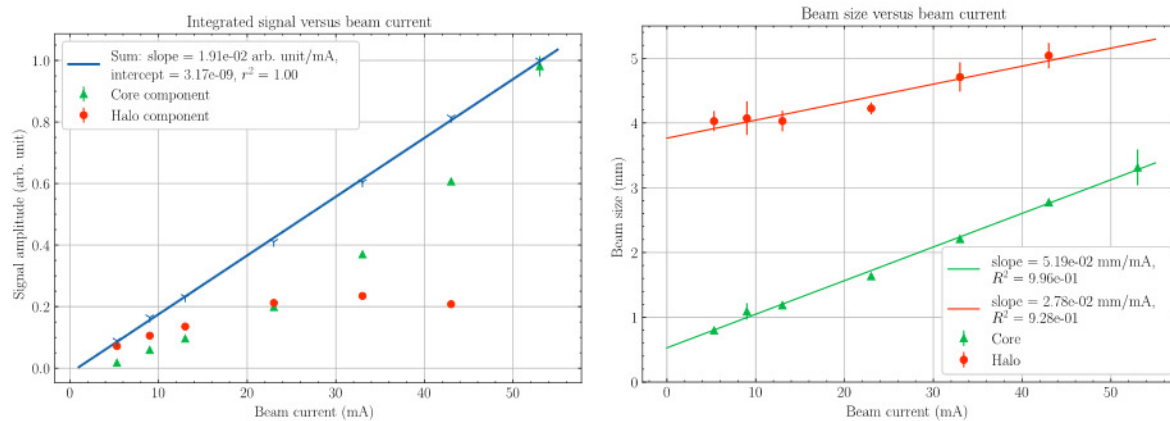


(a) At high current the beam looks almost Gaussian. (b) At low beam current, the beam shows a narrow peak on the top of a large halo.

**Figure 4.19** – Influence of the beam current on the beam shape.

This causes a problem for beam shapes comparisons at different beam intensities. So, how to quantify the beam size? Several methods have been considered. One can simply calculate the mean value and standard deviation of the profile distribution, but the results are strongly biased by the beam position and the asymmetric shape of the profile. A more advanced method consists in performing a least squares curve fitting of the profile with a Gaussian function for recovering the estimated sigma. This method works quite well at high currents but at low currents the halo prevents the beam from performing a correct fitting. To overcome this issue, a second Gaussian function can be added to the fitting routine. The double fit succeeds in correctly

modeling the two components. However, double fits may modelize almost any beam shape and the fitting results are difficult to verify automatically. The method becomes very unstable for high currents. This is why it must be limited to low currents. The last alternative is to use the full width at half maximum (FWHM). Assuming that the beam is more or less Gaussian, the sigma can be calculated as follow  $\sigma = \frac{FWHM}{\sqrt{2\ln(2)}}$ . FWHM computation is also less complicated than least squares fitting.



(a) *Integrated signal versus beam current.* (b) *Sizes of the beam and halo versus beam current.* The blue curve represents the sum of the two components.

**Figure 4.20** – *Influence of the beam current on the profile measurement.*

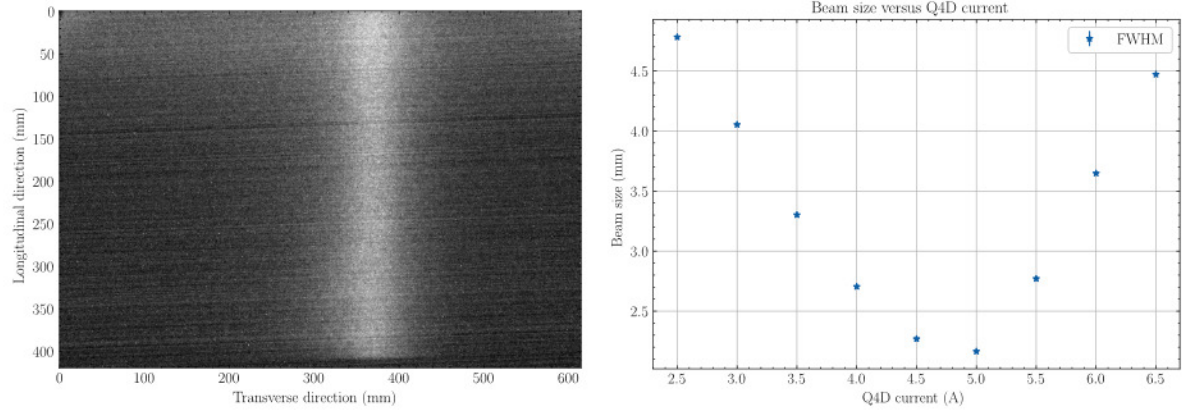
On Fig. 4.20, the double fitting routine was used to monitor the evolution of both beam components. First, the phenomenon described above is clearly visible. At high current the signal tends towards a Gaussian shape, whereas at low current the double Gaussian model seems more realistic. Secondly, the amplitude of the signal is linear with the beam current. At high currents the input signal on the MCP is by several orders of magnitude above the expected signal at ESS. This means that there will be no saturation at ESS with a single-stage MCP.

#### 4.6.4 Beam tuning

The beam tuning is also important to insure a correct measurement of the profile. The IPHI line contains many beam optics elements to control the beam transport. An incorrect adjustment of the beam has significant consequences on the quality of our measurements. Indeed, during the first weeks of testing, we could not get stable and reproducible measurements. An example is given in Fig. 4.21a. One can see that the profile is visible in the image, but with a kind of halo on the top. We have no explanation about the origin of this halo. This effect disappears completely when the beam is properly adjusted.

The optimal parameters were found with the help of a beam physicist using the TraceWin software. In practice, the beam has been adjusted to have the lowest possible convergence all along the test bench. The beam size has been tuned to be close to ESS conditions (around few mm) with the different quadrupoles (Fig. 4.21b). Once the beam was adjusted, all the parameters were frozen. This allowed us to measure the profile correctly.





(a) A poorly beam tune leads to strange signal on the top of the image. (b) The beam size can be set at different sizes thanks to quadrupoles.

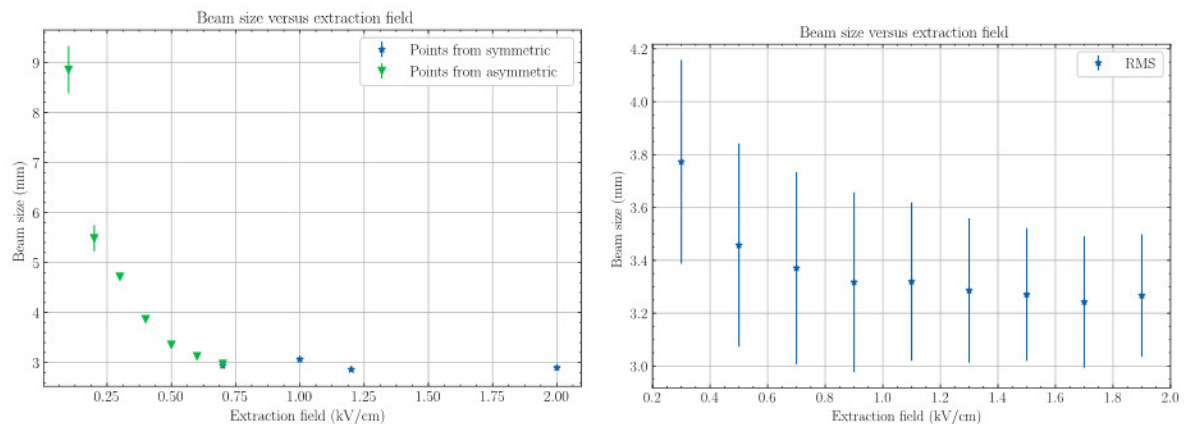
Figure 4.21 – The beam must be finely tuned in order to perform correct measurements.

## 4.7 IPM characterization

In the next sections the most common aspects of IPMs are presented. The goal is to collect as much information as possible about the detectors and their limitations to prepare the final design. Most of the data presented below come from optical IPMs, since many of the acquisitions done with the strips were polluted by strange electronics noises.

### 4.7.1 Beam size convergence

The extraction voltage is an important parameter of an IPM; if the electric field is too low, then profiles will be distorted by the molecular thermal motion and beam space charge effects. Those effects can be compensated by increasing the electrical field in the cage. At a certain point, the beam size will start to converge to its real value. This behavior has been observed with both strip and optical IPMs.



(a) Convergence observed with optical IPM,  $I_{beam} = 10\text{ mA}$  (b) Convergence observed with strips IPM,  $I_{beam} = 30\text{ mA}$

Figure 4.22 – Example of beam size convergence measured with both IPMs.



Fig. 4.22a shows an example of the beam size convergence from the optical IPM. For technical reasons, we have to permute from asymmetric to symmetric mode for achieving high electric field. The swap induced an error on the profile measurement but it can be corrected, see next section 4.7.4. At very low voltage the beam shape is very wide and has no more gaussian shape explaining the huge uncertainty on the size measurement. The strips IPM does not have this issue since it works only in asymmetric mode(Fig. 4.22b).

## 4.7.2 Cross interaction

In the previous chapter we showed that the profile measurement can be greatly affected by the cross interaction between two close IPMs. The easiest solution to minimize this problem is to put grounded disks between each IPM, so each IPM is completely isolated from the other one. The first part of the test chamber was built almost identical to the ESS LWU vessel. It is therefore possible to verify whether the IPM electric field influence on the neighbour IPM is negligible in almost ESS conditions. To check this, one IPM is switched on, while the other is measuring the position and size of the beam. However, the measurement is not so simple for the second IPM since the 3 MeV beam can be deflected by the extraction field of the IPMs. Therefore, we may measure the deviation of the beam pulse instead of the cross interaction. Fig. 4.23 shows the variations of beam position (right) and size (left) measured by IPM2 for different values of the extraction field in the IPM1. The green curve displays the theoretical deviation calculated from the voltage applied to the IPM1. The variation in beam size seems negligible, about  $75\ \mu\text{m}$ . On the other hand, the variation for the position is quite important, but the observed values are very close to the theoretical curve.

The same test has been done with the IPM1, and no shift has been observed when the IPM2 was on. Therefore, the shift measured in IPM2 is due to the deviation of the beam itself.

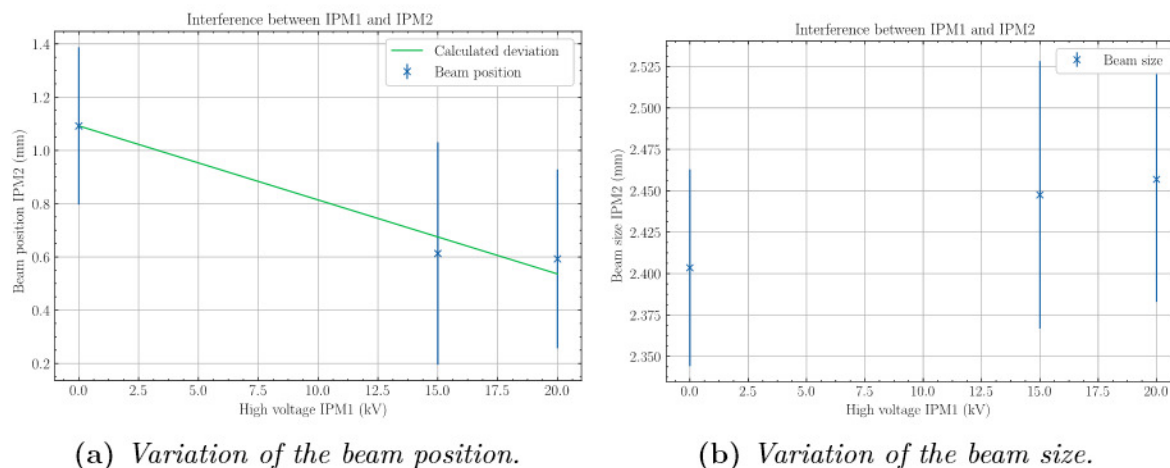
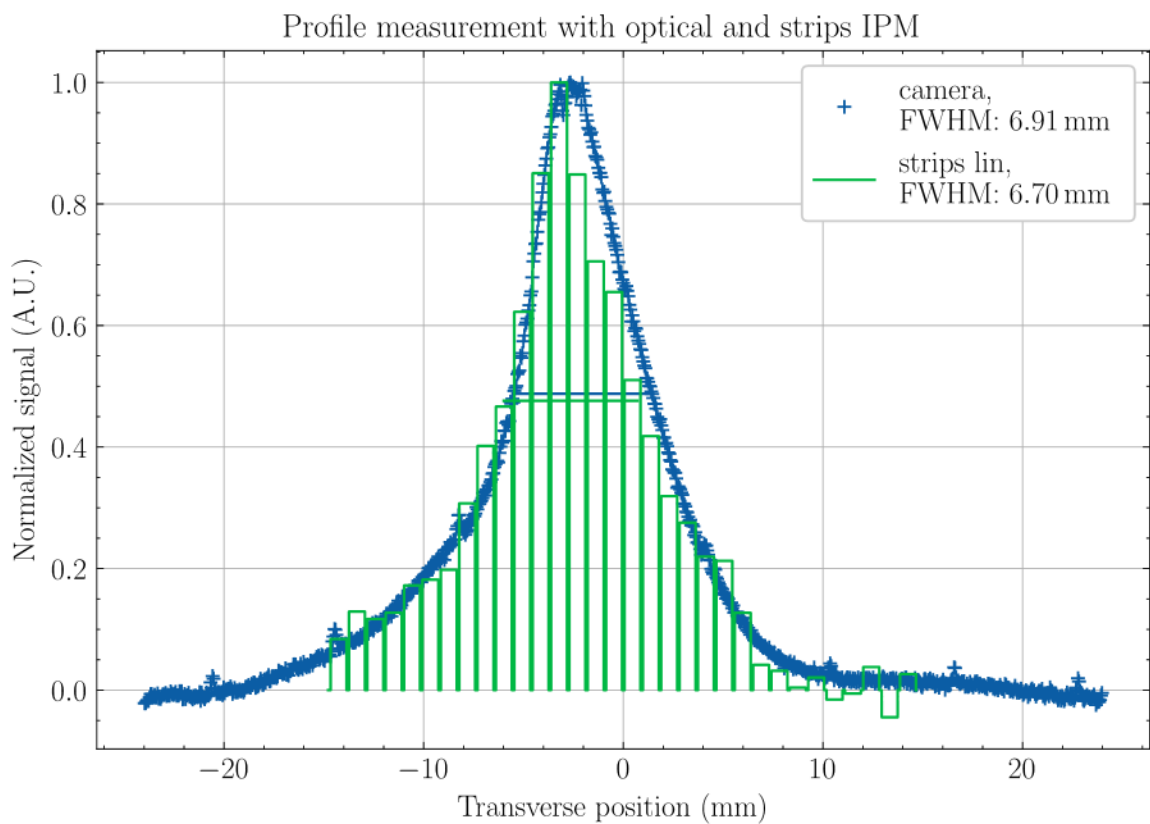


Figure 4.23 – Cross interaction between two IPMs.

### 4.7.3 Comparison size

The IPHI beam may be deflected by the extraction fields of the different IPMs, as a consequence most of the studies have been performed on a single IPM at a time. However some measurements require to use both IPMs at the same time, like for the comparisons between profiles measured with the two different IPM types. This is the only way to check the correctness of the measurement since there were no reference method working correctly during the tests. The superposition of the profile measured with the strips IPM and optical IPM is displayed in Fig. 4.24, showing an excellent agreement. The strips IPM directly measures a number of charges whereas the camera gives a digital pixel value. The conversion factors of each element in the optical IPM have not been quantified, therefore the signal amplitude from the camera data is only scaled, while the x-axis remains unchanged.



**Figure 4.24** – *Superposition of the same beam profile measured with strips IPM and optical IPM.*

The FWHM is used to compare the size measured with both methods. This method is less biased by the position of beam and the total range of the measurement compare to other methods presented in section 4.6.3. Additional steps are required before computing the FWHM. The non working strip is equalized with its two neighbors. A linear interpolation is performed on the strips data to virtually increase the resolution on beam size. From the example given in Fig. 4.24 the FWHM measured for strips is 6.907 and 6.698 for the optical IPM. The results are quite good considering the resolution difference between both readouts.


Note that the beam position measured by both IPMs is different and may be

greatly affected by the steerers and the IPM1. In some cases, a variation of 1.6 mm can be observed.

#### 4.7.4 Field uniformity

Simulations have been performed with COMSOL to cover both cases of asymmetric and symmetric configurations, showing a good electric field uniformity with a better result for the symmetric configuration. Experimentally, the beam can not be moved in non uniform areas of the IPM since they are too far from the IPM center. The uniformity can not be quantified in that way.

A possible workaround consists in intentionally reducing the uniformity of the extraction, so that the beam size and position will be more affected by non-uniformities. The optical IPM has been used in asymmetric configuration with a resistor chain designed for symmetric usage. Since resistor chains are different between asymmetric and symmetric configurations the extraction field will be also different. The electric field in this peculiar configuration can be simulated with COMSOL as shown previously.

Three main effects have been observed from these simulations. Firstly, the beam image is smaller than the real beam size. This focusing effect is constant over the overall detection plane. Secondly, the extraction field tends to pull the beam image in the center of the detector. This effect is linear and null at the IPM center. Thus, the measured displacement is less important on the readout than the reality. Lastly, the beam image intensity is smaller in asymmetric  because some particles are lost in the longitudinal direction. However, this effect can not be measured because the gain of MCP is not perfectly known on the symmetric configuration and cannot be recovered correctly.

We measured the beam size and displacement for several steerer values in the symmetric and asymmetric configurations. The extraction fields were set to a same value for both configurations and all other parameters were frozen. If we suppose that the symmetric mode gives the real beam position and size, hence it is possible to quantify the difference between the simulated and experimental values.

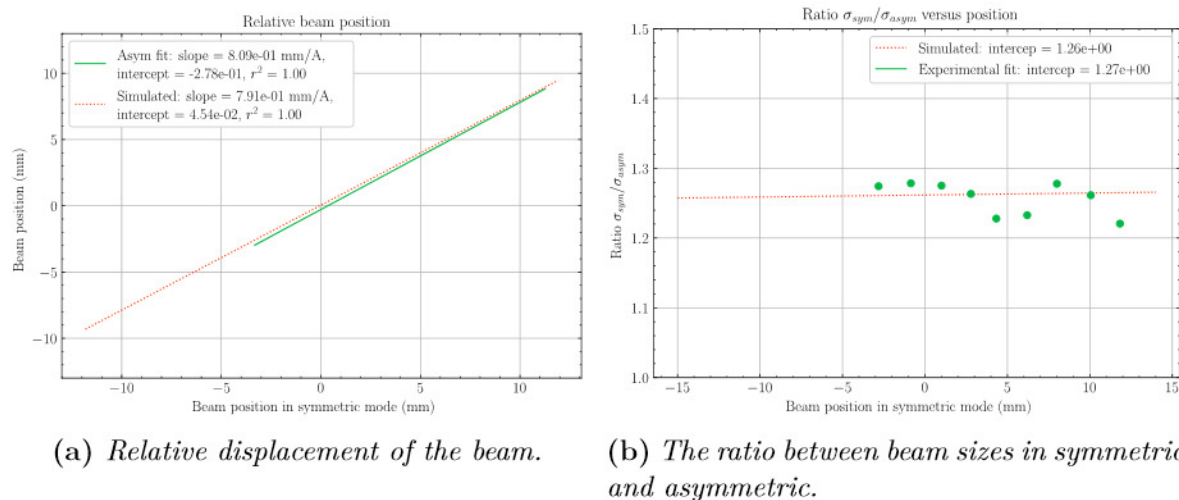


**Figure 4.25** – Verification of the electrical field can be done by switching the field configuration. Two effects can be observed on the beam size and on the position

For several extraction field values in both asymmetric and symmetric modes, the mean value of the slope of the beam displacement has been computed and compared with the results from simulations, see Fig. 4.25a. In a same way, the average ratio between beam size for symmetric and asymmetric configurations has been measured for several positions and the comparisons with simulations is shown in Fig. 4.25b. In both cases, we observe a nice agreement between simulations and measurements.

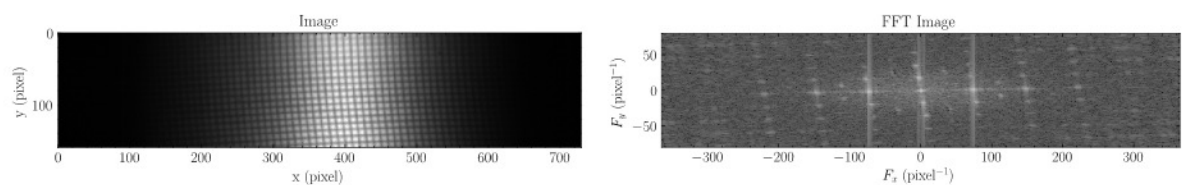
Note that the steerer was not able to cover the full range in position, but we preferred not using the dipole magnet to resume the scan since it may affect the beam size.

The method is clearly not perfect, but it allows to reduce the IPHI uncertainty since it can be done without stopping the accelerator.

### 4.7.5 Grid

Due to the position variations at IPHI, it is difficult to determine the resolution on size and position obtained with the optical IPM. It depends greatly on the run considered and in the best case the confidence interval<sup>6</sup> at 95 % is about  $\pm 5 \mu\text{m}$  on the beam size and  $\pm 30 \mu\text{m}$  on the position. There is also no reference measurement to compare results with.

However, we can try to quantify the spatial resolution of the MCP system and the camera. To measure this resolution, the grid can be used. By increasing the transmission as described in the section 3.5.8 it is possible to significantly increase the contrast of the grid shadow as shown in Fig. 4.26a. Then, the Fourier transform is used to identify the harmonics due to the grid. The resulting Fourier image is visible in Fig. 4.26b. The beam signal is located in the center of the image in a small area (20 by 20 pixels). The other spots that are repeated vertically and horizontally are due to the grid. The peaks closest to the center of the image are the lowest harmonics and it is possible to discriminate between them if their spacings exceed 5 pixels or about  $58.6 \mu\text{m}$ . With this kind of spatial resolution and assuming that the beam does not vary as at IPHI, it is quite possible to achieve the resolution requested by ESS on the pulse position about  $50 \mu\text{m}$ . However, this result would probably be different with a two-stage MCP that tends to spread spots on the phosphorescent screen.



(a) Image with improved contrast on the grid (b) FFT image where the grid harmonics are visible.

**Figure 4.26** – The optical IPM is able to resolve small details. A resolution of  $50 \mu\text{m}$  has been evaluated from the frequency domain

6. For 480 consecutive pulses.



## 4.7.6 MCP

The MCPs have been characterized directly with the IPHI beam because we did not have time to carry out studies before the beam tests. Therefore, we had no information about MCPs before their uses in real beam conditions.

The main characteristic of a MCP is its gain. We cannot give the absolute gain of the MCP since the optical IPM was not calibrated. The signal on the camera was integrated for several MCP voltages from 690 V to 1090 V. The current of the beam was set to low values for avoiding the camera saturation at high MCP gain. Fig. 4.27a displays the relative gain of the MCP and a dynamic of 300 for the considered range. The total range of a MCP is between 600 V and 1000 V, so we can expect an absolute dynamic range of 1000.

The MCP gain influence on the beam size has been checked. The beam current must be high enough to obtain a fittable beam shape. Consequently, the range of the measurement is smaller than previously, as shown in Fig. 4.27b. The slope of the linear regression can be assumed as null, meaning that the MCP gain does not affect the beam size. This tests has been done on both MCPs.

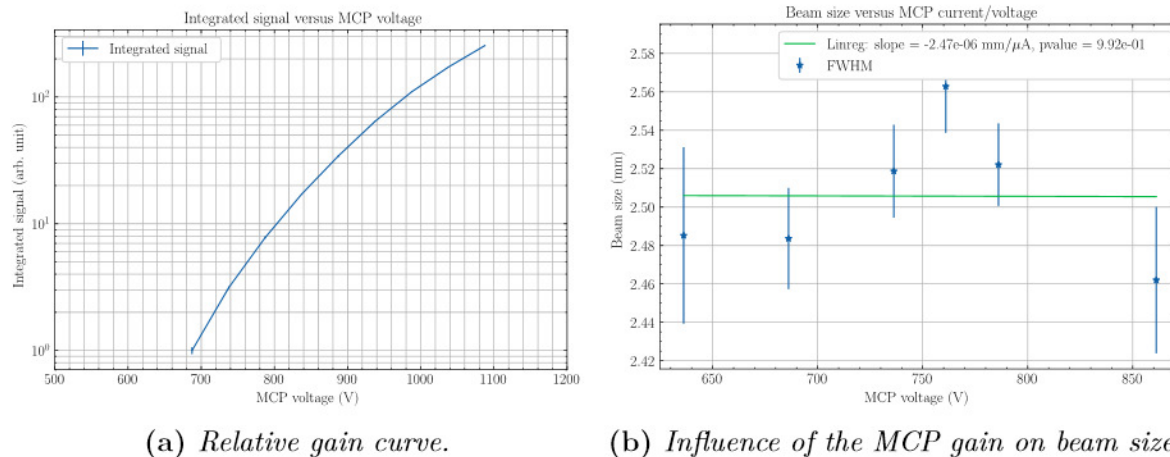


Figure 4.27 – Characterization of the MCPs.

## 4.7.7 Phosphorus screens

A phosphorus screen converts a charged particle into visible photons. The signal amplitude depends on the energy deposition of the particle in the phosphorus layer. In our case, the phosphorus screen is placed just after the MCP output.

### 4.7.7.1 Gain

The signal is proportional to the accelerating voltage between the MCP output and the phosphorus screen. Two screens have been tested during the beam tests: the P43 and the P46. Each screen has its intrinsic characteristics like the yield light, the emission wavelength and the decay time. Fig. 4.28 shows the linear response with the voltage for both screens. According to Hamamatsu, the lifetime of the phosphorus screen is much higher than the MCP one.

Another important thing to check is that there is no influence of the HV applied on the screen and the measured size and position. The influences have been tested for

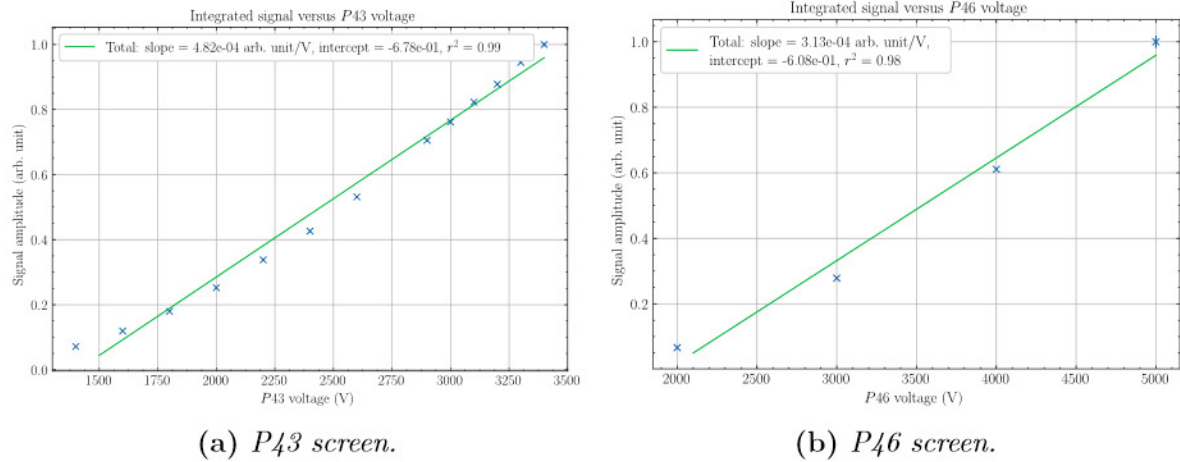


**Figure 4.28** – *Relative image intensity versus phosphorus screen voltage. Both show linear response.*

the two screens and are shown in Fig. 4.29. The beam size exposes small variations less than  $100 \mu\text{m}$ ; errors bars are important due to variations from pulse to pulse. So, the p-value is high and the possibility that the slope is null can not be rejected. Anyway, the variation of beam size remains below the ESS requirement.

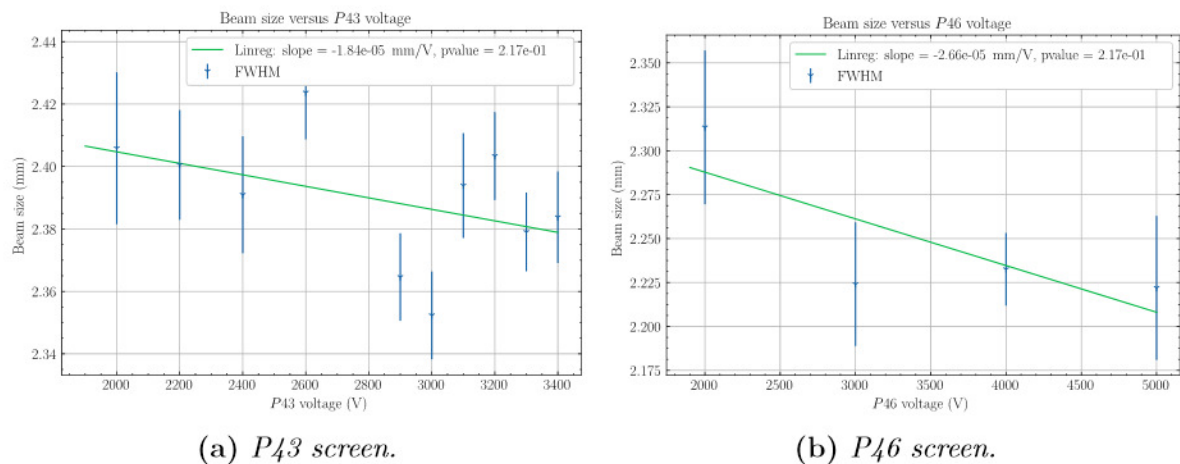


**Figure 4.29** – *Beam size versus phosphorus screen voltage. No significant change of the beam size has been observed.*

#### 4.7.7.2 Timing

The measurement of decay time has been performed by moving the camera trigger at small exposure times. The measurement is a bit more difficult for the fast screen. Indeed, the exposure time is quite similar to the decay time, moreover the delay and the jitter on the exposure time may affect the measurement. We measured for the PointGrey camera a delay of  $25 \mu\text{s}$  and a jitter on the exposure time greater than  $50 \mu\text{s}$ . The measurements for both screens are shown in 4.30.

As expected, the P43 is slow, thus if this screen is used for ESS then the total integration time on camera should be set to 10 ms and not strictly to 2.86 ms. This is not the case with the P46 screen.

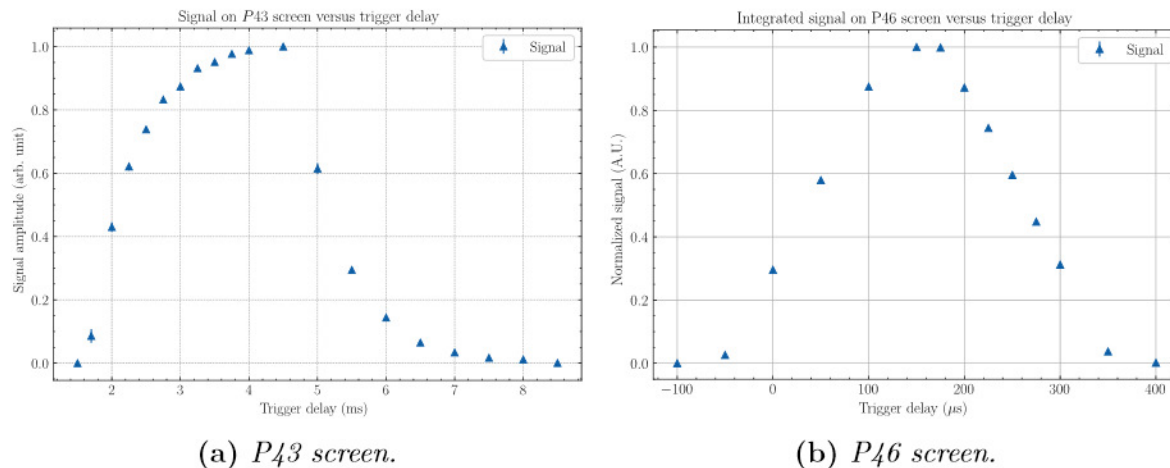


Figure 4.30 – Comparison of temporal response of both phosphorus screens.

#### 4.7.8 Extrapolation to ESS conditions with the strips IPM

One of the critical aspects of the project is the low number of charges expected per pulse. Therefore, the readout must have sufficient sensitivity to ensure the detection. As explained in the previous chapter, the bare strips are very robust against radiation and do not suffer of ageing effect. On the other hand, their sensitivities may be not high enough to be used at ESS.

Table 4.8 – The detection limit of the bare strips systems has been extrapolated from these values.

Run	Beam current (mA)	Charge per pulse linear strips (pC)	Charge per pulse gaussian strips (pC)
1	7.2	0.94	1.05
2	14.97	2.03	1.55
3	27.09	3.72	2.78

The charges on strips was measured by CARMEL for three beam intensities. The values are reported in the Table 4.8. A linear fit is performed on the three points. We assume that the intersection of the linear trend with abscisse axis gives the detection limit. However, this assumption does not take into account several factors. The measurements were performed with a short pulse duration of  $200 \mu\text{s}$ , therefore integration time was set to  $100 \mu\text{s}$ . At ESS the pulse will be 14.3 time more longer, therefore the integration noise is underestimated and the bandwidth of the system is neglected. The system response is also assumed to be linear.

The detection limits evaluated by this method is  $0.5 \text{ mA}$  for gaussian strips and  $1.9 \text{ mA}$  for linear strips. For the following, only the optimistic case ( $0.5 \text{ mA}$ ) is considered. From Bethe equation, the equivalent number of electron/ions pairs is computed with respect to the IPHI conditions measured during the tests:  $I_{beam} = 0.5 \text{ mA}$ ,  $T_{pulse} = 200 \mu\text{s}$  and  $p_{vacuum} = 1.1 \cdot 10^{-7} \text{ mbar}$ . In these conditions the IPHI pulse produces around  $10^5$  ionization byproducts. Therefore, even in the optimistic case, we may be able to measure the beam profile only at the beginning of the Spokes section (the expected signal is around  $10^5$  particles at  $90 \text{ MeV}$  in ESS conditions).




### 4.7.9 Extrapolation to ESS conditions with the optical IPM

Unlike the strips IPM, it is almost impossible to quantify the number of ionization particles without a full calibration of the MCPs. Hence, the extrapolation to ESS conditions is only done on the basis of the Bethe formula, by considering the beam parameters and vacuum conditions measured at IPHI. However a MCP does not suffer of any bandwidth limitation as long as it is not saturated. The exposure time on the camera has been set to 3 ms in order to get realistic electronic noise in the CMOS sensor. We supposed that the signal scales linearly with pressure. The beam current and the pulse duration were set to their lowest value possible at IPHI, respectively 0.7 mA and 50  $\mu$ s. The vacuum level was about  $4 \cdot 10^{-8}$  mbar and its composition was mainly water (conservative assumption), see section 4.6.1. Table 4.9 sums up the weighting factors of each parameter on the extrapolation. For instance, the signal at ESS for 315.8 MeV protons should be around twice of the one measured at IPHI. Finally, should an IPM be install at 2 GeV, the detection would be possible since the signal is 6% higher than the one measured at IPHI.

**Table 4.9** – *Extrapolation to ESS conditions from a real case during the second campaign. The IPHI current was below 0.7 mA with a pulse duration of 50  $\mu$ s. The pressure level was  $4 \cdot 10^{-8}$  mbar with mainly water vapors (conservative hypothesis). The scaling factor for each parameter is calculated from the nominal ESS beam conditions given in Table 2.1. The five first rows give the beam energy at an IPM location along the accelerator.*

ESS energy (MeV)	Bethe Bloch	Pressure	Gas composition	Intensity	Pulse length	Total Signal at IPHI
97.2	$\times 15.5$	$\times 40$	$\times 2.2$	$\div 89$	$\div 57$	$\times 0.27$
231.4	$\times 16.4$	$\times 40$	$\times 2.2$	$\div 89$	$\div 57$	$\times 0.28$
278.9	$\times 29.9$	$\times 40$	$\times 2.2$	$\div 89$	$\div 57$	$\times 0.52$
315.8	$\times 33.4$	$\times 40$	$\times 2.2$	$\div 89$	$\div 57$	$\times 0.58$
628.3	$\times 35.8$	$\times 40$	$\times 2.2$	$\div 89$	$\div 57$	$\times 0.62$
2000	$\times 61$	$\times 40$	$\times 2.2$	$\div 89$	$\div 57$	$\times 1.06$

Fig. 4.31 shows an example of a beam image and corresponding profile acquired in such conditions. The signal on the image looks as made of dots with several spots. Indeed, at this current some channels are no more hit every pulse. Each spot may be related to a hit on a single channel. As explained in section 4.6.3, at really low current the halo component dominates the signal, explaining this coarse profile.

At first glance, it seems to be possible to measure single profiles at nominal ESS conditions. However, this assumption is strongly dependent on the vacuum conditions. Neither the RGA, nor the gauges were calibrated, so the uncertainty may be relevant. On the other hand the assumption on the  composition is conservative.



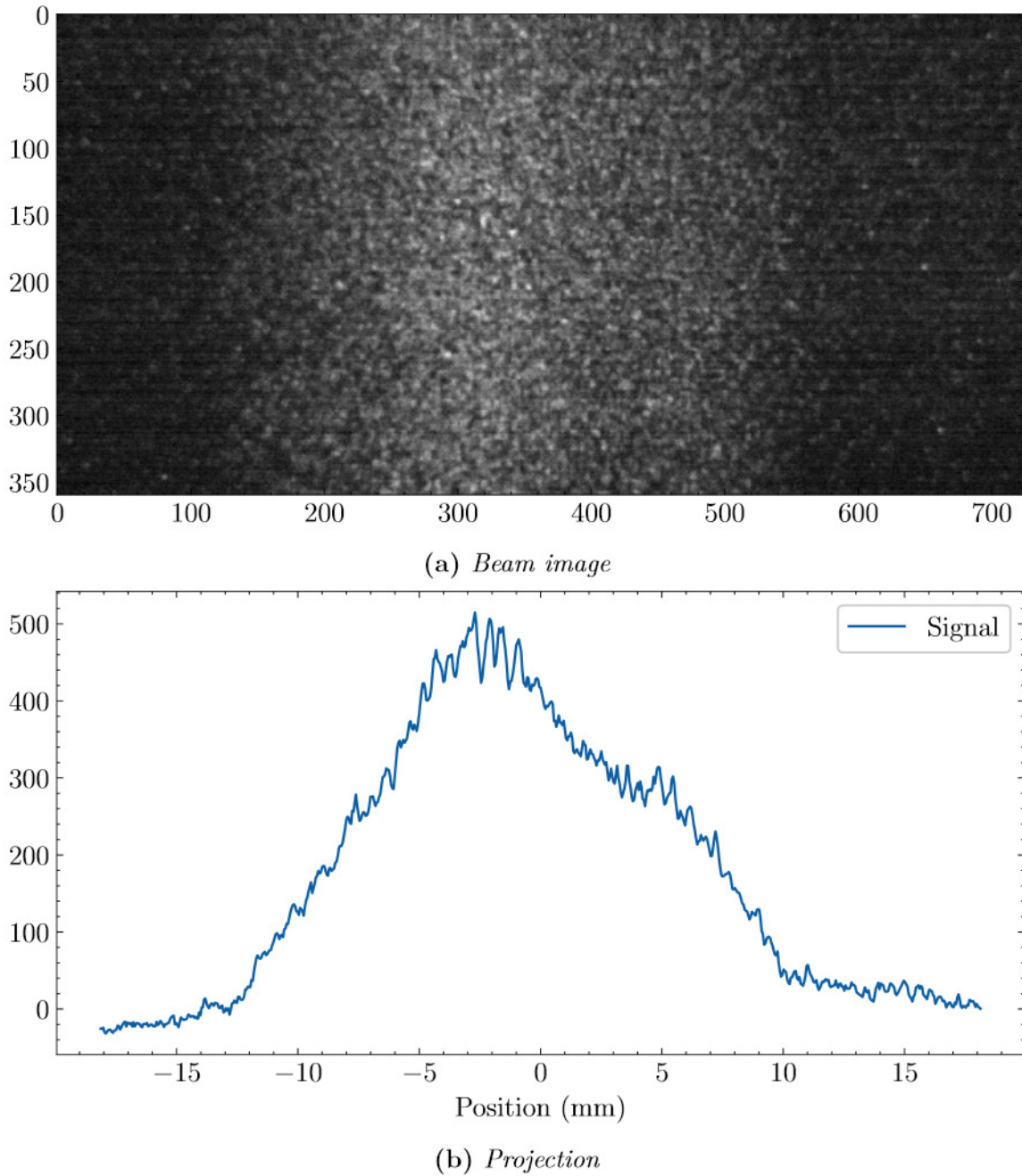
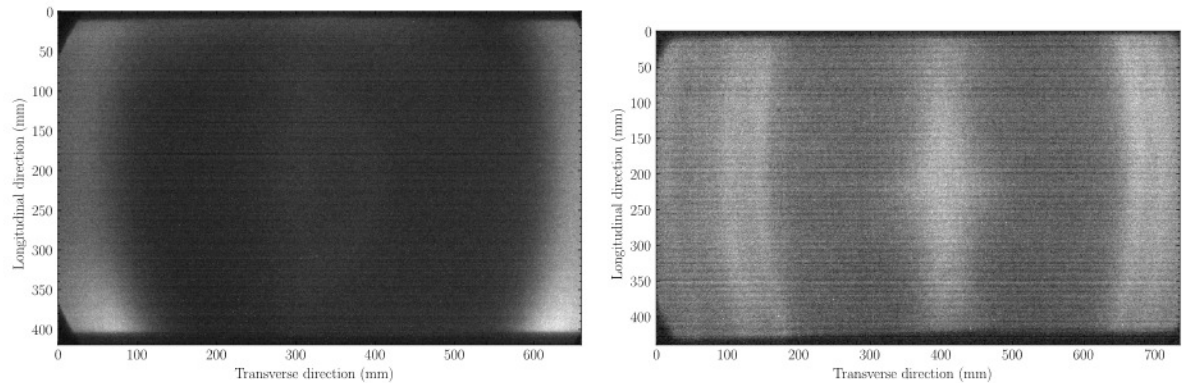


**Figure 4.31** – *Example of profile measurement at very low duty cycle: 0.7 mA, 50  $\mu$ s and  $4 \cdot 10^{-8}$  mbar.*

#### 4.7.10 Electron measurement with MCP

Unfortunately, we were not able to measure any profile in electron mode during the first and the second campaign. Typical pictures in the electron configuration are shown in Figure 4.32. One can see that the profiles cannot be measured correctly since a higher signal is observed on the sides of the MCPs. During the two test campaigns, comparable patterns were observed on the images in electron mode. The positions of these patterns is not related to the beam position and different beam tuning were performed without any impact on the images. The MCPs are in general a little less sensitive to electrons compared to ions at energies between 5 and 10 keV [32]. However,

during tests the signals on the camera were always much higher for electrons than for ions, without any modifications of the gain or the beam conditions. Hence, we suppose that the electron background is huge at IPHI. During tests, permanent magnets have been installed upstream and downstream of the test bench. No clearly improvements have been observed. We still do not know why there are so many electrons.



(a) Profile measurement attempt with electrons, Hamamatsu MCP.

(b) Profile measurement attempt with electrons, Photonis MCP.

**Figure 4.32** – Example of images in electron mode for both MCPs. Some patterns seem to be the same in the edges and middle of the images. The line in the middle is not correlated with the beam.

## 4.8 Summary

This chapter presented all the developments and tests that have been implemented to address the issues raised in Chapter 3, mainly concerning the choice of the most appropriate readout among three readout technologies. The objective was to experimentally prove the proper functioning of the IPM method under conditions close to those of ESS.

First, the feasibility of silicon detectors was verified at the IRMA ion implanter. The results show that detection is possible with dihydrogen ions of 15 keV. However, as soon as the energy is lower or the ions are heavier, the detection is compromised. That is why we have not chosen to continue in this direction.

The design of the prototypes and the test bench focused on the two remaining methods: strips and MCPs. The IPMs and the test bench have been designed to be very versatile, allowing multiple configurations to be tested. Particular attention was paid to system control and vacuum monitoring. The test bench was installed at IPHI, a 3 MeV proton accelerator, and two test campaigns were carried out.

The relevant conclusion from the tests shows that the use of a MCP is mandatory to detect signal at ESS conditions. Hence, the optical IPM is the preferred solution since it provides higher sensitivity with respect to the strips alone. A relative check of the electrical field uniformity has been performed on both asymmetric and symmetric configurations and with an optical IPM. The results from the tests show a good agreement with COMSOL simulations. Unfortunately, the reference measurements were not exploitable in the experimental conditions, but a good agreement between BPMs and IPMs gives more confidence on the measurements.

We validated our detectors and simulation models as much as experimental condition permitted, in spite of the instability of the machine and the unknown beam conditions. A complete characterization of the prototypes has been achieved.

From the lessons learned with the prototype, a final design of the cNPM is delivered, including few modifications from the prototype. This will be presented in the concluding chapter.

## 4.9 Bibliography

### References

- [1] Jacques Chaumont et al. “A medium energy facility for variable temperature implantation and analysis”. In: *Nuclear Instruments and Methods in Physics Research* 189.1 (1981), pp. 193–198. ISSN: 0167-5087. DOI: [https://doi.org/10.1016/0029-554X\(81\)90145-2](https://doi.org/10.1016/0029-554X(81)90145-2) (cit. on p. 86).
- [2] P. Paris et al. “Description and performance of the isocele 2 separator”. In: *Nuclear Instruments and Methods in Physics Research* 186.1 (1981), pp. 91–98. DOI: [https://doi.org/10.1016/0029-554X\(81\)90892-2](https://doi.org/10.1016/0029-554X(81)90892-2) (cit. on p. 86).
- [3] V Kraus et al. “FITPix — fast interface for Timepix pixel detectors”. In: *Journal of Instrumentation* 6.01 (2011), pp. C01079–C01079. DOI: [doi:10.1088/1748-0221/6/01/c01079](https://doi.org/10.1088/1748-0221/6/01/c01079) (cit. on p. 88).
- [4] *ADVACAM*. URL: <http://advacam.com/> (visited on 05/17/2019) (cit. on p. 88).
- [5] EMVA. “Emva Standard 1288 Release 3.0”. In: (2010). URL: <https://www.emva.org/wp-content/uploads/EMVA1288-3.0.pdf> (cit. on p. 91).
- [6] *Blackfly 2.3 MP Mono GigE PoE (Sony Pregius IMX249)*. PtGrey. 2019. URL: <https://www.flir.com/products/blackfly-gige/?model=BFLY-PGE-23S6M-C> (visited on 05/06/2019) (cit. on p. 91).
- [7] David Etasse et al. *CARte Acquisition Multivoies ELectromètre*. 2013. URL: <http://faster.in2p3.fr/index.php/introduction/hardware/daughter-boards/61-caramel> (cit. on p. 93).
- [8] David Etasse et al. *FASTER, a modular digital acquisition system based upon a synchronized tree model*. 2013. URL: <http://faster.in2p3.fr/index.php/about-faster> (cit. on p. 93).
- [9] *DDC316, 16-Channel Current-Input 16-Bit Analog-to-Digital Converter*. 2008. URL: <http://www.ti.com/product/DDC316> (cit. on p. 93).
- [10] T. Chaventré and D. Cussol. *ROOT Histogram Builder*. 2012. URL: <http://faster.in2p3.fr/index.php/rhb> (cit. on p. 93).
- [11] *iseg, high voltage power supplies*. iseg Spezialelektronik GmbH. 2. URL: <https://iseg-hv.com/en> (cit. on p. 93).
- [12] *EPICS, a set of Open Source software tools, libraries and applications developed collaboratively and used worldwide to create distributed soft real-time control systems for scientific instruments such as a particle accelerators, telescopes and other large scientific experiments*. EPICS Collaboration. 2019. URL: <https://epics-controls.org/> (visited on 11/22/2018) (cit. on p. 94).
- [13] Mark Rivers. *areaDetector, an application for controlling area (2-D) detectors, including CCDs, pixel array detectors, and online imaging plates*. 2019. URL: <http://cars9.uchicago.edu/software/epics/areaDetector.html> (visited on 11/22/2018) (cit. on p. 95).
- [14] The HDF Group. *Hierarchical data format version 5*. 2000-2010. URL: <http://www.hdfgroup.org/HDF5> (cit. on p. 95).



- [15] Dirk Zimoch. *StreamDevice, a generic EPICS device support for devices with a "byte stream" based communication interface*. 2019. URL: <https://paulscherrerinstitute.github.io/StreamDevice/> (visited on 11/22/2018) (cit. on p. 95).
- [16] Murali Shankar. *EPICS Archiver Appliance, an implementation of an archiver for EPICS control systems that aims to archive millions of PVs*. 2019. URL: [https://slacmshankar.github.io/epicsarchiver\\_docs/index.html](https://slacmshankar.github.io/epicsarchiver_docs/index.html) (visited on 11/22/2018) (cit. on p. 95).
- [17] Saint-Gobin. *Crystal Scintillation Materials*. 2019. URL: <https://www.crystals.saint-gobain.com/products/crystal-scintillation-materials> (visited on 05/22/2019) (cit. on p. 97).
- [18] Crytur. *Scintillation and Laser materials*. 2019. URL: <https://www.crytur.cz/materials/> (visited on 05/22/2019) (cit. on p. 97).
- [19] *Status report on the saclay high-intensity proton injector project (IPHI)*. (Vienna, Austria). Geneva, Switzerland: JACoW Publishing, 2000 (cit. on p. 97).
- [20] Raphael Gobin et al. "High Intensity Beam Production at CEA/Saclay For The IPHI Project". en-us. In: *Proceedings of the 22nd Int. Workshop on ECR Ion Sources ECRIS2016* (2016). DOI: doi:10.18429/jacow-ecris2016-wepp01 (cit. on p. 97).
- [21] F. Senée et al. "Increase of IPHI Beam Power at CEA Saclay". In: *Proc. 9th International Particle Accelerator Conference (IPAC'18)*. (Vancouver, BC, Canada). International Particle Accelerator Conference 9. Geneva, Switzerland: JACoW Publishing, June 2018, pp. 694–696. DOI: doi:10.18429/JACoW-IPAC2018-TUPAF016 (cit. on p. 98).
- [22] S. van der Walt, S. C. Colbert, and G. Varoquaux. "The NumPy Array: A Structure for Efficient Numerical Computation". In: *Computing in Science Engineering* 13.2 (Mar. 2011), pp. 22–30. ISSN: 1521-9615. DOI: 10.1109/MCSE.2011.37 (cit. on p. 99).
- [23] Eric Jones, Travis Oliphant, Pearu Peterson, et al. *SciPy: Open source scientific tools for Python*. 2019. URL: <http://www.scipy.org/> (cit. on p. 99).
- [24] J. D. Hunter. "Matplotlib: A 2D Graphics Environment". In: *Computing in Science Engineering* 9.3 (May 2007), pp. 90–95. ISSN: 1521-9615. DOI: 10.1109/MCSE.2007.55 (cit. on p. 99).
- [25] Charles Sidney Burrus. *Fast Fourier Transforms*. 2012 (cit. on p. 99).
- [26] Charles Sidney Burrus, Ramesh Gopinath, and Haitao Guo. *Introduction to Wavelets and Wavelet Transforms: A Primer*. 1997 (cit. on p. 100).
- [27] Adhemar Bultheel and Daan Huybrechs. "Wavelets with applications in signal and image processing". In: (2014). URL: <http://citeseerx.ist.psu.edu/viewdoc/download?doi=10.1.1.724.1544&rep=rep1&type=pdf> (cit. on p. 100).
- [28] Rene Brun and Fons Rademakers. "ROOT — An object oriented data analysis framework". In: *Nuclear Instruments and Methods in Physics Research Section A: Accelerators, Spectrometers, Detectors and Associated Equipment* 389.1-2 (Apr. 1997), pp. 81–86. DOI: 10.1016/s0168-9002(97)00048-x (cit. on p. 100).

- [29] I. Antcheva et al. “ROOT — A C++ framework for petabyte data storage, statistical analysis and visualization”. In: *Computer Physics Communications* 180.12 (2009), pp. 2499–2512. DOI: <https://doi.org/10.1016/j.cpc.2009.08.005> (cit. on p. 100).
- [30] Richard Szeliski. *Computer vision : algorithms and applications*. Springer, 2010. ISBN: 1848829345 (cit. on p. 101).
- [31] G. Bradski. “The OpenCV Library”. In: *Dr. Dobb’s Journal of Software Tools* (2000) (cit. on p. 101).
- [32] Joseph Ladislav Wiza. “Microchannel plate detectors”. In: *Nuclear Instruments and Methods* 162.1-3 (June 1979), pp. 587–601. DOI: 10.1016/0029-554x(79)90734-1 (cit. on p. 116).



# Chapter 5

## Conclusion and outlook





## Contents

---

<b>The cold NPM project for ESS . . . . .</b>	<b>125</b>
Preliminary design review . . . . .	125
Prototypes and test bench development . . . . .	126
Beam tests at IPHI . . . . .	126
<b>Ongoing works and final design . . . . .</b>	<b>127</b>
Background signal estimation . . . . .	127
MCP calibration . . . . .	128
Remote acquisition system . . . . .	128
Final IPM design and production . . . . .	129
<b>Bibliography . . . . .</b>	<b>133</b>

---

## The cold NPM project for ESS

Intense neutron sources are very difficult to achieve. Historically, nuclear reactors have been widely used as intense neutron sources. In Europe the situation is quite critical because most of research reactors will close within the next decade. In this context, the European Spallation Source is being built close to Lund, in Sweden. ESS will push back the limits of existing spallation sources by means of a high and powerful linear accelerator. To ensure the safety of the machine during the commissioning and operations, many diagnostics are foreseen along the accelerator.

This thesis describes the design of one of these diagnostics: the Ionization Profile Monitor (IPM). IPMs are based on the ionization of the residual gas. This is one of the most effective methods, but it is nevertheless quite complex to implement since an IPM operates in vacuum. The first IPMs dated back to the 1960s but the method has been improved significantly with progress in detector, electronics and computer science. The IPM is now mature and used in several installations. In this thesis, the existing methods have been reviewed in order to find the best solution that may match with the ESS requirements. This was first achieved by simulations and, in a second phase, by building and testing prototypes.

### Preliminary design review

I started my PhD thesis on October 1<sup>st</sup> 2016, 5 months after the kick-off meeting and 4 months before the Preliminary Design Review (PDR). The NPM project for the cold accelerator part was identified as a difficult task with no guaranty about the feasibility of such a monitor, therefore a GoNoGo gate was set for the PDR. In other words, green light to begin the PDR activities would only be given if preliminary studies would receive positive signs to the following challenges:

- Very low counting rates: there are low due to firstly the weak residual gas pressure ( $10^{-9}$  mbar) and secondly due to the low ionization cross-sections that decrease at high energy (90 MeV to 2 GeV). Both negative effects have to be compensated by high sensitivity and low noise readouts. Once identified, they have to be assessed to cope with these conditions.

- Electric field uniformity: its uniformity must be particularly good to avoid "mirage effects", i.e. forcing the ionization by-products to drift in the parallel direction of the electric field. To achieve such a goal, spaces between IPMs are required. Unfortunately, the vacuum chamber geometry was already frozen (in May 2016, just after the Kick-Off) with small spaces, which would not ease the work.
- Space Charge (SC): one of the ESS requirements is to measure the profile with a 10% width accuracy. The large SC of ESS is due to the electric field of the proton beam which generates a huge electric field proportional to its energy and its intensity. The low energy ionization by-products are particularly sensitive to this electric field. They are deviated resulting in an enlargement of the measured beam profile. This effect could not be estimated by simple calculations and sophisticated simulations were developed to solve this issue.

My first urgent tasks when I joined the NPM team at Saclay were to estimate counting rates and to participate to the readout choice to check compliance to the requested low sensitivity. The PDR took place at ESS Lund on January 31<sup>st</sup> 2017, where we presented our preliminary results giving confidence on the IPM feasibility. The GoNoGo gate was passed successfully, opening to the next phase of the project. In this phase, we needed to demonstrate through prototype design, beam tests and calculations that IPM fulfilled the ESS requirements. We also needed to provide a final solution for the manufacturing of the IPMs.

## Prototypes and test bench development

An IPM must be self-consistent on its support, here a flange CF200. This imposes to have all the HV connectors, the grounding, the readout system attached on it meaning that once the IPM is integrated, it can be inserted into the test bench vacuum CF200 aperture, like a drawer. Originally, 3 readout types were considered. The Timepix option had to be discarded due to incompatibility with ion detection. Finally two readouts were selected: a conductive strips plane and a MCP read by a CMOS camera. Two reference systems were also installed, one based on fluorescence and an interceptive screen with 3 solid scintillators. The bench was made of two parts; the first had similar dimensions of the ESS LWU, with 2 IPM locations and another one, on the second part. The strips IPM could be polarized in asymmetric mode, whilst MCP IPM could be operated on both modes. All along the integration, we encountered many vacuum problems, which were solved by baking. We currently reached  $2\text{-}3 \cdot 10^{-7}$  mbar. We also faced sparks when reaching 30 kV with high voltage connectors weakly insulated and connection boxes. In parallel, I greatly improved the uniformity of the IPM electric field by tuning the resistor bridge, but also by inserting a disk in the vacuum chamber, with a circular aperture as large as the beam pipe. This is mandatory to avoid the cross-interaction between both IPM electric field tilted at  $90^\circ$  with respect to each other. I also implemented the software for several applications control systems (HV, pressure probes...) using the EPICS framework.

## Beam tests at IPHI

We installed the test bench on mid-2017 at IPHI. The first beam was delivered and there was no diagnostic working on IPHI, only an ACCT located upstream of

our bench and a Faraday cup working as beam dump. Moreover the commissioning of IPHI was not done for the higher energy part (downstream the RFQ, at 3 MeV). Before to obtaining a beam profile, we needed two weeks of tuning with a beam dynamic physicist in order to adjust the deviation dipole, the correction steerers and the quadrupoles. However the beam presented a strange behavior showing a position oscillation. Charging effects on our detectors were suspected by all the experts. A couple days later, the BPM finally observed the same position oscillations confirming our measurements. IPHI has not yet an explanation of this effect. Our IPMs had an important role in the characterization of this effect.

We also discovered that the beam presents 2 components: a mix of a core and narrow beam at high beam intensity and a larger component at low intensity. Another concern was to make systematic studies due to difficulties on the reproducibility of the beam. Nevertheless, it was useful to have such versatile facility where we were able to regain the expected MCP behavior. Many measurements were done, allowing investigating many parameters and preparing the second beam tests in September 2018.

The goal of the second test was to focus on the profile measurement feasibility in nominal ESS conditions, in ion mode since simulations already shown that electron detection could not be used for profile purposes. During this last campaign, we finally worked in such beam conditions, and even worse than the ESS ones. These results are summarized in the Table 4.9 demonstrating the feasibility of the measurement of the beam profile for each pulse beam with ESS nominal conditions.

## Ongoing work and final design

The following sections present current actions for the design of the final detectors as well as the more distant perspectives.

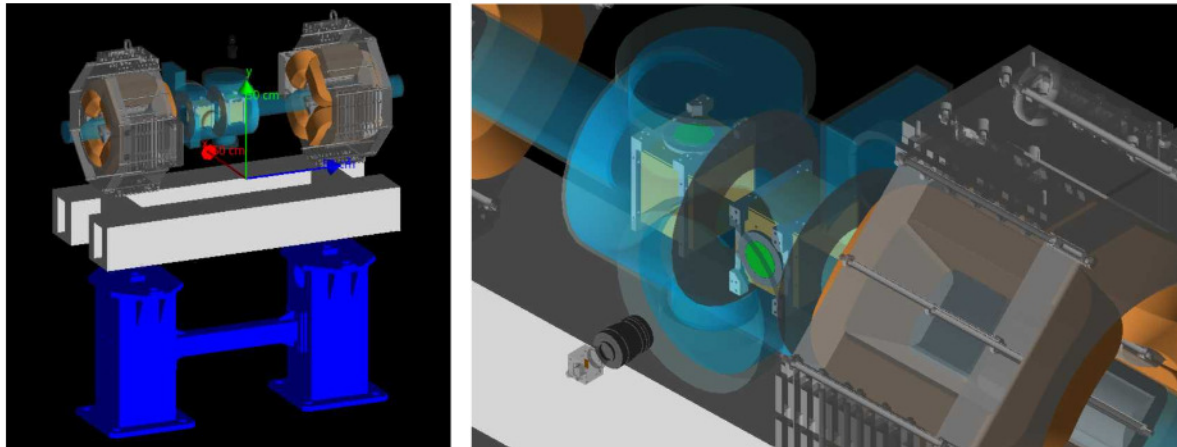
### Background signal estimation

During the project reviews we were asked to study the influence of background noise on the IPM readouts. This is a complex task because it requires enough background particle information and a realistic geometry.

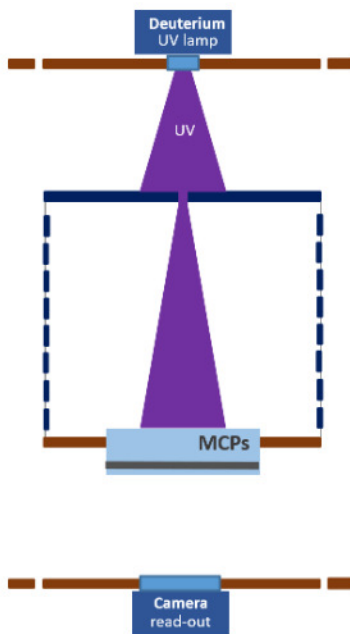
A Geant4 simulation has been prepared in order to answer this request. The simulation includes a mixed geometry including shapes made from primitive geometry (LWU, support, MCP) and complex elements imported from CAD files (IPM, camera, magnet). Fig. 5.1 shows the implemented geometry of the LWU with the two IPMs, the quadrupoles and the cameras with their sensors. The choice of the physics list can be quickly modified using the predefined lists in Geant4. The elements to be studied use the Sensitive Detector mechanism enabling to save information about the particles passing through them. As the data flow is important, the simulation results are saved using the ROOT interface provided in Geant4. The simulation uses the new multithreading features of latest versions of Geant4 and an OpenMPI layer has been added [1, 2]. The simulation code is completely ready and the background particle information that was only made available very recently needs only to be included to launch the simulations.

I hope that this work will continue and lead to results that may provide additional knowledge.



(a) *The LWU and two quadrupoles.*(b) *Zoom on the two IPMs.***Figure 5.1** – *The geometry implemented in Geant4.*

## MCP calibration

**Figure 5.2** – *The calibration of the MCP is done with a VUV lamp.*

experiment.

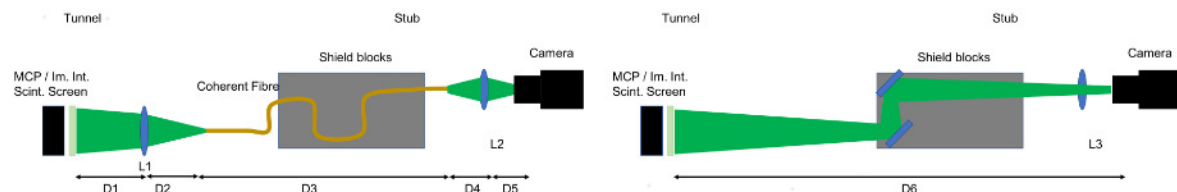
## Remote acquisition system

In the case where the radiation background should shorten the MCP lifetime down to a year, it would be necessary to set a camera at remote distance in a shielded area. Two solutions are investigated to transport the image over up to 10 m, where the camera can be shielded in the bottom of the nearby Stub. The solution to get

MCPs are mandatory to measure a profile with IPM in the ESS conditions. Unfortunately, these devices are sensitive to ageing effects. The gain will decrease over time in the impacted areas by ions. Since the ESS beam will be stable in position, the MCP region in front of the beam will be more affected.

Therefore, at some point the profile measurement will be no longer reliable. To overcome this phenomenon it is necessary to calibrate the MCP regularly, i.e. perform a gain mapping and correct the profile by a software adjustment. This requires an uniform and stable source that routinely irradiates the MCP. The most common method relies on a VUV source [3]. MCPs become sensitive to the photoelectric effect for wavelengths shorter than 200 nm. The most basic VUV sources are deuterium discharge lamps that have broadband emission with a peaks at 160 nm [4, 5]. It is also possible to generate VUV with excimer lasers or by using high order harmonic generation. Thermoionic emission was discarded due to the requirements imposed by the superconducting cavities. We are also considering the use of Electron Generator Arrays [6, 7]. The calibration is currently being tested on the IPM test bench and Fig. 5.2 shows the principle of the

a camera detecting single events, i.e. an ion hitting the MCP is been studied at ESS. The document presents two alternative imaging systems: the first one using a fiberscope and lenses is sketched on Fig. 5.3a, while the other one based on 2 mirrors and an objective lens can be seen on Fig. 5.3b.



(a) *The profile image is transported through an optical fiber bundle.* (b) *The profile image is reflected on mirrors.*

**Figure 5.3** – *Two solutions are foreseen for remote acquisitions of the profile measurement [8].*

Using a first order evaluation of the system transmission, one can start by selecting the focal lens required to make conjugate images. For the lens L1, the magnifications for the MCP is set, so as the geometrical aperture coupling light into the fibre.

The geometrical transmission for 0.5 numerical aperture of the fiberscope is about  $3 \cdot 10^{-5}$  while it is a factor 4 below for the second system. Such an attenuation encourages to purchase stacked double MCP for increasing the output light.

The fiber attenuation is an important property to take into account. For instance, for silica fibers, this can be as low as a few dB/km. We intent to use plastic coherent fibers. The material used is PMMA. This material is rather cheap, and it presents good optical quality and rather good transmission, typically 0.5 dB/m at 500 nm. However, a full characterization of the system with the selected fiber will have to be done in order to prove and demonstrate the performance of the system. Lenses transmissions can be close to 100% with anti-reflection coating.

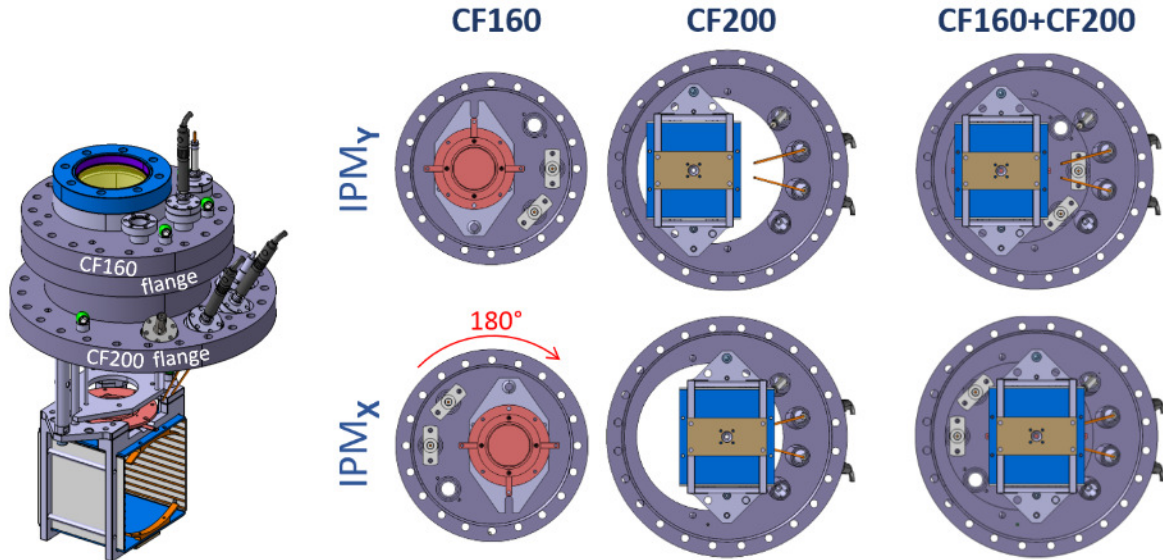
## Final IPM design and production

The final IPM will use double stage MCP polarized in symmetric HV configuration. IPMs will probably be ready before the accelerator reaches nominal conditions. The double stage MCPs will allow measurements during the accelerator commissioning. The use of a double stage MCP reduces the maximal resolution achievable but this reduction is less important that the one induced by the remote acquisition system. The MCP with a strips readout provides the best performances in term of sensitivity and speed but needs a specifically designed readout electronics. Whereas an optical MCP exposes decent performances with a high resolution and the acquisition relies only on COTS cameras. At the end the optical solution has been chosen. In any case the design of IPMs allows to easily upgrade the readout for future improvements. The HV symmetric setup provides a very good electric field uniformity with only field correctors. This configuration also reduces the maximum potential to apply to electrode.

The final IPMs will be produced following the ESS requirements for the superconducting cavities meaning that the IPMs will be assembled within an ISO-5 clean room environment.



During the tests at IPHI, we used a simple CF200 flange to support the IPM (Fig. 4.5). For the manufacturing of the IPM, we thought that two independent flanges CF200 and CF160 (Fig. 5.4) will ease the assembling process and the maintenance in clean room environment. This later configuration presents different advantages.



(a) A 3D drawing of the new design. (b) The new design allow to remove MCP easily and is independent to the IPM direction.

Figure 5.4 – The new IPM design [9].

Once the complete IPM set is mounted on the LWU, alignment can be done by measuring all sight pods on the CF200. Then, if the MCP has to be removed (unscrew the CF160), the IPM cage linked to the CF200 stays fixed. The MCP can be changed but no alignment is necessary. This new configuration is compliant with a better reliability of the IPM since the MCP change may be done quickly, with no impact on alignment. The IPMs X and Y are similar: while X is centered on the CF200 LWU viewport, Y is shifted by 36 mm to its CF200 axis. The trick for mounting both IPMs, is to rotate the CF160 by 180° with respect to the CF200 flange. This is of great interest for manufacturing purposes.

For assembling the whole IPM, it is more convenient to prepare first the CF200 and all its belonging items, and then the CF160 ones. It allows minimizing the MCP in oxygen atmosphere. Furthermore, the set made of CF160 and MCP holder is light with a small lever arm easy to manipulate.

The IPMs will be delivered by pair and the first pairs are expected to be delivered to ESS at the middle of 2020.

Let's finish this manuscript from a perspective that goes beyond the ESS project. IPHI is a unique machine, but has suffered delays in the past due to unfortunate circumstances. Over the last three years, a new dynamic is underway to fully exploit the accelerator capabilities. Today, IPHI is the first step of a new national compact neutron source: SONATE [10]. As stated in the first chapter, the LLB is closing its last research reactors this year. Some estimates show that the availability of neutrons at the national level will fall by more than 90% within the next 10 years.

During the tests, the versatility of IPHI greatly helped to characterize the IPMs.

However, some tests were limited by a lack of beam information during operation. Indeed, only two types of diagnosis were available: BPMs and BCMs. IPMs are a very interesting solution for IPHI because they measure the size and the position in a non-intrusive way. A close collaboration has started in order to provide to IPHI an IPM system that fulfill the present and future needs. This new project will greatly benefit from the studies and experiences presented in this thesis.





## Bibliography

### References

- [1] J. Allison et al. “Geant4 developments and applications”. In: *IEEE Transactions on Nuclear Science* 53.1 (Feb. 2006), pp. 270–278. DOI: 10.1109/tns.2006.869826 (cit. on p. 127).
- [2] A. Dotti et al. “Extending Geant4 Parallelism with external libraries (MPI, TBB) and its use on HPC resources”. In: *2015 IEEE Nuclear Science Symposium and Medical Imaging Conference (NSS/MIC)*. Oct. 2015, pp. 1–2. DOI: 10.1109/NSSMIC.2015.7581867 (cit. on p. 127).
- [3] T. Giacomini et al. “Ionization Profile Monitors - IPM @ GSI”. In: *Proc. DIPAC2011*. (Hamburg, Germany). 2011, pp. 419–421. URL: <http://accelconf.web.cern.ch/AccelConf/DIPAC2011/papers/tupd51.pdf> (cit. on p. 128).
- [4] *Electron Generator Arrays*. Deuterium lamps. 2019. URL: <https://www.hamamatsu.com/eu/en/product/light-and-radiation-sources/lamp/deuterium-lamp/index.html> (visited on 07/01/2019) (cit. on p. 128).
- [5] *Deuterium Lamps*. Newport. 2019. URL: <https://www.newport.com/f/deuterium-lamps> (visited on 07/01/2019) (cit. on p. 128).
- [6] K. Satou et al. “A Prototype of Residual Gas Ionization Profile Monitor for J-PARC RCS”. In: *Proc. EPAC2006*. (Edinburgh, Scotland). 2006, pp. 1163–1165. URL: <http://accelconf.web.cern.ch/AccelConf/e06/PAPERS/TUPCH065.PDF> (cit. on p. 128).
- [7] *Electron Generator Arrays*. Photonis. 2019. URL: <https://www.photonis.com/products/electron-generator-arrays> (visited on 07/01/2019) (cit. on p. 128).
- [8] Cyrille Thomas. *NPM CDR, Optical Systems for the NPM Long Distance Imaging*. Tech. rep. 2019 (cit. on p. 129).
- [9] Jacques Marroncle. *NPM CDR, Towards cNPM manufacturing*. Tech. rep. 2019 (cit. on p. 130).
- [10] A Marchix et al. “Saclay Compact Accelerator-driven Neutron Sources (SCANS)”. In: *Journal of Physics: Conference Series* 1046 (June 2018), p. 012009. DOI: 10.1088/1742-6596/1046/1/012009. URL: <https://doi.org/10.1088/1742-6596/1046/1/012009> (cit. on p. 130).



# Acronyms

- ACCT** AC Current Transformer. 26
- BCM** Beam Current Monitor. 25
- BEM** Boundary Element Method. 53, 54
- BIF** Beam Induced Fluorescence. 29
- BLM** Beam Loss Monitor. 26
- BPM** Beam Position Monitor. 99, 102, 103, 117
- CA** Channel Access. 94
- CAD** Computer-Aided Design. 52
- CARAMEL** CARte Acquisition Multivoies ELectromètre. 93
- CEA** Commissariat à l’Energie Atomique et aux énergies alternatives. 17
- CERN** Organisation européenne pour la recherche nucléaire. 31
- CF** ConFlat Flange. 40
- CMOS** Complementary Metal Oxide Semiconductor. 91, 96, 115
- CNRS** Centre National de la Recherche Scientifique. 17
- CS** Control System. 94
- CSNS** China Spallation Neutron Source. 9
- CT** Current Transformer. 25
- DCCT** Direct-Current Current Transformer. 26
- DTL** Drift Tube Linac. 20
- ECR** Electron Cyclotron Resonance. 18
- EPICS** Experimental Physics and Industrial Control System. 94
- ESFRI** European Strategy Forum on Research Infrastructures. 10
- ESS** European Spallation Source. 39, 40, 42, 43, 45, 52, 55, 61, 64–69, 76, 86–88, 91, 94–96, 98, 99, 105, 106, 108, 111, 113, 115, 117
- FASTER** Fast Acquisition System for nuclEar Research. 93
- FC** Faraday Cup. 25
- FCT** Fast Current Transformer. 26
- FEM** Finite Element Method. 53, 54
- FFT** Fast Fourier Transform. 99



- FPM** Fluorescence Profile Monitor. 29, 40, 96, 97, 102
- HDF** Hierarchical Data Format. 95, 99
- HEBT** High Energy Beam Transport. 21
- HV** High Voltage. 48, 49
- icBLM** ionization chamber Beam Loss Monitor. 27
- II** Image Intensifier. 96
- ILL** Institut Laue-Langevin. 8
- INFN** Istituto Nazionale Fisica Nucleare. 19
- IPHI** Injecteur de Protons à Haute Intensité. 97–99, 102, 105, 106, 109, 111, 112, 115, 117
- IPM** Ionization Profile Monitor. 40–45, 47–49, 52–55, 57–63, 71, 74, 76, 86, 88–91, 93–96, 99, 101, 103, 107–112, 115, 117
- IRFU** Institut de Recherche sur les lois Fondamentales de l’Univers. 17
- JSNS** Japanese Spallation Neutron Source. 9
- LEBT** Low Energy Beam Transport. 18
- LHC** Large Hadron Collider. 27
- linac** Linear Accelerator. 28
- LLB** Laboratoire Léon Brillouin. 8
- LWU** Linac Warm Unit. 40, 47, 58, 59, 66, 95, 108
- MCP** Micro-Channel Plate or Multi-Channel Plate. 74–76, 91–94, 97, 99, 104, 106, 110–112, 115–117
- MEBT** Medium Energy Beam Transport. 20
- MPS** Machine Protection System. 27
- nBLM** neutron Beam Loss Monitor. 27, 98
- NN** Nearest Neighbors. 56, 57
- NPM** Non-invasive Profile Monitor. 39–41, 96
- ODE** Ordinary Differential Equation. 55
- OPI** OPerator Interface. 94
- PCB** Printed Board Circuit. 86, 89, 92
- PDE** Partial Differential Equation. 50
- PS** Proton Synchrotron. 31
- PSI** Paul Scherrer Institute. 9
- PV** Process Variable. 94
- RBF** Radial Basis Function. 56, 57
- RFQ** Radio Frequency Quadrupole. 97

**SANS** Small Angle Neutron Scattering. 6

**SNS** Spallation Neutron Source. 9

**softIOC** software Input/Output Controller. 94

**WS** Wire Scanner. 28, 39, 40



# List of Figures

1.1	Neutron and X-ray radiography of a dagger sheath . . . . .	6
1.2	Ranges of distances and times of existing neutron scattering techniques . . . . .	7
1.3	Schematic view of the spallation process . . . . .	9
1.4	Status and outlook of neutron sources (from the ESFRI report) . . . . .	10
1.4a	Evolution of thermal neutron sources from the neutron discovery to a near future. . . . .	10
1.4b	Evolution of the European neutron facilities over the next 15 years. . . . .	10
2.1	ESS neutron source brightness compared to others existing neutron sources . . . . .	16
2.2	A simplified representation of the ESS linac . . . . .	17
2.3	The ESS proton source and the LETB . . . . .	18
2.4	An RFQ structure bunches, focuses and accelerates charged particles by means of four poles that modulate the RF wave. . . . .	19
2.4a	The four copper vanes of a RFQ . . . . .	19
2.4b	Cut view of the transverse field. . . . .	19
2.4c	Longitudinal modulation leading to an accelerating field . . . . .	19
2.5	Building blocks of the MEBT . . . . .	20
2.6	A 3D drawing of a DTL tank . . . . .	20
2.7	ESS medium beta elliptical cavities cryomodule . . . . .	21
2.8	The Tungsten wheel target inside the monolith structure . . . . .	22
2.9	Scheme of the 15 neutron instruments that will be available at the start of the user program. . . . .	24
2.10	A simplified schema of a passive current transformer . . . . .	25
2.11	A 3d drawing of the ESS button BPMs designed at DESY . . . . .	26
2.12	The ionization chamber of an icBLM . . . . .	27
2.13	Scheme of a BIF setup used at GSI. . . . .	30
2.14	Three different implementations of IPMs on three different accelerators . . . . .	32
2.14a	One of the IPM at IFMIF . . . . .	32
2.14b	One of the IPM at GSI . . . . .	32
2.14c	The future IPM for the PS . . . . .	32
3.1	The LWU vessel located between two quadrupole magnets and two cryomodules . . . . .	41
3.2	Visual explanation of how an IPM works . . . . .	41
3.3	Typical mass stopping power plot a proton . . . . .	44
3.4	Expected number of ionization by-products per centimeter at ESS nominal conditions according to the Bethe equation . . . . .	46



3.5	The LWU geometry implemented in Molflow+ . . . . .	47
3.6	Simulated profile pressure in the center of IPMs. . . . .	48
3.7	Non-uniformities leading to mirage effects on the profile measurement . . . . .	48
3.8	A drawing of LWU and its implementation in COMSOL . . . . .	52
3.9	3D Mesh elements included in the COMSOL software . . . . .	52
3.10	Comparison between BEM and FEM for two different IPM configurations . . . . .	53
3.10a	Configuration 1 solved with BEM. . . . .	53
3.10b	Configuration 1 solved with FEM. . . . .	53
3.10c	Configuration 2 solved with BEM. . . . .	53
3.10d	Configuration 2 solved with FEM. . . . .	53
3.11	Interpolations and integrations are critical steps of the particle tracking . . . . .	57
3.11a	Interpolations on a randomly sampled sinus functions. The RBF interpolation gives good accuracy compared to the others two interpolations (NN and Shepard). . . . .	57
3.11b	Integrations of motion and position in a constant electromagnetic field. Euler (and RK) gains numerical energy whereas the Boris method shows excellent accuracy over time. . . . .	57
3.12	Transverse comparison between symmetric and asymmetric configuration . . . . .	58
3.12a	Symmetric configuration. . . . .	58
3.12b	Asymmetric configuration. . . . .	58
3.13	Influence of shielding disks on the IPM electric field . . . . .	59
3.13a	Electric field without disk . . . . .	59
3.13b	Electric field with disks . . . . .	59
3.14	IPM geometry in COMSOL . . . . .	60
3.15	Resistor chain . . . . .	60
3.16	Particle tracking for real symmetric field configuration with and without correctors . . . . .	61
3.17	Particle tracking for real asymmetric field configuration with and without configuration . . . . .	62
3.18	Electrical simulations of a 50/450 $\mu\text{m}$ grid . . . . .	64
3.19	Maxwell-Boltzmann distribution for some species of ESS residual gas . . . . .	65
3.20	Energy and emission angle of the ionized electrons . . . . .	66
3.20a	Electron energy distribution. . . . .	66
3.20b	Electron emission angle distribution. . . . .	66
3.21	Results from particle tracking with electrons considering initial energy . . . . .	66
3.21a	Relative error on $\sigma_{beam}$ for different extraction fields. . . . .	66
3.21b	Relative error on $\sigma_{beam}$ at constant extraction field of 1 keV/cm for various magnetic fields. . . . .	66
3.22	Effect of beam current and energy on the profile measurement . . . . .	69
3.22a	Error on the profile measurement with $H_2^+$ ions, due to space charge effects for several beam energy ( $E_{beam} = 62.5$ mA). . . . .	69
3.22b	Error on the profile measurement with $H_2^+$ ions, due to space charge effects for several beam current ( $E_{beam} = 90$ MeV). . . . .	69
3.23	Final simulation of beam measurement with particles tracking considering the non-uniformities, initial momentum and space charge effect. . . . .	69
3.23a	Profile measurement with electrons . . . . .	69
3.23b	Profile measurement with $H_2^+$ ions . . . . .	69
3.24	Typical circuit of a charge amplifier with an operational amplifier . . . . .	71

3.25	Energy deposition in a silicon layer for ions and electron at low kinetic energies . . . . .	72
3.25a	Energy deposition in a silicon layer for various ions . . . . .	72
3.25b	Energy deposition in a silicon layer for electrons . . . . .	72
3.26	Principle of a simple semiconductor detector . . . . .	73
3.27	Sectional view of a MCP . . . . .	75
3.28	Schematic views of how a MCP works . . . . .	75
3.28a	SEM picture of MCP holes . . . . .	75
3.28b	Description of how an MCP amplifies incident particle. . . . .	75
4.1	IRMA installation . . . . .	87
4.1a	Schematic view of the implanter. . . . .	87
4.1b	The source is in the cage in background. The test bench was installed on the target chamber, on the left. . . . .	87
4.2	IRMA setup . . . . .	87
4.2a	The TimePix chip is just behind the Faraday cup. . . . .	87
4.2b	A plate with a drilled hole reduced the incoming current. The beam is scanned on the plate. . . . .	87
4.3	Main results from IRMA tests with $H_2^+$ ions . . . . .	88
4.3a	ToT image at 15 keV . . . . .	88
4.3b	ToT image at 12 keV . . . . .	88
4.3c	Total signal on the sensor with respect to the ion energies. . . . .	88
4.4	The gain has changed after the irradiation . . . . .	88
4.5	One of the IPM prototypes . . . . .	90
4.6	The DDC316 architecture with dual integrators . . . . .	93
4.7	Asymmetric or symmetric configuration . . . . .	94
4.7a	Asymmetric configuration. The readout is grounded while the extracting electrode is at a certain potential. . . . .	94
4.7b	Symmetric configuration. The readout and extracting the electrode are at opposite potential. . . . .	94
4.8	EPICS network setup during beam tests . . . . .	95
4.9	IPM test bench . . . . .	96
4.10	Schematic view of IPHI accelerator . . . . .	97
4.11	The test bench installed at the IPHI accelerator . . . . .	98
4.11a	The casemate of IPHI. The test bench is visible in foreground . . . . .	98
4.11b	The test bench fully equipped. . . . .	98
4.12	An example of a beam image recorded by the camera . . . . .	100
4.13	Example of charge signal recorded on one strips . . . . .	101
4.13a	Full signal over a 45 sec. . . . .	101
4.13b	Zoom on one beam pulse. . . . .	101
4.14	Beam profile measurement with the $Y_3Al_5O_{12}(Ce)$ screen . . . . .	101
4.14a	Image on screen . . . . .	101
4.14b	Projection on $x$ axis . . . . .	101
4.14c	Projection on $y$ axis . . . . .	101
4.15	Image recorded with the FPM system . . . . .	102
4.16	Two types of RGA spectra recorded during the tests . . . . .	103
4.16a	An RGA spectrum dominated by water peaks. . . . .	103
4.16b	An RGA spectrum after few days of pumping or baking. . . . .	103

4.17	Beam position versus time, measured with a BPM and an IPM . . . .	104
4.18	Histograms of the beam positions and sizes for 480 consecutive pulses	104
4.18a	Histogram of positions. . . . .	104
4.18b	Histogram of sizes. . . . .	104
4.19	Influence of the beam current on the beam shape. . . . .	105
4.19a	At high current the beam looks almost Gaussian. . . . .	105
4.19b	At low beam current, the beam shows a narrow peak on the top of a large halo. . . . .	105
4.20	Influence of the beam current on the profile measurement. . . . .	106
4.20a	Integrated signal versus beam current. The blue curve represents the sum of the two components. . . . .	106
4.20b	Sizes of the beam and halo versus beam current. . . . .	106
4.21	The beam must be finely tuned in order to perform correct measurements	107
4.21a	A poorly beam tune leads to strange signal on the top of the image. . . . .	107
4.21b	The beam size can be set at different sizes thanks to quadrupoles.	107
4.22	Example of beam size convergence measured with both IPMs . . . . .	107
4.22a	Convergence observed with optical IPM, $I_{beam} = 10$ mA . . . . .	107
4.22b	Convergence observed with strips IPM, $I_{beam} = 30$ mA . . . . .	107
4.23	Cross interaction between two IPMs. . . . .	108
4.23a	Variation of the beam position. . . . .	108
4.23b	Variation of the beam size. . . . .	108
4.24	Superposition of the same beam profile measured with strips IPM and optical IPM . . . . .	109
4.25	Verification of the electrical field can be done by switching the field configuration . . . . .	110
4.25a	Relative displacement of the beam. . . . .	110
4.25b	The ratio between beam sizes in symmetric and asymmetric. . . . .	110
4.26	The optical IPM is able to resolve small details. . . . .	111
4.26a	Image with improved contrast on the grid shadow. . . . .	111
4.26b	FFT image where the grid harmonics are visible. . . . .	111
4.27	Characterization of the MCPs . . . . .	112
4.27a	Relative gain curve. . . . .	112
4.27b	Influence of the MCP gain on beam size. . . . .	112
4.28	Relative image intensity versus phosphorus screen voltage . . . . .	113
4.28a	P43 screen. . . . .	113
4.28b	P46 screen. . . . .	113
4.29	Beam size versus phosphorus screen voltage. . . . .	113
4.29a	P43 screen. . . . .	113
4.29b	P46 screen. . . . .	113
4.30	Comparison of temporal response of both phosphorus screens . . . . .	114
4.30a	P43 screen. . . . .	114
4.30b	P46 screen. . . . .	114
4.31	Example of profile measurement at very low duty cycle. . . . .	116
4.31a	Beam image . . . . .	116
4.31b	Projection . . . . .	116
4.32	Example of images in electron mode . . . . .	117
4.32a	Profile measurement attempt with electrons, Hamamatsu MCP.	117

4.32b	Profile measurement attempt with electrons, Photonis MCP. . .	117
5.1	The geometry implemented in Geant4 . . . . .	128
5.1a	The LWU and two quadrupoles. . . . .	128
5.1b	Zoom on the two IPMs. . . . .	128
5.2	The calibration of the MCP is done with a VUV lamp . . . . .	128
5.3	Two solutions are foreseen for remote acquisitions of the profile measurement . . . . .	129
5.3a	The profile image is transported through an optical fiber bundle.	129
5.3b	The profile image is reflected on mirrors. . . . .	129
5.4	The new IPM design . . . . .	130
5.4a	A 3D drawing of the new design. . . . .	130
5.4b	The new design allow to remove MCP easily and is independent to the IPM direction. . . . .	130





# List of Tables

1.1	Neutron classification according to the neutron energy and wavelength	4
2.1	ESS nominal conditions . . . . .	18
2.2	Overview of ESS neutron instruments . . . . .	23
3.1	Mean excitation energy, average energy to produce a pair and density values for several mediums at Normal Temperature and Pressure (NTP)	45
3.2	Expected residual vacuum gas characteristics in the cold part of the ESS Linac, provided by ESS vacuum group . . . . .	45
3.3	Comparison of expected number of electrons between calculation using Bethe equation and results from Garfield++ . . . . .	47
3.4	Example of deviation of the trajectory of a particle in an IPM . . . . .	55
3.5	Resistor chain characteristics for the field degraders in the symmetric IPM . . . . .	61
3.6	Resistor chain characteristics for the field degraders and curved electrodes in the asymmetric IPM . . . . .	62
3.7	Properties of common semiconductors used as radiation detectors. . . . .	74
4.1	Main characteristics of the MCPs used during the beam tests . . . . .	91
4.2	Main features of the Sony IMX249 sensor . . . . .	92
4.3	Magnification for several common focal lengths . . . . .	92
4.4	Positions and sizes of the first half of gaussian strips . . . . .	93
4.5	Properties of the 3 scintillator screens used as reference measurement	97
4.6	Comparison between IPHI and ESS accelerators . . . . .	98
4.7	Summary of the two campaigns . . . . .	99
4.8	The detection limit of the bare strips systems has been extrapolated from these values . . . . .	114
4.9	Extrapolation to ESS conditions from a real case during the second campaign . . . . .	115



# Résumé en Français

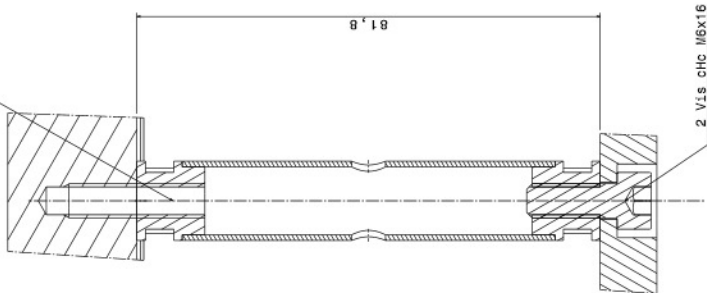


# Drawings of the prototypes and test bench

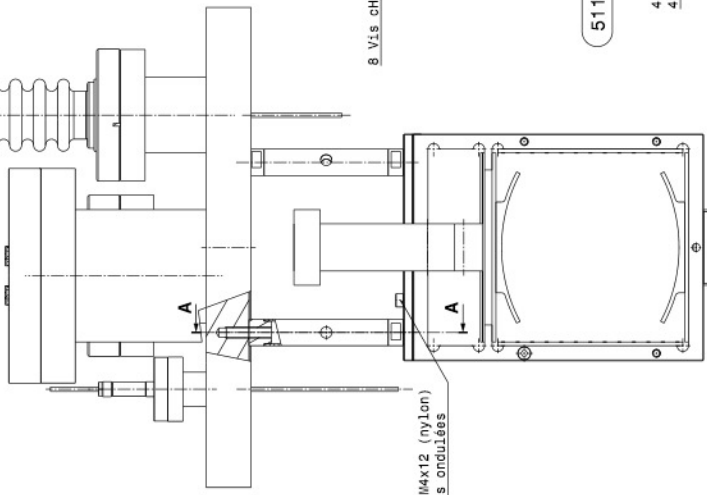


A-A

2 Tiges filetées M6x30



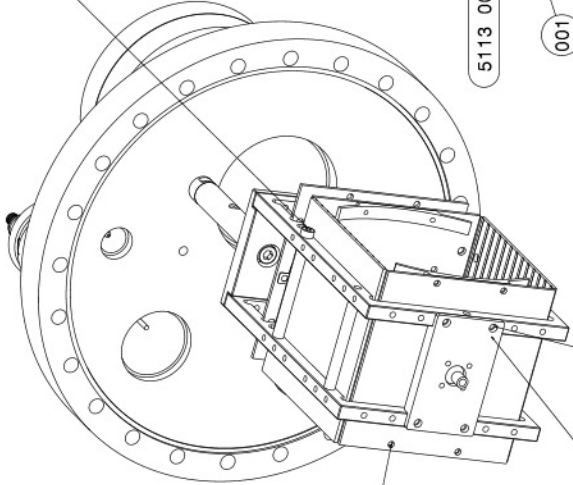
8 Vis chc M4x12 (nylon)  
8 Rondelles ondulées



8 Vis chc M3x6

5113 004

4 Vis chc M5x10 (nylon)  
4 Rondelles ondulées



8 Vis chc M4x16  
8 Rondelles ondulées

5113 005

001

5113 003

5113 002

5113 006

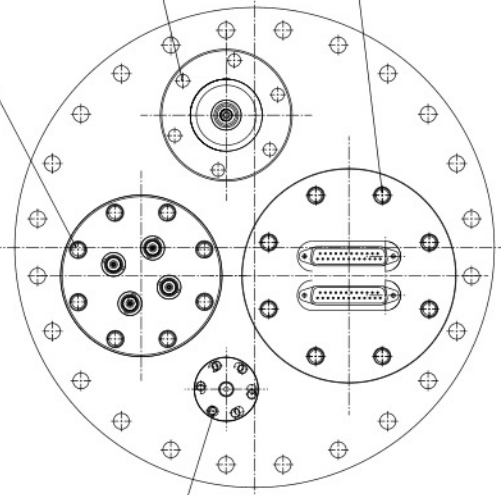
5113 007

8 Vis H M6x50  
16 Rondelles N8  
8 Ecrous H M8

6 Vis H M6x35  
12 Rondelles N6  
6 Ecrous H M6

8 Vis H M6x50  
8 Rondelles N6  
16 Ecrous H M6

6 Vis H M4x20  
12 Rondelles M4  
6 Ecrous H M4



PROJET	COLLEGE	DATE	WPT
001			
DESIGNER	DATE	PROVISORE	
001			
DATE DE REALISATION	DATE DE DELAI	DATE DE DELAI	

**ESS-Diagnostics**  
 IPM Prototype  
 IPM strip=Montage Vertical  
 Ensemble montage Vertical  
 Date: 11/11/11

71 P061 DM- 5112 000 PA  
 71 P061 DM- 5112 000 PA







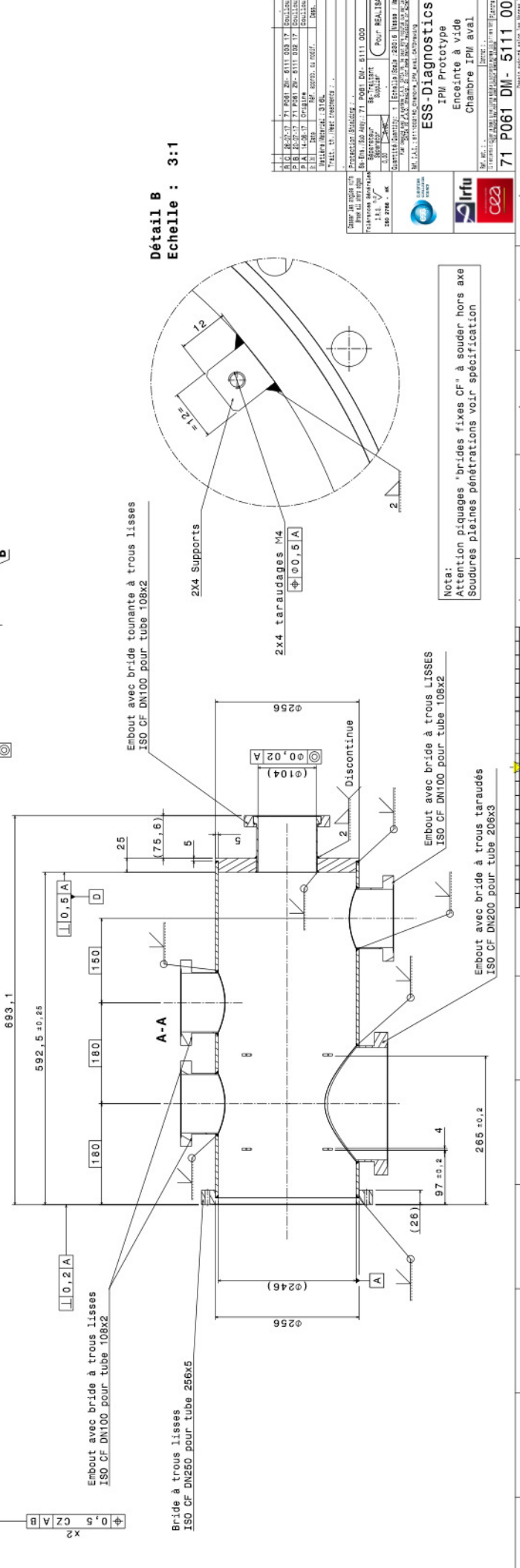
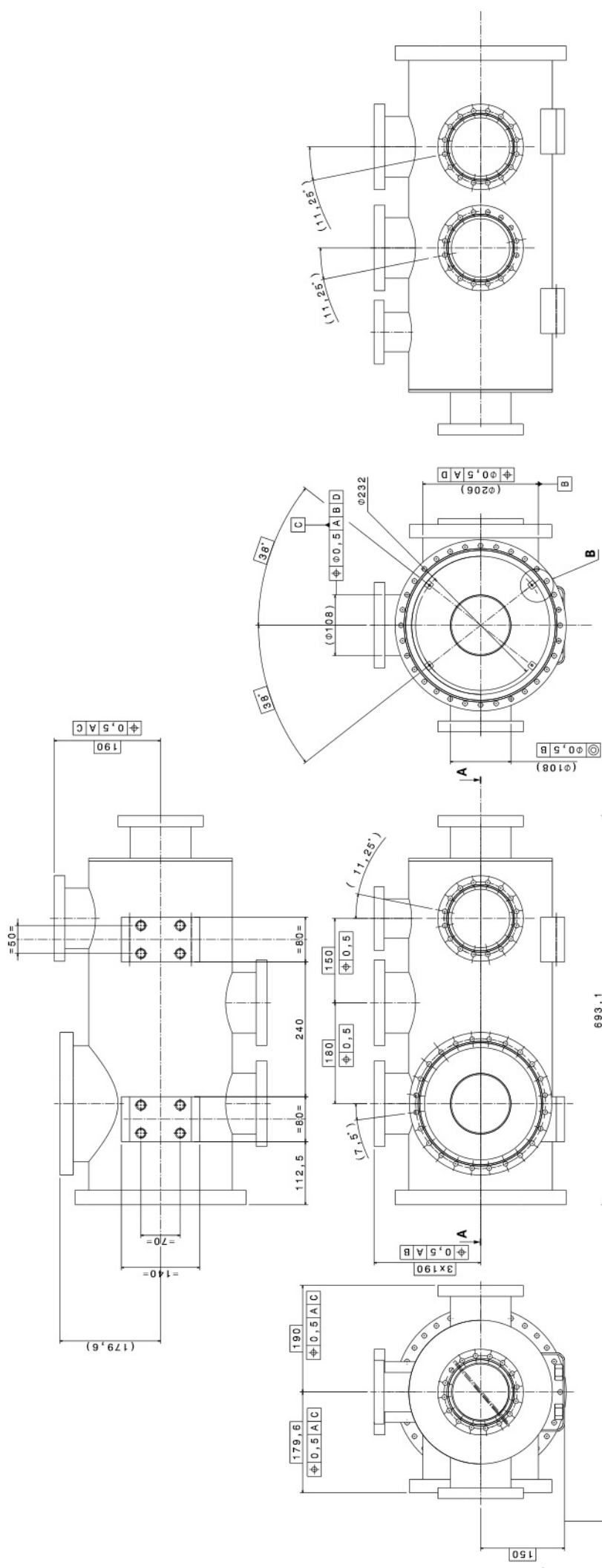












Détail B  
Echelle : 3:1

Notes:  
Attention piquages "brides fixes CF" à souder hors axe  
Soudures pleines pénétrations voir spécification

PROJET	71 P061 DM- 5111 000	DATE	03/08/2015
DESIGNER	...	REVISION	...
DATE	03/08/2015	REVISION	...
PROJET	71 P061 DM- 5111 000	DATE	03/08/2015
DESIGNER	...	REVISION	...
DATE	03/08/2015	REVISION	...

ESS-DIAGNOSTICS  
 IPM Prototype  
 Enceinte à vide  
 Chambre IPM aval

71 P061 DM- 5111 002 RC  
 03/08/2015

# Conference proceeding and scientific documents

# Design and development of Ionization Profile Monitor for the Cryogenic sections of the ESS Linac

F. Benedetti, P. Abbon, F. Belloni, G. Coulloux, F. Gougnaud, C. Lahonde-Hamdoun, P. Le Bourlout, Y. Mariette, J. Marroncle, J.P. Mols, V. Nadot, L. Scola and G. Tauzin

CEA Saclay, Institut de Recherche sur les lois Fondamentales de l'Univers  
Gif-sur-Yvette, France

R. Tarkeshian and C. Thomas  
European Spallation Source ERIC  
Lund, Sweden

**Abstract**—Saclay CEA/IRFU is working for the delivery of five Non-Invasive Profile Monitors in the frame of the in-kind contribution agreement signed with the European Spallation Source. Neutrons will be produced by spallation reactions of 2 GeV proton beam impinging on a Tungsten target. To accelerate protons a powerful linear accelerator of 5 MW is under construction. Diagnostic devices are mandatory tools for the tuning and protection of the machine. The non-invasive profile monitors provide a measurement of the beam profile in transverse directions to the beam propagation. This project raises several physical and technical challenges including low signal detection of ions or electrons, profile distortions induced by the beam Space Charge effect and non-uniformities of electric field. Simulation and model of the critical aspects of the detector have been performed in order to prove the performance and the feasibility of the detector. A series of prototypes has been built with different readout types, and tested in real conditions at the 3 MeV proton accelerator IPHI. All of them show some advantages and drawbacks revealed by the tests in real beam conditions. In this paper we present the results of the tests for the various configuration readout systems to agree with the model and simulation of the detector. In concluding remarks, we will discuss the performance of the prototypes and point out the camera-based one to be the more suitable for the final design.

**Index Terms**—Beam diagnostic, Linear proton accelerators, MCP, Strip detector, Particle beam measurements

## I. INTRODUCTION

**T**HE European Spallation Source (ESS) will be a European research infrastructure dedicated to neutronic science. The source is currently under commissioning at the ESS site in Lund, Sweden, and will be the brightest pulsed neutron source. The production of neutrons is ensured by the spallation process: high energy protons will impinge on a tungsten target. To accelerate the protons a powerful 2 GeV linear accelerator is being built. The accelerator can be schematized in two parts. The first part accelerates the beam up to 90 MeV by mean of conventional room temperature RF cavities. Then a

The project was supported by the French in-kind contribution to ESS (AIK 7.3).

F. Benedetti is with the Département d'Électronique des Détecteurs et d'Informatique pour la Physique, Commissariat à l'Énergie Atomique et aux énergies alternatives, Saclay, 91400 France, (email: florian.benedetti@cea.fr).

cold part using superconducting cavities cooled with liquid helium is used to reach the highest energies. An overview of the ESS linac is shown in Fig. 1, and Table I gives its main characteristics.

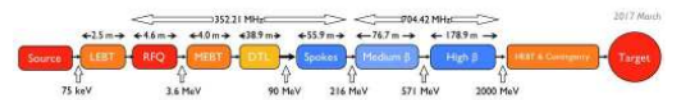


Fig. 1. A simplified representation of the ESS linac. The IPMs will be installed in the cryogenic part (blue).

At ESS, both invasive and non-invasive profilers will be installed along the accelerator. The beam profile will be also recorded at the target location and upstream of the beam dump [1]. The invasive measurements are mainly done with wire scanners. These devices cannot handle the huge beam peak power of ESS at nominal conditions (125 MW), and will be only used at low beam duty cycle [2]. Therefore, Non invasive Profile Monitors (NPM) will take over for higher beam power. In fact, the NPM refers to two types of devices depending on the detection principle. Fluorescence Profile Monitors (FPM) [3] are foreseen in the "warm" parts of the accelerator whereas Ionization Profile Monitors (IPM) will be implemented exclusively in the cryogenic part of the accelerator. Five pairs of IPMs are foreseen at several locations.

TABLE I  
ESS LINAC CHARACTERISTICS

Characteristic	Value
Energy	2 GeV
Pulse current	62.5 mA
Pulse duration	2.86 ms
Repetition rate	14 Hz
Duty cycle	4 %
Power (peak)	5 MW (125 MW)
Radio Frequencies	352.21 MHz 704.42 MHz



## II. IONIZATION PROFILE MONITORS

### A. State of art

The first use of IPMs dates back to the 1960s [4]. In the 90s, the raise of the MicroChannel Plates have permitted to measure profiles [5], [6] in more critical working conditions. The IPM method is now mature and used in several installations [7]–[10]. Recently, the interest in semiconductor detectors has grown [11] and first results looks promising [12].

The different technologies of detection, presented just before, have been reviewed in order to select the most efficient one with respect to the ESS requirements.

### B. Principle of operation

An Ionization Profile Monitor (IPM) is a non-invasive detector that measures the transverse profile of a beam. Its principle of operation is shown in Fig. 2 and can be summarized in 3 main steps:

- 1) Beam protons pass through the vacuum, inducing ionizations of the residual gas molecules: electron/ion pairs are created.
- 2) Inside the IPM, a strong electric field drives electrons or ions towards a segmented readout system.
- 3) The profile is reconstructed in one transverse direction. For a complete profile, a pair of IPMs, rotated by 90° with respect to each other, is mandatory.

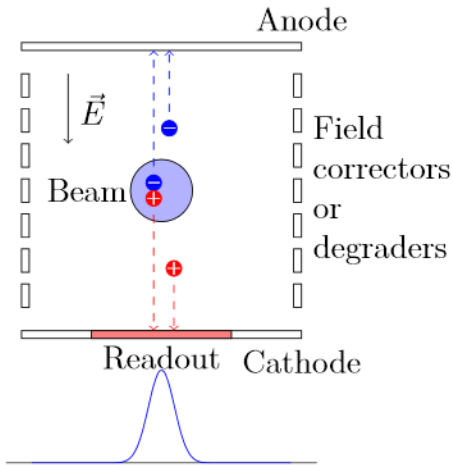


Fig. 2. Visual explanation of how an IPM works. The electric field between the electrodes can be reverted by inverting the polarity, giving the possibility to detect ions or electrons. Field correctors or degraders, left and right, improve the field uniformity.

One can note that an IPM forces the charge collection with an electrical field, whereas a FPM is passive and detects within a certain solid angle. On the other hand, the implantation of IPMs is more complex since it operates in vacuum.

Simulations were done in order to check the feasibility of the IPM design for the given ESS conditions. Each simulation focused on the following hot topics:

- Quantification of the ionization signal in terms of number of produced electron/ion pairs for ensuring that the signal is sufficiently high for reconstructing a profile per pulse

beam, despite of the low gas pressure and relatively small ionization cross section at high proton energy.

- The extraction field must be as uniform as possible in order to lead efficiently and correctly the ionization by-products toward the readout.
- The space charge effect induced by the beam and the initial momentum of ionization electrons/ions, which may distort the profile, must be evaluated.
- The choice of an efficient readout technology which must match the ESS working conditions.

All these points will be presented in the next sections.

## III. ELECTRON/ION RATES

The IPMs rely on the by-product collection of the ionized residuals gas. The number of ionized particles gives the signal strength which has to be compliant to the readout sensitivity. Therefore, the number of ionization particles, that are created by the beam itself along the residual gas, must be evaluated.

### A. Calculation using Bethe model

For heavy charged particles like protons, the main interaction is due to electromagnetic interactions of the incident particle with the orbiting electrons of the medium. The Bethe equation describes the mean rate of energy losses per distance unit by a heavy charged particle as follows [13, p. 446]:

$$-\left\langle \frac{dE}{dx} \right\rangle = K \rho \frac{Z}{A} \frac{z^2}{\beta^2} \left[ \frac{1}{2} \ln \left( \frac{2m_e \beta^2 \gamma^2 T_{max} c^2}{I^2} \right) - \beta^2 \right] \quad (1)$$

where  $K$  is a constant factor defined by  $K = 4\pi N_a r_e^2 m_e c^2$ ,  $r_e$  is the classical electron radius,  $m_e$  is the electron mass,  $N_a$  the Avogadro constant and  $c$  the speed of light in vacuum.  $Z$ ,  $A$  and  $\rho$  are respectively the atomic number, the mass number and the density of the given medium. The mean excitation energy  $I$  is the only non-trivial variable in the Bethe equation [14]. The maximum transfer energy for one collision  $T_{max}$  is given by the following equation:

$$T_{max} = \frac{2m_e \beta^2 \gamma^2 c^2}{1 + \frac{2\gamma m_e}{M} + \left(\frac{m_e}{M}\right)^2} \quad (2)$$

where,  $M$  and  $m_e$  are respectively the incident particle and electron masses. The  $\beta$  and  $\gamma$  variables have their normal significance as Lorentz factors.

When the medium is a mixture of several compounds, its mean stopping power needs to be calculated as the sum of the mean stopping power of its components weighted by their mass proportion. By introducing  $W$ , the average energy for producing an ion/electron pair in a medium [15], [16], one can estimate the number of ion/electron pairs created in a given readout length  $\Delta x$  of materials as:

$$N_{total} = \sum_{n=First}^{Last} \frac{\left\langle \frac{dE}{dx} (\rho_n, I_n, A_n, Z_n) \right\rangle}{W_n} \Delta x \quad (3)$$

The Bethe formula can be implemented in a C++ code once the composition of the medium and the  $I$  value of each compound is known. The expected pressure in the cryogenic part at ESS is around  $10^{-9}$  mbar, and the gas composition is given by the following: 79%  $H_2$ , 10%  $CO$ , 10%  $CO_2$  and 1%  $N_2$



### B. Calculation using PAI model

The Garfield++ software [17] also has been used to compute the number of primary ionizations. This software is normally intended for the modelization of gaseous detectors. It allows to simulate the creation of electron/ion pairs due to the ionization of gas by an incident particle, the transport and amplification of these electrons in the gas and the signal induced on a readout plane. In our case, we simulated only the pair creation in the residual gas. For this step Garfield++ uses Heed ++ [18], a C ++ code that implements the photoabsorption and ionization (PAI) model [19].

Table II summarizes the results of the two previous calculations done for different IPM positions along the ESS linac, and the factor ratio between the methods.

TABLE II  
COMPARISON OF EXPECTED NUMBER OF ELECTRON/ION PAIRS PER cm BETWEEN CALCULATION USING BETHE EQUATION AND RESULTS FROM GARFIELD++.

Energy	$N_{Bethe}$	$N_{garfield}$	Factor
97.2	100210	52537	0.52
231.4	54970	27463	0.50
278.9	49160	26124	0.53
315.8	45850	23769	0.52
628.3	33600	17522	0.52

### C. Limitations

The estimation strongly depends on various vacuum parameters that have not been measured yet. In consequence, the calculated values give only a coarse approximation. Also, the measurement of the  $W$  parameter includes the delta ray (or secondary ionization) electrons, hence the  $W$  value is biased [4], [13] for the case at hand, since the IPMs work at very low pressure. The real  $W$  values may be higher than the ones given in references, therefore the real number of ionization pairs may be 2 to 4 times lower than the expected number.

## IV. PROFILE DISTORTIONS

### A. Extraction field

The IPMs can be seen as parallel plate detectors. In an ideal case, these plates are infinite sized. The extraction field is then completely oriented in a single direction, normal to the detection plane and the projection of the profile on this plane is perfect. In reality, the plates have finite dimensions, comparable to the gap between the two electrodes. In these conditions the field is no more uniform. In addition, the cross-interaction between the electric fields of two close by IPMs is very strong. The non-uniformity of the electric field is very problematic because it creates mirage effects and prevents the correct measurement of the beam profile. To overcome this effect, two solutions have been considered:

- Using field correctors or field degraders [10]. This is done by placing conductors on each side. Each corrector is set to a certain potential in order to constrain the field.
- Putting grounded conductors between the two IPMs [10] to protect against the IPM cross-interaction.

COMSOL has been mainly used for the simulations of extraction fields, and a particle tracking algorithm has been implemented in C++. The code integrates the motion of particle due to the Lorentz force:

$$\vec{F} = m \cdot \vec{a} = q \cdot (\vec{E}(\vec{r}, t) + \vec{v} \times \vec{B}(\vec{r}, t)) \quad (4)$$

Fig. 3 shows an example of results given by the particle tracking. Without the corrections, the reconstructed profile is 35% wider than reality. The shift in position is due to the cross interaction between the two IPMs. When corrections are enabled, the obtained transverse profile is much better: the error on the profile width is only 0.4% and there is no more shift in position.

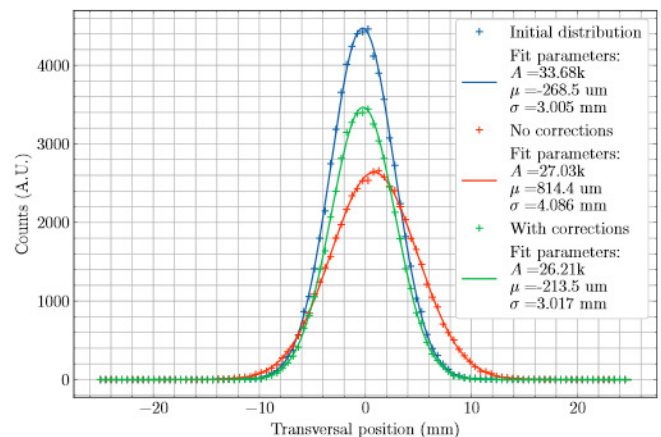


Fig. 3. A simulation of profile measurement with particle tracking for two real field configurations: without correction and with corrections. The initial proton (blue) beam is assumed to be Gaussian with  $\sigma_{beam} = 3$  mm (blue). Without correction, a shift of 1 mm and a broadening of 35% are observed (red). The corrections allows to negate the two previous distortions (green).

### B. Space Charge effect

In the context of IPMs, the Space Charge effect refers to the influence of the beam itself on the profile measurement. An ESS bunch is about  $10^9$  protons, therefore bunches generate a strong electromagnetic field while moving along the accelerator, and the electrons or ions are affected by this electromagnetic field while drifting to the read-outs in a IPM.

The estimation of this electromagnetic field is necessary to ensure that the profile measurement is not too strongly affected by the space charge effects. For this reason, a simulation code has been developed conjointly by ESS and CEA/Saclay. The code computes the electric field of a 3D Gaussian distributed bunch in the moving frame  $\bar{K}$  (rest frame for bunches) [20]. The electric field is transformed into an electromagnetic field in the laboratory frame  $K$  (rest frame for IPMs) by the Lorentz transformations of electromagnetic fields:

$$\mathbf{E} = \begin{pmatrix} \gamma \bar{E}_x \\ \gamma \bar{E}_y \\ \bar{E}_z \end{pmatrix}, \quad \mathbf{B} = \begin{pmatrix} -\gamma v_b \frac{\bar{E}_y}{c^2} \\ \gamma v_b \frac{\bar{E}_x}{c^2} \\ 0 \end{pmatrix} \quad (5)$$

Then, the motion of the electrons or ions is integrated thanks to the equation (4).

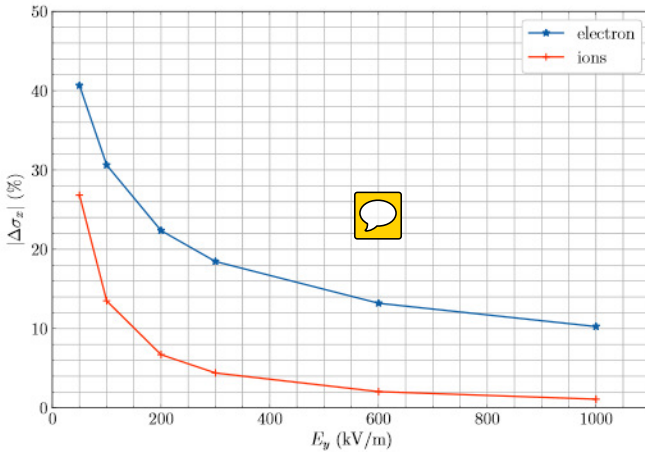


Fig. 4. Error on the profile measurement, for electrons and  $H_2^+$  ions, due to space charge effects versus the extraction field. The beam is assumed to be a Gaussian with  $\sigma_x = \sigma_x = 2$  mm

Using the code, it has been shown that space charge effect can be partially compensated by a high extraction field value. It has been seen that profiles from electrons seem to be more affected by space charge effect than from ions. In the Fig. 4, a general example of the ESS beam size measured from profiles obtained with ions and electron is presented, and for various values of the electric field strength. The beam size has been chosen to be 3% smaller than the nominal value. The values of the field strength used in the simulation are chosen in a range that is technically achievable. Within that range it can be seen that the minimization of the space charge effect is limited. It is also clear that the effect is stronger for electrons than for ions.

In the case of ESS beam, the ions and electrons feel a permanent electric field from the HV cage of the IPM, and an variable field due to the bunched structure of the beam. The duty cycle of the variable beam plays a role in the distortion of the profiles. In the case of electrons, due to their small mass, they will reach the detector within the passage of one bunch. Therefore, they feel the combined forces most of the time along their path. In the case of the ions, it takes the time of many bunches for them to reach the detector. Hence, the forces from the bunch are weighted by the duty cycle of the varying electric field. For the case of ESS, the bunches are 3 ps, and the period between them is 2.84 ns. So the integrated force seen by the ions has less strength than in the case with electrons.

The expected uncertainty for the beam size measurement is 10%. The presented case shows the impact of the space charge can be strong, but yet the retrieved values are still within the requirements for the measurement uncertainty. Larger beam sizes are associated with weaker space charge effect, hence, the designed instrument is expected to deliver reliable information on the ESS beam profile and size.

A workaround to totally counterbalance even more the space charge effects consists in adding a magnetic field parallel to the extraction field with a magnet [8]. However, this solution is not possible at ESS since the available space is too limited.

Consequently, the profile measurements will be performed with ions.

More detailed reviews of the simulations of space charge effects for the ESS IPM project are available here [21], [22].

### C. Initial momentum

A first approximation of the initial speed of ions can be done thanks to the distribution of Maxwell-Boltzmann. The speed of the fastest ion  $H_2^+$  is below 5000 m/s. A field of few hundred volts per centimeter is more than enough to compensate this effect, therefore the thermal motion for ions can be completely neglected.

Garfield++ can be used again since it also gives the energy distribution of the ionization electrons as well as the angular distribution. The energy distribution spread up to keV range but most probable energies are below 50 eV. The ions has supposed to be emitted with the opposite momentum. In consequence, the beam measurement with electrons is also more affected by the initial momentum than the measurement with ions. This enforces even more the necessity to measure the profile with ions at ESS.

## V. READOUT TECHNOLOGIES

### A. Strips

Conductive strips is the simplest method to implement. Electrodes are etched on a PCB with a thin layer of copper. When electrons or ions move towards the electrodes, they induce a current that can be calculated by mean of Ramo-Schockley theorem [23], [24]. The induced current is then integrated by a front end electronic.

A COTS (Component Of The Shelf) front end electronics has been selected for this purpose: the CARMEL card from the FASTER platform. This solution is developed by the LPC laboratory at Caen in France. CARMEL is a charge digitizer card based on the DDC316 chip from Texas Instruments. Each card provides 32 input channels and two cards can be plugged in an AMC mother board. The mother board is compatible with  $\mu$ TCA crates.

This method is very robust and radiation hard since strips are passive components. However, strips alone can not be used when the signal is too low, and it is necessary to find a way to amplify the signal.

### B. MCPs

A MicroChannel Plate (MCP) generates electrons from incident particles [25]. When a particle hits the MCP hole entrance, secondary electrons are emitted. Due to difference of potential, secondaries are drawn towards the channel output and strike hole walls again, creating more and more electrons. Then, electrons are collected on a detection plane. The detection plane can be a phosphorus screen which converts electrons to visible photons or conductive strips. Both solutions have been implemented.

A vision system is necessary to record light from the phosphorus screen. A camera with a lens should be sufficient in the case at hand. High resolution is not mandatory, so pixels



could be relatively big in order to increase light collection and dynamic range. Sony IMX249 fits well with these prerequisites, so the FLIR Blackfly-PGE-23S6M-C camera has been selected.

Unfortunately MCPs suffer of aging effect, the gain is not stable and decreases over the time. Therefore, a calibration must be performed to correct the gain from time to time.

### C. Silicon detectors

The last solution consists of a pixelated silicon detector. When a charged particle passes through the silicon it deposits its energy and electron/hole pairs are created. Then, the charge carriers drift in the semiconductor due to the bias voltage, and the induced signal is read by an embedded electronic. A single particle may create thousands of secondaries, therefore silicon detectors are very sensitive and interesting for IPMs.

The use of silicon detectors seems very promising but detection is not assured for ions at low energies since the stopping range is comparable to the deadlayer of silicon detectors. The feasibility of silicon detection for IPM with ions had to be checked. To this end, a small test bench has been developed and installed in a ion-implant facility: IRMA [26]. The test has been done with a tailored TimePix [27], [28] detector, kindly provided by the CERN-BI team.

The most crucial result of the test at IRMA is shown in Fig. 5. The detection seems possible at 15 keV, however at slightly lower energy 12 keV, the signal completely vanishes. Therefore, this solution has been discarded since it give almost no margin for error.

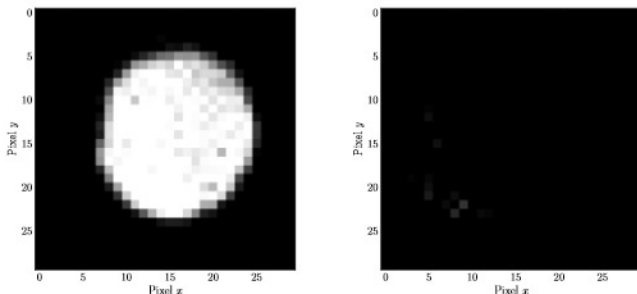


Fig. 5. Images of Time over Threshold signal from a TimePix chip for a incident  $H_2^+$  beam at 15 keV (left) and 12 keV (right).

## VI. PROTOTYPES DESIGN AND TEST SETUP

### A. IPM and test bench design

The simulations presented in the previous sections show that the profile measurements with IPMs may match the ESS requirements. However, some critical points, particularly the choice of the readout, were not fully clear, so the feasibility had to be proven experimentally. For this purpose three prototypes have been manufactured. The design of the prototypes is independent of the readout technology, so the readout can be changed with only few operations. A prototype using a MCP is shown in Fig. 6

A test bench has been developed in order to validate the prototypes. The bench can be split into two different independent

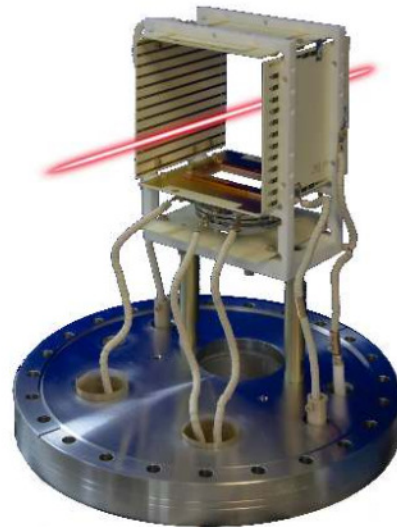


Fig. 6. One of the IPM prototypes. Here the readout is a MCP, visible through the rectangular slit. The copper lines on each side are the field correctors.

parts. The first part (upstream) tries to mimic the ESS LWU chamber inside which two IPMs can be inserted. The idea is to be close to the ESS conditions in term of high voltages and electrical fields. The second part (downstream) offers one more IPM slot and two viewports for reference measurements in order to compare with the IPMs ones. Two solutions have been considered for the reference measurements: fluorescence profile monitors (FPMs) and scintillating screens. The IPMs can be mounted independently in Y or X direction thanks to their design, thus it is even possible to measure the same profile direction with all three IPMs.

### B. Control System

The whole system is almost fully compatible with the version 3.16 of EPICS base. The PointGrey GigE cameras are well supported by the AreaDetector module. A custom plugin, developed by ESS, performs a gaussian fit on every image of the profile. Raw images are saved into HDF5 files. This format allows to combine various datasets together, for instance the raw IPM images with some beam information. Since all high voltage power supplies have their own SPCI Ethernet interface, a simple softIOC with StreamDevice is enough to control and monitor them. Three OPIs have been developed in order to control cameras, power supplies and a motor (geobrick) to move scintillating screens vertically to intercept the beam or to be safely moved far from it. These OPIs run under the BOY module of the ESS Control System Studio version 4.5. An Archiver Appliance records and saves slow process variables from the power supplies, the vacuum systems and the accelerator.

### C. IPHI accelerator

IPHI is a high intensity linear proton accelerator located at CEA/Saclay. This project started in the late of 90's [29] but protons were accelerated up to 3 MeV in April 2016 [30].



Proton plasma is created by an electron cyclotron resonance source, and transported toward a radio frequency quadrupole (RFQ) by a low energy beam transport line. An iris ensures a fine tuning of the current, and two solenoids focus and filter the plasma before the injection in the RFQ. Then, the protons are accelerated up to 3 MeV and bunched with a frequency of 352 MHz by the RFQ. A medium energy beam transport line, downstream from the RFQ, contains focusing elements, steerers, dipole magnet and beam diagnostics. The dipole magnet can distribute the protons over two beam lines.

The main line has a dedicated beam stop of 300 kW, allowing the commissioning of the accelerator at high intensity and duty cycle. The secondary line is more modular but restricted to lower intensity and duty cycle (few hundred Watt). In 2018, this line was open for external user experiments [31].



Fig. 7. Picture of the IPHI installation. The IPM test bench is also visible in the foreground.

## VII. RESULTS FROM IPHI TESTS

### A. First measurements

Two test campaigns were accomplished at IPHI. In the first campaign, the correct operation of the IPMs was checked, the beam was finely tune and first measurements were performed. In the second campaign, further studies were carried out and the first results were confirmed. During both campaigns, the beam was tune to minimize its divergence in the dispersive plane. Both types of IPM have been working in both campaigns.

The optical IPM gives directly an image of the beam in longitudinal and transverse direction. The processing of data is done as follow. First, dead pixels are removed and the image is cropped to a region of interest. Then, a FFT filter is applied for reducing the noise due to sensor if necessary. The profile is reconstructed by summing all pixels in the longitudinal direction. Fig. 8 shows an image acquired from the optical IPM. One can see the shadow of a grid that is placed right in front of the MCP input. The grid has a pitch of  $450\ \mu\text{m}$  and a wire size of  $50\ \mu\text{m}$ . This gives an idea of the resolution that can be achieved with the optical IPM.

The strips measure the profile in only one transverse direction. The data processing is different because the acquisition is done continuously. First, the pedestals are removed and

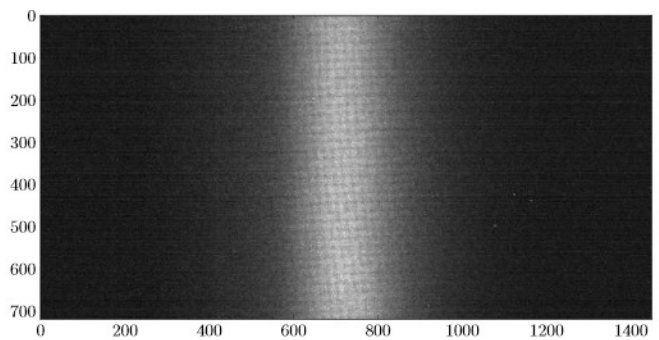


Fig. 8. An example of a beam projection image recorded by the camera. The image covers an area of 38 mm by 18 mm.

a search is performed in the whole dataset to find events corresponding to a pulse. Fig. 9 shows the same profile measured by both IPMs.

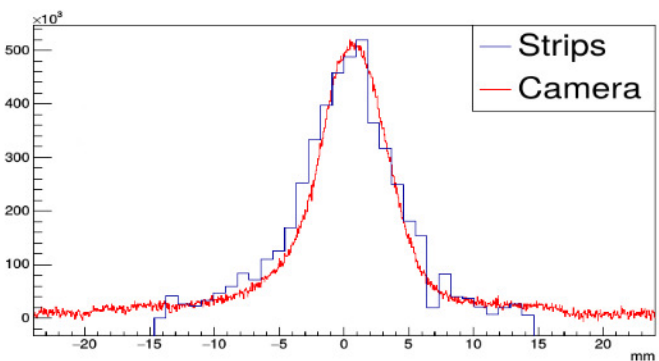


Fig. 9. Superposition of the same beam profile recorded with the strips and optical IPMs.

### B. Comparison with IPHI diagnostics

Unfortunately, there is no profile measurement on the IPHI beam line, therefore the measurement of the beam profile can not be compared to an existing diagnostic. However, a complete system of Beam Profile Monitors (BPM) and AC Current Transformer (ACCT) are installed on IPHI. The beam can be also scanned with electrostatic steerers and the current is tuned by an iris aperture close to the source. An IPM is able to measure position and current of a beam, even if it is firstly intended for profile measurement.

An example of beam scanning is illustrated in Fig. 10. The sharp steps are due to steerers whereas the small transitions between two steps are the variations of beam position from pulse to pulse. This is not a desirable effect and it has limited the measurement of the position resolution. The reason of this effect is not clear and may be due to the short pulse duration time used during the tests.

The same can be done for the beam current. The signal is measured at several beam currents for a fixed IPM gain. IPMs response is very linear over an important current range. At IPHI, the number of particles collected by the MCP is an order of magnitude higher than the one expected at ESS, and no

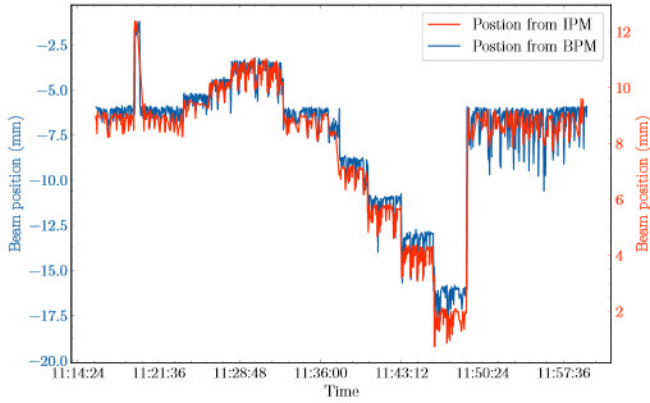


Fig. 10. Beam position over the time, measured with the BPM and the optical IPM. A steerer has been used to move the beam (step transitions). However, small variations between two steerer steps were not expected.

channel saturation has been observed on the MCP signal. This means that a single stage MCP will not suffer of saturation effect at ESS.

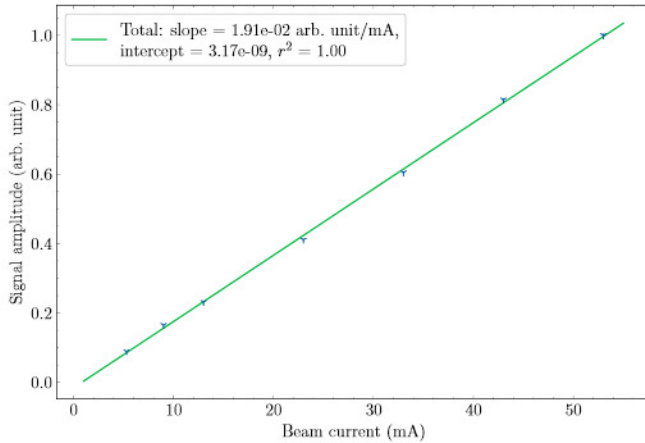


Fig. 11. Evolution of the signal with the beam current. The evolution has a good linearity over an important current range, and no saturation has been observed.

### C. Extrapolation to ESS condition

One of the important studies conducted at IPHI is the estimation of the detection limit. The objective is to determine which readout can detect the signal in ESS conditions. However the conditions at IPHI are different from the ones of ESS. The proton energy at IPHI is 3 MeV, and according to Bethe equation, the cross section is 60 times higher compared to 2 GeV proton. The vacuum level is also higher by one or two decades. To compensate for these two factors it is possible to reduce the beam current and pulse duration.

For bare strips readout, the number of charges collected was measured for several beam currents, and the intersection of the sensitivity curve with the noise level gives a rough idea of the limit of detection. However, this method greatly underestimates the integration noise of the electronics because the IPHI pulses are very short. According to the first results,

the detection limit is just above the most favorable case of ESS. Measuring with bare strips seems difficult in ESS conditions.

Unlike the strips IPM, it is almost impossible to quantify the number of primary particles without a complete calibration of the MCP. Therefore, the extrapolation is done by calculating the Bethe formula with respect to the beam parameters and vacuum conditions measured at IPHI. The beam current and the pulse duration were set to their lowest values, respectively 0.5 mA and 50  $\mu$ s. The pressure was about  $4 \cdot 10^{-8}$  mbar. In these conditions the Bethe scaling is equal to one for the worst ESS case (628.3 MeV), and the resulting profile is shown in Fig. 12. The measurement may be possible at ESS even with a single stage MCP.

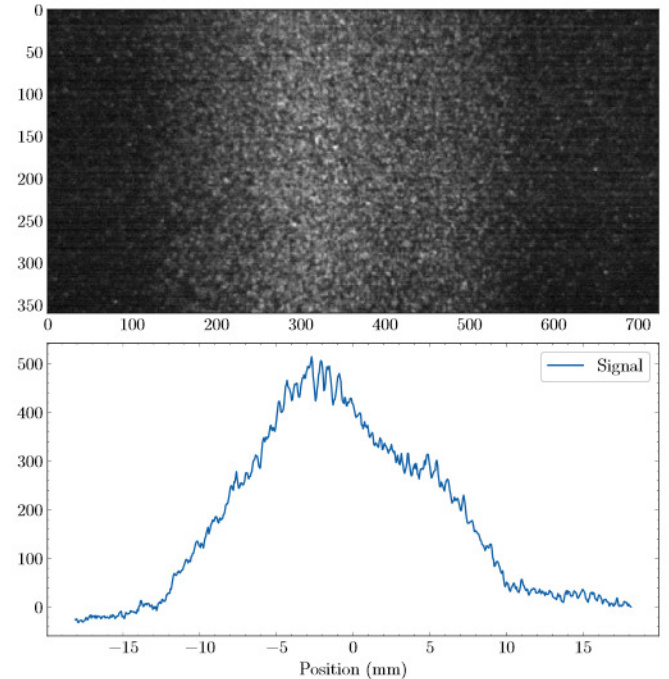


Fig. 12. Image of the beam profile at the lowest current and pulse duration possible at IPHI (0.5 mA, 50  $\mu$ s). In these conditions, the signal is close to the one expected at ESS for the worst case. Note that IPHI was not designed to work at such a low current.

## VIII. CONCLUSION

A complete study of all the critical key points concerning the feasibility of this detector has been performed. The expected number of ionization products at the given ESS condition may be enough if the readout is sufficiently sensitive. The non-uniformities of the extraction field can be corrected by hardware corrections, and the distortions of the profile due to space charge effects can be reduced if ions are used and sufficient extraction field is provided to the IPMs. Three readout technologies have been considered and a complete platform has been developed in order to test the different readouts. Two types of IPM have been tested in real beam conditions at IPHI, a 3 MeV proton accelerator. Both strips and MCP were able to measure the beam profile. But approximations to ESS conditions show that the use of MCP is mandatory, therefore the optical IPM is preferred.



The tests at IPHI were a great opportunity to earn experiences and feedback. From this, an improved IPM design is under development. The IPM is now in two part allowing a quick replacement of the MCP without unmounting the cage. A MCP calibration system is also foreseen to monitor and correct the ageing of MCPs.

The production of the IPMs will be done in an ISO-5 particle free environment to insure the compliance with cryogenic cavities. All IPMs will be qualified at Saclay, according to ESS requirements. First detectors will be delivered at ESS in the beginning of 2020 and will be ready for the first protons on dump.

#### ACKNOWLEDGMENT

The authors are grateful to James Storey and his colleagues (CERN, Geneva, Switzerland) for their help with the TimePix detector. We would like to thank Cyril Bachelet and his team (CSNSM, Orsay, France) for their support during the tests at IRMA. We are thankful to our colleagues at IPHI (CEA, Saclay, France) for their assistance and availability during two beam test campaigns. Finally, we thank all people from the ESS collaboration for their fruitful exchanges and support that help us to design the monitors.

#### REFERENCES

- [1] T. Shea, "Proton beam measurement strategy for the 5 MW European Spallation Source target," in *Proc. IBIC2013*, 2013, pp. 349–352. [Online]. Available: <http://accelconf.web.cern.ch/AccelConf/IBIC2013/papers/tupc02.pdf>
- [2] B. Cheymol, A. Jansson, and T. J. Shea, "Wire scanner design for the European Spallation Source," in *Proc. IBIC2013*, 2013, pp. 830–832. [Online]. Available: <http://accelconf.web.cern.ch/AccelConf/IBIC2013/papers/wepf10.pdf>
- [3] C. Thomas *et al.*, "Design and implementation of non-invasive profile monitors for the ESS LEBT," in *Proc. IBIC'16*, 2016, pp. 551–554. [Online]. Available: <http://accelconf.web.cern.ch/AccelConf/ibic2016/papers/tupg80.pdf>
- [4] W. DeLuca, "Beam Detection using Residual Gas Ionization," in *Proc. PAC1969*, 1969, pp. 813–822. [Online]. Available: [http://accelconf.web.cern.ch/AccelConf/p69/PDF/PAC1969\\_0813.PDF](http://accelconf.web.cern.ch/AccelConf/p69/PDF/PAC1969_0813.PDF)
- [5] J. Krider, "Residual gas beam profile monitor," *Nuclear Instruments and Methods in Physics Research Section A: Accelerators, Spectrometers, Detectors and Associated Equipment*, vol. 278, no. 3, pp. 660 – 663, 1989. [Online]. Available: [https://doi.org/10.1016/0168-9002\(89\)91188-1](https://doi.org/10.1016/0168-9002(89)91188-1)
- [6] K. Wittenburg, "Experience with the Residual Gas Ionisation Beam Profile Monitors at the DESY Proton Accelerators," in *Proc. EPAC1992*, 1992, pp. 1133–1135. [Online]. Available: [http://accelconf.web.cern.ch/AccelConf/e92/PDF/EPAC1992\\_1133.PDF](http://accelconf.web.cern.ch/AccelConf/e92/PDF/EPAC1992_1133.PDF)
- [7] K. Satou, N. Hayashi, S. Lee, and T. Toyama, "A prototype of Residual Gas Ionization Profile Monitor for J-PARC RCS," in *Proc. EPAC2006*, 2006, pp. 1163–1165. [Online]. Available: <http://accelconf.web.cern.ch/AccelConf/e06/PAPERS/TUPCH065.PDF>
- [8] T. Giacomini, P. Forck, J. D. Villiers, J. Dietrich, and D. Liakin, "Ionization Profile monitors - IPM @ GSI," in *Proc. DIPAC2011*, 2011, pp. 419–421. [Online]. Available: <http://accelconf.web.cern.ch/AccelConf/DIPAC2011/papers/tupd51.pdf>
- [9] D. K. Morris *et al.*, "Operational use of ionization profile monitors in the Fermilab Main Injector," in *Proc. NA-PAC2011*, 2011, pp. 519–521. [Online]. Available: <http://accelconf.web.cern.ch/AccelConf/PAC2011/papers/mop222.pdf>
- [10] J. Egberts, "IFMIF-LIPAc Beam Diagnostics. Profiling and Loss Monitoring Systems," Theses, Université Paris Sud - Paris XI, Sep. 2012. [Online]. Available: <https://tel.archives-ouvertes.fr/tel-00772158>
- [11] J. Storey *et al.*, "Development of an Ionization Profile Monitor Based on a Pixel Detector for the CERN Proton Synchrotron," in *Proc. IBIC2015*, 2015, pp. 470–473. [Online]. Available: <http://accelconf.web.cern.ch/AccelConf/IBIC2015/papers/tupb059.pdf>
- [12] —, "First Results From the Operation of a Rest Gas Ionisation Profile Monitor Based on a Hybrid Pixel Detector," in *Proc. IBIC'17*, 2017, pp. 318–322. [Online]. Available: <http://accelconf.web.cern.ch/AccelConf/ibic2017/papers/we2ab5.pdf>
- [13] Tanabashi *et al.*, "Review of particle physics," *Phys. Rev. D*, vol. 98, p. 030001, Aug 2018. [Online]. Available: <https://www.doi.org/10.1103/PhysRevD.98.030001>
- [14] S. Kamakura, N. Sakamoto, H. Ogawa, H. Tsuchida, and M. Inokuti, "Mean excitation energies for the stopping power of atoms and molecules evaluated from oscillator-strength spectra," *Journal of Applied Physics*, vol. 100, no. 6, p. 064905, sep 2006. [Online]. Available: <https://www.doi.org/10.1063/1.2345478>
- [15] J. Weiss and W. Bernstein, "Energy required to produce one ion pair for several gases," *Physical Review*, vol. 98, no. 6, pp. 1828–1831, jun 1955. [Online]. Available: <https://www.doi.org/10.1103/physrev.98.1828>
- [16] H. Bichsel, D. H. Peirson, J. W. Boring, A. Green, M. Inokuti, and G. Hurst, "Average energy required to produce an ion pair, ICRU Report 31," *Journal of the International Commission on Radiation Units and Measurements*, vol. 16, no. 2, pp. 18–32, may 1979.
- [17] H. Schindler, R. Veenhof *et al.* (2019) Garfield++ - simulation of tracking detectors. [Online]. Available: <http://garfieldpp.web.cern.ch/garfieldpp/>
- [18] I. Smirnov, "Modeling of ionization produced by fast charged particles in gases," *Nuclear Instruments and Methods in Physics Research Section A: Accelerators, Spectrometers, Detectors and Associated Equipment*, vol. 554, no. 1-3, pp. 474–493, dec 2005. [Online]. Available: <https://www.doi.org/10.1016/j.nima.2005.08.064>
- [19] W. W. M. Allison and J. H. Cobb, "Relativistic Charged Particle Identification by Energy Loss," *Annual Review of Nuclear and Particle Science*, vol. 30, no. 1, pp. 253–298, dec 1980. [Online]. Available: <https://www.doi.org/10.1146/annurev.ns.30.120180.001345>
- [20] R. Wanzenberg. (2010, May) Nonlinear Motion of a Point Charge in the 3D Space Charge Field of a Gaussian Bunch. Hamburg, Germany. [Online]. Available: [http://www.desy.de/~mpywar/paper/2010/Internal\\_Report\\_M\\_10-01.pdf](http://www.desy.de/~mpywar/paper/2010/Internal_Report_M_10-01.pdf)
- [21] C. Thomas, F. Belloni, and J. Marroncle, "Space Charge Studies for the Ionisation Profile Monitors for the ESS Cold Linac," in *Proc. IBIC'16*, 2016, pp. 556–559. [Online]. Available: <http://accelconf.web.cern.ch/AccelConf/ibic2016/papers/tupg81.pdf>
- [22] F. Belloni *et al.*, "Space Charge Effects Studies for the ESS Cold Linac Beam Profiler," in *Proc. IBIC'18*, 2018, pp. 371–374. [Online]. Available: <http://accelconf.web.cern.ch/AccelConf/ibic2018/papers/weoc04.pdf>
- [23] S. Ramo, "Currents induced by electron motion," *Proceedings of the IRE*, vol. 27, no. 9, pp. 584–585, sep 1939. [Online]. Available: <http://doi.org/10.1109/JRPROC.1939.228757>
- [24] W. Shockley, "Currents to conductors induced by a moving point charge," *J. Appl. Phys.*, vol. 9, no. 10, p. 635, 1938. [Online]. Available: <http://doi.org/10.1063/1.1710367>
- [25] J. L. Wiza, "Microchannel plate detectors," *Nuclear Instruments and Methods*, vol. 162, no. 1-3, pp. 587–601, jun 1979.
- [26] J. Chaumont, F. Lalu, M. Salome, A.-M. Lamoise, and H. Bernas, "A medium energy facility for variable temperature implantation and analysis," *Nuclear Instruments and Methods in Physics Research*, vol. 189, no. 1, pp. 193 – 198, 1981. [Online]. Available: [https://doi.org/10.1016/0029-554X\(81\)90145-2](https://doi.org/10.1016/0029-554X(81)90145-2)
- [27] X. Llopart, R. Ballabriga, M. Campbell, L. Tlustos, and W. Wong, "Timepix, a 65k programmable pixel readout chip for arrival time, energy and/or photon counting measurements," *Nuclear Instruments and Methods in Physics Research Section A: Accelerators, Spectrometers, Detectors and Associated Equipment*, vol. 581, no. 1, pp. 485 – 494, 2007. [Online]. Available: <https://doi.org/10.1016/j.nima.2007.08.079>
- [28] V. Kraus, M. Holik, J. Jakubek, M. Kroupa, P. Soukup, and Z. Vykydal, "FITPix — fast interface for timepix pixel detectors," *Journal of Instrumentation*, vol. 6, no. 01, pp. C01 079–C01 079, jan 2011. [Online]. Available: <https://doi.org/10.1088/1748-0221/6/01/c01079>
- [29] P.-Y. Beauvais *et al.*, "Status report on the saclay high-intensity proton injector project (IPHI)," in *Proc. EPAC2000*, 2000, pp. 283–285. [Online]. Available: <http://accelconf.web.cern.ch/AccelConf/e00/PAPERS/THOAF202.pdf>
- [30] R. Gobin *et al.*, "High intensity beam production at CEA/Saclay for the IPHI project," in *Proc. ECRIS2016*, 2016, pp. 83–85. [Online]. Available: <http://accelconf.web.cern.ch/AccelConf/ecris2016/doi/JACoW-ECRIS2016-WEPP01.html>
- [31] F. Sene *et al.*, "Increase of IPHI Beam Power at CEA Saclay," in *Proc. IPAC'18*, 2018, pp. 694–696. [Online]. Available: <http://accelconf.web.cern.ch/AccelConf/ipac2018/doi/JACoW-IPAC2018-TUPAF016.html>



**Title :** Design of non-invasive profile monitors for ESS proton beam

**Key words :** *Proton accelerator, Beam diagnostics, Instrumentation, Detector*

**Abstract :** The European Spallation Source (ESS) will be a research infrastructure dedicated to sciences using neutrons as probes. The source is currently under construction in Lund, Sweden, and will be the world's brightest pulsed source of neutrons. As its name suggests, the production of neutrons is ensured by the spallation process : high energy protons will impinge a tungsten target. To accelerate the protons, a powerful 2 GeV linear accelerator is being built. The accelerator can be split in two parts. A "hot" part is responsible for acceleration up to 90 MeV. Then a "cold" part made of superconducting cavities cooled with liquid helium is used to reach the highest energies. The high intensity of 62.5 mA and the long pulse of 2.86 ms repeated 14 times per second, lead to an incredible beam power of 5 MW in average and 125 MW in peak. The knowledge of the beam is therefore mandatory to ensure the commissioning, i.e. the beam tuning in order to achieve a proper and safe functioning of the machine. Different diagnostics will be installed along the accelerator to fulfil these tasks. This thesis deals with the development of a non-invasive transverse profiler for the cold part of the ESS accelerator : the Ionization Profile Monitor (IPM). The thesis focuses on critical aspects of the IPMs to guarantee its feasibility in ESS beam conditions. These monitors are based on the ionization of the residual gas induced by the proton beam inside the beam pipe. A transverse electrical field is generated between both parallel plates of the IPM. The electrons or ions drift, with respect to the electric field, towards a segmented detector allowing the reconstruction of the beam profile in one transverse direction. For a complete transverse profile, it is necessary to add a second profiler tilted by 90°. Several challenges for facing IPM to the ESS conditions, which may compromise their use, are described :

- The weak counting rates due to the low ionization cross-sections at high energy (90 to 2000 MeV) and to the low residual gas pressure of 10-9 mbar.
- The electric field homogeneity inside the IPM, which is relevant for insuring a precise profile measurement, was not obvious in the narrow vacuum chambers devoted to them.
- The large Space Charge Effect of the beam, distorting the measured profile by deviating the ionization by-product trajectories. This fundamental aspect may compromise the use of an IPM for beam profile measurements.

Once these former studies done, we selected the three reliable read-out systems based on :

- Conductive strips read by a multichannel charge integrator.
- Micro-Channel Plates coupled with phosphor screen (pMCP).
- A silicon detector developed at CERN and foreseen for the future PS beam profiler.

This work was the object of the Preliminary Design Review (PDR 2017/01) marking the beginning of the construction phase of the different prototypes. Preliminary tests discarded the possibility of using silicon detectors due to the low ion energies. Starting from scratch, IPMs, reference monitors and a test bench were designed and installed at the IPHI proton accelerator at Saclay. Close ESS conditions were achieved to validate an IPM solution and our simulations. The test campaigns showed that an MCP is mandatory to detect signal. Moreover, the optical IPM (pMCP + Camera) is the preferred solution since it provides higher sensitivity. Feedbacks from the prototype test campaigns, allows us to deliver an IPM final design presented during the Critical Design Review (CDR 2019/02) leading to the beginning of the production phase.

**Titre :** Conception de profileurs non intrusifs pour le faisceau de protons de ESS

**Mot clés :** *Accélérateur de proton, Diagnostic faisceau, Instrumentation, Détecteur*

**Résumé :** La source européenne de spallation (ESS) sera une infrastructure de recherche dévolue aux sciences utilisant les neutrons comme sonde d'observation. Elle est actuellement en construction à Lund, en Suède, et sera la plus brillante des sources de neutrons pulsées au monde. Comme son nom l'indique, la production des neutrons est assurée par les processus de spallation : des protons à haute énergie bombardant une cible de tungstène. Le faisceau de protons est généré par un puissant accélérateur linéaire de 2 GeV qui peut être divisé en deux parties : une partie "chaude" qui accélère les protons jusqu'à 90 MeV, suivie d'une partie « froide » constituée de cavités supraconductrices refroidies à l'hélium liquide, permettant d'atteindre les 2 GeV. La forte intensité de 62.5 mA et la longue impulsion de 2,86 ms répétée 14 fois par seconde, conduisent à une puissance moyenne de faisceau de 5 MW et une puissance crête de 125 MW. La connaissance du faisceau est donc indispensable pour la mise en service, c'est-à-dire le réglage du faisceau afin d'assurer un fonctionnement correct et sûr de la machine. Différents diagnostics seront installés le long de l'accélérateur pour remplir ces tâches. Cette thèse traite du développement d'un profileur transverse non invasif pour la partie froide de l'accélérateur de ESS : les Ionization Profile Monitors (IPM). La thèse se concentre sur les aspects critiques des IPM afin de s'assurer de leur faisabilité dans les conditions du faisceau de ESS. Ces moniteurs sont basés sur l'ionisation induite par le passage des protons du gaz résiduel présent dans le tube de l'accélérateur. Un champ électrique est appliqué entre deux plaques parallèles de l'IPM. Les électrons ou les ions dérivent vers un détecteur segmenté permettant de reconstruire le profil dans une direction transverse du faisceau. Plusieurs défis, qui auraient pu compromettre l'utilisation des IPM pour les mesures des profils de faisceau à ESS, sont décrits :

- Les faibles taux de comptage dus aux faibles sections efficaces d'ionisation à haute énergie (90 à 2000 MeV) ainsi qu'aux basses pressions du gaz résiduel de l'ordre de 10-9 mbar.
- L'homogénéité du champ électrique à l'intérieur de l'IPM, essentiel pour assurer des mesures de profils précises mais difficile pour les chambres à vide étriquées des IPM.
- L'importante charge d'espace du faisceau, qui distord le profil mesuré en déviant les trajectoires des produits d'ionisation. Cet aspect fondamental peut remettre en cause l'utilisation d'IPM pour faire des mesures fiables de profil de faisceau.

Une fois ces études terminées, nous avons sélectionné trois systèmes de lecture fiables, basés sur :

- Des pistes conductrices lues par un intégrateur de charge multicanal.
- Des détecteurs à micro-canaux couplés à un écran phosphore (pMCP).
- Un détecteur de silicium développé au CERN, et utilisé en particulier pour le futur profileur du faisceau du PS.

Ces études ont fait l'objet d'une Revue de Conception Préliminaire (PDR 2017/01) marquant le début de la construction des différents prototypes. Les tests préliminaires ont écarté la possibilité d'utiliser des détecteurs au silicium en raison des trop faibles énergies des ions incidents. En partant de zéro, des IPM, des moniteurs de référence et un banc d'essai ont été conçus et installés sur l'accélérateur de protons IPHI à Saclay. Les conditions expérimentales de ESS ont été reproduites afin de valider une solution pour les IPM, ainsi que tester nos modèles. Les campagnes de test ont montré qu'un MCP était nécessaire pour détecter le signal d'ionisation. De plus, l'IPM optique (pMCP + caméra) est la solution recommandée car elle offre une sensibilité plus élevée. Le retour d'expérience accumulé lors des tests des prototypes, nous a permis de proposer une conception quasi finale d'un IPM, présentée lors de la Revue Critique de Conception (CDR 2019/02) menant au début de la phase de production.

